
Scanning Tunneling Microscopy
Studies of Model Systems Relevant to
Catalysis

Ebbe Kruse Vestergaard

Center for Atomic-scale Materials Physics,
Interdisciplinary Nanoscience Center and
Department of Physics and Astronomy,
University of Aarhus, Denmark

PhD thesis
February 2004

This thesis is submitted to the Faculty of Science at the University of Aarhus, Denmark, in order to fulfill the requirements for obtaining the PhD degree in Physics. The studies have been carried out under the supervision of Prof. Flemming Besenbacher in the Scanning Tunneling Microscopy Group at the Department of Physics and Astronomy from February 2000 to January 2004.

Contents

| | |
|---|------------|
| List of Publications | vii |
| 1 Introduction | 1 |
| 1.1 Catalysis - an essential technology in the modern society | 2 |
| 1.2 Catalysis in a future hydrogen society | 4 |
| 1.3 Surface science approach - Gaps in catalysis | 6 |
| 1.4 Outline | 8 |
| 2 Experimental methods | 11 |
| 2.1 Introduction | 12 |
| 2.2 Ultra-high vacuum chamber | 13 |
| 2.3 High-pressure cell | 16 |
| 2.4 Scanning Tunneling Microscopy | 18 |
| 2.4.1 Aarhus STM | 20 |
| 2.4.2 Theory of STM | 21 |
| 2.5 Additional UHV techniques | 23 |
| 3 Theoretical models | 25 |
| 3.1 Introduction | 26 |
| 3.2 Elementary surface processes | 26 |
| 3.3 d-band model | 27 |
| 3.3.1 Adsorption and reactivity | 28 |
| 3.3.2 Modifying the reactivity of metals | 31 |
| 4 Bridging the pressure gap - CO adsorption on Pt surfaces | 33 |
| 4.1 Introduction | 34 |
| 4.2 CO adsorption on Pt(110) | 35 |
| 4.2.1 Pt(110) surface | 35 |
| 4.2.2 Low-pressure CO adsorption on Pt(110) | 36 |
| 4.2.3 High-pressure CO adsorption on Pt(110) | 39 |
| 4.2.4 Discussion | 39 |

| | | |
|----------|---|------------|
| 4.3 | CO adsorption on Pt(111) | 41 |
| 4.3.1 | Previous studies of CO/Pt(111) | 41 |
| 4.3.2 | Experimental results | 42 |
| 4.3.3 | Discussion | 53 |
| 4.3.4 | Conclusion | 56 |
| 5 | Modifications of the active sites on a nickel surface | 59 |
| 5.1 | Introduction | 60 |
| 5.1.1 | Motivation | 60 |
| 5.1.2 | Nickel catalysts | 61 |
| 5.1.3 | Active sites for dissociation | 62 |
| 5.1.4 | Carbon phases on Ni(111) | 63 |
| 5.2 | CO dissociation | 64 |
| 5.3 | Modifying the Ni surface | 67 |
| 5.3.1 | Modifications of the Ni step edges | 67 |
| 5.3.2 | Modifications of the Ni terrace atoms | 71 |
| 5.3.3 | Discussion | 73 |
| 5.4 | Stability of a Au/Ni alloy at HP conditions | 74 |
| 5.4.1 | Experimental results | 75 |
| 5.4.2 | Discussion | 78 |
| 5.5 | Summary | 81 |
| 6 | O₂ adsorption and diffusion on titanium dioxide | 83 |
| 6.1 | Introduction | 84 |
| 6.2 | The rutile TiO ₂ (110) surface | 85 |
| 6.2.1 | Imaging of TiO ₂ (110) with STM | 88 |
| 6.2.2 | Crystal preparation - Type A defects | 88 |
| 6.3 | Oxygen adsorption on TiO ₂ (110) | 94 |
| 6.3.1 | Experimental results | 97 |
| 6.3.2 | Discussion | 105 |
| 6.3.3 | Summary | 111 |
| 6.4 | Diffusion of oxygen on TiO ₂ (110) | 111 |
| 6.4.1 | Diffusion analysis | 112 |
| 6.4.2 | Experimental results | 116 |
| 6.4.3 | Electron densities in semiconductors | 119 |
| 6.4.4 | Model of O ₂ diffusion | 122 |
| 6.4.5 | Diffusion of larger oxygen clusters | 125 |
| 6.5 | Outlook - modifying the reactivity | 126 |
| 7 | Surface oxide formation on platinum | 129 |
| 7.1 | Motivation | 130 |
| 7.2 | Previous studies | 131 |
| 7.3 | High-coverage oxygen structures | 133 |
| 7.4 | Comparison to theoretical results | 138 |
| 7.5 | Conclusion and discussion | 140 |

| | |
|------------------------------|------------|
| 8 Summary and Outlook | 143 |
| Bibliography | 149 |

List of Publications

- [I] *Comment on “High pressure adsorbate structures studied by scanning tunneling microscopy: CO on Pt(111) in equilibrium with the gas phase”*,
E. Kruse Vestergaard, P. Thostrup, T. An, E. Lægsgaard, I. Stensgaard, B. Hammer
and F. Besenbacher, Phys. Rev. Lett. **88**, 259601 (2002).
- [II] *CO-induced restructuring of Pt(110)-(1×2): Bridging the pressure gap with high-pressure STM*,
P. Thostrup, E. Kruse Vestergaard, T. An, E. Lægsgaard and F. Besenbacher,
Jour. Chem. Phys. **118**, 3724 (2003).
- [III] *Electron transfer-induced dynamics of adsorbed oxygen molecules on the TiO₂(110) surface*,
E. Wahlström, E. Kruse Vestergaard, R. Schaub, A. Rønnau, M. Vestergaard,
E. Lægsgaard, I. Stensgaard, and F. Besenbacher, Science, **303**, 511-513 (2004).
- [IV] *CO desorption rate dependence on CO partial pressure over platinum fuel cell catalysts*,
J. C. Davies, R. M. Nielsen, L. B. Thomsen, I. Chorkendorff, Á. Logadóttir,
Z. Lodziana, J. K. Nørskov, W. Li, B. Hammer, S. R. Longwitz, J. Schnadt,
E. K. Vestergaard, R. T. Vang and F. Besenbacher, Submitted to Fuel Cells.
- [V] *High-coverage structures of carbon monoxide adsorbed on Pt(111) studied by high-pressure scanning tunneling microscopy*,
S. Longwitz, J. Schnadt, E. Kruse Vestergaard, R. T. Vang, E. Lægsgaard,
I. Stensgaard, J. K. Nørskov and F. Besenbacher, In preparation.
- [VI] *Adsorbate induced alloy phase-separation: A direct view by high-pressure scanning tunneling microscopy*,
E. Kruse Vestergaard, R. T. Vang, J. Knudsen, E. Lægsgaard, I. Stensgaard and
F. Besenbacher, In preparation.
- [VII] *STM studies of CO dissociation on Ni(111): Influence of steps*,
R. T. Vang, E. Kruse Vestergaard, E. Lægsgaard, I. Stensgaard, J. K. Nørskov and
F. Besenbacher, In preparation.

-
- [VIII] *The adsorption and dynamics of O₂ on the rutile TiO₂(110) surface studied by scanning tunneling microscopy*,
E. Wahlström, E. Kruse Vestergaard, R. Schaub, A. Rønnau, E. Lægsgaard,
I. Stensgaard and F. Besenbacher, In preparation.
- [IX] *Long-range repulsive vacancy-vacancy interactions on rutile TiO₂(110)*,
A. Rønnau, R. Schaub, E. Wahlström, E. K. Vestergaard,
E. Lægsgaard, I. Stensgaard and F. Besenbacher, In preparation
- [X] *Dissociative adsorption of bromine on TiO₂(110) - no evidence of hyper-thermal motion*,
K. Swamy, E. Kruse Vestergaard, P. Thostrup, E. Lægsgaard, I. Stensgaard and
F. Besenbacher, In preparation.
- [XI] *Oxidation of Pt(110)*,
L. Österlund, W. X. Li, E. Kruse Vestergaard, J. Matthiesen, R. T. Vang,
T. M. Pedersen, B. Hammer and F. Besenbacher, In preparation.
- [XII] *Controlling the catalytic selectivity of Ni surfaces by step blocking*,
R. T. Vang, K. Honkala, S. Dahl, E. Kruse Vestergaard, J. Schnadt, E. Lægsgaard,
B. S. Clausen, J. K. Nørskov and F. Besenbacher, In preparation.

CHAPTER 1

Introduction

In this chapter a motivation of the experimental studies described in the thesis is given. Some of the basic concepts of catalysis are outlined together with a brief discussion of different routes towards catalyst design. One of the great future challenges for catalysis is concerned with a forthcoming “hydrogen society”, where hydrogen replaces fossil fuels as the main energy carrier. Some of the technologies necessary to transform our present energy system into a hydrogen-based society are outlined, and some fundamental problems which can be addressed with surface science studies are described. Finally, the concept of surface science model systems is discussed, and a number of gaps between the so-called surface science approach and large-scale industrial catalysis are addressed.

1.1 Catalysis - an essential technology in the modern society

Catalysis is ubiquitous in nature as well as in the chemical industry. From enzymatic processes to the production of ammonia and the refinement of crude oil, catalysis plays a key role. All three processes are essential for life as we know it; many of the vital functions within our body are governed by catalysis, and without the availability of ammonia-based fertilizers the present human population would not be sustainable. Furthermore, one of the main pillars of the modern society is the availability of cheap and abundant energy, which is currently based on fossil fuels. The detailed functioning of catalysts is only understood in a few cases, even though the basic principles of catalysis are indeed rather simple: A catalyst is a compound which increases the rate of a chemical reaction but which is not itself consumed by the reaction. Moreover, a catalyst may selectively favor specific reactions over competing and undesirable reactions. The action of a catalyst is often based on providing new pathways for a given chemical reaction by e.g. facilitating bond breaking of (some of) the reactant molecules and by providing adsorption sites where the reactants can meet and form new products. Designing a good catalyst is thus a delicate balance between, on one hand, having a sufficiently strong interaction to break the relevant bonds in reactant molecules yet, on the other hand, having an interaction which is sufficiently weak not to inhibit the formation and subsequent release of the product molecules.

A large fraction of the catalysts used in the chemical industry belongs to the class of *heterogeneous* catalysts, where the catalyst material is at a different phase (typically solid) than the reactants and products (typically gaseous or liquid). Homogeneous catalysis is also found and is prevalent especially in biological processes like enzymatic reactions. The economical impact of heterogeneous catalysis is enormous. The production of a large range of commercial chemicals comprises one or even several catalytic processes, and most of the chemical industry is thus crucially dependent on catalysis technology. One of the most well-known uses of catalysts in everyday-life is the three-way automobile exhaust catalyst, which oxidizes the poisonous carbon monoxide and unburned hydrocarbons, and reduces the amount of NO_x species, but other catalysts for the production of a variety of chemicals are even more important [1].

Catalytic processes can typically be divided into a number of elementary steps as illustrated in Fig. 1.1: Gaseous reactant molecules adsorb on a catalyst surface, and some of them might dissociate. The adsorbate species diffuse on the surface and encounter other species. Reactions occur and new products are formed, which eventually desorb from the catalyst surface. A key role of the catalyst is to lower the activation barrier of the elementary steps compared to the activation barrier of the gas phase reaction, and in cases where selectivity for a specific reaction is desired, a good catalyst may lower the barrier for certain elementary surface processes while other barriers are kept high. The overall change in the Gibbs free energy throughout a reaction is unaltered by the catalyst, and the equilibrium constant is thus unaffected by the catalytic processes. The rate of a reaction can, however, be many orders of magnitude higher when a catalyst material is present compared to pure gas or liquid phase reactions.

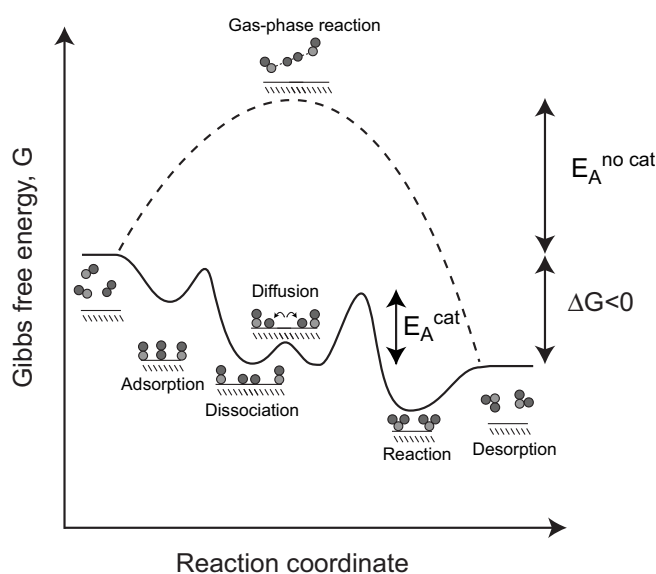


Figure 1.1: Illustration of the elementary steps in heterogeneous catalysis for two (different) diatomic molecules. The dashed line corresponds to an un-catalyzed gas-phase reaction. The rate of the chemical reaction is increased by orders of magnitude when the barrier for each elementary step is (significantly) lower than the barrier for the un-catalyzed reaction.

The search for catalyst materials during the early part of the 20th century was mostly characterized by explorative trial-and-error quests among different combinations of metals, oxides and sulfides, and even today large-scale screening where hundreds of combinations of metals and oxides are tested for catalytic activity in miniaturized parallel reactors is seen as one of the important methods for catalyst development [2, 3]. During the same period of time, fundamental research has, however, also emerged. The basic concepts of surface/gas-phase interactions have been studied and trends in catalytic activity have been derived based on an increasing level of atomistic understanding of the elementary steps. This more fundamental approach to catalysis was initiated by Langmuir early in the 20th century, when he formulated some of the basic ideas of surface science, e.g. the existence of a definite number of checkerboard-like adsorption sites on the catalyst material [4, 5]. Another important concept in catalysis is the idea of “active site”, which was introduced by Taylor in 1925 [6]. He suggested that the Langmuirian idea of a flat surface with a specified number of (identical) adsorption sites might be inadequate, and that under-coordinated surface atoms would probably be more reactive and e.g. enable the formation of more than one adsorbate bond. Since then, a number of examples have indeed confirmed the existence of active sites on surfaces, and the studies of Ni catalysts presented in Chapter 5 provide an example of such site specific reactions.

For many years, the main motivation in surface science research has been the investigation of the elementary processes in heterogeneous catalysis, and one of the ultimate goals of surface science is without doubt to design new and improved catalysts based on a fundamental understanding of the atomic-scale processes involved in the reactions. In a few cases, such surface science based catalyst design has actually been demonstrated [7], but new catalysts are generally still being discovered by a combination of chemical intuition and screening methods. Considering ammonia synthesis as a case study example of the future prospects and possibilities for catalytic research, we find that the iron catalyst which was discovered around 1900 by Haber, Bosch and Mittasch is even today still the most widely used catalyst material for this process. Other minor improvements have followed but all industrially known ammonia catalysts, however, still operate at high-pressure conditions (100 bar) and at high temperatures ($\sim 400^\circ\text{C}$), the rate-limiting step being the breaking of the strong triple-bond in molecular nitrogen [1, 8]. One might thus, disappointedly, be tempted to conclude that the catalyst development has reached saturation within this field, but actually there is still plenty of room for development. If we shift focus from industry to nature, we find a good ammonia catalyst, which is active at ambient pressures and temperatures. The enzyme nitrogenase, which among other things consists of a molybdenum/iron based protein, catalyzes the formation of ammonia from N_2 , electrons and protons, and with the enzyme used as a catalyst the reaction runs at room temperature and atmospheric pressure [8]. We are thus far from reaching the ultimate limit for understanding and developing catalysts - even for chemical reactions where the industrial catalyst in use is more than a hundred years old! It is, however, reasonable to believe that trial-and-error based screening for catalysts may be reaching saturation, and that new breakthroughs will demand fundamental atomic-scale understanding of the complex processes occurring both on metal surfaces but also within nature's own catalysts.

1.2 Catalysis in a future hydrogen society

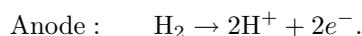
One of the emerging technological areas where surface science based catalyst design may become of great importance is a forthcoming "hydrogen society": The depletion of resources and environmental problems are major drawbacks in the present use of fossil fuels as energy supply, and the finding of sustainable alternatives is therefore of utmost importance. Hydrogen is believed to play a vital role as an energy carrier in a future so-called *hydrogen society* based on the energy supply from renewable sources, and many experts foresee that the *hydrogen era* may soon be initiated. This is witnessed in the large worldwide attention and financial support to hydrogen energy research: In the US, for example, President Bush has recently announced a \$1,2 billion hydrogen fuel initiative to reverse the growing dependence on foreign oil and to establish a stable and secure energy supply [9], and in Iceland large initiatives have been taken to become the first hydrogen society powered by geothermal and hydroelectric energy [10]. The production and utilization of hydrogen as an energy carrier pose great challenges for future catalyst design, and considerable scientific and technological progress must be made before hydrogen can become a viable alternative to fossil fuels.

Several examples of sustainable, catalytic pathways for hydrogen production already exist: For example hydrogen can be produced from water by utilizing the energy of sunlight in a titanium dioxide-based photocatalyst [11, 12], and furthermore, hydrogen can be derived from biomass by catalytical reforming of sugars to hydrogen and CO on platinum-based catalysts [13, 14]. These sustainable methods, however, suffer from relatively low conversion efficiencies at their present stage of development, and the vast majority of the hydrogen production nowadays comes from *steam reforming* of fossil fuels, an endothermic reaction utilizing nickel catalysts for the production of hydrogen and CO from water and methane. Even though steam reforming is still based on the supply of fossil fuels, the reaction may play an important role in the early stages of the transition to a hydrogen-based society. With natural gas being practically a waste product in the oil industry, steam reforming can offer a cheap way of producing hydrogen, and this could help in motivating the development of other hydrogen technologies.

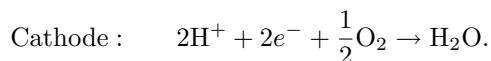
The chemical energy stored in hydrogen molecules is most efficiently used in a fuel cell, where the reaction with oxygen to form water is separated into two partial reactions occurring at different electrodes separated by an ion-conducting electrolyte. The oxidation (liberation of electrons) takes place at the anode and the reduction at the cathode, and the electrons are forced to move through an external circuit whereby the chemical energy can be converted into electricity with very high efficiency.

Several types of fuel cells exist, characterized by having different mobile ions in the cell reaction and different operating temperatures [15]. The basic principle of operation of all types of fuel cells is the same, and only the so-called *polymer electrolyte membrane fuel cell* (PEM-FC) will be discussed here. The PEM-FC is considered to be the most suitable fuel cell for vehicle applications owing to its low operating temperature (80–100°C).

In the PEM-FC, hydrogen is dissociated at the anode:



Protons are conducted through a polymer electrolyte membrane to the cathode, where they react with oxygen and with electrons passing through the external circuit:



The presence of liquid water is vital to the functioning of the membrane, limiting its operating temperature to below 100° C, which puts constraints on the purity of the hydrogen fuel and the choice of catalyst for the anode process. For operation on pure hydrogen (e.g. produced by electrolysis) platinum works well as an anode catalyst, but even small amounts (10–100 ppm) of residual CO in hydrogen produced from steam reforming lead to a degradation of the catalyst efficiency, an effect known as *CO poisoning*. The poisoning effect is due to a high binding energy of CO to the catalyst surface, resulting in a surface covered with CO, and thus no vacant sites for hydrogen dissociation. Since the hydrogen production is most likely to be based on the reformation of fossil fuels for years to come, the problem of CO poisoning has to be solved. Different routes may be considered: One option is to develop new membranes with operating temperatures above 100°C [16], which would diminish the poisoning effect of CO. Another

option is to design new catalyst materials with a lower affinity for binding CO than platinum but which still catalyze the hydrogen dissociation [17]; and finally, the possibility of selectively oxidizing the CO molecules in a H₂/CO mixture may be envisioned [18].

The interaction of CO with catalyst surfaces plays a prominent role for the understanding of the technological processes underlying a future hydrogen society. For hydrogen production, CO is present under conventional steam reforming and water gas shift reactions, and if the exploitation of bio-materials for hydrogen production should ever become viable, a better understanding of the ability to selectively break or preserve C=O bonds on different metals is essential [14]. Concerning the utilization of hydrogen in fuel cells, finding solutions to the CO poisoning problem of the Pt anode catalyst is of utmost importance. Some solutions based on PtRu alloys already exist [19], but a further improvement of the fundamental understanding of the CO/Pt interaction is compulsory. A more general problem, both in catalysis and especially for fuel cell applications, is the high price of Pt, which contributes to the fact that e.g. fuel cell-based automobiles are yet not competitive as compared to conventional gasoline-based automobiles. The basic understanding of platinum's chemical properties could therefore also be set as the starting point for a general search for cheaper compounds with similar characteristics. The studies presented in Chapters 4 and 5 both concern the interaction of CO with metal surfaces and are therefore (partly) motivated in the problems discussed above. In Chapter 4, the interaction of CO with platinum surfaces is investigated at high-pressure conditions, and in Chapter 5, we investigate the dissociation of CO on nickel and utilize the acquired knowledge to design modified nickel surfaces where the catalytic properties of platinum is approached.

1.3 Surface science approach - Gaps in catalysis

Large-scale industrial catalysts are naturally optimized to expose large catalytic surface areas with as little loading of catalytic material as possible. The latter is especially important when expensive transition metals, like Pt, are used as catalysts, but also out of practical convenience, a high surface-to-volume ratio for the catalyst materials is essential. The conventional way of realizing such demands is by depositing the catalytically active materials as nano-particles on high-surface-area porous support materials like alumina or spinel [20, 21]. The support materials impregnated with catalytic particles are typically extruded as pellets, which are stored in tubular reformers where a flow of reactant (and product) gasses pass each catalyst pellet [20, 21]. The complexity of such a system is enormous, and the high pressures and high temperatures invoked under operating conditions make it even harder to acquire fundamental knowledge of the processes occurring at the atomic level during catalytic reactions.

Surface science studies relevant for the understanding of catalysis have traditionally employed great simplifications compared to the industrial conditions described above. In what has now become known as the "surface science approach", single-crystal metal surfaces and their interaction with gasses have been studied under ultra-high vacuum conditions as model systems for large-scale catalysis [1, 5, 22–24]. Such model system studies have yielded an enormous amount of detailed information about the atomic

arrangement and electronic configuration at surfaces, about surface imperfections like steps, kinks, ad-atoms and vacancies, and about surface dynamics such as atomic diffusion and step fluctuations [25]. Gas adsorption and desorption have been extensively studied at low pressures (typically $< 10^{-6}$ mbar) and reaction models have been developed describing the elementary steps of the surface reactions sketched in Fig. 1.1 [1]. In some cases it has even been demonstrated that the activity of a working industrial catalyst can be predicted by such models based solely on data from surface science experiments at ultra-high vacuum conditions [26, 27].

A number of significant gaps are, however, readily identified between the model systems studied by surface scientists and nano-particle catalysts exposed to pressures of several hundred bars. The gaps can be summarized in two main categories: [23, 24, 28]

- Pressure gap
- Materials gap

The pressure gap concerns the enormous difference of at least 9 orders of magnitude between UHV compatible pressures ($\leq 10^{-6}$ mbar) and industrial conditions (from 1 to several hundred bars). To maintain a high adsorbate coverage under low pressure conditions, surface science experiments are typically performed at low temperatures, which may, however, lead to kinetic restrictions or other effects that are different from the industrial conditions. In some cases, it is thus more relevant to discuss a *temperature gap* even though the two gaps are closely connected.

The materials gap comprises the disparity between nano-particles of catalytically active materials supported on porous oxide supports and the single-crystal surfaces studied by surface scientists. When catalyst particles become small, the density of defect sites like steps and kinks grows, and the adsorbate interaction with defects is often very different than what is found on large, flat terraces on single crystals. Such effects can, however, to a certain extent be mimicked by performing experiments on high-index, stepped single-crystal surfaces. Moreover, new properties of nano-particles, like quantum size effects, may be observed as proposed in [29], and the support material may also influence the chemical properties of the catalyst particles when the size is shrunk to a few nanometers [30]. A range of recent studies have addressed such materials gap effects by studying metal nano-particles on single-crystal or thin-film oxide supports (See e.g. [28–33]). An excellent example of the astonishing differences found between single crystal chemistry and the nano-particle properties is provided by the catalytic properties of dispersed gold clusters on, e.g., a titanium oxide support [18, 29, 34, 35]. Gold is known as the most noble metal and is catalytically inactive for virtually any reaction in its macroscopic single-crystal form [36], but when Au nano-particles are considered, a new world of catalytical possibilities appears, and e.g. CO oxidation is facilitated even at low temperatures. The studies of titanium dioxide presented in Chapter 6 are indeed motivated by these findings and aim at understanding the fundamental properties of the material and its interaction with oxygen. Even without Au clusters, the titanium dioxide surface exhibits a tremendously complex oxygen chemistry, and properties unseen on metal surfaces, e.g. charge transfer induced diffusion, are found.

Even on metallic catalyst particles, oxides may form under reaction conditions, thus being the “active” phase in the catalyst. At ambient conditions, metal oxides are indeed

the most stable phase of many metals, and the formation of thin oxide layers on metals is thus a very important issue when considering combinations of the pressure and materials gap [37–39]. CO oxidation on ruthenium serves as a good example of such an effect: Under UHV conditions, ruthenium is a poor CO oxidation catalyst, but under high-pressure reaction conditions, a ruthenium-oxide phase is formed which is an excellent catalyst for CO oxidation [37]. The studies of Pt-oxide formation of the Pt(110) surface presented in Chapter 7 are motivated by such discussions and attempt to discover new “active” phases of Pt-oxide which might be relevant under realistic reaction conditions. In a few studies both the materials and pressure gap have been addressed by exposing oxide-supported metal clusters to high-pressure conditions [40–43], and such studies have indeed contributed significantly to the understanding and bridging of the gaps between fundamental studies of traditional surface science model systems and large-scale applied catalysis. In the present thesis only single crystal surfaces have been studied, and the model systems are thus of a more simple character than the oxide-supported metal clusters discussed above. On the other hand, the scanning tunneling microscope, which has been used in the presented studies is unique in the sense that it facilitates imaging with atomic-scale resolution even at pressures up to 1 bar. Other important aspects of e.g. the pressure gap can therefore be addressed, like structural information of adsorbate phases as a function of pressure.

1.4 Outline

The present thesis consists of a number of different scanning tunneling microscopy (STM) studies spanning the entire range from fundamental research to conceptual ideas for possible catalyst designs. Chapter 2 describes the experimental setup, and some of the concepts for the discussion of metal surface reactivity are briefly discussed in Chapter 3. The subsequent chapters take their starting point in a project concerning the *pressure gap* for CO adsorption on two platinum surfaces (Chapter 4). These studies concern the fundamental question of applicability of surface science model systems, and as we will see in this chapter, STM is indeed an ideal tool to address such questions since it is capable of giving atomically resolved images of adsorbate phases at high-pressure conditions.

The high price of Pt has spurred a search for cheaper compounds with the same catalytic properties [1]. In Chapter 5, we present studies along these lines, where the CO interaction with Ni is characterized and modified in different ways, whereby a Pt-like surface is approached. One of the possible Ni-based compounds, a Au-Ni surface alloy, is studied under high-pressure conditions to evaluate its stability. We find that the alloy undergoes a complete phase-separation, and the atomic-scale details of the process are scrutinized with time-resolved STM movies.

The interaction of oxygen with a titanium dioxide (TiO₂) surface is described in Chapter 6, and the adsorption and diffusion of oxygen on the surface are found to exhibit complex charge induced phenomena which are unseen on metal surfaces. The disparities between oxide and metal surfaces may be regarded as a materials gap, and the presented studies provide new insight into the processes occurring on “active” oxide

support materials.

The last study (Chapter 7) describes the formation of platinum-oxide on a Pt(110) surface upon exposure to high pressures of O₂ or atomic oxygen. Pt-oxide layers were recently proposed to form under realistic reaction conditions for CO oxidation, and the oxide phase was actually suggested to be catalytically more active than the pure metal surface [39]. Our STM studies of platinum-oxide formation provide new insight into the atomic-scale structure of oxide growth on Pt(110). These studies are therefore relevant in a discussion of the materials gap between the traditional metal surface model systems and the (possible) formation of oxides with a significantly different structure and chemistry at high-pressure reaction conditions.

The different experimental studies presented in the thesis are all examples of surface science based investigations of model systems aiming at a fundamental understanding of the underlying atomistic processes for catalytic phenomena on surfaces. The ordering of the chapters reflects an increasing degree of complexity of the studied model systems: The studies of CO adsorption on platinum surfaces at high-pressure conditions are conceptually the most simple, because only molecular adsorption on single-crystal surfaces of pure metals is considered. The nickel studies presented in the subsequent chapter go a step further by scrutinizing not only adsorption but also dissociation and the concept of active sites. The fundamental knowledge thus gained is subsequently used in different suggestions for modified catalysts. The complexity of model systems is further enhanced in Chapter 6 where the metal surfaces are replaced by an oxide surface, TiO₂(110). For such surfaces, the concept of a well-defined, clean and reproducible surface is found to be more problematic than for metal surfaces, and defects in the form of oxygen vacancies are found to play a crucial role for the surface chemistry. Finally, the platinum-oxide studies serves as an example of even larger complexity in that the substrate material itself undergoes changes and new material phases are formed.

CHAPTER 2

Experimental methods

The first one and a half year of the present PhD studies were dedicated to the build-up and testing of the experimental setup used in most of the studies included in this thesis. The setup consists of an ultra-high vacuum (UHV) chamber combined with a small-volume cell facilitating high-pressure scanning tunneling microscopy studies. After a brief introduction to the concepts of UHV, the features of the setup are outlined including the vacuum parts (pumps and valves), a security system and a computer-controlled sample cleaning system. The main experimental technique used in the studies is scanning tunneling microscopy (STM), and the general operating principle of this technique is discussed together with the specific design of the “Aarhus STM”. Finally, a brief section summarizes some of the other available techniques at the chamber.

2.1 Introduction

Surface science was born as a discipline already in the early 20th century when Langmuir and other pioneering scientists developed some of the basic concepts that are still in use [1]. It was, however, the development of ultra-high vacuum techniques in the 1960s that seriously triggered and accelerated the development of the field. This was partly due to the need of easily accessible proper vacuum conditions to facilitate long mean-free path lengths of the electrons and ions used as surface probes, but even more importantly, it was due to the requirement of sufficiently low fluxes of gasses to maintain clean and well-defined surfaces during typical experimental times. For example, Davisson and Germer already published their pioneering results on electron diffraction in 1927, but it was not before proper ultra-high vacuum conditions was developed that the technique now known as low-energy electron diffraction (LEED) became a standard surface science tool [44].

The need for low pressure conditions to maintain clean surfaces can be perceived in a simple way by estimating the time it takes to cover a surface with adsorbed molecules. According to kinetic gas theory, the flux of molecules hitting a given surface can be expressed as

$$F(\text{molecules}/(\text{cm}^2\text{s})) = 2.63 \times 10^{18} \frac{P(\text{mbar})}{\sqrt{M(\text{g}/\text{mole})T(\text{K})}}, \quad (2.1)$$

where P is the pressure, M the molar weight of the gas, and T is the temperature [1]. The standard unit for measuring the adsorbate coverage on surfaces is *monolayer* (ML), where 1 ML corresponds to an adsorbate density equal to the density of surface atoms in the exposed crystal. For metal crystals this density is of the order of 10^{15} atoms/cm², and assuming that every gas molecule encountering the crystal will stick irreversibly to the surface, Eq. 2.1 can be integrated to yield the adsorbate coverage as a function of time, pressure and temperature. The time needed to perform a typical surface science experiment is of the order of 1 hour, and if we demand that the number of gas molecules hitting the surface should correspond to less than a coverage of 1 ML within the duration of the experiment, we find that the pressure for a room temperature gas should be less than $1.8 \cdot 10^{-10}$ mbar.¹ The typical base pressure of UHV chambers is $\leq 10^{-10}$ mbar and, furthermore, not all of the molecules present in the *rest gas* adsorb irreversibly on the surface. It should thus be possible to maintain a clean and well-defined surface for at least a few hours in a UHV chamber.

The unit of gas exposure typically employed in the surface science literature upon (deliberate) gas dosing is named after Langmuir, and 1 Langmuir (1 L) is defined to correspond approximately to the gas exposure necessary to form a monolayer of adsorbates (again assuming a sticking probability of one). The unit is thus defined as: $1 \text{ L} = 10^{-6} \text{ torr}\cdot\text{s}$, where the torr unit is defined as: $760 \text{ torr} = 760 \text{ mmHg} = 1000 \text{ mbar}$. The Langmuir and monolayer units will be used throughout the thesis to characterize exposure and coverage, respectively, when discussing the interaction between gasses and

¹In the calculation the gas is assumed to consist of hydrogen molecules. Typically the *rest gas* in a UHV chamber is a mixture of hydrogen, carbon monoxide and water.

surfaces.

2.2 Ultra-high vacuum chamber

The UHV chamber is equipped with a variety of techniques for preparing and analyzing surfaces together with a multitude of pumps, valves and gauges for maintaining the desired low-pressure conditions (see Fig. 2.1). The main chamber is pumped by a magnetically levitated turbopump (Leybold) with a capacity of 340 ℓ/s and an ionpump (Varian) with a capacity of 240 ℓ/s . Furthermore, the chamber is equipped with a titanium sublimation pump, which reduces the amount of hydrogen in the rest gas. The pressure in the chamber is measured by an ionization gauge (Varian) and the rest gas is monitored with a Balzers quadrupole mass spectrometer. The pumping of the gas lines and the differential pumping of the mass spectrometer and an ion gun is done with a small Leybold turbopump with a capacity of 50 ℓ/s . The pressure in this differential pump line is measured by another ionization gauge (Varian). The chamber is connected to a high-pressure cell (HP cell), which is pumped together with the gas lines from a gas purification system by a two-stage Varian turbopump (70 ℓ/s). This type of turbopump enables the use of an oil-free scroll pump as backing pump, which further minimizes the pollution of the high-pressure part of the system. Finally, the chamber is equipped with a load lock, also pumped by the Varian turbopump, enabling sample transfer to and from the UHV chamber without venting the entire chamber. The pressure in the HP cell is monitored by two MKS Baratron covering in total the range from 10^{-4} torr up to 1000 torr. The low-pressure side of the Varian turbo is additionally equipped with a Balzers Full-Range pressure gauge capable of following the pressure from 1 atm down to UHV. The Full-Range gauge is a combination of a Pirani and a cold cathode gauge. All forepump pressures are monitored by Pirani gauges (Leybold). A vertical sample manipulator (Thermionics) is installed at the center axis of the chamber. The manipulator is fully rotatable, thereby introducing an intrinsic leak in the system which is, however, counteracted by a two-stage pumping system; The first stage is at low vacuum (forepump) and the second stage is pumped by a small 20 ℓ/s ionpump (Thermionics).

To protect the pumps in case of serious leaks and to avoid accidental venting of the chamber in case of power failures, a security system has been built to control the pneumatic valves shown in Fig. 2.1. A schematic drawing of the security system input is shown in Fig. 2.2. The system is based on simple relay contacts in the pressure gauges and pump controllers. In case of a failure, one (or more) of the relays will open its circuit and the security system will close the relevant valves, protecting both the chamber and the pumps. To reopen the valves, the security system must be manually reset, thereby ensuring that the problem has been solved. Each input to the security system can, however, be bypassed which is necessary, for example, when the pneumatic valves must open for pumping down the chamber after a venting. In addition to the valve control, a power interlock system is integrated in the security system, to ensure that filament-containing devices in the chamber (except for the ion gauges) are shut off if a failure occurs.

The vertical manipulator contains a sampleholder, which can be rotated and trans-

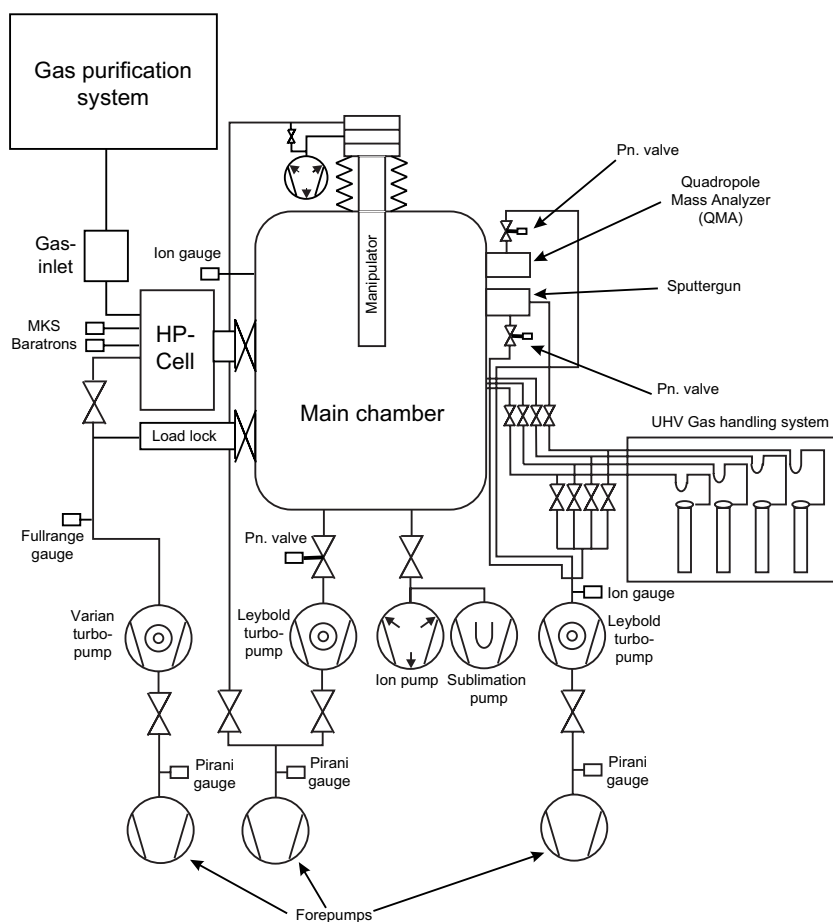


Figure 2.1: Schematic drawing of the UHV chamber with vacuum components.

lated in the vertical direction with computer-controlled step motors. Translation in the horizontal plane is enabled by a manually controlled X-Y stage. The manipulator contains a dewar connected to the sampleholder via a copper braid, which renders the cooling of samples with liquid nitrogen possible. Because of non-negligible thermal resistance in the braid and due to heat transfer from other parts of the system, the minimum temperature is limited to approximately 140 K. A filament for sample annealing is situated in the sampleholder of the manipulator radiating the backside of the samples to avoid damage to the single crystal surfaces. The filament can be negatively biased relative to the sample, which gives the possibility of heating via electron bombardment. The sample is externally grounded, and the current from electron bombardment, sputtering or other processes in the chamber can thus be monitored. The maximum temperature accessible is ~ 1500 K, which is the melting point of the thermocouple material.

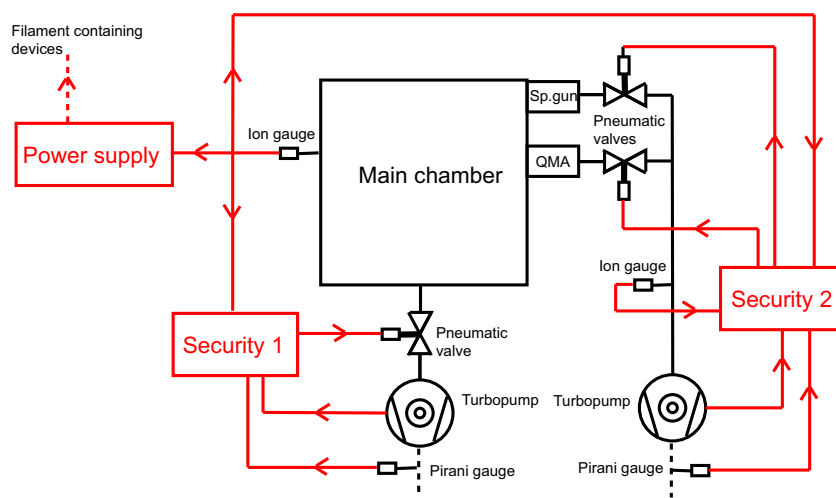


Figure 2.2: Schematic drawing of the security system for the UHV chamber. The relay-based electrical signals are drawn in red to distinguish them from the pump lines.

The crystals used for experiments in the chamber are all mounted in 1 mm thick tantalum plates with a Chromel/Alumel thermocouple junction pressed against the backside of the crystal. A variety of crystals are present in the chamber in a “garage” system where the Ta holders are stacked and easily transferred to and from the manipulator by using a horizontally mounted linear transfer rod. The manipulator contains matching female Chromel/Alumel connectors and once a Ta holder with a crystal is in the manipulator, the temperature is continuously monitored. The cleaning of samples is done by repeated cycles of sputtering with Ar^+ ions and annealing at elevated temperatures. The procedure has been automated with a computer program controlling the ion gun, the Argon (and possibly oxygen) gas inlet, the ion pump, and a Eurotherm temperature controller (see Fig. 2.3). The computer program continuously checks the pressure in different parts of the UHV system, and the cleaning procedures are terminated in a safe way if any error is found. Gas inlet is controlled with analog signals (0–10 V) from the computer to a high-voltage supply (0–1.25 kV) controlling the piezo valves. All other communication is done via RS-232 serial communication. The annealing ramps are controlled with PID regulation by the Eurotherm temperature controller, which sends a 0–10 V signal to a filament supply. The computer program thus merely monitors the temperature during annealing and only interrupts in case of a failure. Oxygen can be supplied during annealing, which is, for example, relevant for Pt and Ni crystals in the initial cleaning phases for carbon removal.

The UHV chamber is equipped with a thermal gas cracker and three metal evapora-

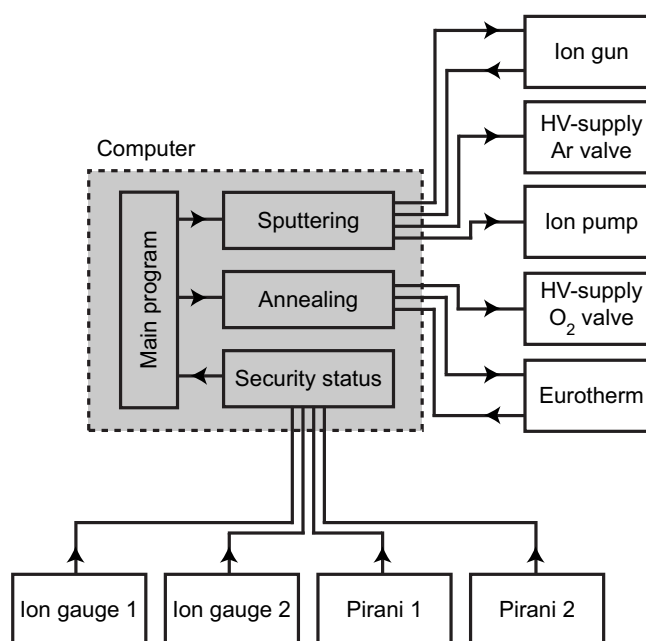


Figure 2.3: The computer controlled communication during automated cleaning of crystals.

tors. The gas cracker (Oxford Applied Research, TC-50) uses a narrow tube which is heated by electron bombardment to dissociate gas molecules, and cracking efficiencies on the order of 50% is obtained for, e.g., oxygen, as described in Chapter 7. Two of the metal evaporators are home-built and consist of simple tungsten crucibles containing the metals for evaporation. The crucibles are heated resistively with currents of the order of 7–11 A. The third evaporator is a commercial 4-pocket evaporator (Oxford Applied Research, EGC04) capable of evaporating up to four different metals at the same time. The Oxford evaporator uses electron bombardment of 1–2 mm thick rods of the different metals, and, as a great advantage compared to the home-built evaporators, the flux of ionized metal atoms is monitored with a grid in front of the rods.

2.3 High-pressure cell

The UHV chamber is equipped with a high-pressure cell (HP-cell) containing a high-pressure STM (HP-STM). With a linear transfer rod the sample can be moved from the manipulator in the UHV chamber through a gate valve to the HP Cell. Initial cleaning and inspection of the crystals is done with standard surface science techniques in the UHV chamber before transferring the sample to the HP cell. When the clean and well-characterized sample is positioned in the HP-STM, the gate valve is closed and the

cell is pressurized with up to 1 bar of purified gas. The free volume of the HP cell is approximately 0.5ℓ , thus minimizing the gas consumption. The HP-STM is in principle identical to the Aarhus UHV-STM described below in section 2.4.1, but the small size of the cell necessitates a more compact design, for which reason no cooling or heating facilities are integrated in the HP-STM [45]. Heating is, however, possible by an external heating of the entire cell, which is e.g. utilized in the experiments described in section 4.2.

The HP cell consists of a stainless steel cross with a window at the top flange, enabling visual inspection of the sample transfer with a video camera. The STM is attached at the bottom flange and valves and pressure gauges are attached at the sides. The pumping is shown schematically in Fig. 2.1. All metal parts of the STM and the cell have been electrochemically gold-plated to minimize reactions with the high-pressure gasses inside the cell. The pressure is currently limited to 1 bar because of the top window, which is not designed to withstand pressure from the inside. The STM itself, however, is not limited to this pressure and the possibility of installing another type of window is being considered, motivated e.g. by the experiments presented in Section 4.3.

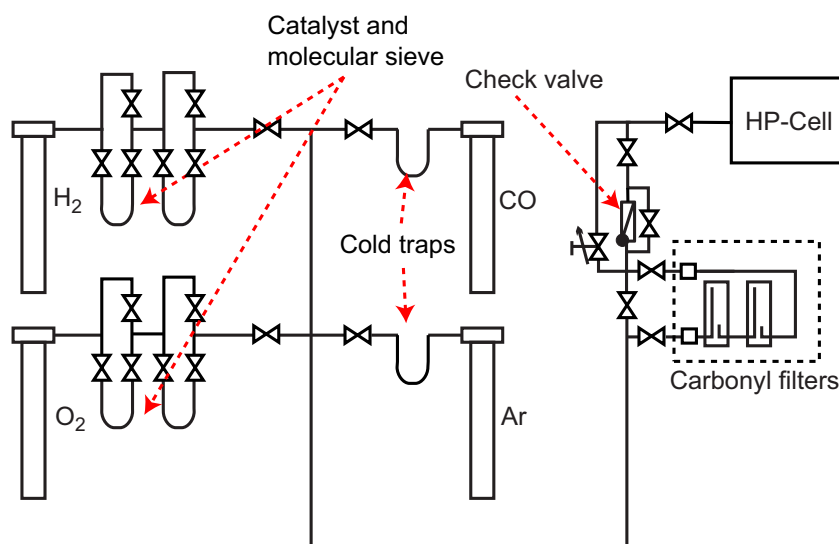


Figure 2.4: Sketch of the gas-inlet system for the HP cell.

Gas is admitted to the HP Cell through a Nupro valve or a leak valve as shown in Fig. 2.4. A check valve is added to the gas inlet system to enable the formation of gas mixtures in the cell. Mixtures are readily formed by successive admission of pure gasses to the cell with intermediate evacuation of the gas lines. The check valve efficiently blocks any back-flow of gas from the HP cell to the gas system during evacuation. Gas purification is of immense importance in high-pressure experiments as even small fractions of impurities will have a significant partial pressure at 1 bar, which could lead to

fallacious interpretations of the experimental results. For this reason, a dedicated gas purification system has been built for the HP cell. The system is sketched in Fig. 2.4, showing molecular sieves, catalyst containers or cold traps for purification depending on the type of gas. Finally, a filter for Ni carbonyl species is placed close to the HP cell. The filter is employed when CO experiments are performed, because CO reacts with Ni in stainless steel forming volatile Ni carbonyls, which are transported with the gas. All tubes in contact with the CO gas are made of copper, but the valves contain stainless steel parts and contact with Ni is therefore unavoidable. The carbonyl filter is therefore placed as close as possible to the HP cell. With the filter in use, no sign of Ni has been found on the crystals, as judged from AES performed in the UHV chamber after HP experiments. As seen in Fig. 2.4, the carbonyl filter contains two filters. The first filter consists of activated carbon powder heated to temperatures $\geq 150^\circ\text{C}$, whereby Ni carbonyl species transported with the gas dissociate on the high-surface area carbon. The second filter contains alumina and traps CO_2 molecules, which may be produced on the small Ni particles formed in the first filter.

2.4 Scanning Tunneling Microscopy

The UHV chamber is equipped with two scanning tunneling microscopes, one in the main chamber and one situated in the high-pressure cell. Since STM is the main technique used in the studies presented in this thesis, this section will be devoted entirely to the description of its function and design, and to a discussion of the interpretation of STM images.

The development of the STM in 1982 by Gerd Binnig and Heinrich Rohrer [46] launched a revolution in the field of surface science. With this technique it was for the first time possible to obtain images with atomic resolution in real space over a vast range of area sizes ranging from a few Ångströms to several micrometers. The STM was the first example of a still growing family of local scanning probe techniques, with which only a few surface atoms are studied at a time [47]. This is in striking contrast to earlier conventional surface science techniques like low-energy electron diffraction (LEED), X-ray photoelectron spectroscopy (XPS), Auger electron spectroscopy (AES) etc., which are all averaging techniques probing macroscopic surface areas.

The operational principle of the instrument is surprisingly simple: A sharp metal tip is brought into close proximity (a few Å) of a conducting surface and a small voltage difference between the surface and the tip is applied. Due to the quantum mechanical phenomenon of tunneling between the exponentially decaying wave functions in the vacuum region of the tip and the surface, a small current will flow between the two parts even when they are not in mechanical contact. As will be demonstrated in Section 2.4.2, this current is strongly dependent on the tip-surface distance, which makes it possible to acquire images with atomic resolution. Imaging is normally done in so-called *constant current* mode where a feedback loop constantly adjusts the distance to the surface to maintain a constant, user-defined tunnel current while the tip is raster-scanned in the x - y directions of the surface plane. The height modulations performed to keep the tunnel current constant are recorded and used to construct topographic STM

images. The operational principle of the STM is illustrated in Fig. 2.5. Throughout this thesis a standardized color scale has been used for representing height variations in the STM images. The color scale runs from black, representing depressions on the surface, through red to yellow, representing high protrusions. Where nothing else is stated, the color scale has been optimized in each single image to emphasize the relevant details.

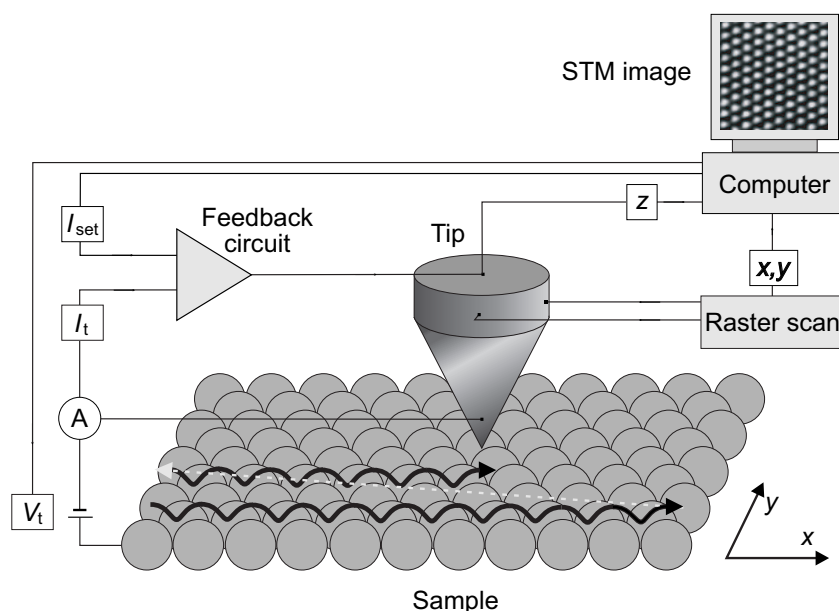


Figure 2.5: Schematic illustration of the principles of STM. The sharp tip is raster scanned across the surface at a distance of a few Ångström, and a feedback loop controls the height of the tip whereby the tunneling current is kept constant. The height modulations of the tip is used to construct a computer image of the surface.

Some of the great advantages of STM compared to averaging surface science techniques is its ability to investigate single atoms, defects, local environments in e.g. alloys, at step edges or at nanometer-size islands grown on surfaces, and the ability of STM to follow the dynamics at surfaces in real time has certainly revolutionized the study of diffusion phenomena. The local nature of the technique with its capability of obtaining atomic-scale information is thus its strength, but at the same time it can be a pitfall. Special care must be taken when performing STM experiments to avoid so-called *tunnel vision*: The technique lacks the averaging characteristics of diffraction techniques and focusing on (interesting) details may lead to erroneous generalizations unless precautions are taken. To avoid such pitfalls, all studies presented here are based on a large number of measurements performed on many different locations on the crystals. Another drawback of the STM compared to other surface science techniques is its lack of chemical specificity.

2.4.1 Aarhus STM

The atomic-scale precise positioning and control of two macroscopic objects, the STM tip and a single crystal surface, each with sizes of several millimeters, is a tremendous challenge in the design of a working STM. In the CAMP group, all STMs are home-built, which gives us the advantage of in-house technical assistance and advice [45, 48]. Fig. 2.6 shows a schematic drawing of the Aarhus STM: The sample (1) mounted in the tantalum sample holder (2) is clamped into contact with the top plate of the STM by two springs (3). The top plate (4) is in firm contact with an aluminium cradle (5), which serves as a “heat reservoir” keeping the crystal at a reasonably constant temperature during cooling experiments. The tip (6) is made by electrochemical etching of a tungsten wire and it is mounted on a tip holder at the end of a scanner tube (7). The scanner tube is made from a piezo-electric material divided into four equal sections coated with conducting gold layers. On the outside, each tube segment is isolated from the others, whereas on the inside they are interconnected. By application of antisymmetric high voltages to opposite electrodes, the two segments expand and contract, respectively, resulting in a deflection of the tube. This is the basis of the x - y scanning of the STM, and it explains how a centimeter-sized object is controlled on a sub-Ångström scale since a voltage of 1 V leads to a lateral displacement of ~ 50 Å. By applying a voltage to the inner electrode relative to the outer four segments, the entire tube is contracted and the tip-surface separation is thus adjustable on a sub-Ångström scale as well. A constant tunneling current during scanning is thus achieved by continuously adjusting the bias on the inner electrode of the scanner tube.

The scanner tube is glued to a ZrO_2 rod (8), which is going through another piezo-electrical tube. This second tube is a linear motor, called the inchworm (9), and it is used for the coarse approach of the tip to the surface. The inchworm consists of three sections, where the upper and lower sections simply clamp and unclamp the rod while the center section expands or contracts, thus facilitating a worm-like motion of the rod, whereby a coarse approach of 1 mm can be done in approximately 1 minute. The tunneling current is monitored during coarse approach, and the inchworm is stopped as soon as a preset current is reached.

The STM is attached to the top plate through three electrically insulating quartz balls (10), which minimize thermal conductivity between sample (top plate) and STM. The Al cradle can be cooled by pressing a “cold finger” (11) cooled with liquid nitrogen against the cradle. In this way it is possible to achieve a sample temperature of ~ 110 K while keeping the STM at room temperature (RT) by counter heating with a Zener diode (12) placed at the bottom of the STM. During scanning, the cold finger must be retracted and the cradle hangs freely in the suspension springs (13). The temperature of the cradle (and thereby the sample), however, only rises 5–10 K per hour owing to the large heat capacity of the cradle. The Al cradle may also be heated by Zener diodes (not shown in the figure) enabling experiments at elevated temperatures up to ~ 400 K.

The suspension springs holding the STM while scanning has a low resonance frequency (~ 3 Hz), effectively damping out high frequency vibrations coming from the outside. The compact design of the STM gives it a very high resonance frequency in the kHz-range and no further vibrational damping is necessary - even with three turbo

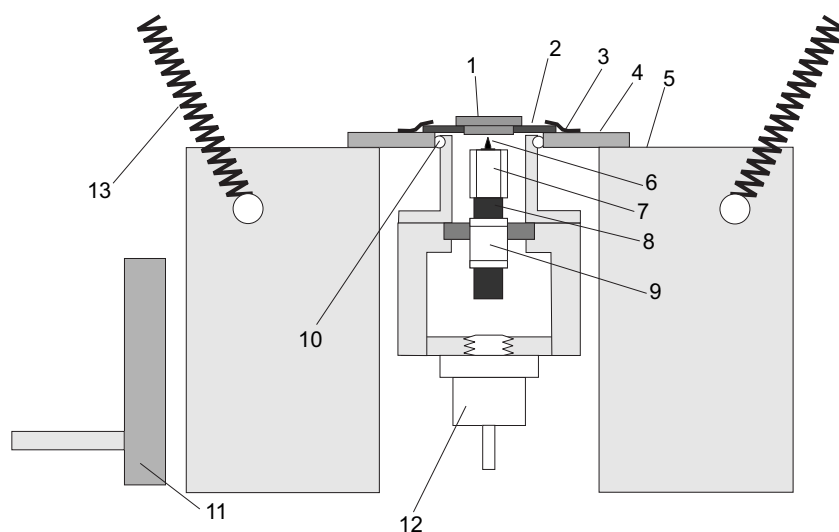


Figure 2.6: *Cross-sectional side view illustrating the main features of the Aarhus STM. (1) Sample; (2) sample holder; (3) springs; (4) top plate; (5) Al cradle; (6) W tip; (7) scanner piezo tube for x-y-z motion; (8) ZrO₂ rod; (9) inchworm piezo tube; (10) quartz balls; (11) cold finger with LN₂ feedthrough; (12) Zener diode for counter-heating the STM during sample cooling; (13) suspension springs.*

pumps attached to the chamber. Furthermore, the high resonance frequency enables fast-scanning, and several constant current images can be recorded per second. It is therefore possible to follow the dynamics of a variety of processes which would be too fast to be investigated with commercially available STMs.

2.4.2 Theory of STM

The tunneling between tip and surface is a far from simple many-body problem, which has not yet been solved exactly. The main obstacle is that the configuration of the tip apex is unknown during scanning and, furthermore, the interaction between the tip and the surface is likely to be so strong that the system cannot be described as two separate, weakly interacting systems [49]. New theoretical approaches have attempted to consider these problems (see e.g. [50]), but most of the theoretical descriptions of the tunneling process are based on a simplified treatment introduced by Tersoff and Hamann [51, 52] using the Bardeen Transfer-Hamiltonian approach [53] to determine the transfer matrix element in a perturbative calculation. This approach neglects interactions between surface and tip, so that the corresponding wave functions can be calculated separately. The

tunnel current is to first order described by a sum over all tip and surface states:

$$I_t = \frac{2\pi e}{\hbar} \sum_{\mu,\nu} f(E_\mu)(1 - f(E_\nu + eV_t)) |M_{\mu,\nu}|^2 \delta(E_\mu - E_\nu), \quad (2.2)$$

where $f(E)$ is the Fermi function, μ refers to the tip states with energies E_μ , and ν refers to the corresponding surface states. The Fermi functions ensure that tunneling occurs from a filled tip state ($f(E_\mu)$) into an empty surface state ($1 - f(E_\nu + eV_t)$) at positive bias voltage. The factor eV_t accounts for the applied voltage, and $M_{\mu,\nu}$ is the tunneling matrix element between tip states, ψ_μ , and surface states, ψ_ν . The delta function shows that only elastic tunneling of electrons is considered in this approximation. Tersoff and Hamann calculated the matrix element in the limit of small bias voltage and under the assumption that the tip state is well-described by a spherically symmetric s -wave function. They found a strikingly simple expression for the tunnel current,

$$I_t \propto V_t \sum_{\nu} |\psi_\nu(\vec{r}_0)|^2 \delta(E_\nu - E_F) = \rho(E_F, \vec{r}_0), \quad (2.3)$$

which shows that the tunnel current is proportional to the bias voltage and to the local density of states (LDOS), ρ , at the Fermi level evaluated at the center of curvature of the tip apex (\vec{r}_0). Within the Tersoff-Hamann formalism it is therefore found that images of constant current follows the surface contours of constant LDOS.

The exponential decay of the surface wave functions in the vacuum region results in an exponential dependence of the tip-surface separation for the tunnel current,

$$I_t \propto V_t \exp\left(-\frac{\sqrt{8m\phi}z}{\hbar}\right) \quad (2.4)$$

where ϕ is the effective tunneling barrier height (average work function of tip and surface), m is the electron mass and z is the tip-surface separation [51]. This exponential dependence is indeed the underlying basis for the ability of the STM to obtain atomic resolution: Small variations in height (a few Å) result in orders of magnitude changes in the tunnel current, and even if the tip is not perfectly sharp, a single protruding atom from the tip will carry the main part of the tunneling current.

The Tersoff-Hamann formalism is - despite its crude approximations - the generally applied theory when interpreting STM images. On clean metal surfaces the contours of the LDOS generally follow the geometrical topography of the surface, and an unambiguous assignment of protrusions to individual atoms is possible. On oxide surfaces, however, or when adsorbates are present on metal surfaces, this simplified interpretation of STM images is impeded. The first simple calculations of the contrast of adsorbates in STM images were performed by Lang, who represented the metal surface by a jellium model [54]. He found that different adsorbates are imaged as protrusions or depressions depending on whether they add or subtract to the LDOS at the Fermi level. When scanning non-metallic surfaces like oxide surfaces, the use of the simplified expression for the tunnel current, Eq. (2.3), is in general not possible due to the presence of a band gap. By applying a bias voltage typically around half of the band gap size, a tunnel current

can be drawn, but the geometrical interpretation is far from simple as in the case of metal surfaces.

The interpretation of STM images is thus very complicated in situations where the surface is either covered by adsorbates or is non-metallic. In these cases it is now common to compare the STM images to *simulated* STM images from e.g. DFT calculations to reach unambiguous conclusions in the interpretations. In this thesis different examples of counterintuitive STM imaging of surfaces are provided. In Chapter 5, for example, the Au atoms in a Au/Ni surface alloy are found to be imaged as depressions even though they are geometrically located at a height similar to that of the Ni atoms. The differing imaging characteristics of various atoms in such alloys complicate the analysis of STM data, because either theoretical simulations of STM images or complementary experimental techniques are necessary in order to interpret the STM images. On the other hand, such effects are also a useful tool, as we will see in Chapter 5, as they facilitate the study of local effects around a specific constituent in an alloy. In general, however, the STM technique does not possess the ability to chemically distinguish between different species. Scanning tunneling spectroscopy (STS) has been shown to give chemically specific information in a few cases [55, 56], but this usage of the STM technique is in general limited to low temperatures and has not been employed in the present thesis work.

2.5 Additional UHV techniques

In addition to the STMs, the UHV chamber is equipped with three other standard surface science tools, Auger electron spectroscopy (AES), low-energy electron diffraction (LEED) and temperature-programmed desorption (TPD), and the basic features of these techniques are briefly summarized in the following. For a more thorough description of these techniques the reader is referred to textbooks like [44, 57].

AES probes the surface with electrons, which kick out core electrons from the atoms in the studied sample. The holes thus formed can be filled either by radiative recombination (photons) or by sending out so-called Auger electrons carrying away part of the released energy as kinetic energy. The energy distribution of the latter electrons ejected from the crystal gives a chemical fingerprint of the elements in the sample, and AES thus possesses the chemical specificity that the STM technique lacks. LEED utilizes the wave nature of electrons to probe the crystal structure of surfaces. The diffraction pattern of scattered electrons is recorded on a fluorescent screen and for simple structures this can be used to directly determine the unit cell of surface atoms or adsorption structures. LEED also has the potential of giving much more detailed information about relaxations of the outmost atomic layers than other techniques by considering multiple scattering processes and simulating the observed spot intensities as a function of electron energy, so-called I(V) analysis. This, however, is not the purpose of the LEED system installed at the UHV chamber described here.

The surface sensitivity of AES and LEED arises from the short inelastic mean free path lengths for electrons in metals at low energies. For electron energies in the interval from 1–1000 eV, the mean free path is on the order of a few Ångströms, and electrons

with no energy losses will therefore only emerge from the outmost atomic layers. The LEED system is a Varian reverse view LEED, and the AES is a PHI system with a single-pass cylindrical mirror analyzer (CMA) for detection of electrons.

The third technique, TPD, probes the desorption energy of adsorbates by thermal desorption spectroscopy; the crystal with adsorbed species is heated with a temperature ramp of 1–3 K/s in front of a mass spectrometer, which is continuously recording the ion signal at a few selected masses. At specific temperatures, peaks can be observed, and various theoretical models can subsequently be employed to extract the desorption energy and in some cases even details about the desorption mechanism. Another more simple application of TPD is the investigation of adsorbate coverage: The integrated TPD signal can be used as a relative measure of the coverage, and in cases where it is possible to compare the data with integrated results from well-known structures, the absolute coverage can even be determined. This method is e.g. utilized in Chapter 7 where the amount of oxygen in an oxide phase is determined in this way.

CHAPTER 3

Theoretical models

In this chapter the so-called *d*-band model describing gas adsorption and reactivity on surfaces will be introduced and discussed. The qualitative understanding provided by the model of the adsorption trends throughout the transition metal group is emphasized along with ideas for reactivity modifications of the metals.

3.1 Introduction

The crucial role of ultra-high vacuum techniques in experimental surface science is matched by a similar revolution within the theoretical description of surfaces initiated by the advent of modern computer technology. The ever increasing development of successively faster computers has been the cornerstone in many theoretical approaches to the description of the complicated many-body problems involved in surface science. Starting from exactly solvable models like Langmuir isotherms of adsorption, theorists have turned to methods like density functional theory (DFT), which is an iterative approach to the many-body problem and which therefore demands high computer power. DFT has now developed into one of the most important and prominent tools in surface science, and in a large number of cases quantitatively good agreement has been found between theoretical predictions based on DFT calculations and experimental results. Besides calculating theoretical values of adsorption energies, structures, reaction rates etc., another important issue for theorists is to create theoretical and conceptual frameworks or models, where simple concepts rationalize the wealth of results concerning the elementary physics and chemistry at surfaces. Such models are inherently qualitative; Any quantitatively predictive model would necessarily lose its simplicity and general concepts would be lost in lengthy calculations. An example of such a model is the so-called *d*-band model by Hammer and Nørskov [58–60], which will be described and exemplified in the following sections.

The concepts discussed in this chapter are applicable for the discussion of adsorption and reactions (dissociation) on metal surfaces as discussed in Chapters 4 and 5, and e.g. the concept of “active sites”, which is of major importance in catalysis can be rationalized within this framework, as discussed below. A conceivable route for surface science based catalyst design could consider concepts from models like the *d*-band model, where the reactivity of a given surface can be tuned in different ways by alloying or by the formation of (strained) bimetallic overlayers. When metal-oxide surfaces are considered (as in Chapter 6), yet another parameter is, however, found which plays an important role for the reactivity of the surface. As we will see in Chapter 6, the position of the chemical potential in oxide surfaces plays a key role for the surface reactivity, and different concepts may therefore be feasible for a surface science based design strategy for new catalysts when oxides are considered.

3.2 Elementary surface processes

As discussed in Section 1.1, most catalytic processes involve the dissociation of di- or polyatomic species, whereby new species are created, which can react with each other and finally leave the surface as products. Each catalytic reaction can in general be divided into a number of elementary processes, e.g. adsorption, dissociation, diffusion, reaction or desorption (See Fig. 1.1). The elementary processes are often activated, meaning that the system must pass an energy barrier along the reaction path from the initial state to the final state. The state of the involved molecule(s) at this barrier is called the transition state, and the energy difference between the transition state energy and the

initial state local energy minimum is called the activation energy, E_a . In general the activated elementary processes can be described by an Arrhenius expression,

$$r = \nu \exp(-E_a/k_B T), \quad (3.1)$$

where the prefactor, ν , depends on the curvature of the potential energy surface, k_B is the Boltzmann constant and T is the temperature.

From the Arrhenius equation one may erroneously be lead to the conclusion that the best catalytic material is the one with the lowest activation energy for all elementary processes of a given reaction, but activation energies and adsorption energies are correlated, and low-barrier materials therefore often bind intermediates or products so strongly that desorption is inhibited and the surface is *poisoned* by the adsorbates. The optimal catalyst is a compromise with intermediate values of activation and adsorption energies, and this general rule is known as the Sabatier principle [61]. A clear manifestation of the Sabatier principle can be observed in so-called “volcano curves” of catalytic reactivity, exhibiting a maximum somewhere in the middle of the transition metal group for various reactions, as illustrated in Fig. 3.1. To the far right at the noble metals, the adsorbate binding is weak, but the activation barriers are too high, and to the far left the barriers are small, but the adsorbates are bound too strongly to the surface. The Sabatier principle is discussed and rationalized below after the introduction to the *d*-band model.

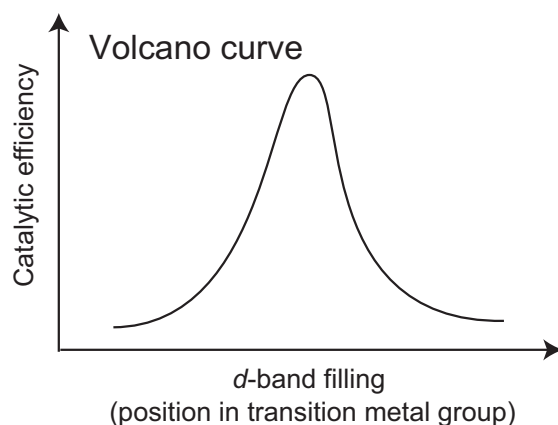


Figure 3.1: Schematic drawing illustrating the concept of volcano curves. Typically metals somewhere in the middle of the transition metal group are the best catalysts for a given reaction. This finding illustrates the Sabatier principle (See text).

3.3 d-band model

The *d*-band model is an example of a conceptually simple model for gas/surface interactions, yet capable of grasping the trend of adsorption energies throughout the transition

metal group and describing the effect of e.g. alloying and the different adsorbate binding energies at various sites on surfaces. The model takes its starting point in the interaction of adsorbate electrons with the valence states of the surface atoms. In the metal, the highly itinerant s and p -band electrons form a broad band of states whereas the d -band electrons form a relatively narrow band owing to the small coupling matrix element between the more localized d orbitals. DFT calculations have shown that the interaction of an adsorbate state with a broad band (sp) leads to a broadening and a downshift in energy of the metal-adsorbate derived states, whereas the interaction with a narrow band (d) is well-described by the formation of bonding and antibonding states similar to what is seen in molecular bonds (See Fig. 3.2).

According to the d -band model, the key parameter for evaluating bond strengths between adsorbates and transition metal surfaces is the (energy-) position of the d -band center with respect to the Fermi energy, $\epsilon_d - \epsilon_F$. If the d -band center is close to the Fermi level, a large fraction of the antibonding states between the adsorbate and the surface will be pushed above the Fermi level and emptied, resulting in a strong bond to the surface. A d -band center relatively far below the Fermi level, on the other hand, might give rise to both bonding and antibonding levels being populated (below the Fermi level), which would therefore result in a weaker binding energy of the adsorbate to the surface.

3.3.1 Adsorption and reactivity

A relatively simple way of understanding the bond strengths of adsorbates on transition metal surfaces follows readily from the considerations above: Focusing on the late part of the transition metal group, Fig. 3.2 describes the interaction of oxygen states with the d -band from different metals.¹ When moving to the left in the transition metal group, the d -band is gradually emptied and the d -band center hence approaches the Fermi energy. The noble metals, on the other hand, exhibit a low-lying d -band center, because the d -band is filled with electrons. More antibonding states are thus filled with electrons for the noble metals, and the weak adsorbate binding observed experimentally when moving to the right in the transition metal group is thus rationalized. Gold is indeed *noble* because the d -band center for this particular metal is so low-lying that the interaction with virtually any adsorbate gives rise to a large fraction of antibonding states being filled with electrons.

The interaction of CO with transition metal surfaces, which has been the topic of much of the work in this thesis, can be discussed in similar terms. For molecular adsorbates like CO, however, often more than one adsorbate level is interacting with the d -band. For CO both the 5σ and $2\pi^*$ levels contribute to the binding, as illustrated in Fig. 3.3. The 5σ CO level is occupied with two electrons when CO is in the gas phase whereas the $2\pi^*$ is empty. When CO adsorbs on transition metal surfaces, a certain fraction of the 5σ -derived antibonding states are shifted above the Fermi level and are thereby emptied. In this way the CO molecule effectively donates electrons to the metal. On the other hand, some of the $2\pi^*$ -derived bonding states are shifted below the Fermi

¹Similar arguments for bond strengths can be employed for the left part of the transition metal group.

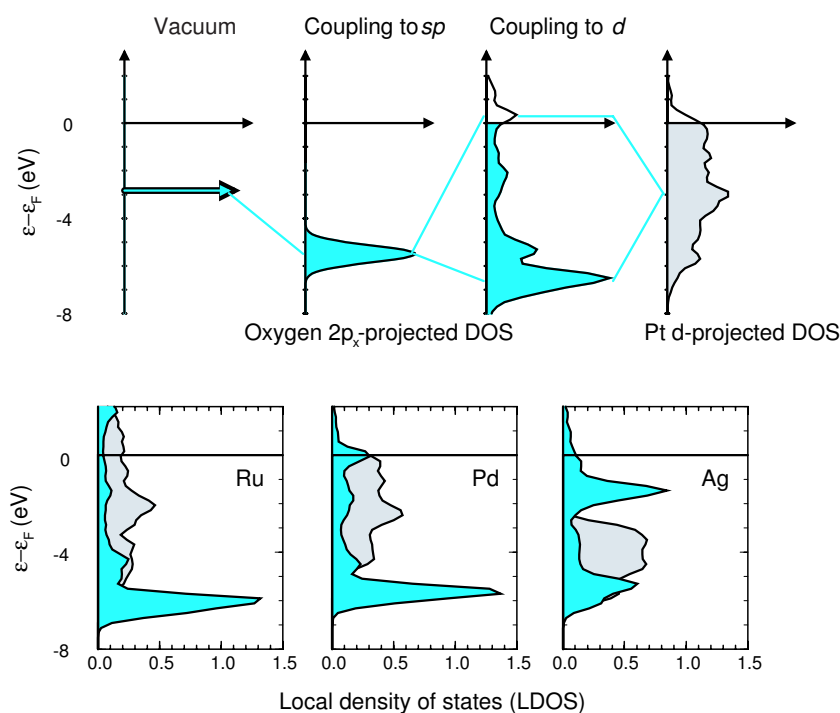


Figure 3.2: *Top: Illustration of the coupling of adsorbate states (here oxygen) to the sp-band, resulting in a broadening, and the coupling to the d-band (here Pt) whereby bonding and antibonding states are formed. Bottom: Variations in d-band position are seen to shift the antibonding states with respect to the Fermi level: For Ag virtually all antibonding states are occupied and the binding energy is therefore very small. The blue area is the adsorbate projected density of states (here oxygen) and the grey area is the metal d-band states. Adapted from [60].*

level and are thereby filled. The metal thus also donates electrons to the molecule. The adsorption is therefore often described as a donation/back-donation process - a terminology adopted from the so-called Blyholder model [62], which qualitatively gives the same picture of CO adsorption as the *d*-band model.

Returning to the Sabatier principle and volcano curves for the catalytic activities discussed above, the correlation between barriers and binding energies can also be rationalized with simple arguments. Recently, a compilation of a broad range of theoretical results on adsorption energies and dissociation barriers for a number of adsorbates were published by Nørskov *et al.* [61]. All adsorbates exhibited linear relationships between the two energies with a slope close to one - so-called Brønsted-Evans-Polanyi (BEP) relations. Moreover, the different molecules adsorbed at different surfaces constituted a single line thus forming a “universality class” of possible pairs of barriers and binding

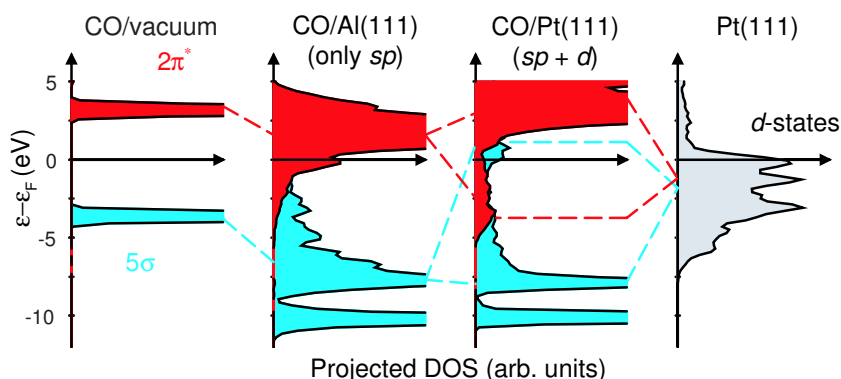


Figure 3.3: CO adsorption on transition metal surfaces according to the d -band model. Both 5σ and $2\pi^*$ states contribute to the bonding. For aluminium (an example of a non-transition metal) a broadening and down-shift of the levels is observed, whereas the interaction with platinum leads to the formation of bonding and antibonding states. Adapted from [60].

energies. The linear dependence between the two energies finds a reasonable explanation in the fact that the transition state for many molecules is very final-state-like. The molecular bond is rather stretched in the transition state, and the molecules have therefore to a large degree lost their molecular characteristics. The transition state geometries are similar for many molecules which explains the formation of a single universality class.

Different distinct universality classes are, however, found when other transition state geometries, e.g. at defects, are considered, and such effects together with the d -band shifts often found at defect sites lead to a rationalization of the concept of “active sites” on a surface; At defects like step edges and kink sites, the reduced coordination of the metal atoms results in a diminished d -orbital overlap compared to the terrace atoms. The concomitant narrowing of the d -band leads to an upward shift, and when adsorbates interact with step and kink atoms, more anti-bonding states are pushed above the Fermi level, and the binding energy becomes larger. Such an effect is, for example, observed to play a role for the roughening of Pt(110) surfaces upon the interaction with CO, which is discussed in Chapter 4. Furthermore, the special geometry at, e.g., step edges often stabilizes the transition state to a larger degree than what is found at terrace sites, and the barriers for reactions and dissociation of molecules are thereby lowered compared to the barriers elsewhere on the surface. This will be exemplified and discussed in Chapter 5.

A volcano curve can in principle be constructed for a given reaction by modelling the kinetics with the linear relationship between activation barrier and adsorption energy as input. By the construction of such models, a narrow window of, e.g., adsorption energies can be found giving significant catalytic activity. This has been demonstrated

in [61, 63] for ammonia synthesis and in [17] for PEM-FC anode reactions. In this way, an explanation of the catalytic activity of certain metals for specific reactions can be given, and it might, furthermore, be possible to predict or design new tailor-made catalysts for specific purposes by adjusting the *d*-band position to yield the optimum adsorption energies and barriers. Such “*d*-band position engineering” can be employed in a number of ways, as discussed below.

3.3.2 Modifying the reactivity of metals

According to the *d*-band model and the BEP-relations discussed above, a possible route for modifying the reactivity of a metal is to alter the energy of the *d*-band center relative to the Fermi energy. Considering the adsorption energy trends for transition metals, the variations in the position of the *d*-band are caused by the different degree of filling, but modifications of the electronic properties of a single metal could in principle lead to similar results.

One route towards *d*-band position engineering consists of changing the width of the *d*-band. A large amount of DFT calculations has established that the *d*-band filling for a given metal stays constant if the band width is changed [60], and the *d*-band center is accordingly constrained to move to account for the changes, as illustrated in Fig. 3.4 (the so-called *rigid-band model*). The width of the *d*-band can be modified by subjecting the metal to strain; Compressive or tensile strain will lead to an increased or diminished overlap, respectively, of the *d*-electron orbitals from the metal atoms, and the altered overlaps will change the (local) width of the *d*-band according to the tight-binding theory [64]. To keep the band-filling, the *d*-band center is shifted downwards when a metal is subjected to compressive strain and, correspondingly, upwards for tensile strain.

Strained metal surfaces can be realized experimentally by growing pseudomorphic overlayers of one metal on top of another metal. This has for example been observed for Pt overlayers on Au(111) [65], where the binding energy of CO molecules is increased compared to Pt(111), and for Pt overlayers on Ru(0001), where the CO binding energy is diminished [66]. The nearest neighbor distance on Pt(111) is 2.78 Å, and a comparison to the atomic distances on Au(111) (2.88 Å) and Ru(0001) (2.71 Å) is thus seen to be in good agreement with the discussion above.

Another route towards *d*-band position engineering is through alloying. The effect on the *d*-band position by either alloying a given metal with another or creating an overlayer, has been studied in detail with DFT calculations in [67], where a large number of *d*-band shifts are presented. Combining such information with knowledge of the *d*-band position dependence of the relevant adsorption energies, a search for the optimal bimetallic alloy for a given reaction can in principle be initiated according to the universality classes described above. It should, however, once more be emphasized that the *d*-band model only provides qualitative trends, and that more sophisticated theoretical calculations are necessary when a quantitative comparison of, e.g., adsorption energies on alloys is desired.

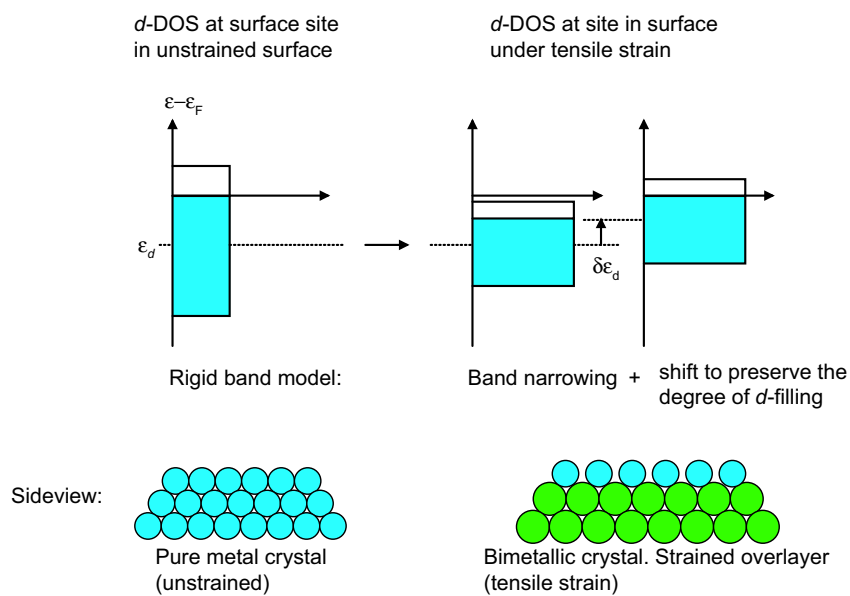


Figure 3.4: **Top:** Illustration of the effect of tensile strain on an overlayer. Due to the decreased overlap of the d -orbitals, the d -band width is diminished, and to preserve the filling it shifts up in energy. Adapted from [60]. **Bottom:** Side-view illustration of the tensile strain of epitaxially grown overlayers of a metal on top of another metal crystal with a larger lattice constant.

CHAPTER 4

Bridging the pressure gap - CO adsorption on Pt surfaces

In this chapter, two studies of the CO adsorption structures on Pt(110) and Pt(111) at high-pressure conditions are presented. The development of structures is followed as a function of pressure from UHV conditions up to 1 bar, and comparison is made to the high-coverage structures obtainable by low-pressure dosing at lower temperatures. The results lead to the conclusion that the “surface science approach” is indeed relevant for the understanding of the adsorption structures found at high-pressure conditions. Care must, however, be taken with respect to kinetic limitations at low-temperature and low-pressure conditions. A number of high-coverage CO structures are reversibly formed on Pt(111) at intermediate pressures, and the relevance of these observations in the context of CO poisoning on PEM-fuel cell anode catalysts is briefly discussed.

4.1 Introduction

Platinum is one of the most versatile metals in catalysis [1]. It is utilized in the automotive three-way catalyst, where oxide-supported Pt clusters catalyze the oxidation of CO and unburned hydrocarbons [68] and it is, furthermore, one of the most widely used materials for electro-catalytical applications, in which its chemical stability under both oxidizing and reducing conditions is of great importance [1]. As mentioned in the introduction (Chapter 1), platinum or platinum-based alloys are, e.g., used as catalysts in PEM fuel cells both on the anode side for hydrogen dissociation and on the cathode side for the reaction between protons and adsorbed oxygen to form water [69].

The understanding of the interaction of CO with platinum surfaces is highly important from an industrial point of view, and CO has, furthermore, often been used as a typical “probe” molecule in surface science studies. The adsorption of CO on platinum and other transition metal surfaces has therefore become some of the most studied and most discussed systems within the surface science community [1]. Virtually all applicable surface sensitive tools have been used to characterize the interaction of CO with platinum surfaces, but most of the information, however, has been obtained under low-pressure conditions with CO pressures up to $\sim 10^{-6}$ torr. This fact has of course spurred a debate of the relevance and applicability of the results at more realistic pressure and temperature conditions in catalysis, and especially recent studies by Somorjai and co-workers [70–72] have indicated that new adsorption structures and phenomena, unseen at low-pressure conditions, occur when platinum surfaces are exposed to high pressures of CO. These findings have indeed been one of the main motivations for the present studies, where we have re-investigated this apparent gap between low and high-pressure conditions for the CO/Pt system. We have performed experiments on two low-index Pt surfaces, Pt(110) and Pt(111), which exhibit very different properties under UHV conditions. Pt(110) reconstructs in its clean state, but CO adsorption is known to lift the reconstruction, which results in a rough surface with a high step density [73]. Pt(111), on the other hand, is unreconstructed in its clean state, and CO adsorption does not alter the hexagonal packing of the topmost Pt layer. The two surfaces thus serve as examples of very different adsorption systems for CO/Pt, where questions concerning pressure gap effects can be addressed in each case.

Besides the interest spurred by the pressure gap debate, the purpose of the studies has been to obtain atomic-scale information about the adsorption structures formed especially at intermediate CO pressures relevant e.g. at typical PEM fuel cell conditions. As discussed in Chapter 1, a major problem for the commercialization of PEM fuel cells is the so-called *CO poisoning*, which severely reduces the fuel cell efficiency even at very low CO concentrations (10–100 ppm) [17, 69, 74]. At a total pressure of 1 bar on the anode side, such concentrations correspond to a CO partial pressure of 10^{-2} – 10^{-1} mbar, which is indeed within the range of the studies presented below.

4.2 CO adsorption on Pt(110)

The adsorption of CO on Pt(110) has become a prototypical example in the literature of adsorption-induced structural transformations on a surface, and the system has been studied both from a theoretical point of view [73, 75] and with a large range of experimental techniques [39, 71, 73, 76–80]. Furthermore, the oxidation of CO on Pt(110) has been found to result in complex two-dimensional concentration patterns [81–83], and a recent HP-STM study suggested that a reactive oxide phase participates in the CO oxidation reaction at high-pressure conditions [39].

After a brief introduction to the clean surface and a discussion of CO adsorption at low-pressure conditions, we present studies following the CO adsorption structure on Pt(110) at pressures from UHV conditions up to 1 bar with atomic-scale resolution. The high-pressure adsorption structures are compared to the structures formed at lower temperatures under low-pressure conditions, and it is concluded that the atomic-scale structures of high-coverage CO phases are identical in the two different pressure regimes as long as surface equilibration is not hindered by kinetic barriers at the low temperatures.

4.2.1 Pt(110) surface

Pt(110) is one of the few metal surfaces that reconstructs even in its clean state. Together with Au and Ir it forms a class of late $5d$ transition metals all exhibiting a (1×2) reconstruction of the (110) surface, known as the *missing-row reconstruction* because it consists of $[1\bar{1}0]$ -oriented close-packed rows with every second row missing. Removing one half of the rows increases the *effective* surface area, but at the same time the microfacets created consist of small (111) facets with a lower surface energy. The surface energy of the (1×2) missing-row structure is therefore found to be 0.27 meV/atom lower than the unreconstructed (1×1) structure [84]. On the mesoscopic scale Pt(110) exhibits a characteristic buckling structure with ridges of more than 10,000 Å in length in the $[1\bar{1}0]$ direction and a periodicity in the $[001]$ direction of approximately 1,500 Å. The meso-scale structure consists of regions of long, almost kink free, $[001]$ steps separating relatively large top and bottom terraces with a width of 100–1000 Å. The height difference between the top and bottom terraces of the mesoscopic pattern is approximately 30 Å, and at the end of the ridges, areas are found with a high kink and step density, the so-called “fish-scale structure” [85, 86]. Examples of the mesoscopic structure together with the local atomic-scale structure are shown in Fig. 4.1. The origin of the mesoscopic roughening is discussed in [85], where it was argued that the structure is the equilibrium surface structure and that the mesoscopic periodicity is a result of stress-induced self-organization. This interpretation has, however, been questioned by other groups [87].

The Pt(110) surface was cleaned by repeated cycles of sputtering (800 eV Ar^+ ions) and annealing in UHV at 1000 K combined with 800 K annealing for 10 minutes in $5 \cdot 10^{-7}$ torr O_2 to remove residual carbon impurities. This procedure resulted in a clean surface exhibiting the (1×2) reconstruction on the microscopic scale with the mesoscopic buckling superimposed as described above. Some areas exhibiting an impurity-induced 1×3 reconstruction were initially encountered [86, 88], but after several cleaning cycles only the equilibrium (1×2) reconstruction remained.

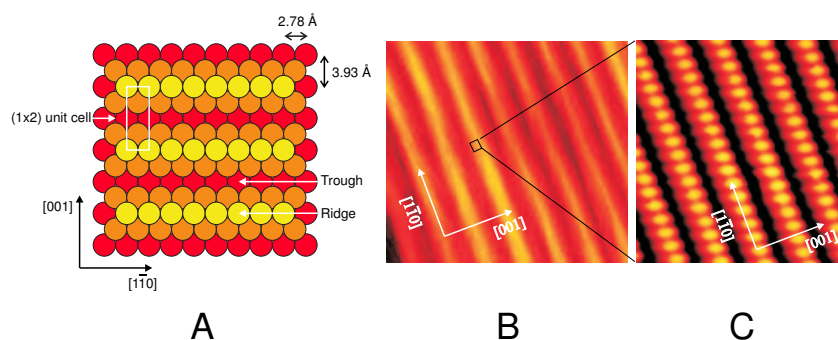


Figure 4.1: **A:** Ball model of the Pt(110) surface illustrating the (1×2) missing-row reconstruction. **B+C:** STM images of the mesoscopic ($6000 \times 6000 \text{ \AA}^2$) and the atomic-scale structure ($45 \times 45 \text{ \AA}^2$) of Pt(110).

4.2.2 Low-pressure CO adsorption on Pt(110)

From spectroscopic studies, CO is known to adsorb in on-top sites on the Pt(110)-(1×2) surface [77, 80]. At a CO coverage of approximately 0.2 ML, platinum atoms begin to move out from the ridges to the troughs in the missing-row structure creating “hole”-like structures on the surface. An atomistic model for this was proposed already in 1989 by Gritsch *et al.* [78], and recently Thostrup *et al.* published STM and DFT results describing the further development of the structure at higher CO exposures [73, 89]. After prolonged CO exposure at room temperature a disordered pattern of (1×1)-patches develops on the surface, and by comparison to Monte Carlo simulations, Thostrup *et al.* concluded that in order to reach equilibrium structures on the surface, it is necessary to anneal the CO/Pt(110) to $\sim 100^\circ\text{C}$ or to perform the experiments at elevated temperatures [73, 89]. Fig. 4.2 shows the development and coalescence of holes on the Pt(110) surface as a function of increasing CO exposure at 100°C . Upon coalescence, the (1×1) patches form characteristic channels along the [001] direction (perpendicular to the close-packed $[1\bar{1}0]$ rows). The saturation coverage of CO at this temperature is approximately 0.8 ML [73], and a good agreement with the Monte Carlo simulations presented in [73] suggests that these high-step-density, channel-like structures are the equilibrium phase of CO/Pt(110) at 100°C and low-pressure conditions.

A well-ordered adsorption structure with a CO coverage of 1 ML can, moreover, be obtained by cooling down the crystal from 600 K to room temperature in 10^{-7} mbar CO. In this way, a (2×1) structure is created, consisting of an unreconstructed Pt(110)-(1×1) surface with CO adsorbed on every platinum atom but tilted in different directions on every second atom [76]. The tilting gives rise to a characteristic *zig-zag* pattern observed in STM images, as seen in Fig. 4.3. The van der Waals diameter of CO, which is a typical measure of the intermolecular distance in condensed phases, is 3.2 \AA [76], and this value is higher than the interatomic Pt distance along the $[1\bar{1}0]$ direction (2.78 \AA). Strong repulsions are thus to be expected if CO is adsorbed on every Pt atom, and the

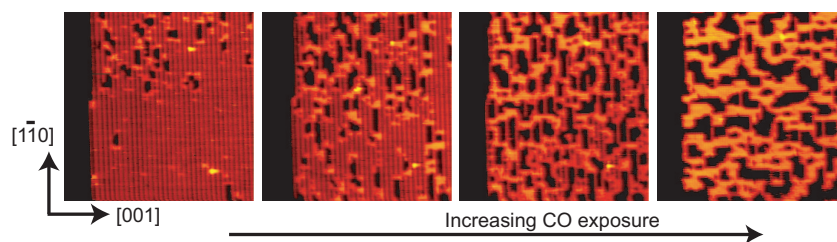


Figure 4.2: STM images ($300 \times 300 \text{ \AA}^2$) from an STM movie following the development of CO induced structures on Pt(110) during CO dosing ($P=2 \cdot 10^{-9}$ mbar). The saturation coverage of CO is ~ 0.8 ML at this pressure and temperature.

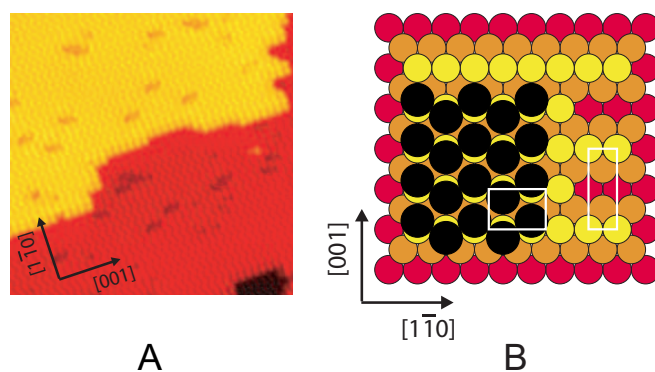


Figure 4.3: **A:** STM image ($141 \times 147 \text{ \AA}^2$) of the (2×1) zig-zag structure of CO on Pt(110) formed by cooling down the crystal from 600 K to RT with a background pressure of CO. **B:** Ball model of the (2×1) structure. The white rectangles indicate the unit cells of the (2×1) adsorption structure (left) and the (1×2) missing-row structure (right), respectively. The black filled circles illustrate the tilted CO molecules.

tilting can therefore be rationalized as a way of accommodating the high density packing of the CO molecules. As opposed to the rough equilibrium structure formed at lower CO coverage (0.8 ML), the step density is rather low when the (2×1) structure is formed and large terraces are found on the surface.

The zig-zag appearance as seen with STM in the (2×1) structure is a clear signature of the tilted CO molecules, but at lower CO coverage the molecules are actually not imaged directly with STM. In the (2×1) structure the molecules are locked into place by the strong mutual interaction, but in the low-coverage, channel-like structures the CO molecules are free to vibrate while still being bound to a single Pt atom - so-called *frustrated* vibration or motion [90]. Such motion requires very little energy and therefore occurs on a much faster timescale than the scanning speed of the STM, which impedes

STM imaging of the molecules. Furthermore, the tip-molecule interaction may also play a role for the apparent invisibility of the CO molecules at lower CO coverage as suggested in [91]. In the STM image in Fig. 4.3 the tilting of the CO molecules is seen to be diminished near the step edges. Most likely, the molecules at the step edge “lean out” to give more room for the other molecules, thereby “unlocking” the frozen tilting of the nearest molecules.

The appearance of such diverse structures for CO/Pt(110) depending on temperature and coverage can be rationalized by considering simple *d*-band and Pt coordination number arguments as done in [73, 89]: The *d*-band position of platinum depends on the metal coordination number, as discussed in Chapter 3 for e.g. step edges, and the binding energy of CO is therefore found to scale linearly with the Pt coordination number as shown in the graph in Fig. 4.4A reproduced from [73]. The CO-induced hole formation on the Pt(110) surface and the subsequent formation of channel-like structures is thus an example of a delicate energy balance between Pt-Pt bond breaking and CO-Pt bond formation: The energy gained from adsorbing CO on a (low-coordinated) Pt adatom instead of a ridge atom compensates the energy cost to create an adatom from a ridge atom (~ 0.25 eV per bond breaking), and at finite temperatures entropy thus favors a configuration with multiple adatoms, whereby the hole creation is rationalized [73]. At an intermediate CO coverage (e.g. 0.8 ML as in Fig. 4.2), energy is gained by rearranging the Pt atoms in a way that gives a high step density, as this provides low-coordinated adsorption sites (six-fold coordinated) for the CO molecules, and the high-coordinated sites below each step (nine-fold coordinated) is simply left free of adsorbates (see Fig. 4.4B). When the CO coverage approaches 1 ML, however, each Pt atom must adsorb a CO molecule, and the energy gain at the low-coordinated Pt-sites is thus compensated by a similar energy loss at the high-coordinated Pt atoms according to Fig. 4.4A.

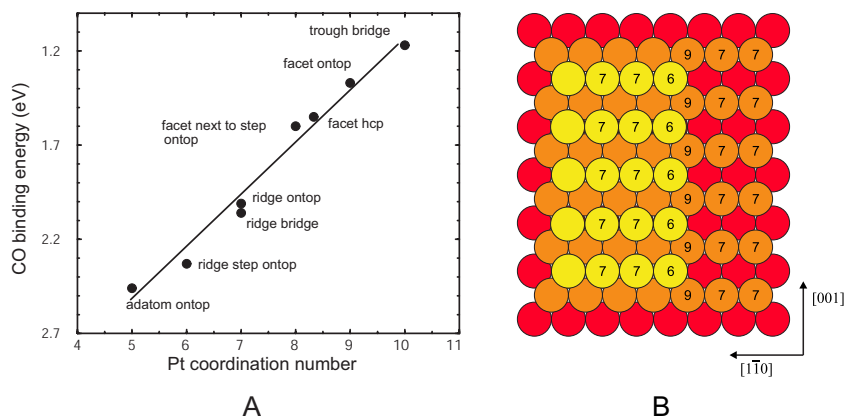


Figure 4.4: **A:** Calculated CO chemisorption energies at different positions on the Pt(110) surface (adapted from [73]). **B:** Ball model illustrating the various coordination numbers of Pt atoms at a step edge on the Pt(110)-(1 \times 1) unreconstructed surface.

It is thus reasonable to find large terraces accompanied with the (2×1) structure since the high CO coverage necessitates the adsorption of CO on each Pt atom, whereby the energy gain from step edges is removed. Such substantial rearrangements of Pt atoms are inhibited at room temperature and the cooling down from higher temperatures in a background gas of CO is therefore necessary to reach an equilibrated high-coverage structure of CO on Pt(110).

4.2.3 High-pressure CO adsorption on Pt(110)

The adsorption of CO on Pt(110) at high pressures has previously been investigated with STM by McIntyre *et al.* [71] and Hendriksen *et al.* [39]. In none of the cases, however, with atomic-scale resolution. McIntyre *et al.* found that HP-CO exposure lead to relatively flat terraces separated by multiple height steps, but no details on the adsorption structure were revealed. To investigate if CO adsorption on Pt(110) exhibits any pressure gap effects, i.e. whether or not the adsorption structures formed at high pressures are similar to the ones formed at low-pressure conditions, we performed high-resolution STM experiments both in the UHV chamber up to 10^{-3} mbar CO and in the high-pressure cell from 10^{-3} mbar up to 1 bar of CO. All experiments were performed at a temperature of 100°C to facilitate equilibration of the adsorption structures at the surface as discussed above. Fig. 4.5 summarizes the findings with examples of STM images from different pressure regions: At low pressures, $\sim 10^{-7}$ mbar (A), the channel-like structures depicted in Fig. 4.2 are recognized with long, almost kink-free channels along the [001] direction, which gives rise to a relatively high step density on the surface. These structures persist (B) up to a pressure of approximately 10^{-3} mbar CO, where the step edges start to round (C), and larger terraces are created. At 1 bar of CO large terraces are found on the surface in agreement with the studies presented in [71], and zooming in on the terraces (D) we recognize the (2×1) zig-zag structure of the CO molecules.

The multiple height step edges discussed by McIntyre *et al.* upon HP-CO exposure have not been observed in our experiments. It may be speculated that the findings in [71] could be impurity related; the Pt crystal used in these studies was maintained in a relatively high pressure (10^{-5} torr) during transfer from a preparation chamber to the high-pressure cell and the cleanliness might therefore be a problem. From other studies, impurities have, e.g., been known to give rise to reconstructions and faceting of the surface [86, 88].

4.2.4 Discussion

In the experiments presented above we observed that the well-known (2×1) CO structure is found at 1 bar of CO on the Pt(110) surface, and we have thus bridged the pressure gap between UHV-based studies and adsorption structures at high-pressure conditions for this system. It is, however, important to realize that a simple comparison between the CO exposure at low temperatures and the high-pressure results would *not* lead to a good agreement between the high-coverage structures formed in the two different pressure regimes. The delicate energy balance of the CO/Pt(110) system discussed above gives

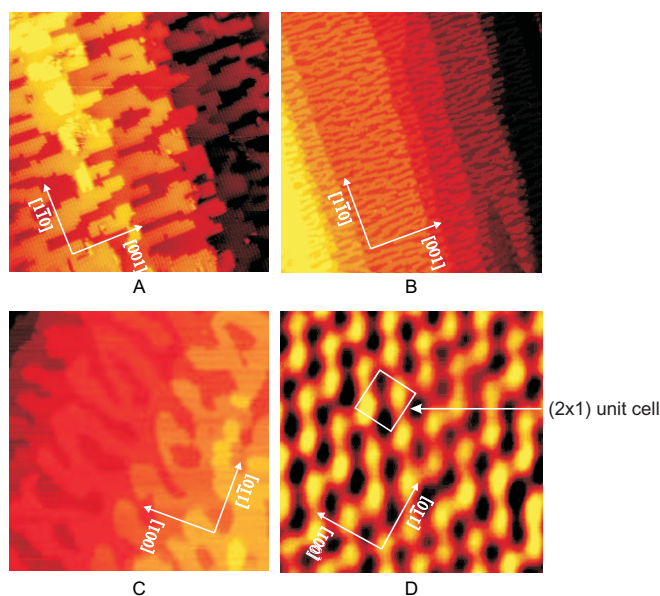


Figure 4.5: STM images of Pt(110) at 373 K at different CO pressures. **A:** 10^{-7} mbar, $300 \times 300 \text{ \AA}^2$; **B:** 10^{-5} mbar, $1000 \times 1000 \text{ \AA}^2$; **C:** 10^{-2} mbar, $700 \times 700 \text{ \AA}^2$ and **D:** 1000 mbar, $30 \times 30 \text{ \AA}^2$.

rise to kinetic hindrance when CO is dosed at low temperatures: The CO adsorption energies on Pt(110) have sufficiently large variation as a function of the Pt coordination number to induce surface restructuring, and if the thermal energy is too low to accommodate the necessary mass transport of Pt atoms for equilibration, a rough surface will be found even after prolonged CO exposure [73, 89]. This is indeed what is observed when CO is dosed at room temperature and low-pressure conditions on Pt(110); At such conditions, the rearrangement of Pt atoms to form extended terraces with low step density is impeded and a rough structure of (1×1) patches is found instead. The studies presented in this section, however, show that the formation of the relevant high-coverage structures is possible also under UHV conditions: By cooling down the crystal from 600 K to RT in a low-pressure background of CO, a sufficient amount of thermal energy is available to facilitate the Pt restructuring while the temperature is gradually lowered and the CO coverage thus slowly raised. In this way, large flat terraces exhibiting the (2×1) adsorption structure can be formed, which is identical to the surface morphology and adsorbate structure observed at 100°C and 1 bar of CO. The conclusion of the CO/Pt(110) studies is therefore that the structures observable under low-pressure conditions are indeed highly relevant for the understanding of gas adsorption at high-pressure conditions as long as the pertinent kinetic barriers can be overcome at low temperatures.

4.3 CO adsorption on Pt(111)

The Pt(111) surface is the facet with the lowest surface free energy due to the dense hexagonal close-packing of the platinum atoms on this surface. For this reason, the Pt(111) surface is the most abundant facet on supported nanoparticles, and adsorption studies on Pt(111) - especially at high-pressure conditions - are thus highly relevant for the understanding of the chemistry at real Pt catalysts. The cleaning procedure for Pt(111) consisted of sputtering and annealing cycles similar to the cleaning of the Pt(110) surface. As opposed to Pt(110), the Pt(111) surface is unreconstructed in its clean state, and CO adsorption does not lead to any structural rearrangements of the surface Pt atoms. When discussing pressure gap effects, CO adsorption on Pt(111) thus serves as a representative example of a different class of adsorption systems than CO/Pt(110), because the kinetic barriers for equilibration may be expected to be lower when only adsorbate rearrangements are necessary. From the STM data discussed in this section it is, however, concluded that care must still be taken when comparing high-coverage adsorption structures formed under different pressure and temperature conditions. Similarities between the two pressure regions are indeed found but differences also exist.

In the following a brief summary of previous studies of CO/Pt(111) relevant for the present work is presented, subsequently followed by a presentation of the experimental results, where the CO adsorption structures are followed from UHV pressures up to 1 bar of CO in the same way as for the Pt(110) surface. A comparison is made to low-temperature studies, and the section is finalized with a discussion of the relevance of the findings in the context of PEM fuel cell catalysis.

4.3.1 Previous studies of CO/Pt(111)

An impressively large number of surface science studies have addressed the interaction of CO with the Pt(111) surface and a range of different adsorption structures have been observed under low-pressure and low-temperature conditions (see e.g. [92]) and at high-pressure conditions [70, 72, 93]. Room-temperature exposure of CO on the Pt(111) surface at low pressures ($< 10^{-6}$ mbar) leads to a $c(4\times 2)$ -2CO structure with a mixture of on-top and bridge-bonded CO molecules and with a rather low saturation coverage ($\theta_{\text{CO}}=0.5$ ML) compared to the ~ 1 ML coverage obtained on the Pt(110) surface [94–96]. A hexagonal packing of CO with a lattice distance equal to the van der Waals diameter would yield a coverage of ~ 0.75 ML on Pt(111), and intuitively it would therefore be expected that there is room enough for a denser packing of the CO molecules than what is obtained at RT. At low-temperature conditions a range of high-density CO adsorption structures are found which can be categorized as domain-wall structures, where regions of the $c(4\times 2)$ structure are separated by high-density domain walls of CO molecules (see e.g. [97]). Furthermore, a hexagonally symmetric adsorption structure with a CO density of ~ 0.68 ML has been found after prolonged exposure at 170 K [96].

Jensen *et al.* were the first to obtain STM images of the Pt(111) surface in a background pressure of one atmosphere of CO [70]. A new structure was observed consisting

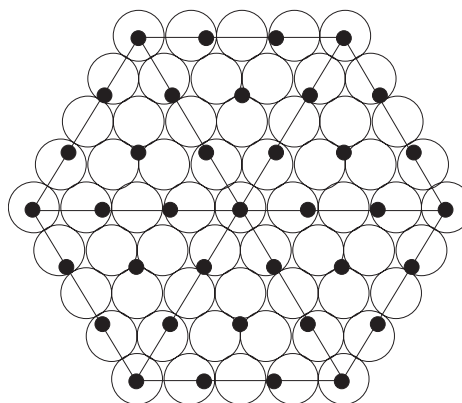


Figure 4.6: Ball model of the (4×4) -9CO adsorption structure at 1 bar of CO proposed by Jensen *et al.* [70]. The CO structure exhibits hexagonal symmetry with the high symmetry directions aligned to the underlying platinum substrate (non-rotated).

of a hexagonal pattern with a periodicity of 12 ± 1 Å, and it was suggested that the observed structure was a moiré pattern due to interference effects between two hexagonal lattices with different lattice constants formed by the CO overlayer and the Pt substrate, respectively.¹ No atomic resolution of CO or Pt was, however, obtained in the studies by Jensen *et al.*, for which reason only indirect evidence for the suggested model was presented. A model for the CO layer was nevertheless proposed, in which the CO formed a hexagonal lattice, rotationally aligned to the Pt substrate and with a lattice constant of 3.7 Å and a resulting coverage of 0.56 ML. The proposed model (depicted in Fig. 4.6) is not equivalent to any of the structures found after prolonged CO exposures at low temperatures, and this fact led the authors to suggest the existence of a pressure gap for CO/Pt(111), i.e. an inequivalence between high coverage studies performed at low-temperature conditions and at high-pressure conditions, respectively. Only 1/9 of the CO molecules in the unit cell are observed to be positioned in on-top sites, which can be compared with spectroscopic studies using Sum Frequency Generation (SFG). In an SFG study by Su *et al.*, the amount of CO adsorbed in on-top sites was found to decrease when the pressure was raised above 150 torr [72], compatible with the suggested model in [70]. The SFG study in [72] was, however, contradicted by Rupprechter *et al.* in [93] where similar SFG studies showed that the on-top signal was almost independent of the CO pressure. After the presentation of our STM results in the following section, a comparison to the SFG studies will be made.

4.3.2 Experimental results

To investigate the apparent pressure gap for CO/Pt(111), high-resolution STM images were acquired following the development of adsorption structures as a function of the

¹The concept of a moiré pattern will be explained below.

CO pressure from UHV conditions up to 1 bar of CO. All experiments were performed at room temperature. At pressures higher than $\sim 10^{-6}$ mbar, a range of different structures, all characterized by large hexagonal super-structures, were found. The size of the unit cell varied as a function of pressure from ~ 7.7 Å at 10^{-6} mbar to ~ 12.0 Å at 1 bar of CO. Examples of such STM images from different pressure regimes are shown in Fig. 4.7. The qualitative features of the hexagonal moiré pattern found by Jensen *et al.* are thus recognized in our experiments, but as we will see below, we find that their proposed model for the CO adsorption structure is wrong. In some of our STM images atomic resolution was obtained, and we find that the CO molecules indeed form hexagonally dense structures as suggested in [70], but the structures are rotated with respect to the underlying Pt substrate. In the STM images at intermediate pressures ($\lesssim 10^{-2}$ mbar), atomic resolution of the CO-layer has, however, been impossible; Whenever high-resolution images were obtained at these pressures, the atomic-scale details revealed the Pt atoms instead of the CO molecules. The moiré super-structures was, however, observable in the entire pressure range from $\sim 10^{-6}$ mbar to 1 bar, and from the orientation and size of the moiré pattern combined with atomically resolved images of the clean Pt(111) surface, the CO overlayer structure could be determined as a function of pressure. To extract such information, the geometrical concepts of moiré structures will be discussed in the following section, whereby a general relation between the CO structure and the observed moiré pattern is derived.

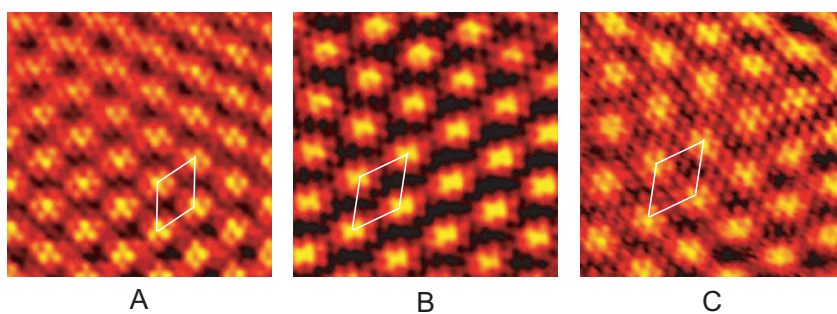


Figure 4.7: STM images (60×60 Å²) of CO/Pt(111) at different pressures; **A**: $1.3 \cdot 10^{-2}$ mbar; **B**: 130 mbar; **C**: 950 mbar. Low-pass frequency filtering has been applied to the images to enhance the atomic-scale details.

Moiré patterns

The superposition of two hexagonal layers with different lattice constants and different orientation gives rise to so-called moiré patterns, which in a simple way can be thought of as the two-dimensional analogue to the one-dimensional *beating frequency* between two harmonic functions with nearly identical frequency. The analogue is illustrated in Fig. 4.8, where the result of adding two one-dimensional sine curves is compared to the result of adding two hexagonal lattices.

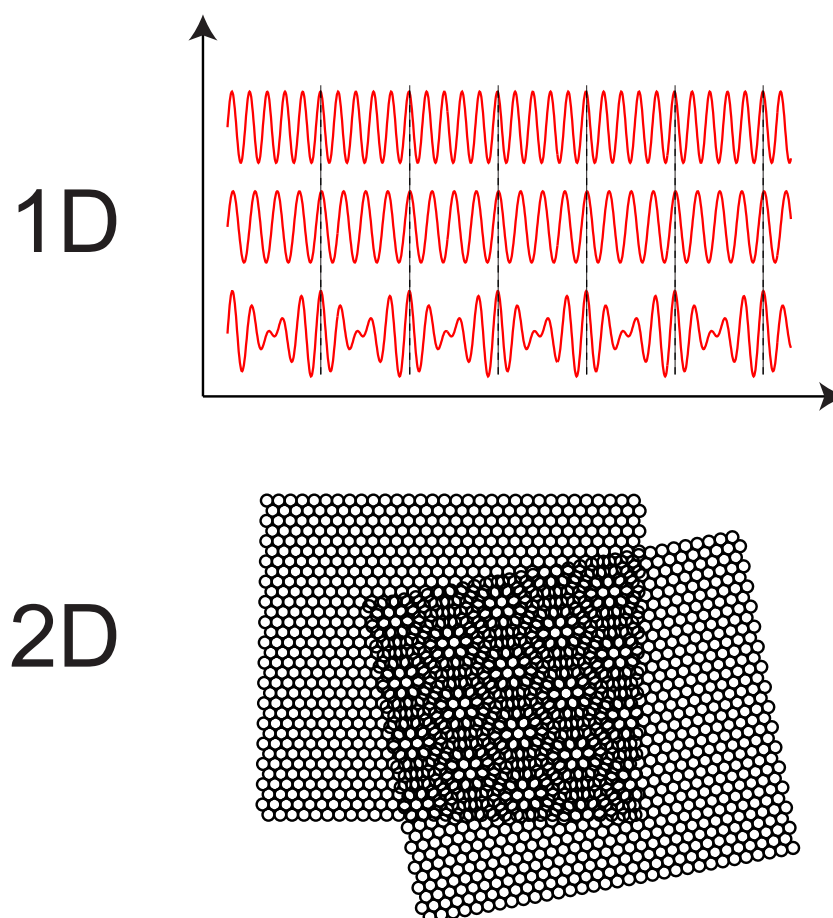


Figure 4.8: **Top:** The addition of one-dimensional sine functions with similar wavelength leads to an interference pattern with a low-frequency amplitude modulation of the oscillations, the so-called beating frequency. **Bottom:** The addition of two-dimensional hexagonal patterns gives rise to similar effects where the in-phase and out-of-phase regions constitute a “low-frequency” array with hexagonal symmetry, the so-called moiré pattern.

The mathematical foundation of such interference effects can be found in the sum formula for sine functions,

$$\sin(A) + \sin(B) = 2 \sin \frac{1}{2}(A + B) \cos \frac{1}{2}(A - B), \quad (4.1)$$

which shows that the addition of two sine functions can be described as an amplitude modulated sine wave. When the frequencies of the two sine functions are of similar

size, the amplitude modulation (last term in Eq. 4.1) will exhibit a long wavelength periodicity, whereby the beating (one-dimensional) or moiré pattern (two-dimensional) can be found as a superstructure. In the two dimensional case, the relevant parameter determining the moiré periodicity is not the “frequency” (or atom-atom distance) but the *wave vectors* for each of the hexagonal lattices. A hexagonal lattice can be described as the superposition of three plane waves intersecting each other at 60° angles, as illustrated in Fig. 4.9, and a wave vector, \vec{q} , for a hexagonal lattice is here defined as a vector pointing in one of the three high-symmetry directions of the plane waves constituting the hexagonal lattice (green arrows in Fig. 4.9) and having a length corresponding to the reciprocal value of the wavelength of the plane waves. It should be noted that the wavelength, λ , of the three waves in a hexagonal lattice is not the same as the nearest neighbor distance on Pt(111), a_{Pt} , but rather $\lambda = \sqrt{3}a_{Pt}/2$, which is illustrated in the lower part of Fig. 4.9.

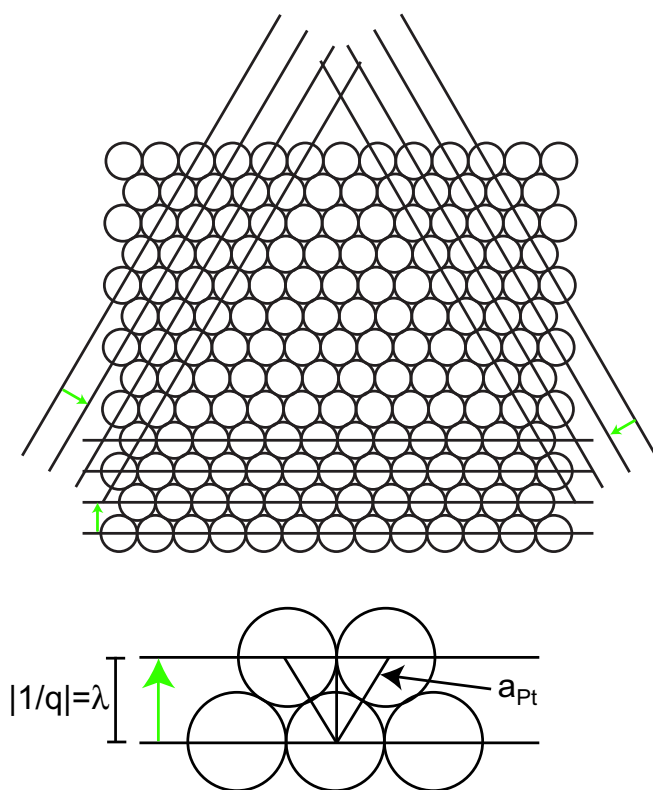


Figure 4.9: **Top:** Ball model of a hexagonal lattice illustrating the three plane waves constituting the lattice. Green arrows indicate vectors along the wave vector direction for each plane. **Bottom:** Illustration of the geometrical relation between wave vector and Pt-Pt distance.

By geometrical scrutiny, a formula similar to Eq. 4.1 can be derived showing that the summation of two-dimensional hexagonal patterns results in an amplitude modulated hexagonal pattern, where the amplitude modulation - or moiré pattern - is determined by the wave vector difference between the two original patterns. In the case of CO on platinum, we therefore get:

$$\vec{q}_M = \vec{q}_{CO} - \vec{q}_{Pt}, \quad (4.2)$$

where the \vec{q}_x 's are the wave vectors for the moiré pattern (M), the CO structure and the platinum surface, respectively.

Fig. 4.10 shows a schematic drawing of the result of adding two hexagonal lattices as viewed in reciprocal space. The top part of the figure sketches the two hexagonal lattices and the resulting moiré pattern. One of the three wave vectors of the plane waves constituting the hexagonal lattice has been marked for the Pt substrate lattice (green) and the CO overlayer (red), respectively. The difference vector gives rise to the moiré pattern (black) also depicted in the drawing. From the middle part of Fig. 4.10 the following geometrical relations can be obtained by use of cosine and sine relations:

$$q_{CO}^2 = q_{Pt}^2 + q_M^2 - 2q_{Pt}q_M \cos(180^\circ - \alpha) \quad (4.3)$$

$$\sin(\theta) = \frac{q_M}{q_{CO}} \sin(180^\circ - \alpha), \quad (4.4)$$

where θ is the angle between CO and Pt layers and α is the angle between the Pt hexagon and the moiré structure. The lower part of Fig. 4.10 gives a relation between the angle α and the *smallest angle*, Ψ , between the Pt substrate and the moiré lattice:

$$180^\circ - \alpha = 60^\circ - \Psi \quad (4.5)$$

Using Eq. 4.3 together with Eq. 4.5 the size of the CO wave vector, q_{CO} , can be extracted without any actual resolution on the CO molecules; only moiré angles and distances relative to the platinum substrate are needed to extract the orientation and lateral dimensions within the CO layer. Such a method has been utilized in the following for the CO coverage determinations in the pressure range from $\sim 10^{-6}$ mbar up to $\sim 10^{-1}$ mbar. At higher pressures atomic resolution of the CO molecules has been obtained and direct determinations of the CO coverage were thus easily obtained by simply measuring the distance between individual CO molecules. The coverage determination based on Eqs. 4.3 and 4.5 has also been tested for these higher pressures and good agreement is found between calculated coverages and the coverages measured directly.

The reasoning of moiré patterns presented above is all done in the framework of a simple addition of harmonic functions with different wavelengths and orientations. "Real" atoms or molecules are of course not sinusoidal and, furthermore, the simple summation which results in a high-frequency wave with the mean wavenumber of the two original waves and a low-frequency amplitude modulation, has nothing to do with the atomic-scale details of the structures found for overlayers on surfaces; The height of CO on Pt can not simply be described as the local height of CO added to the local height of Pt. The moiré unit cell extracted by considerations like above is, however,

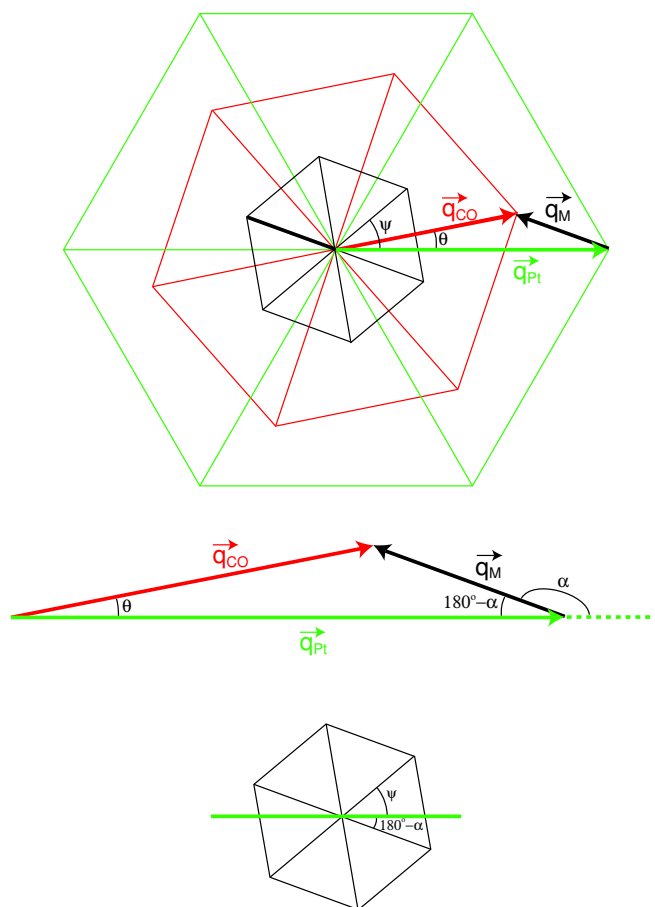


Figure 4.10: Schematic drawing illustrating the geometrical concepts for the derivation of Eqs. 4.3–4.5 from Eq. 4.2. The vectors and hexagons are sketched in reciprocal space. **Top:** The subtraction of two wave vectors gives rise to a moiré wave vector, which constitutes one of the plane waves in the moiré pattern (see Eq. 4.2). **Middle:** Trigonometrical relation between the wave vectors of the three hexagonal lattices; θ is the Pt-CO angle and α is the Pt-moiré angle. **Bottom:** The smallest angle, *Psi* ($\leq 60^\circ$), between the Pt substrate and the moiré structure is given by Eq. 4.5.

relevant for the discussion of surface structures. The unit cell describes the cell of coherence between the two hexagonal lattices, and this cell will show up also in experiments even though the internal structure within the cell may not resemble the model of simple addition. STM measures the local density of electronic states, and for some adsorption systems the imaging might even be reversed so that highly protruding overlayer molecules (adsorbed e.g. at on-top sites) are imaged as depressions. The origin of the

moiré pattern formation observed in STM is therefore probably a complicated combination of electronic and geometrical effects. Nevertheless, the coincidence cell between the two hexagonal lattices will also show up in STM [98].

Much of the moiré pattern analysis presented below has been performed in reciprocal space instead of directly on the STM images. If the moiré pattern is considered as an amplitude modulation of the CO lattice, a two-dimensional Fourier transform of the STM images will exhibit a folding of two hexagonally symmetric sets of delta-functions. This is indeed what is observed as seen below in e.g. Fig. 4.11. When atomic resolution is obtained with the STM within the moiré unit cell, a Fourier transformed STM image clearly reveals the moiré hexagon and an additional CO hexagon, which also in some cases contains faint satellite peaks from the folding with the moiré pattern. Higher order peaks of the moiré pattern are usually also revealed at high-resolution conditions, which illustrates that a simple sinusoidal description of the height variations within the unit cell is not correct although it grasps the main features of the surface structures.

High-pressure results

Fig. 4.11 shows an example of a high-resolution STM image of CO/Pt(111) obtained at a CO pressure of ~ 1 bar at room temperature conditions. The individual CO molecules are resolved and the coverage can thus be determined directly. The figure, moreover, shows a Fourier transform of the image, in which the hexagonally symmetric spots constituting the moiré pattern are revealed together with six fainter spots from the CO molecules. From the Fourier transformed image, the angle and intermolecular distances of the CO layer are readily obtained, and a model for the adsorption phase of CO at 1 bar can be derived.

The extracted lattice parameters from numerous STM images acquired at 1 bar of CO show that the molecules form a moiré structure which is compatible with a commensurate structure having a $\sqrt{19} \times \sqrt{19}R_{23.4^\circ}$ -13CO unit cell. The CO molecules form a hexagonally close-packed overlayer rotated $\theta = 9.5^\circ$ with respect to the Pt substrate in the same direction as the 23.4° -rotation of the moiré pattern, which is revealed both directly in the STM images and in the Fourier transformed image presented in Fig. 4.11. The structural model of the CO adsorption phase is sketched in the ball model in the right part of Fig. 4.11. The lateral registry of the adsorption phase with the Pt substrate cannot be judged from the STM image even though a geometric interpretation, where on-top adsorbed CO is imaged highest (as suggested in the ball model), is tempting. Such a geometrically appealing lateral registry is supported by density functional theory calculations by Bjørk Hammer [99]: The CO adsorption energy was calculated for three different $\sqrt{19} \times \sqrt{19}R_{23.4^\circ}$ -13CO structures each exhibiting a hexagonal packing of the CO molecules. In the three structures, one of the CO molecules was fixed to either an on-top site, a bridge site or a hollow site. The structure fixed to the on-top positions (i.e. the model sketched in Fig. 4.11) was found to be energetically preferred over the other two structures with ~ 0.4 eV per CO molecule.

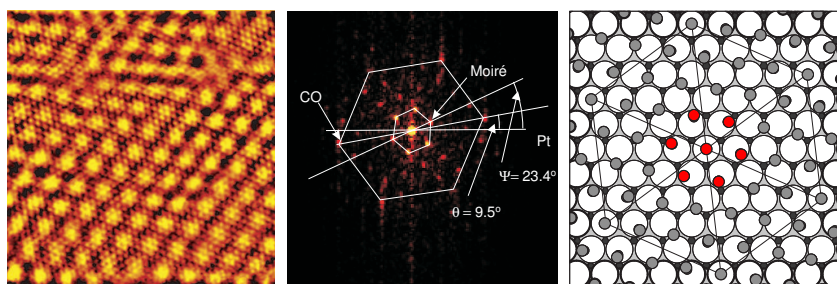


Figure 4.11: **Left:** High-resolution STM image ($110 \times 120 \text{ \AA}^2$) of the CO adsorption structure on Pt(111) at a CO pressure of ~ 1 bar. The single molecules can be seen together with the moiré structure. Fourier filtering has been employed to highlight the atomic-scale details. **Middle:** Fourier transform of the STM image in the left part of the figure. A small hexagon of bright spots corresponding to the moiré pattern is observed in the middle of the image. A number of higher order peaks are, furthermore, seen, and a larger hexagon corresponding to the CO structure is also revealed. The angle between the high-symmetry directions of the CO structure and the Pt substrate, θ , is indicated in the image together with the angle between the moiré pattern and the Pt substrate, Ψ . **Right:** Ball model illustrating the commensurate $\sqrt{19} \times \sqrt{19}$ -moiré unit cell, which is found to be in good agreement with the CO adsorption structure at 1 bar.

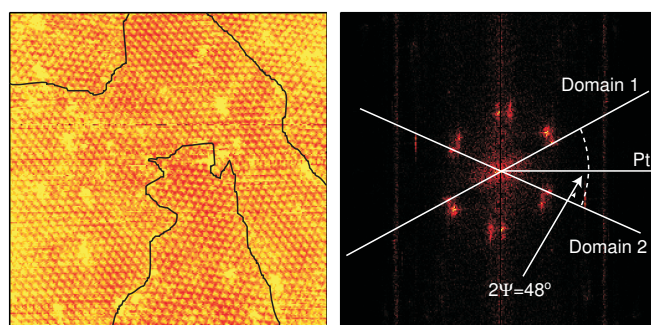


Figure 4.12: **Left:** Zoom-out STM image ($500 \times 500 \text{ \AA}^2$) of the CO/Pt(111) moiré structure at a CO pressure of ~ 1 bar. Two rotational domains can be identified in the image. **Right:** Fourier transform of the STM image. Two distinct hexagons are revealed, each rotated $24 \pm 2^\circ$ with respect to the high-symmetry direction of the underlying Pt substrate. No resolution of Pt atoms can be seen in such images, but the orientation of the crystal is known from STM images acquired under UHV conditions.

At a CO pressure of 1 bar, two rotational domains are found for the adsorption structure, which is in good agreement with the presented model. Fig. 4.12 shows an example of an STM image, where two domains of the moiré pattern can be identified either directly on the STM image or in the Fourier transformed image (right part of the figure), which exhibits two distinct hexagons. This finding is a direct proof that the model of the CO adsorption structure proposed by Jensen *et al.* (Fig. 4.6) is wrong. If the high-symmetry directions of the CO structure were aligned with the high-symmetry directions of the platinum substrate (as suggested in [70]), only one domain of the structure would be found. Only rotated overlayers exhibit two rotational domains of the adsorption structure.

Turning towards the adsorption structures found at intermediate pressures (10^{-6} mbar–1 bar), Fig. 4.13 summarizes the STM results obtained for the CO adsorption structures. The two graphs in the figure follow the development of the moiré lattice constant and the angle with respect to the Pt substrate, Ψ . The unit cell of the moiré structure is continuously expanding as a function of increasing pressure, but saturation occurs around 0.1–1 mbar, where the high-pressure $\sqrt{19} \times \sqrt{19}$ structure is approached. At the lower pressures, the continuous increase in the moiré lattice constant suggests that the CO adsorption structures are incommensurate with the underlying Pt substrate. Two different pressure regimes can be identified when the angle of the moiré lattice is investigated: At lower pressures ($\leq 10^{-2}$ mbar) the angle is fixed at $\sim 30^\circ$, which is a high-symmetry angle for the hexagonal lattices. Only one domain of the moiré structure is found for these pressures in agreement with the symmetry. Above the transition pressure ($> 10^{-2}$ mbar), the 23.4° angle is approached and two domains are accordingly found for the structures similar to the findings at 1 bar presented in Fig. 4.12.

The reversibility of the formation of different hexagonal CO adsorption structures was investigated by comparing the moiré patterns formed at a given pressure but prepared by two different methods: First, the pressure was increased from UHV conditions to the desired CO pressure and the adsorption structure was studied by STM. Subsequently, the pressure was lowered from 1 bar to the chosen CO pressure and STM images were acquired again. We found no difference in adsorption structures in the two cases, and it is therefore concluded that the moiré patterns change reversibly as a function of the CO pressure at room temperature conditions, and the adsorbed CO must be in equilibrium with the gas phase (at least within the studied pressure range, $> 10^{-6}$ mbar). These findings are relevant for the discussion of CO poisoning in fuel cells, as we will see below.

From the geometrical considerations on moiré structures discussed above (Eqs. 4.3–4.5), the coverage of CO can be extracted and these results are summarized in Fig. 4.14. A continuous increase in coverage is seen from the lowest coverages of 0.52 ML - very close to the well-known $c(4 \times 2)$ structure formed at UHV pressures - up to 0.68 ML in the $\sqrt{19} \times \sqrt{19}$ structure. The $c(4 \times 2)$ structure is stable even when the chamber is completely evacuated to UHV pressures after high-pressure exposure, and the (room temperature) reversibility of CO adsorption thus only holds for the higher CO coverages at high and intermediate CO pressures.

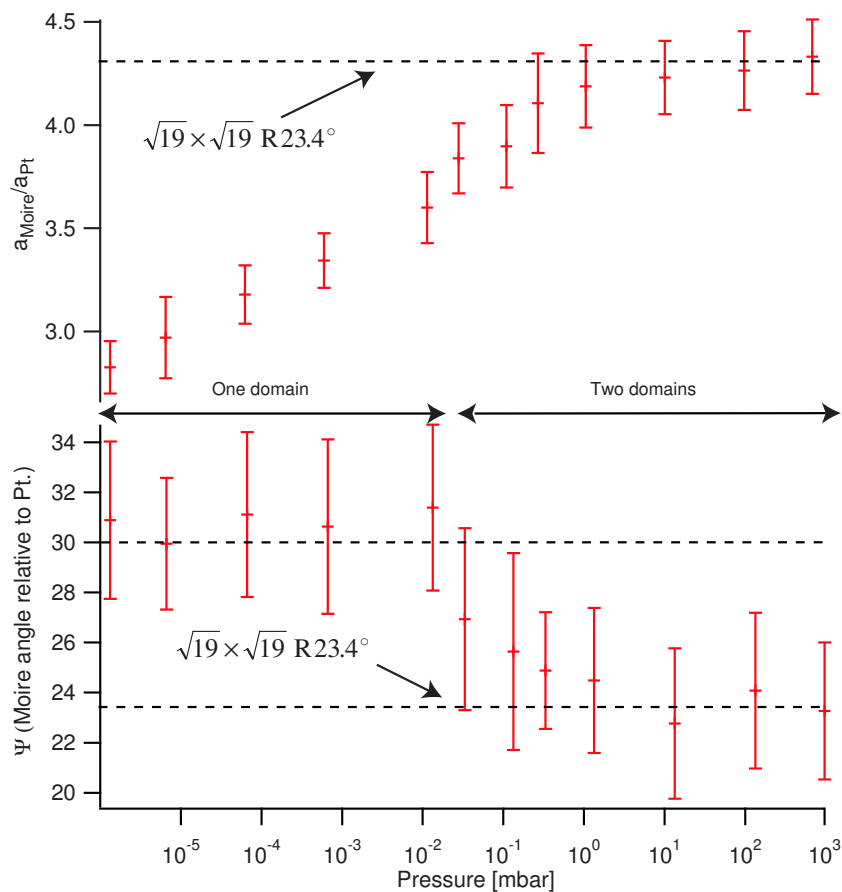


Figure 4.13: Compilation of STM-based investigations of the CO/Pt(111) moiré structures formed at room temperature conditions in the pressure range from 10^{-6} mbar up to 1 bar. The upper part of the graph displays the lattice constant ratio between the moiré unit cell and the platinum substrate, and the lower part displays the moiré angle relative to the high-symmetry directions of platinum. At pressures higher than 10^{-2} mbar two rotational domains are found of the moiré structures, whereas investigations at lower pressures only reveal a single domain.

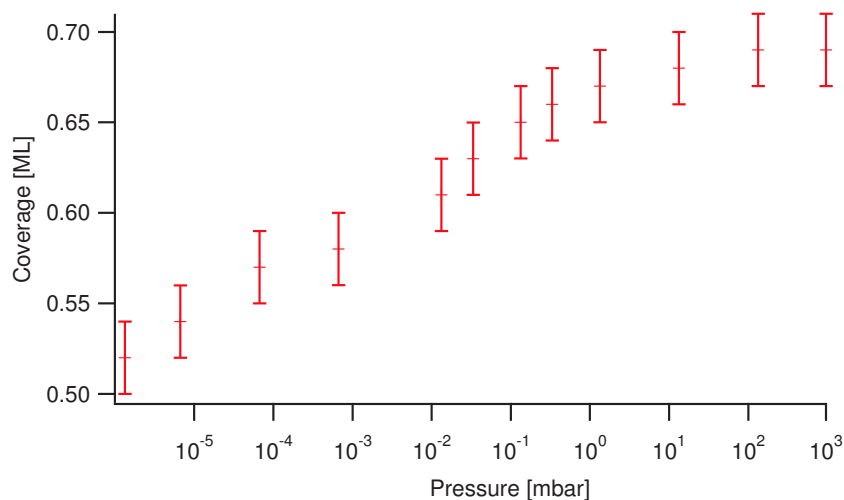


Figure 4.14: CO coverage displayed as a function of pressure. The data points at high-pressure conditions ($> 10^{-2}$) have been obtained by a direct inspection of the CO molecules in atomically resolved STM images, and the data points at lower pressures have been calculated from the moiré structures by using Eqs. 4.3 and 4.5.

Low-temperature CO/Pt(111) results

To investigate the adsorption structures for CO on Pt(111) at the low-pressure side of the pressure gap, the surface was exposed to CO at low-temperature conditions. Figure 4.15 shows a striped domain structure, which is formed upon CO exposure at 100 K. We have not investigated the atomic-scale details of this structure, but the stripes certainly bear no resemblance to the HP moiré structures described above. The structure is consistent with earlier LEED and EELS studies at 100 K where the adsorbate was found to exhibit an island-like structure [100]. At 100 K, the CO molecules are probably not able to equilibrate, and the adsorption structures formed are metastable and should therefore not be compared to the equilibrium structures formed at high-pressure conditions.

Exposing the surface to CO at slightly higher temperatures, here 170 K, is found to be more appropriate for the comparison with the high-pressure studies. As mentioned in the introduction of the chapter, Ertl and co-workers have found a hexagonally symmetric CO structure with a coverage of 0.68 ML after prolonged exposure at 170 K [96], and in our STM images at 170 K we indeed recognize the moiré structure with the same $(\sqrt{19} \times \sqrt{19})R23.4^\circ$ -13CO unit cell as the one found in the HP studies (see Fig. 4.16). The 170 K is thus apparently a sufficiently high temperature for CO to settle into its equilibrium structure. A comparison between high-coverage adsorption structures formed at low temperature conditions and high-pressure conditions, respectively, is, however, not straightforward: A number of domain wall structures which are unseen at high-pressure conditions are found at intermediate temperatures between the 170 K used in the above

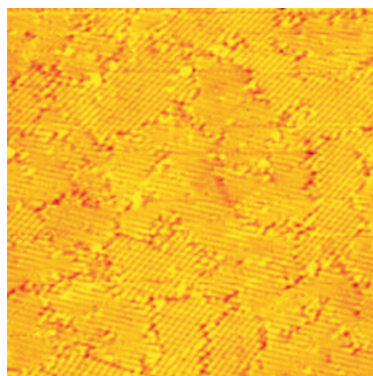


Figure 4.15: *Striped domain structure formed from low-pressure CO adsorption on Pt(111) at 100 K ($500 \times 500 \text{ \AA}^2$).*

experiment and room temperature (see e.g. [97]). At the corresponding coverages at intermediate pressures, the incommensurate moiré patterns were found. It is possible that the domain wall structures observed in the range from 170 K to room temperature are kinetically hindered structures similar to the striped structure observed at 100 K (Fig. 4.15), but it is probably more correct to conclude that even though similar adsorption structures are found on both sides of the pressure gap, differences are also observed. The finding of the $\sqrt{19} \times \sqrt{19}$ -structure at 170 K, however, show that no large fundamental differences exist when CO adsorption is concerned on the two different sides of the pressure gap. This is the most important conclusion of the studies, since CO/Pt(111) has previously been used as an example of the opposite, i.e. to illustrate the fundamental difference between high-pressure studies and experiments formed at low-temperature and low-pressure conditions [70, 72]. It is, however, clear that care must be taken when comparing adsorption structures from the two sides of the gap.

4.3.3 Discussion

Returning to the Sum Frequency Generation (SFG) studies in [72, 93], these results may be compared to the HP-STM studies presented in this chapter. Su *et al.* found a steep drop in the on-top coverage of CO when the pressure was increased from UHV to high-pressure conditions [72], but Rupprechter *et al.*, on the other hand, observed a rather constant amount of CO adsorbed in on-top positions with a slight increase of $\sim 40\%$ and a weak broadening and shift of the vibrational peak [93].

In the saturated room-temperature CO structure on Pt(111) at UHV conditions, the coverage is $\theta = 0.5 \text{ ML}$ and the ratio of on-top sites to the total number of CO molecules is 1:2. In our proposed model for the adsorption structure at 1 bar, only one CO molecule sits directly in an on-top position, but six other molecules (surrounding the on-top molecule) are adsorbed in nearly-on-top sites (marked by red balls in the model in Fig. 4.11). The on-top occupancy is thus almost 7:13 at 1 bar, comparable to the

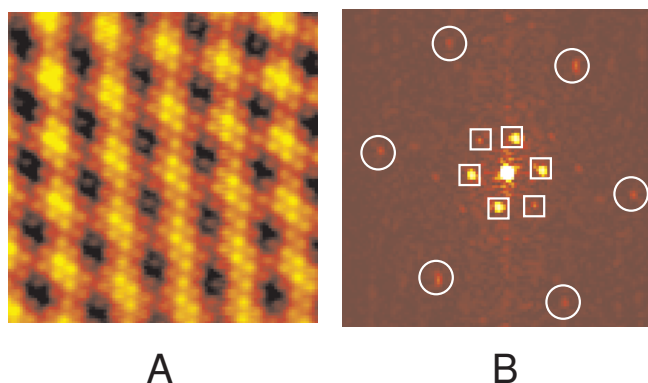


Figure 4.16: Low-pressure CO adsorption on Pt(111) at 170 K. **A:** Atomically resolved moiré structure formed by CO on Pt(111) at 170 K. Frequency filtering has been performed to enhance the atomic-scale details. **B:** Fourier transform of the STM image. Peaks corresponding to both the moiré and adsorbate periodicities are clearly distinguished and are marked with squares and circles, respectively. Compare to Fig. 4.11.

ratio in the UHV experiments. The total CO coverage at 1 bar is, however, higher ($\theta_{CO}=13/19 \text{ ML} \sim 0.68 \text{ ML}$) and the density of on-top adsorbed CO therefore increases by $9/19 \sim 47\%$. Our experimental results and proposed model at 1 bar are thus found to be in good agreement with the complementary experiments by Rupprechter *et al.* In both types of experiments, a small increase in the number of nearly-on-top adsorbed CO is found, and the broadening and the shift of the SFG peak observed in [93] are probably due to the small shift away from the on-top position which is seen for six out of seven of the CO molecules in the structure proposed from our STM studies. As suggested in [93], the discrepancy between the two SFG studies is probably due to gas absorption of the IR light in the studies presented in [72].

At intermediate pressures, our STM studies revealed a range of incommensurate moiré structures, and unfortunately a similar determination of the lateral registry between the CO layer and the Pt substrate as was done for the $\sqrt{19} \times \sqrt{19}$ -structure is not possible, since the incommensurate structures are impossible to handle with DFT calculations. Without the lateral registry, STM cannot be used to determine the amount of e.g. on-top adsorbed CO molecules, and it has therefore only been possible to compare the on-top occupancy at 1 bar with the SFG results from the two groups. The rather constant amount of on-top adsorbed CO at intermediate pressures found by Rupprechter *et al.*, however, indicates that some of the CO molecules in the incommensurate structures are indeed adsorbed in near-on-top positions.

It is interesting to note that electrochemical STM studies by Villegas *et al.* of CO adsorption on Pt(111) in a liquid phase reveal a structure, which is identical to the $\sqrt{19}$ -structure suggested by our HP experiments, at a range of electrode potentials [101]. It is intriguing that similarities exist at the atomic level between high gas pressures and

effective high pressures in electrochemistry, but structures with an even denser packing of the CO molecules are, however, also found in the electrochemical studies, where a (2×2) -3CO structure with a coverage of $\theta=0.75$ ML is reported [101]. This coverage is comparable to a hypothetical van der Waals packing of CO molecules on Pt(111) as mentioned above. It would thus be very interesting to image the CO/Pt(111) system at pressures higher than 1 bar to investigate whether or not the (2×2) -3CO structure would also show up in the gas experiments, but unfortunately we are limited to 1 bar because of the window in the high-pressure cell. The dense (2×2) -3CO structure has also been observed on the Rh(111) surface at high pressures of CO [102].

The observed transition from a pressure region with prevalence of high-symmetry (30° rotated) structures to a pressure region where the $\sqrt{19} \times \sqrt{19}$ structure is approached might indicate that different interactions are important for the equilibration of the adsorbate structures in the two regimes. Theoretical modelling by Grey *et al.* has suggested that finite size effects would give rise to high-symmetry angles of the moiré pattern either with respect to the overlayer orientation or to the substrate orientation [103–105]. At intermediate pressures and coverages, we indeed find the 30° rotated structures, and our results thus evidence a rather strong influence of the substrate lattice on the moiré structures in this pressure region. If we interpret the substrate influence as a finite size effect, as suggested by Grey *et al.*, the finite Pt terrace width and especially the symmetrically oriented step edges thus determine the orientation of the moiré structures at intermediate pressures. At higher pressures the seemingly more arbitrary 23.4° rotation is found. The $\sqrt{19}$ -structure is neither high-symmetrically oriented with respect to the platinum substrate or to the CO layer, and one may interpret this as a sign of a weakened influence of the substrate orientation on the moiré angle. The $\sqrt{19}$ -structure is probably coincidentally the hexagonally symmetric structure in the relevant CO coverage range with the largest number of favorable adsorption sites. If we look at the ball model in Fig. 4.11, we find that all the CO molecules can be ascribed to adsorption in near-on-top or near-bridge positions, which is in good agreement with the favored adsorption sites found in other studies [97].

The experimental finding of a continuous variation of the CO coverage as a function of pressure has also been observed for other metal surfaces at high-pressure conditions. Recent results by Quiros *et al.* have shown that the adsorption of CO on Ni(111) gives rise to a range of ordered structures which are continuously compressed when the pressure is varied from 10^{-6} mbar to 1 bar [106]. The continuous variations of densely packed adsorbate structures may thus turn out to be a more general phenomenon for CO adsorption on close-packed metal surfaces at high pressure conditions.

CO Poisoning of PEM Fuel Cells

The reversibility of the CO adsorption observed in the experiments during pressure variations is important for the understanding of fundamental aspects of fuel cell chemistry. As discussed in the introduction (Chapter 1) one of the present technological problems with PEM fuel cells is the CO poisoning, which inhibits hydrogen dissociation on the Pt-based electrodes whereby the activity of the fuel cell is drastically diminished. Pt-Ru alloys have been shown to be more tolerant to high-levels of CO in the gas [19], but to

enable a further development of improved tolerance for anode catalysts, a fundamental understanding of such alloying effects is necessary. At present two mechanisms have been proposed and are debated in the literature:

- *The bifunctional effect* [107], where the effect of Ru on the CO tolerance is explained primarily by the ability of Ru to dissociate water and form OH-groups, which oxidize the CO to CO₂ at the relevant anode potentials [108, 109].
- *The ligand effect*, focusing on the altering of Pt's chemical properties upon alloying with Ru. Both experimentally [66, 110] and theoretically [17, 74] the Pt-CO bond strength in a Pt-Ru alloy has been found to be significantly reduced compared to the bond strength on pure platinum.

An important question in this debate concerns the question of whether the adsorbed CO molecules on the platinum catalyst are in equilibrium with the gas phase or if they are irreversibly adsorbed at the operation temperatures of the fuel cell (80–100°C) [17, 74]. From the STM experiments presented above, it was concluded that the structures formed at room temperature in the pressure range from 10⁻⁶ mbar to 1 bar are indeed in equilibrium with the gas phase, and it may thus reasonably be concluded that equilibrium conditions will also be found at the higher temperatures typically invoked in PEM fuel cells. Furthermore, the CO coverage extracted from the STM experiments exhibits a continuously increasing dependence on the CO pressure. At equilibrium conditions the CO and H₂ molecules will compete for sites on the catalyst surface and a lowering of the Pt-CO bond strength will thus lead to a lower equilibrium CO coverage and thereby increase the amount of available sites for H₂ dissociation. From our experiments we therefore conclude that the ligand effect must be taken into account when discussing the effect of Ru and other modifications of Pt-based fuel cell catalysts. This, however, does not exclude that the bifunctional effect could also be of importance under real fuel cell conditions where water is present also.

The finding of equilibrium conditions between the gas phase and the adsorbates has furthermore been supported by recent studies by Davies *et al.* in which the CO desorption rate was studied from a high area platinum fuel cell catalyst [111]. By investigating the isotopic exchange of CO on the catalyst and extracting the desorption rate as a function of CO pressure, a substantial exchange between the gas phase and the adsorbed CO was shown to take place even at room temperature. Moreover, DFT calculations have revealed that an increase in the CO pressure leads to higher coverages and a concomitant drop in the CO binding energy, thus further supporting the interpretation [111].

4.3.4 Conclusion

Our experimental findings for CO adsorption on Pt(110) and Pt(111) show that the adsorption structures formed at HP conditions are similar to structures which can be formed under low-pressure conditions at low temperatures. If CO exposure is performed at too low temperatures, kinetic limitations are observed at both surfaces. Nevertheless, by taking care of the relevant kinetic barriers for the systems, it has been shown that the high-coverage structures found at high-pressure conditions can indeed also be formed

at low-pressure conditions. For CO adsorption on Pt(110), the relevant high-coverage structure can be obtained by cooling down in a CO atmosphere whereby thermal energy is available for equilibration of the surface, and on Pt(111), the CO high-coverage structures found at 1 bar can similarly be formed by low-pressure CO dosing at 170 K. Even though other domain-wall structures are found at intermediate temperatures, we conclude that no true pressure gap exist between CO exposure at high-pressure conditions and at low temperatures and low pressure, respectively. It is, however, clear that care must be taken when directly comparing specific adsorption structures from the two sides of the gap.

Furthermore, we have found that the CO adsorption structures above 10^{-6} mbar change reversibly with pressure, and the relevance of these findings for the fundamental understanding of CO poisoning in PEM fuel cells has been discussed. Supported by complementary experimental findings and DFT calculations, we conclude that ligand effects must play a role when the CO tolerance on Pt-based anode catalysts is modified by alloying with e.g. Ru.

CHAPTER 5

Modifications of the active sites on a nickel surface

In this chapter, experimental studies of the interaction of CO with a Ni(111) surface are described. The rate of CO dissociation is found to be much higher on nickel steps than on the nickel terrace sites, and the insight thus gained is used in three different approaches aiming at modifying the reactivity of the nickel crystal. We demonstrate that it is indeed possible to inhibit the dissociation of CO by blocking the “active” step sites, and this ability to preserve C=O bonds on modified nickel surfaces may be of interest for different catalytic applications. One of the studied modifications of the nickel surface involves the formation of a Au/Ni surface alloy, which furthermore modifies the reactivity of the terrace atoms. We have investigated the stability of this alloy at high-pressure conditions and found that high pressures of CO induce a complete phase separation of the surface alloy. By following the phase separation in real-time with STM movies, we arrive at a model for the de-alloying.

5.1 Introduction

5.1.1 Motivation

In the previous chapter, the versatility of platinum in catalysis was discussed as a motivation for the presented studies, and there is no doubt that platinum will play a major role also in the future, e.g. as an anode material in fuel cells. One of the main problems with platinum-based catalysts in general is, however, the high price of the metal, and instead of focusing on platinum-based alloys for solving e.g. the CO poisoning problem of anode catalysts, one might be tempted to seek similar reactivities for other alloys based on different metals. For this to be a viable route, the “host” material must be cheap and have characteristics resembling those of Pt, and a natural choice could therefore be to start out from nickel. In this chapter we focus on the interaction of CO molecules with a Ni(111) surface. The binding energy of CO on nickel and platinum surfaces are of similar magnitude [58], but when it comes to reactions like the dissociation of CO, nickel is more reactive than platinum; CO is known to dissociate even at fairly low temperatures (~ 400 K) and at UHV compatible pressures on nickel surfaces [112].

The studies presented in this chapter can be seen as small steps along the route from nickel towards a more noble material, approaching “cheap platinum”. We have investigated the interaction and especially the dissociation of CO on the Ni(111) surface, and through atomic-scale studies we have found that the step sites play a major role for the dissociation process. This knowledge have lead us to suggest three different routes towards blocking of the dissociation channel, whereby the catalytic properties with respect to CO dissociation might approach the reactivity of the platinum surface. One of the suggestions, a Au/Ni surface alloy, simultaneously modifies the reactivity of the Ni terrace atoms, and in addition to the inhibition of CO dissociation, the binding energy of CO molecules is lowered. The Au/Ni system might therefore be a candidate to substitute platinum-based alloys in PEM fuel cells, and for this reason we tested the stability of the alloy under high-pressure conditions. The experimental results, however, reveal that high pressures of CO lead to a complete phase separation of the surface alloy. The finding of a high-pressure induced phase separation raises interesting fundamental questions in the context of the pressure gap: What is the physical reason for the destabilization of the alloy when the CO pressure is increased from UHV to ambient conditions? To answer such questions, we have acquired STM movies following the temporal evolution of surface structures at high-pressure conditions, and we find that the formation of nickel carbonyl species may play an important role at high-pressure conditions. Preliminary experiments where water and CO are co-adsorbed at high-pressure conditions indicate that the alloy phase separation may be inhibited by the presence of water, and the prospect of using Au/Ni alloys as PEM fuel cell catalysts may thus still be conceivable.

In the following, the applications of nickel in catalysis involving CO are briefly discussed. Subsequently, the concept of active sites is considered with special focus on the dissociation of CO on nickel surfaces. Our experimental studies of CO dissociation are based on the detection of carbon with STM, and the relevant carbon phase on Ni(111) is therefore described before embarking upon the discussion of the experimental results. In Section 5.2, direct atomic-scale evidence is presented showing that the step sites on

Ni(111) are the active sites for CO dissociation. This knowledge is used in Section 5.3, where Ag, Au and S atoms are utilized to block the dissociation reaction by modifications of the step sites. Section 5.3.2 discusses the lowering of the CO binding energy on a Au-Ni surface alloy, and finally, Section 5.4 describes our high-pressure experiments, where CO is shown to induce a phase separation of the Au-Ni surface alloy.

5.1.2 Nickel catalysts

Nickel is used as a catalyst for a variety of industrial applications including steam reforming and CO methanation (inverse steam reforming) [1, 113], and it is used as an anode material in solid oxide fuel cells [15]. Steam reforming is one of the most important technological applications of nickel catalysts. The reforming process is a reaction between natural gas, e.g. methane, and water to form CO and H₂ (so-called synthesis gas or “syn gas”),



and this reaction will probably be even more important in a future hydrogen society for the production of hydrogen. The syn gas is, furthermore, the basis for a wealth of other processes like the production of methanol and other chemicals, and the hydrogen from the syn gas is used for the production of ammonia.

One of the technological challenges in steam reforming is to avoid the formation of carbon-deposits, so-called “coking” of the catalyst, which is a possible side-reaction when running the steam reforming process at a low water-to-carbon ratio. Coking leads to a deactivation of the catalyst and breakdown of the catalyst pellets, which may cause a self-accelerating situation with blockage of the reactor tubes, formation of “hot spots” and further coking [114]. A number of solutions to this problem have been proposed, e.g. the SPARG process where H₂S is added to the gas flow resulting in adsorbed sulfur atoms which inhibit coking [115]. Furthermore, a recent solution based on surface science studies suggested that Au/Ni surface alloys would be a promising non-coking steam reforming catalyst, because Au destabilizes the binding of carbon to the Ni atoms [7].

In CO methanation, CO and hydrogen are reacted to form methane and water,



The established basis for the methanation process is the hydrogenation of “active” surface carbon species, which are formed by the so-called disproportionation of CO, also known as the *Boudouard reaction* [1, 23],



In the following sections, the Boudouard reaction will be studied in detail, and atomic-scale information will be presented, which explains the inhibition of the reaction by co-adsorbates like sulfur, silver and gold. Goodman and co-workers have previously shown that sulfur lowers the rate of the methanation reaction [116], and the STM experiments presented in this chapter thus provide an atomistic explanation of this well-known

inhibition effect. The blocking of the CO dissociation reaction on Ni and the thus following inhibition of the CO methanation reaction may be of high relevance for certain catalytical processes where the dissociation of CO is unwanted. Recent publications by Dumesic and co-workers concerning the low-temperature formation of hydrogen from biomass-derived hydrocarbons (e.g. sugars), provide an interesting example of the relevance of such selective control of CO dissociation [13, 14]: At the reaction conditions in the experiments described by Dumesic and co-workers, the formation of methane and other alkanes from CO and H₂ is thermodynamically favorable, and a selective catalyst preserving CO bonds is therefore needed to reach a reasonable hydrogen yield from the biomass,



An essential characteristic of the investigated Pt catalyst was therefore the ability to avoid the breaking of the C=O bonds, but again the high price of platinum may pose a barrier for such routes towards sustainable hydrogen production. Modifications of Ni crystals to block the dissociation of CO (Boudouard reaction) would thus be highly relevant in this context.

5.1.3 Active sites for dissociation

The main objective of the studies presented below has been to show that the Ni steps are the active sites for CO dissociation on Ni(111) and to demonstrate how the modification of steps leads to changes of the reactivity of nickel surfaces. It is well-known that steps in general are the more reactive sites on surfaces [1, 117–119], which was also discussed in Chapter 3. The first discussion along these lines was made already in 1925 by Taylor [6], but it was, however, not until 1997 that Zambelli *et al.* provided the first direct STM-based evidence of such an effect, by showing that the steps on a Ru(0001) single-crystal surface are the active sites for NO dissociation. Dahl *et al.* quantified this effect for N₂ dissociation on Ru(0001), using density functional theory calculations (DFT) and detailed experiments to show that the dissociation at the steps has an activation energy which is more than 1 eV lower than on the terraces [118].

Concerning the sites for CO dissociation on nickel surfaces, Bengaard *et al.* recently published extensive DFT studies of steam reforming on nickel, which, among other things, showed that step sites are more active for CO dissociation than terrace sites [120]. Experimental results by Nakano *et al.* [112, 121, 122] and Erley *et al.* [117] have confirmed these findings, but their experimental evidence is, however, rather indirect. By scrutiny of the growth mode of carbon on Ni upon CO exposure, we provide a more direct experimental proof of the relevance of step sites for CO dissociation. Furthermore, we show that the step sites on Ni(111) can be blocked for CO dissociation, which further corroborates the fact that steps are indeed the active sites and at the same time provides ideas for Ni-based catalysts with the ability to preserve C=O bonds.

5.1.4 Carbon phases on Ni(111)

In industrial applications of nickel catalysts like steam reforming, many different types of carbon growth are seen. The different carbon types depend on feed stock and temperature [113], and the formation of so-called encapsulating carbon, pyrolytic carbon, carbon whiskers and carbon nanofibers have been reported [113, 123]. On single-crystal nickel surfaces, however, only two ordered phases of carbon are found: A carbide phase formed at temperatures below ~ 600 K and a graphite phase formed at higher temperatures [124]. Since all of our experiments have been performed at temperatures ≤ 500 K only the carbide phase is of relevance for the following discussion.

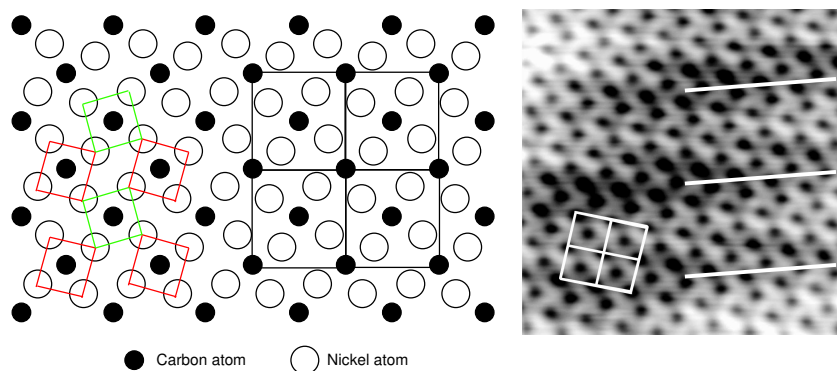


Figure 5.1: **Left:** Model of the Ni(111) carbide phase with the “clock” reconstruction of the topmost Ni-layer. The red and green squares illustrate the local (100)-like structure which is rotated clockwise and anticlockwise, respectively, and the $c(2 \times 2)$ grid in the right part of the sketched model shows the square-like structure of the carbon atoms. **Right:** STM image ($45 \times 48 \text{ \AA}^2$) of the carbide phase. A ($5 \times 5 \text{ \AA}^2$) grid shows the $c(2 \times 2)$ carbon structure, and the three white lines indicate the stripe structure arising from the incommensurability of the overlayer. Figure adapted from [124].

The carbide phase on the Ni(111) surface has been studied by LEED [125] and STM [124]. The phase consists of a so-called “clock” reconstruction of the Ni(111) surface, where the topmost atomic layer has a local (100)-like structure with squares consisting of four nickel atoms rotated $\sim 15^\circ$ clockwise and anticlockwise, respectively, as seen in the schematic model in the left part of Fig. 5.1. The reconstruction of the nickel surface causes a $\sim 10\%$ mass reduction of the topmost nickel layer. The carbon atoms form a square-like $c(2 \times 2)$ structure, which is incommensurate with the Ni substrate, and the incommensurability results in a striped appearance, which is readily observed in STM images. An example of a high-resolution STM image of the carbide structure is shown in the right part of Fig. 5.1. The carbon atoms are imaged as depressions and the striped structure (indicated with white lines in the figure) allows for the identification of the carbide structure with STM even without having genuine atomic resolution, which greatly simplifies the studies presented below.

5.2 CO dissociation

When exposing a Ni(111) surface to CO at 400 K, carbon atoms are formed according to the Boudouard reaction, $2\text{CO} \rightarrow \text{C} + \text{CO}_2$, as described above. High-resolution STM images of the Ni(111) surface after CO exposure reveal the existence of small carbidic islands even after small exposures of CO (5 L), thereby confirming that carbon formation and thus CO dissociation has taken place (See Fig. 5.2). The carbide islands are exclusively observed on the upper terrace of the Ni steps, which is reasonable, because the Ni atoms at these sites are more free to move and thereby accommodate the 10% mass reduction observed in the reconstruction.

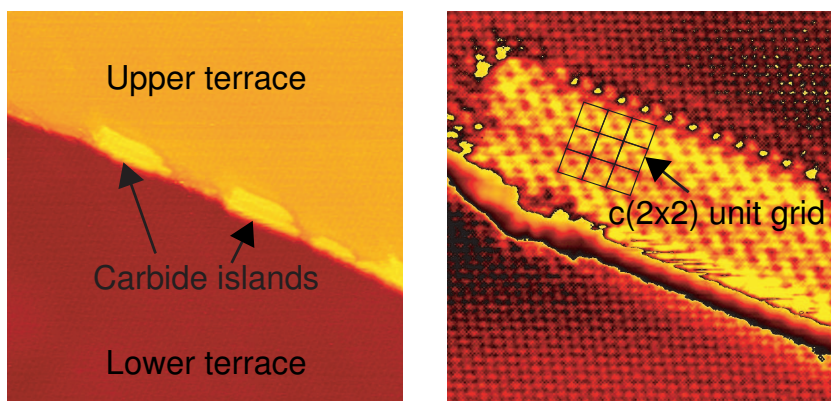


Figure 5.2: **Left:** STM image ($500 \times 500 \text{ \AA}^2$) of Ni(111) after exposure to 5 L CO at 400 K. Small islands are revealed at the upper site of the Ni-steps. **Right:** Zoom-in ($80 \times 80 \text{ \AA}^2$) on one of the islands shows the carbide clock-reconstruction, thus confirming that the islands consist of carbon atoms.

The above observations are in good agreement with STM images by Nakano *et al.* [112, 122], who also found carbide islands to grow from the step edges. The nucleation site for carbide islands is, however, not necessarily the same as the dissociation site for the CO molecules. Carbon atoms are probably mobile on the nickel surface at 400 K, and even though it may be tempting to conclude from images like the ones shown in Fig. 5.2 that CO dissociates at step sites, the finding of carbide at the step edges may simply be related to carbide phase growth at these particular sites and not to CO dissociation. To further investigate the properties of CO dissociation, we have thus performed prolonged CO exposures and observed the growth of carbide islands. The results are depicted in Fig. 5.4 where the average width of the carbide phase perpendicular to the step edge direction is plotted versus the CO exposure. The figure clearly demonstrates that carbide formation saturates already after the formation of a few rows of adsorbed carbon atoms. The extremely fast saturation of carbide growth is a key argument concerning the determination of the active site for CO dissociation: When carbon atoms attach to the steps, the step sites are passivated and no further dissociation can take place. If the CO

molecules could dissociate on the terraces, mobile carbon atoms would be available and the growth of the carbide phase would continue until the entire terrace was covered. One might then argue that the growth of the carbide phase could be the limiting step leading to saturation, and not the dissociation of CO. The carbide phase is, however, known to grow unlimitedly as soon as carbon is available on the surface: Ethylene molecules, for example, dissociate at the Ni(111) terrace sites under similar conditions as the ones used for the CO experiments, and full monolayer coverage of carbide is found even after small exposures of ethylene [124, 126]. The saturation of carbide growth observed in our experiments is thus direct evidence that the step sites are the active site for CO dissociation. The observation of islands with several carbon rows (but still only a few rows) in the right part of Fig. 5.2 indicates that the carbon atoms formed through the Boudouard reaction are indeed mobile, and further growth of existing carbide islands is thus possible as long as other step sites are still vacant for CO dissociation supplying carbon atoms. As soon as all steps are blocked, the growth, however, saturates.

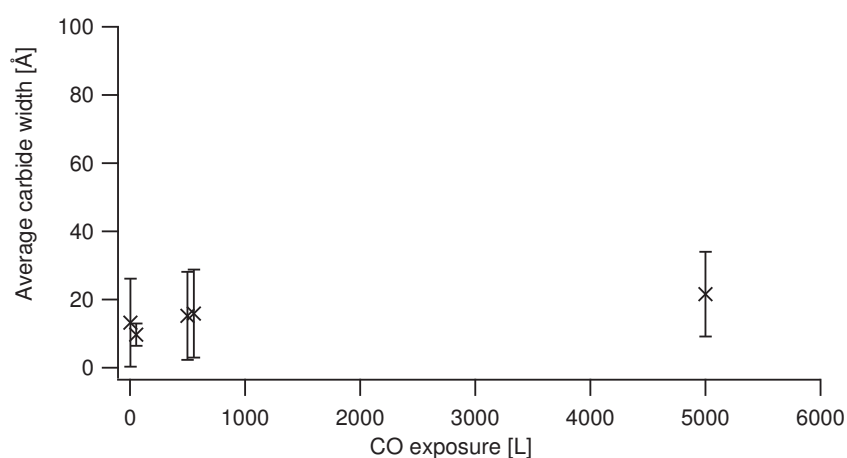


Figure 5.3: Investigation of the carbide island growth as a function of CO exposure. The measure for island growth is the average carbide width perpendicular to the step edges. Saturation is found after exposure of a few Langmuir of CO.

The activation barrier for CO dissociation on the Ni steps can be roughly estimated by evaluating the lower temperature limit for the onset of nickel-carbide formation. Fig. 5.4 shows three STM images obtained after exposing the Ni surface to CO at different temperatures, and we find that no carbide growth can be observed at temperatures below 375 K. In a first approximation, it is reasonable to assume that the rate of CO dissociation follows an Arrhenius equation,

$$r = \nu \exp(-E_a/k_B T), \quad (5.5)$$

with a typical value of the prefactor of $\nu=10^{11} \text{ s}^{-1}$ [127]. For observations to occur in the timescales of our experiments the rate must be in the order of magnitude of 1 per second, which gives an estimate of the activation energy of $E_a \sim 0.8 \pm 0.3 \text{ eV}$.¹

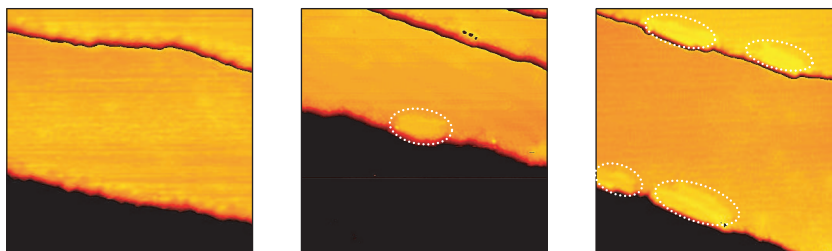


Figure 5.4: STM images ($300 \times 300 \text{ \AA}^2$) acquired after CO exposure at different temperatures, 350 K, 375 K and 400 K, respectively. Carbide formation is seen at and above 375 K. The color scale has been repeated on the upper terraces to highlight the details at each single step edge. The carbide islands are marked with dotted ellipses.

A similar method cannot be used to obtain an estimate of the energy barrier for terrace dissociation of CO, because no such events have ever observed in our experiments. A lower bound of the energy barrier can, however, be estimated: No change in carbide density is found when the CO exposure is varied by three orders of magnitude (from 5 L to 5000 L), and furthermore the ratio between step sites and terrace sites is of the order of 1:100. According to our measurements, the rate for terrace site dissociation must therefore be at least five orders of magnitude lower than step site dissociation. Using Eq. 5.5, this can be converted to an activation barrier, and we find that the barrier for terrace site dissociation of CO is at least 0.3 eV higher than the barrier for step site dissociation.

One could argue that the procedure for estimating the CO dissociation barrier described above contains a pitfall, and that what is actually determined is the barrier for reconstructing the Ni surface and forming the carbide phase rather than the barrier for dissociating CO. From ethylene adsorption studies, however, it has been found that the carbide phase can be formed at temperatures down to 350 K [128], and the observed

¹The large uncertainty reflects the crudeness of the barrier estimate performed here. The uncertainty has been calculated by assuming a 25 K uncertainty on the temperature, a 3 orders of magnitude uncertainty on the prefactor and a 2 orders of magnitude uncertainty on the rate.

onset of CO-induced carbide formation at 375 K is thus not related to a barrier for the formation of carbide but is indeed related to the dissociation of CO molecules.

The extracted energy barrier is significantly lower than the barrier of 2.1 eV found by density functional theory calculations performed by Bengaard *et al.* [120]. Even with the large uncertainty imposed by our crude evaluation method, it is impossible to arrive at any reasonable agreement between the two results. A number of possible explanations for the apparent discrepancy can be envisioned: For example the CO coverage along the step edge may differ from the terrace coverage and this could influence the calculated activation energy. Furthermore, we cannot rule out that hydroxyl groups might be present at the step edges, and that such species may facilitate alternative dissociation routes instead of the Boudouard reaction. These ideas are currently being investigated with DFT calculations by Nørskov and co-workers [129].

5.3 Modifying the Ni surface

5.3.1 Modifications of the Ni step edges

As mentioned in the introduction (Sec. 5.1), the overall objective of the Ni studies presented in this thesis was to modify the reactivity and thus approach the characteristics of platinum. The following sections each describe different routes to block the step sites of Ni(111). As indicated by the results above, the Boudouard reaction is actually self-blocking in the sense that carbide formation on the step edges blocks the active site for further dissociation. On the other hand, the studies presented here only concern the interaction of a single gas with the nickel surface. In most cases, several gasses will be adsorbed, and the carbon atoms in the carbide layer will react with the other adsorbates whereby a sustained carbon production might be achieved. For some reactions, a total blocking of the CO dissociation with the result that no carbide is ever formed may be desirable, and for such reactions the self-blocking is clearly not sufficient.

The first modification to be considered is the adsorption of Ag along the step edges, and we show that this is indeed a possible route for inhibiting the CO dissociation. Secondly, the same type of experiment will be described for Au atoms, where we find a similar blocking effect in addition to the modification of terrace sites due to alloying, and finally sulfur adsorption will also be shown to exhibit the blocking effect on CO dissociation. The growth modes of Ag, Au and S on Ni(111) are already described in the literature, and the account given here will thus be kept brief as the focus of the present study is the exploitation of these adsorbates for the CO/Ni system rather than the actual investigation of Ag, Au and S growth on the surface.

Ag modifications

Ag atoms are deposited on the Ni(111) surface by using one of the home-built evaporators described in Chapter 2. At room temperature, Ag grows as very large islands from the Ni steps [130]. Typical island widths and inter-island distances are 1000–2000 Å and 3000–5000 Å, respectively, and the growth mode of Ag thus indicates a very large mobility of Ag atoms on Ni(111) at RT (see Fig. 5.5A).

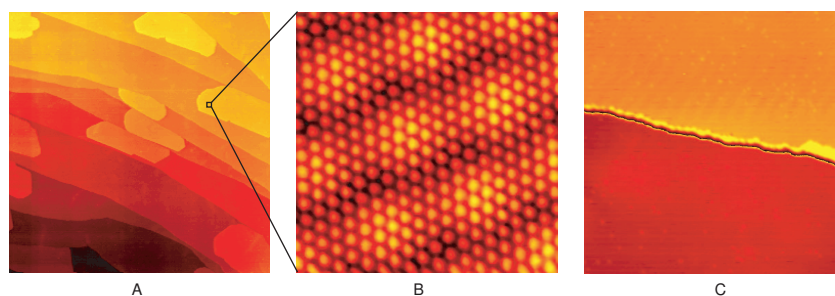


Figure 5.5: **A:** STM image ($7000 \times 7000 \text{ \AA}^2$) showing the growth of large Ag islands on Ni(111) at RT deposition. **B:** Zoom-in ($50 \times 50 \text{ \AA}^2$) on a Ag island showing a moiré pattern due to the lattice mismatch between Ag and Ni. **C:** STM image ($500 \times 500 \text{ \AA}^2$) after annealing to 800 K. The bright brim at the step edge is the Ag atoms.

When zooming in on the Ag islands a moiré pattern is found, like the ones discussed for CO on Pt(111) in Sec. 4.3 (Fig. 5.5B). With atomic resolution on the Ag atoms, the Ag interatomic distance can be determined, and it is found that the Ag layer grows with the same lattice constant as bulk Ag. The moiré pattern thus arises from the large (16%) lattice mismatch between Ni (2.49 Å) and Ag (2.89 Å) combined with a 2° rotation of the Ag layer with respect to the underlying Ni substrate [130]. If we expose the as-deposited Ag/Ni system with its large Ag islands to CO, carbide growth is of course observed since many step sites are still vacant for CO dissociation. Even the step edges where Ag islands are located exhibit some degree of carbide formation, which again confirms the mobility of the carbon atoms along the step edge at the dosing temperatures (as discussed in section 5.2). When the Ag/Ni system is annealed at 800 K, however, all large Ag islands disappear and instead a bright brim, which covers the Ni steps, is revealed in the STM images (Fig. 5.5C). Annealing of the Ag/Ni system is never observed to result in any alloy formation, which is in contrast to the Au/Ni system discussed below, but the annealing, however, has a large influence on the CO dissociation rate: When the annealed Ag/Ni system is exposed to CO, no carbide islands were ever found - even after prolonged exposure (5000 L), and we therefore conclude that the addition of Ag to the step edges effectively impedes the dissociation of CO on Ni(111).

Au modifications

Inspired by the success with step blocking using Ag deposition on nickel, thereby inhibiting CO dissociation, we have investigated if Au could facilitate the same effects. The deposition of Au on Ni(111) was done with a home-built evaporator in the same manner as with the Ag deposition, and the growth of Au on the surface initially follows the same route as Ag on Ni: At room temperature deposition Au islands are nucleated at the Ni steps. The inter-island distances are significantly smaller than for Ag and the diffusion rate of Au therefore seems to be lower. Fig. 5.6A shows the initial growth of Au on Ni(111) and when zooming in, a misfit dislocation structure can be observed instead of the moiré structure found for the Ag/Ni system (Fig. 5.6B) [131, 132]. Similar misfit dislocation structures are also observable on Ag islands after annealing.

Annealing of the Au/Ni(111) system leads to large deviations from what was seen for Ag/Ni. Even though Au and Ni are immiscible in the bulk, a surface alloy is formed upon annealing to 800 K, and subsequent STM images of the alloy show a mixture of protrusions and depressions on the surface (Fig. 5.6C) [130]. By correlating the density of depressions with the amount of Au deposited on the surface, it can be concluded that each depression corresponds to a single Au atom substituted into the Ni surface [132]. The Au atoms are imaged as depressions due to electronic effects although they are situated in the same surface layer as the Ni atoms [132]. This issue was discussed in Section 2.4.2, and the Au/Ni(111) surface alloy thus serves as an instructive example of the possible misinterpretations of STM images if one relies on simple geometrical interpretations. As opposed to the annealed Ag/Ni surface, no bright brim of Au atoms is revealed along the step edges, which at a first glance might indicate that Au is not a good candidate for step blocking. Keeping in mind, however, the peculiar STM imaging properties of Au on this surface, it is not straight-forward to determine whether Au is present at the steps or not.

In order to determine if Au atoms actually do wet the Ni step edges upon annealing, we prepared a very dilute Au/Ni(111) surface alloy, so that a random distribution of Au atoms would result in a large number of free Ni step sites where CO dissociation and subsequent carbide formation could take place. An example of an STM image of such an alloy after exposure to CO at 400 K is shown in Fig. 5.6D. The image clearly shows that no carbide islands are formed even though the density of Au is very small. We thus conclude that Au must be wetting the step edge and that the annealed Au/Ni(111) system therefore also is a possible candidate as a Ni-based catalyst with the ability to preserve C=O bonds.

S modifications

The last example of Ni step edge modifications presented here is the addition of sulfur. Earlier studies of the effect of sulfur additives were mentioned in the introduction to the Ni studies, and e.g. Goodman and co-workers have already many years ago shown that sulfur inhibits CO dissociation on Ni surfaces [116]. The result of our sulfur studies is thus well-known, but the explanation provided by our scrutiny of the CO dissociation process shines new light on these classical studies and shows that the inhibiting effect of

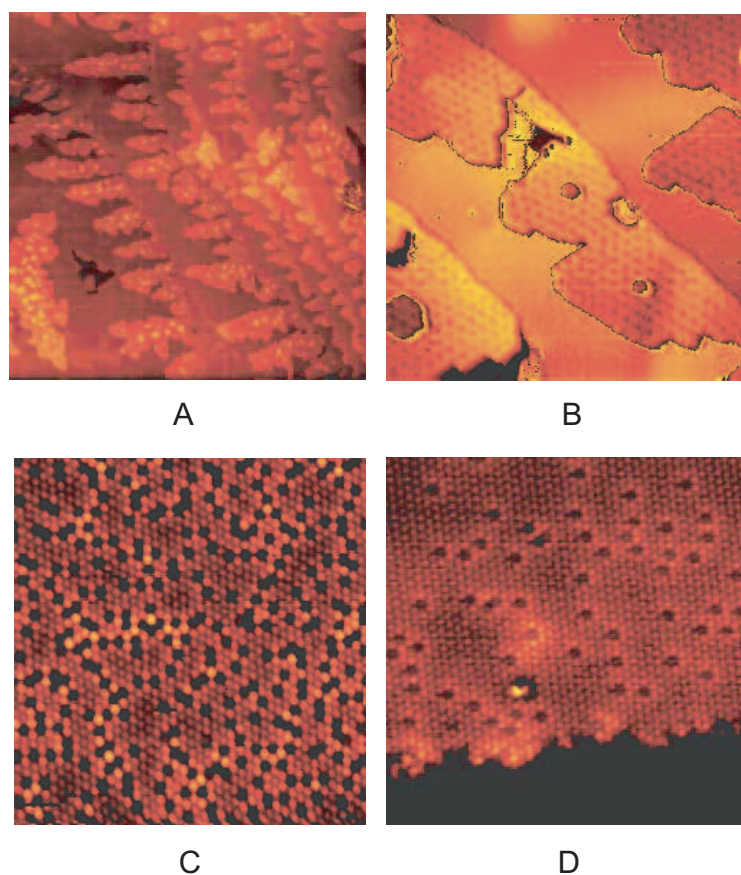


Figure 5.6: **A:** STM image ($5000 \times 5000 \text{ \AA}^2$) showing the initial growth of Au islands at the Ni steps. **B:** Zoom-in ($700 \times 700 \text{ \AA}^2$) on the Au islands revealing the misfit dislocation loops. **C:** STM image ($100 \times 100 \text{ \AA}^2$) of the AuNi alloy formed after annealing the surface to 800 K. **D:** STM image ($100 \times 100 \text{ \AA}^2$) of the AuNi alloy after CO exposure at 400 K. No sign of carbide formation is observed along the step edges.

sulfur is indeed closely related to the step edges, like the effect of Ag and Au described above.

A number of different phases of sulfur on Ni(111) exists [133–135], but in this study we will focus on the adsorption structures formed by depositing sulfur at 400 K. This is the temperature of the CO dissociation experiments, and by choosing the same temperature for sulfur deposition we avoid ambiguities like whether a blocking effect is due to the mere presence of sulfur at the steps or a combination of the presence and a temperature-induced reconstruction of the sulfur phase. Sulfur is deposited onto the surface by backfilling the UHV chamber with H_2S , which decomposes on Ni at these

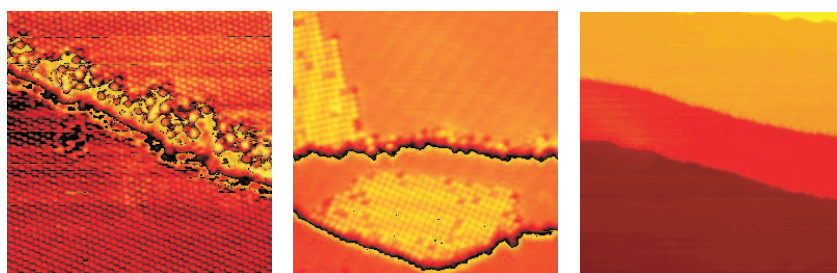


Figure 5.7: **Left:** STM image ($100 \times 100 \text{ \AA}^2$) showing sulfur atoms at a Ni(111) step edge after a 5 L exposure of H_2S at 400 K. **Middle:** STM image ($200 \times 200 \text{ \AA}^2$) showing the nucleation of $\sqrt{39} \times \sqrt{39}$ -type sulfur islands at the nickel steps. **Right:** STM image ($500 \times 500 \text{ \AA}^2$) of a S/Ni(111) surface exposed to 500 L CO at 400 K. No carbide islands can be observed at the step edges.

temperatures, leaving sulfur atoms on the surface. Fig. 5.7 shows an STM image after exposing the Ni(111) surface to 5 L of sulfur. The single sulfur atoms are revealed at the step edges and at certain areas well-ordered phases are also found, which can be identified as a $\sqrt{39} \times \sqrt{39}$ structure with a characteristic almost quadratic unit cell [134]. The growth of the $\sqrt{39}$ structure is problematic when investigating the CO dissociation because of the similarities to the carbide phase, and the H_2S exposure was therefore kept very low in the CO dissociation experiments. To prove that even a minute amount of sulfur is able to block the dissociation of CO at the step edges, we exposed the surface to 0.5 L of H_2S followed by a 500 L CO exposure, both performed at 400 K. STM images were acquired at several different places on the surface before and after the CO dosing to compare the density of sulfur or carbide islands at the step edges. We found no difference in the coverage of islands, and we therefore conclude that sulfur has the same inhibiting effect on the step edge dissociation channel for CO as observed for Ag and Au.

5.3.2 Modifications of the Ni terrace atoms

Returning to the Au/Ni surface alloy it is clear that not only the step edges but also the terrace atoms are modified upon Au deposition. Considering e.g. the prospects for substituting Pt-based alloy catalysts for PEM fuel cells with modified Ni-based catalysts, further investigations of the effect on the CO stability on the Ni terraces induced by the alloying with Au atoms are therefore highly interesting. Previously, Ni atoms in the Au/Ni surface alloy have been shown to exhibit different chemical behavior compared to clean nickel surfaces [7, 136, 137], and to further elucidate the Au-induced modifications of the CO binding on Ni(111), we have performed CO-TPD and STM experiments.

Fig. 5.8 shows a collection of CO-TPD spectra, where the Au/Ni surface alloy has been saturated with CO at different alloy compositions with varying concentrations of Au. The CO dosing was performed at room temperature and a clear shift both in sat-

uration coverage (area under the peaks) and peak position is revealed from the data, indicating that Au lowers the binding of CO to the nearby Ni atoms. These findings are in agreement with similar experiments by Holmblad *et al.* [136].

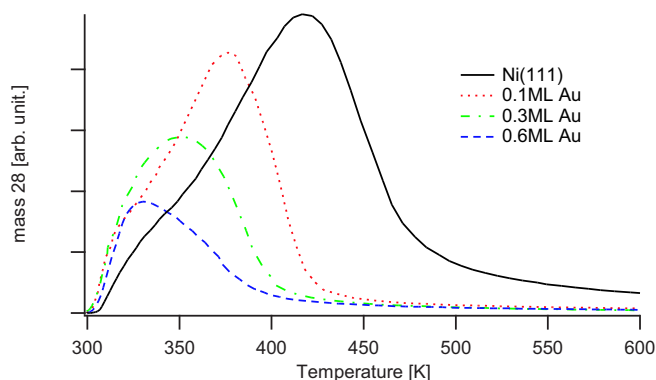


Figure 5.8: CO-TPD spectra on different Au/Ni surface alloys with varying concentrations of Au. In each case the surface was saturated with CO at RT and subsequently heated with a ramp of 2 K/s.

Fig. 5.9 shows an STM image of the CO adsorption structure on a very dilute alloy when the surface is saturated with CO at room temperature. It is well-established that CO saturates in a $c(4 \times 2)$ -2CO structure with a coverage of 0.5 ML at room temperature on the Ni(111) surface with tilted CO molecules occupying a mixture of hcp and fcc threefold hollow sites, as sketched in the ball model in the right part of Fig. 5.9 [138–140]. This CO structure is recognized on the large Au-free areas in the dilute alloy as indicated on the STM image in the figure. Different domains of the $c(4 \times 2)$ structure can be observed together with a number of holes, the density of which is in good agreement with the density of Au atoms before CO exposure. The two grids with the rectangular symmetry of the $c(4 \times 2)$ -2CO structure that have been added to the STM image, show that one CO molecule is missing at each *hole*, and we therefore conclude that CO does not adsorb in hollow sites next to Au atoms in the alloy (see the ball model in Fig. 5.9). The ball model furthermore demonstrates that five other CO molecules bind to Ni atoms, which are coordinated to Au: Three of the CO molecules bind to two modified Ni atoms, and two of the molecules are only coordinated to one modified Ni atom. These five molecules are probably the ones that show up as less strongly bound CO in the TPD spectra, whereas the one missing CO molecule accounts for the decrease in the saturation coverage of CO as a function of Au concentration.

Our investigations of the Au/Ni surface alloy thus indicates that this system may be a very promising candidate, e.g., as an anode catalyst for PEM fuel cells, where the binding energy of CO on the currently used platinum-based catalysts is too high. In Section 5.4 we will, however, see that high-pressure exposures of CO destroy the alloy, whereby the catalyst design ideas are (at a first glance) turned into an instructive example of the pressure gap between UHV studies and realistic catalytic conditions.

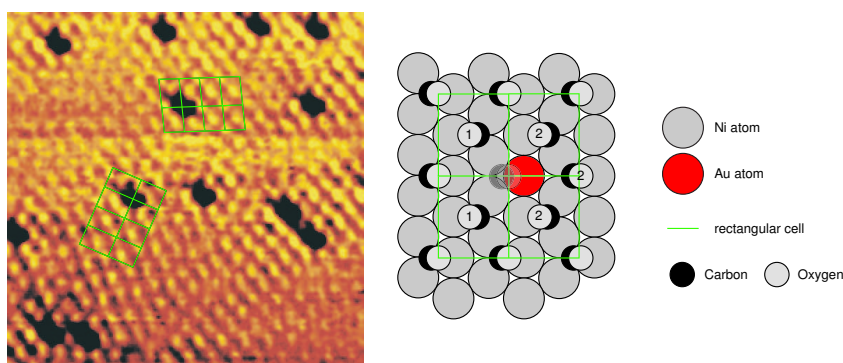


Figure 5.9: **Left:** STM image of the saturated CO adsorption structure at UHV conditions and room temperature. The grid shows the $c(4 \times 2)$ -2CO rectangular cell, and the depressions are thus ascribed to missing CO molecules at the Au atoms. **(Right):** The ball model illustrates the $c(4 \times 2)$ -2CO adsorption structure on Ni(111) and the binding of CO in the vicinity of a Au atom in the alloy. Numbers on CO molecules refer to the number of modified Ni atoms in the threefold hollow site of the molecule.

5.3.3 Discussion

The results presented in the sections above show that nickel crystals can be modified and that the step reactivity for CO dissociation can be dramatically reduced by the adsorption of different species along the step edges. The results are thus in good agreement with the general ideas of the conceptual models discussed in Chapter 3: The under-coordinated step atoms both have a higher lying d -band and at the same time the special step site geometry probably stabilizes the transition state of the dissociating molecule whereby the dissociation barrier is lowered. As soon as other adsorbates are present at the step edges, the d -band of the step atoms is altered and the special nickel geometry is no longer present. Fig. 5.10 illustrates the variety of sites and the d -band widths and shifts for the systems discussed in this section. In addition to the step modifications (B+C in the figure), the modified chemical properties on the terraces are illustrated (A+D) by a broadening of the d -band and a concomitant down-shift of the d -band center in accordance with theoretical calculations [67].

Our experimental findings of the effect of step blocking are in general agreement with other studies [120], and besides providing a route for carbon-free Ni-based catalysts, the studies of step blocking definitely establish that the step sites are indeed important for the dissociation of CO. Our conclusions are in good agreement with the conclusions from similar STM studies on the clean Ni(111) surface by Nakano *et al.* [112,122], but the AES data presented by these authors seem to be in disagreement with our findings. When the Ni(111) surface is exposed to CO, a continuous increase in carbon coverage has been detected with AES by Nakano *et al.*, which is in striking contrast to the saturation observed with STM in our studies. We have no direct explanation of the discrepancy, but the carbon formation observed by Nakano *et al.* might be enhanced by

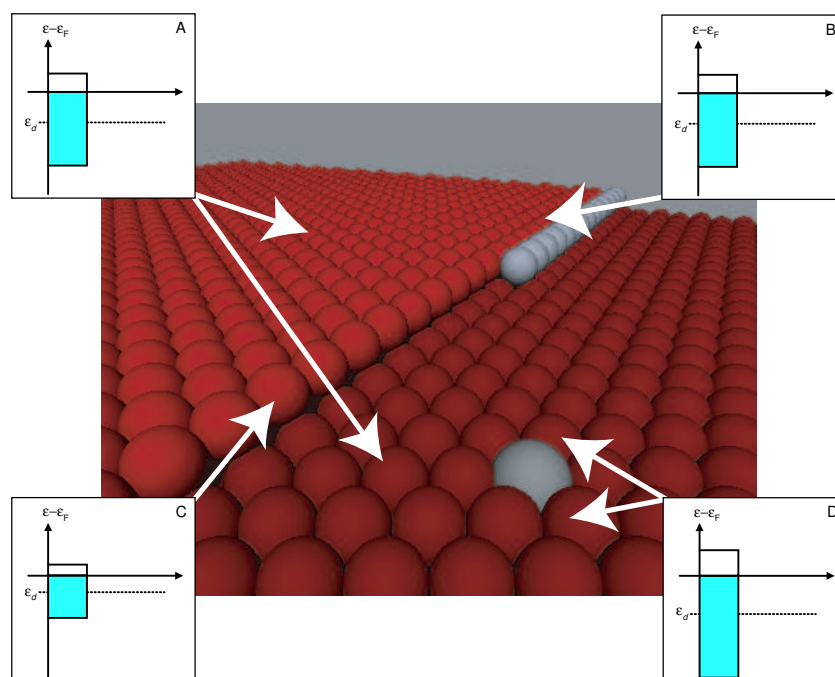


Figure 5.10: Illustration of the various d-band positions on a modified nickel crystal.

the electron beam from the AES, or one might envision that small amounts of defect sites are created by the electron beam which subsequently serves as CO dissociation sites for further carbon growth.

5.4 Stability of a Au/Ni alloy at HP conditions

The previous sections concerning the reactivity of clean and modified nickel have only included studies performed at low-pressure conditions. As discussed in the introduction (Chapter 1), this is indeed the standard “surface science approach” to the description of the fundamental steps in catalysis, but nevertheless large differences may show up when such model systems are exposed to high-pressure conditions of reactive gasses. In the following, focus will be on the effects of raising the CO pressure on the Au/Ni(111) surface alloy described above. Adsorption-induced effects on the composition of alloys have previously been described and suggested in the work by Nerlov *et al.* concerning methanol synthesis on Cu/Ni and Cu/Co [141] and in the DFT studies by Christoffersen *et al.* on Pt/Ru alloys [17, 142]. In both cases segregation to the surface of the more reactive alloy constituent was found, which is readily explained by a higher gain in adsorption energy on the reactive metal than the cost in energy by phase separating the alloy. The HP-STM studies presented here demonstrate that similar effects are observed

on the Au/Ni(111) surface alloy upon CO exposure at high-pressure conditions. Considering the possibilities of using Au/Ni alloys as anode materials in fuel cells, the study of CO adsorption at high-pressure conditions is highly relevant. Although hydrogen is the main constituent of the anode gas in a fuel cell, CO interacts much more strongly with the surface (hence the CO poisoning effect), and we thus expect that any pressure gap effect is more likely to be induced by the presence of CO than by hydrogen. Our experimental results reveal that high pressures of CO lead to a complete phase separation of the Au/Ni surface alloy. Scrutinizing the phase separation process, we are led to a model involving nickel carbonyl formation, and the underlying mechanism of the destabilizing effect of CO on the alloy can thereby be addressed.

5.4.1 Experimental results

In the final part of Section 5.3, the adsorption of CO on dilute Au/Ni(111) surface alloys under low-pressure conditions was discussed. We found that the sites next to Au neighbors were unoccupied by CO molecules, which correlated well with the observed decrease in saturation coverage revealed by TPD experiments as a function of Au coverage. No tendency for phase separation is observed under the low-pressure conditions, not even after prolonged CO exposure, and this is in striking contrast to what is seen when exposing the surface alloy to high pressures of CO. Fig. 5.11 shows an STM image after CO exposure at 1 bar, and it clearly demonstrates that large morphological changes take place at the high-pressure conditions. The surface is covered with small irregular clusters, persisting even after the high CO pressure is pumped away and the surface is brought back to the UHV chamber (See Fig. 5.11A).

Atomically resolved zoom-in images between the clusters reveal the clean Ni(111)-(1×1) structure with no Au atoms alloyed into the topmost layer (Fig. 5.11B), suggesting that the clusters consist of Au atoms and that the surface alloy has undergone a complete phase separation. Subsequent annealing under UHV conditions restores the original surface alloy, which indeed indicates that Au is still present in the surface region after the high-pressure exposure. From an analysis of the height distribution of the islands we find that most islands have an apparent height in the STM images of ~ 3.2 Å, whereas $\sim 10\%$ of the islands have a height of ~ 5.6 Å (see inserted line scan in Fig. 5.11A). The height of 3.2 Å corresponds well to the height measured for Au islands on Ni(111) after RT evaporation, and could therefore reasonably be ascribed to monolayer islands of Au. The height difference between the two types of islands is 2.4 Å, which is in good agreement with the step height of Au(111) (2.35 Å), and the taller islands can therefore be associated with double-layer Au islands. Assuming that the clusters consist entirely of Au, we estimate a Au coverage of 0.24 ± 0.04 ML after high-pressure exposure when starting out with a Au coverage of 0.32 ± 0.04 ML (determined from the initially step-nucleated Au islands). The apparent slight drop in Au coverage probably arises from bulk diffusion of Au at the 800 K annealing, which is performed prior to the high-pressure experiments to create the alloy [132]. Based on the above experimental findings, we hence conclude that all the observed clusters must be Au clusters and that the surface alloy has undergone a complete phase separation.

The timescale for phase separation at 1 bar is too fast for us to follow the evolution of

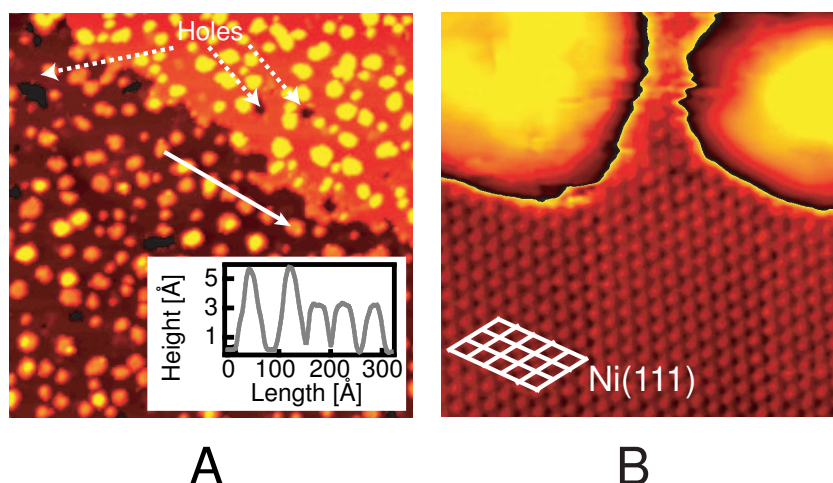


Figure 5.11: **A**) STM image ($1000 \times 1000 \text{ \AA}^2$) of Au/Ni(111) after exposure to 1 bar of CO at room temperature. The surface is covered with islands and moreover a few holes are observed (dashed white lines). The line scan (indicated by the (lower) white arrow) shows islands of two different heights. **B**) Atomic resolution of an area between the islands ($60 \times 60 \text{ \AA}^2$) reveals a clean Ni(111) surface.

structures with STM, so in order to scrutinize the dynamics of the process, experiments were performed at slightly lower CO pressures, in the range from 5–40 torr. In this pressure range, we were indeed able to follow the dynamics and evolution of the phase separation as a function of time by acquiring so-called STM movies. Fig. 5.12 shows a series of STM images from an STM movie acquired at a CO pressure of 10 torr.² The movie reveals that the Au cluster formation starts at the Ni steps. Ni atoms are removed and Au clusters are nucleated and left behind in the wake of the moving step. The process is non-uniform; on each step we find certain areas where a large fraction of the Ni atoms from the terrace is removed at a given time, whereas other areas are nearly intact. Apparently, the Ni atoms removed from the step edge leave the surface, because no nucleation of Ni-islands is ever observed, only the removal of step atoms takes place.

²The movie can be seen in its full length at <http://www.phys.au.dk/camp/movies/carbonyl.mpg>.

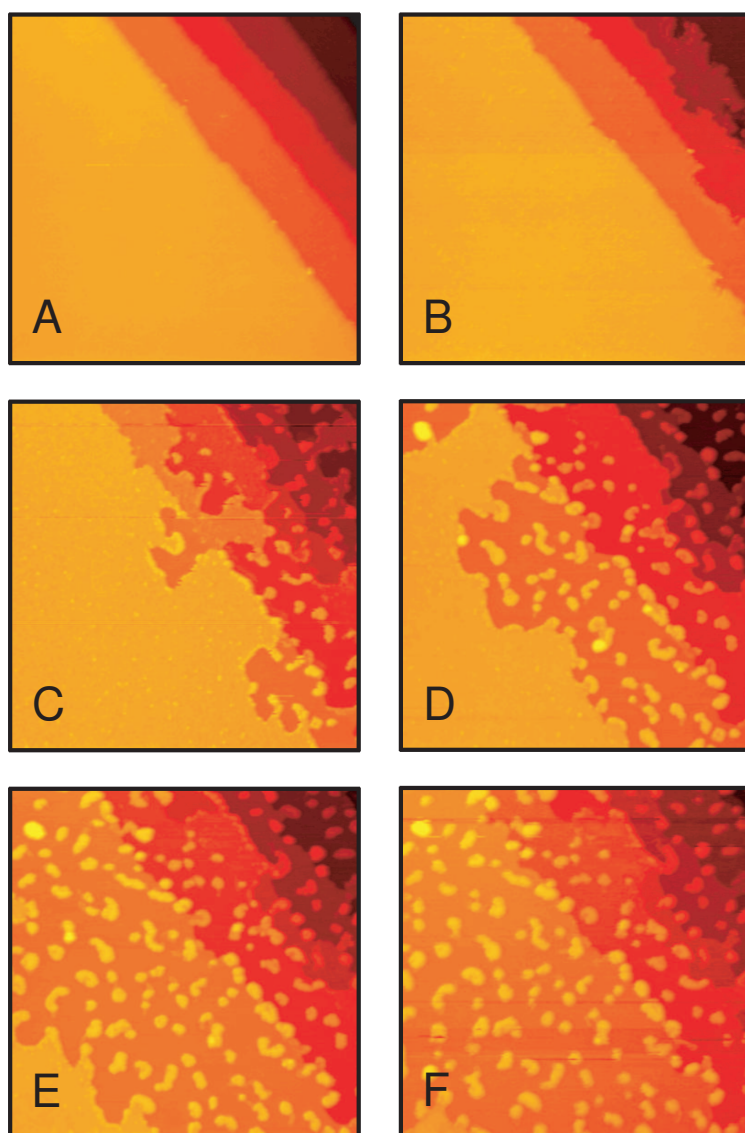


Figure 5.12: **A-F**) STM images ($1000 \times 1000 \text{ \AA}^2$) taken from an STM movie recorded in 10 torr CO at room temperature. Time of exposure: **A**) 0 min, **B**) 25 min, **C**) 50 min, **D**) 75 min, **E**) 100 min, **F**) 125 min.

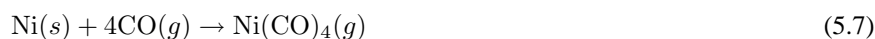
To quantify the rate of removal of Ni atoms and the hence following nucleation of Au clusters, the average movement of the Ni steps (step flow) is determined as a function of time (see Fig. 5.13A). Even though the process is not uniform, this quantity still contains information about the general evolution of the phase separation. Fig. 5.13A shows that the phase separation is characterized by an *incubation* period in which the step edges do not move, followed by a transition to a region where the step edges move with an approximately constant velocity. The incubation time varies largely across the surface, but the final velocity of the step flow can reasonably be used as a parameter for describing the reaction rate on the surface. The reaction rate (final step flow velocity) has been investigated at varying pressures in the range from 5–40 torr. In Fig. 5.13B, the reaction rate is plotted as a function of pressure, and we observe that the rate at which Ni atoms are removed scales as a power law as a function of the CO pressure with a reaction order of approximately one, i.e.

$$r_{\text{phase separation}} \propto p_{\text{CO}}^{1.1} \quad (5.6)$$

The removal of Ni atoms from the step edges does not stop after the completion of the phase separation, and even on clean nickel surfaces the step edges are not static at high pressures of CO. The rate of removal of nickel atoms is, however, severely reduced compared to the step flows measured on the Au/Ni alloy, and at a first glance the movement of the step edges may therefore seem to stop when the topmost layer of nickel atoms is removed and the Au atoms have formed clusters on the surface. Prolonged CO exposure at 1 bar is, however, observed to result in a continuous (slow) removal of nickel atoms from the step edges, and furthermore “holes” are emerging on the Ni terraces. The formation of holes is probably initiated around defects like dislocations, and these observations give further support to the conclusion that the Ni removal is intrinsic for the Ni crystal and that the rate of removal is merely enhanced by the presence of Au. The initial stage of hole formation can be observed in the STM image presented in Fig. 5.11A.

5.4.2 Discussion

Inspired by the removal of nickel atoms inducing the phase separation of Au/Ni at high pressures of CO, a model based on nickel carbonyl formation is presented in the following. Nickel carbonyl formation is a well-known process capable of dissolving Ni atoms from a Ni crystal during exposure to high pressures of CO [143–146], and the process is actually used industrially for the refinement of nickel (the so-called Mond process [147]). Even though the adsorption of CO on Ni surfaces is one of the most studied gas/solid systems, only few studies have been devoted to the dissolution process leading to the formation of Ni carbonyl species, i.e.



The reaction is found to occur with a measurable rate at pressures above $\sim 10^{-1}$ mbar and temperatures below 250°C [143, 146], which is coincident with the investigated pressure and temperature range in our experiments (>5 torr, room temperature). Furthermore, steps and defects have been found to play a dominant role for the reaction

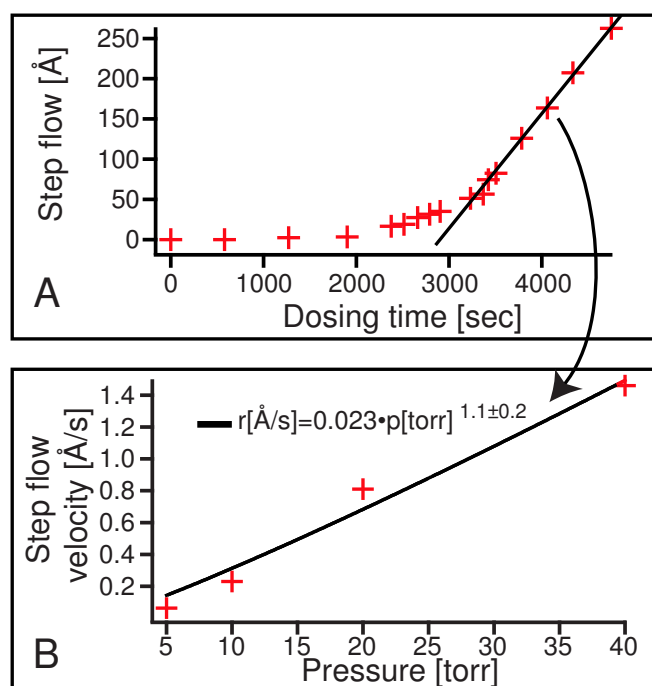


Figure 5.13: **A)** Graph showing the average step flow as a function of exposure time. Note the initialization phase (until approximately 2,000 seconds of CO exposure) and the linear phase after approximately 3,500 seconds. **B)** Plot of the reaction rate of carbonyl formation (step flow velocity taken from the linear part of graphs like A)) versus CO pressure.

rate of the nickel carbonyl formation [146], which further corroborates the idea that the observed removal of nickel atoms in our experiments is correlated with the formation of carbonyl species. A variety of CO reaction orders for carbonyl formation on nickel crystals and powders have been reported in the literature with values ranging from 0.63 to 2.9 [143, 145], the most recent value obtained on Ni(111) being 2.9 [145]. It is thus observed that our extracted reaction order of ~ 1 is compatible with earlier findings for carbonyl formation on the surface, especially when taking into account that our system is not clean Ni but a Au/Ni surface alloy. We thus propose that the phase separation of the Au/Ni surface alloy occurs because of the formation of nickel carbonyl species at the step edges, and that these species are volatile and therefore leave the surface. Due to the removal of atoms, the step edge moves and Au atoms diffuse along the step edge to form clusters, which are left behind on the new terrace in the wake of the moving step. Fig. 5.14 illustrates the basic ideas of the model in a simplified ball model.

The observed incubation time and non-uniformness of the phase separation might indicate that certain specific sites are the only active sites for carbonyl formation at the

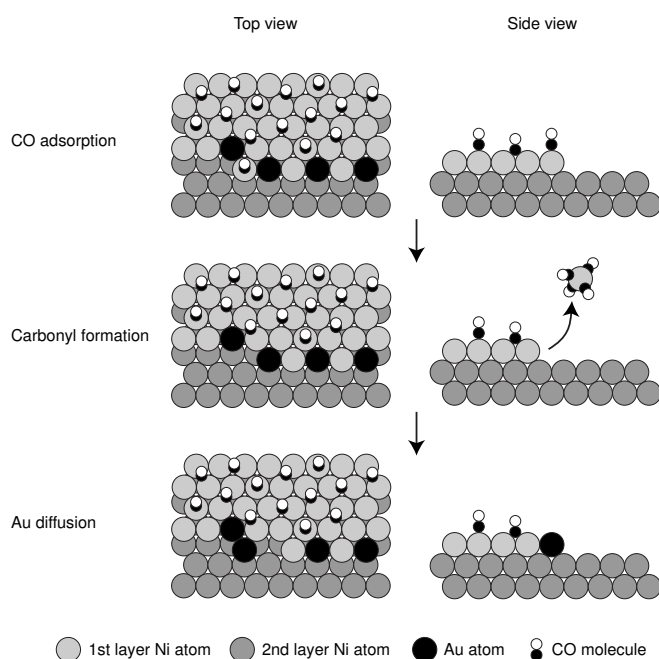


Figure 5.14: *Ball model illustrating the phase separation model. Left: Top view, Right: Side view. The CO molecules are placed in the $\sqrt{7} \times \sqrt{7}$ structure suggested by high-pressure experiments by Quiros et.al. [106]. The top model shows the adsorption of CO, in the middle a Ni atom is removed, and the bottom model illustrates the subsequent diffusion of a Au atom to form a cluster at the step edge. Only Au atoms at the step edge have been depicted to simplify the illustrated model.*

step edges. For example, one could envision that steps with a high kink density would have a higher carbonyl formation rate than low-kink density steps. This seems reasonable, as also discussed in [146], because the low coordination of kink atoms probably would render the creation of a carbonyl energetically more favorable, whereby the Ni atom is removed from the surface.

Finally, the question of the enhancement of Ni removal by the presence of Au in the Ni layer is addressed. As we saw in Section 5.3, the Au atoms have an inhibiting effect on the CO adsorption and the general reactivity of nearby nickel atoms is lowered by the presence of Au. At a first glance it may therefore seem counter-intuitive that Au should have a promoting effect on the formation of $\text{Ni}(\text{CO})_4$. On the other hand, the effect of Au on the nearby Ni atoms may actually turn out to be valuable for the carbonyl process. One could envision that the formation of nickel carbide would render further CO adsorption energetically unfavorable, and that carbonyl formation hence would be inhibited at carbide-covered step edges. The promoting effect of Au atoms on the carbonyl production may thus be of a more indirect nature, where the Au atoms inhibit the dissociation

of CO and the subsequent formation of carbide, whereby the step atoms are kept free and available for carbonyl formation. The non-uniformity of the reaction rate observed in our experiments might, along these lines, be explained by the existence of varying degrees of Au at the step edges making some areas partly carbide-covered and others more or less ready for carbonyl production immediately after high-pressure exposure of CO.

Considering the energetics of CO adsorption on the Au/Ni alloy compared to adsorption on the bare nickel surface, another possible explanation of the promoting effect of Au may also be envisaged: From the TPD spectra presented in section 5.3, CO is found to bind less strongly to the Au/Ni surface alloy compared to the binding energy on pure nickel, and if the decrease in binding energy is larger than the energy cost to perform the phase separation, removing the nickel atoms from the topmost surface layer will be energetically favorable, as seen in our experiments. It would be interesting to investigate such a possible effect further using DFT calculations.

As an outlook on the presented high-pressure studies, it is intriguing to mention that very preliminary and on-going experiments suggest that the Au/Ni surface alloy may actually be stabilized at high pressures of CO when high pressures of water (saturated vapor pressure) is also present at room temperature conditions. No systematic investigations have been pursued at the time of the writing of the present thesis, but e.g. the formation of hydroxyl groups from water dissociation at the Ni step edges may be envisioned to participate in the inhibition of carbonyl formation. These preliminary findings indicate that the Au/Ni alloy may still be considered as a candidate for PEM fuel cell anode catalysts, since water is indeed present in such systems.

5.5 Summary

In this chapter a range of experiments have been presented with the common theme of CO interaction with modified nickel surfaces. Special attention has been paid to the ability to block the nickel steps with other adsorbates, whereby the CO dissociation is found to be inhibited. Furthermore, it has been shown that a Au/Ni surface alloy becomes unstable at high CO pressures due to the formation of nickel carbonyl species. The main purpose of the studies presented here has been to demonstrate that nickel can be modified in a manner whereby the catalytic properties of platinum are approached. This has been shown to be possible when only CO is considered as an adsorbate and when the pressure is limited to low-pressure conditions. It is, however, also clear that much work is still needed before actual catalyst design can be pursued from such fundamental considerations.

CHAPTER 6

O₂ adsorption and diffusion on titanium dioxide

In this chapter, experimental results are presented of the adsorption and diffusion of oxygen on a rutile titanium dioxide surface. The adsorption process is rather complex, involving a number of different oxygen-related adsorbates. By following the interaction between the oxygen adsorbates, the intrinsic nature of these is derived and a general model for the oxygen adsorption process on titanium dioxide is discussed. The diffusion of the oxygen adsorbate species on titanium dioxide is investigated, and we find that a hitherto unseen process based on charge transfer-induced hopping governs the diffusion process. The studies presented in this chapter show that the availability of electrons in the conduction band plays a major role for the chemistry on oxide surfaces, and such findings thus indicate new possible routes for improvements of oxide-based catalysts.

6.1 Introduction

Metal oxides constitute an interesting and very diverse class of materials with a wealth of applications, ranging from high- T_c superconductors to catalyst materials. Their surface properties are crucial in processes like photocatalysis, catalyst support, gas sensors, and for passivation of metal surfaces against corrosion or for biocompatible applications [148, 149]. The scientific knowledge about oxide surfaces is, however, sparse compared to the surface science of metals. Many oxides are insulators, which inhibits the use of most of the arsenal of standard surface science tools, and furthermore, the complexity of oxide phases is much larger than the rather simple *fcc*, *bcc* and *hcp* crystal structure of metals, and the characterization and structural computations are therefore inherently more difficult for oxides. Many of the transition metal oxides exist in a variety of forms with different stoichiometries due to a range of possible oxidation states of the metals. The complexity thus induced is the property that makes e.g. cerium oxide an interesting “active” support for automobile catalysts, where it serves as an oxygen storage material which releases oxygen under reducing conditions and “stores” oxygen by re-oxidation under oxidizing conditions [150]. The complexity of stoichiometrically different oxide phases is, however, also one of the issues that makes surface science experiments on transition metal oxides a tremendous challenge. Even small variations in preparation conditions may completely alter the properties of the oxide, and the reproducibility of experimental results can therefore be a serious challenge.

Most metal oxides are large band-gap semiconductors or insulators, but some of the oxides can become conducting by the introduction of defects like oxygen vacancies or metal interstitials, which are formed upon crystal preparation (sputtering and annealing) under ultra-high vacuum conditions [148]. In many cases it is thus possible to use surface science tools to investigate these so-called reducible oxides, but the reducibility also renders the comparison of experiments performed on different crystals difficult, since many of the chemical properties may be governed by the defect concentrations.

In recent years, rutile titanium dioxide (TiO₂) has emerged as the prototypical oxide system for surface science studies, which is partly owing to its technological versatility and partly owing to its reducibility and the ability to prepare a conducting crystal under UHV conditions with sputtering and annealing cycles. Titanium dioxide is utilized in a multitude of different technological applications ranging from white pigment in paint, toothpaste and candy [151] to photocatalyst in e.g. solar cells [12, 152], active support in oxidation catalysts [18, 30, 34], “self-cleaning” super-hydrophilic coatings for windows [153] and as the surface layer on Ti-based bio-compatible implants [149, 154]. A large amount of studies have been initiated on titanium dioxide surfaces since it was shown in 1972 by Fujishima and Honda that TiO₂ could be used as a photocatalyst to split water to hydrogen and oxygen without the application of an external voltage [11]. Another great motivator for titanium dioxide studies was provided by the pioneering work of Haruta in 1989, where he showed that nanoclusters of Au supported on TiO₂ could serve as a good CO oxidation catalyst even below room temperature [34]. Especially this latter observation has spurred many surface scientist to enter the field of metal oxides and metal cluster growth on oxides, and a large number of investigations and suggestions have been made during the last decade to explain the peculiar behavior of

Au nanoparticles on TiO₂ [29, 35, 42, 155–162]. Much of the existing knowledge of the chemistry on oxide surfaces and on oxide-supported metal particles is, however, based on macroscopic measurements with averaging techniques, and there is an enormous lack of fundamental knowledge concerning the atomic-scale details of the interaction of oxide surfaces with adsorbates. With local probe techniques like STM it is possible to characterize the interaction of adsorbates with oxide surfaces and follow the adsorption and diffusion of species at the single molecular level, and such studies will indeed have a great impact on the general understanding of the surface chemistry on oxides, as we will see in the following.

The studies presented in this chapter focus on the interaction of oxygen molecules with TiO₂. Oxygen is an important reactant both in oxidation catalysts (e.g. CO oxidation on Au/TiO₂) and as an electron scavenger in photocatalytic processes on TiO₂ [163–166]. Furthermore, oxygen is used to re-stoichiometrize the oxide surface, which is often done during crystal preparation [167], and it is therefore highly important to have a basic understanding of the oxygen interaction with the surface. From our experimental results presented below we find that the oxygen chemistry on TiO₂ surfaces is extremely complex compared to gas adsorption on metal surfaces. The position of the chemical potential in the TiO₂ band gap is found to play a key role for the oxygen chemistry, and these findings open up new possible routes for designing and tailoring the reactivity of oxide-based catalysts.

6.2 The rutile TiO₂(110) surface

Titanium dioxide exists in three different polymorphs: rutile, anatase and brookite. Most of the surface science studies performed so far have, however, been on the rutile crystal [148, 167]. A ball model of the rutile bulk structure is shown in the upper part of Fig. 6.1. The most stable facet of rutile TiO₂ is the (110) surface, and flat, nearly-stoichiometric TiO₂(110) surfaces are readily prepared by polishing and subsequent sputtering and annealing under UHV conditions. The UHV annealing reduces the otherwise insulating crystal (band gap ~ 3 eV) sufficiently for it to become bulk conducting, whereby all standard surface science tools can be utilized to characterize the surface structure without charging problems.

In the TiO₂ bulk, oxygen vacancies and titanium interstitials are the predominant defects after sputtering and annealing cycles [167, 170–174]. These defects introduce n-type donor levels in the band gap, whereby the bulk conductivity is enhanced. The oxygen vacancies form F-centers (color centers) in the crystal which trap electrons ~ 0.75 eV below the conduction band and give rise to the characteristic dark blue color of the reduced crystals [167, 171, 175]. Preferential sputtering of oxygen during crystal preparation leads to a surplus of Ti atoms in the surface region and during the subsequent annealing, Ti interstitials diffuse into the bulk [176]. Under oxidizing conditions (annealing in a background of oxygen), the Ti interstitials diffuse from bulk to the surface region and a regrowth of new titanium oxide layers can be observed. Depending on the oxygen annealing temperature different relative amounts of titanium and oxygen can be found in the regrown layers; at 500 K–800 K a number of so-called sub-oxide structures

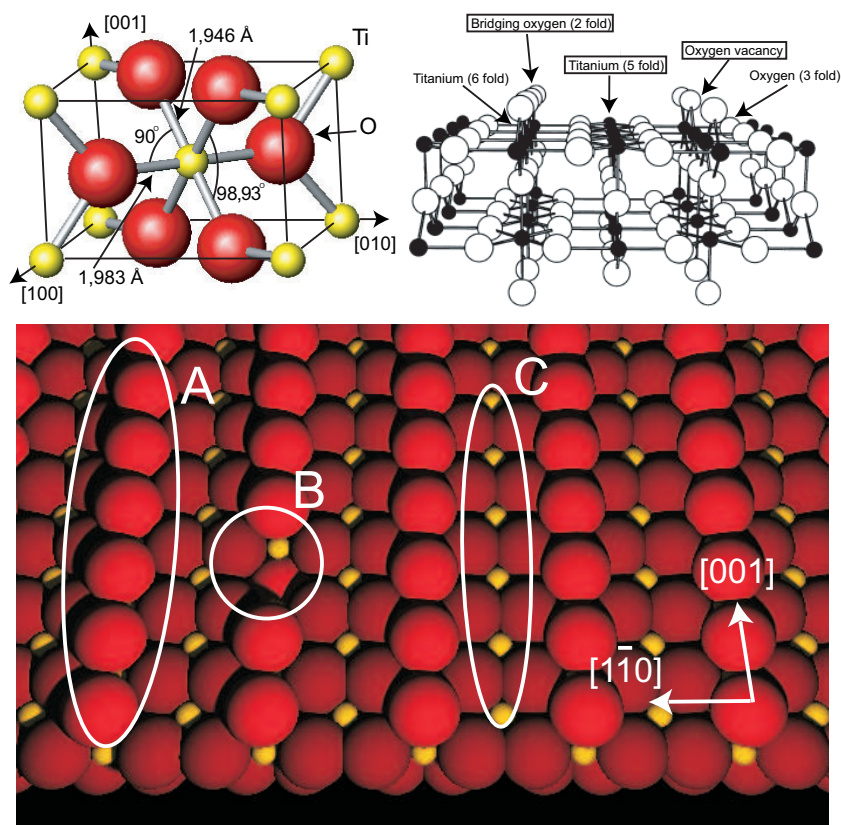


Figure 6.1: **Top Left:** Unit cell of bulk rutile TiO₂ reproduced from [168]. Each Ti atom (yellow balls) is coordinated to 6 oxygen atoms (red balls). **Top Right:** Ball-and-stick model visualizing the variety of different coordinations of oxygen and titanium atoms in the surface region. Adapted from [169]. The most important coordination features (for the present studies) have been emphasized with boxes around the text. **Bottom:** Ball model (top view) of the TiO₂(110) surface. Alternating rows of bridging oxygen atoms (A) and five-fold coordinated Ti atoms (C) can be seen. A single oxygen vacancy is illustrated in the figure (B).

are formed (hexagonal rosettes and strands), whereas oxygen annealing above 800 K leads to regrowth of the stoichiometric (1×1) surface [177].

The Ti interstitials introduce electronic defect states in the band gap in a similar manner to the donor states created by the oxygen vacancies. The Ti interstitial states are, however, located very close to the conduction band ($\sim 2\text{--}50$ meV) [173, 174], and they are therefore completely ionized at RT. The introduction of n-type donor levels from the two defect types pins the chemical potential close to the conduction band, which is

important for the applicability of the STM since the TiO_2 crystal would otherwise be electrically insulating. Furthermore, our experimental studies have revealed that the position of the chemical potential have an enormous influence on the surface chemistry as we will see in Section 6.4.

A ball model of the $\text{TiO}_2(110)$ surface is shown in the upper right and the lower part of Fig. 6.1. The surface is characterized by alternating rows of fivefold coordinated titanium atoms and so-called bridging oxygen atoms (located in a bridge position between two underlying sixfold coordinated Ti atoms) in the $[001]$ direction. The surface composition is an ideal bulk truncation, and it has been studied in detail with surface X-ray diffraction (SXRD) [178] and STM [167, 169]. Two types of point defects can be distinguished with STM on the $\text{TiO}_2(110)$ surface, the so-called Type A and Type B defects [169]. The most abundant surface defect is the Type A defect, which in the past has been attributed both to oxygen vacancies on the bridging oxygen rows and to hydroxyl species [169, 179, 180]. A bridging oxygen vacancy is illustrated in Fig. 6.1, and it is now generally agreed that the Type A defects on freshly prepared crystals should be ascribed to oxygen vacancies [167]. A scrutiny of the defect properties with STM, however, reveals inhomogeneities even on freshly prepared surfaces and, as discussed in Section 6.2.2, the assignment is thus not straightforward. The Type B defects are revealed in some STM images as slightly darker areas and the current interpretation ascribes them to some kind of subsurface defect (e.g. subsurface oxygen vacancies), but no direct proof of the validity of such assignment has yet been given [169].

The bridging oxygen vacancies have been studied with a variety of experimental techniques including X-ray photoemission spectroscopy (XPS) [181], ultraviolet photoelectron spectroscopy (UPS) [182], electron energy loss spectroscopy (EELS) [183, 184] and STM [169, 179, 185]. The bridging oxygen vacancies at the surface are found to introduce donor levels ~ 0.75 eV below the conduction band minimum similar to the donor levels formed by bulk oxygen vacancies, and there is general agreement that the electronic states are located around the underlying Ti cations, giving rise to Ti^{3+} -like signatures in electron spectra [167, 182–184]. Furthermore, the $\text{TiO}_2(110)$ surface and the bridging oxygen vacancies have been studied with DFT calculations by a number of groups [186–191]. Some theoretical indications have been found of the electronic donor states introduced in the band gap by the oxygen vacancies [188], but these findings have recently been questioned by other groups, and it generally seems as if DFT has difficulties in describing these states [167, 191].

As opposed to most metal crystals, titanium dioxide crystals only have a finite lifetime in the laboratory. The reduction induced by the sputtering and annealing cycles slowly changes the properties of the crystal and when a certain reduction level is reached, it is no longer possible to re-stoichiometrize the surface by oxygen annealing. On such highly-reduced crystals a sub-oxide Ti_2O_3 -like (1×2) surface termination is found [167]. All the experiments described in this thesis are, however, performed on crystals which are only reduced to a degree where the (1×1) surface structure (as seen in Fig. 6.1) is prevalent after each preparation. The color of our crystals are thus typically somewhere in the range from medium to dark blue.

6.2.1 Imaging of TiO₂(110) with STM

STM imaging of the TiO₂(110) surface is mostly performed with a positive bias voltage on the crystal, which is the natural choice with the chemical potential being pinned close to the conduction band minimum by the TiO₂ defect states. Tunneling therefore occurs from filled tip states to empty conduction band states in the crystal. The TiO₂(110) surface constitutes an excellent example of the difficulties associated with simple geometrical interpretations of STM images, as mentioned in Chapter 2. Fig. 6.2A shows a typical example of an STM image of the freshly prepared TiO₂(110) surface. Protruding rows are easily resolved with a distance corresponding to the TiO₂(110) unit cell shown in Fig. 6.1, but it is now generally agreed that the protrusions seen by STM should be ascribed to the Ti rows and *not* to the geometrically protruding bridging oxygen rows, which would otherwise be an intuitively appealing guess [167, 192]. Fig. 6.2B shows a plot of the electronic density of states in TiO₂, which rationalizes the peculiar imaging of the surface: The density of states in the conduction band are primarily derived from Ti-orbitals, whereas the states in the valence band are more O-like. Since tunneling is performed from filled tip states into empty conduction band states in the TiO₂ crystal it is intuitively reasonable to find the highest protrusions (as seen with STM) located near the Ti rows, even though these rows are geometrically low compared to the bridging oxygen rows. Theoretical simulations of STM images based on DFT calculations furthermore confirm the assignment of the protruding rows seen with STM to the rows of Ti atoms [179].

All STM images of the TiO₂(110) surface presented in this thesis have been acquired with a bias voltage of 1.25 V. This voltage is found to give the most stable imaging conditions minimizing interactions between tip and e.g. adsorbates on the surface. Scanning at higher voltages severely alters the surface and can e.g. lead to re-oxidation of the vacancies in the scanned area [169]. Scanning at lower voltages, on the other hand, increases the tip-surface interaction whereby tip-induced diffusion, desorption or reactions of the adsorbates become a problem. The tunnel current is kept very low in the range from 0.05 nA to 0.2 nA, which is also found to be a reasonable range to avoid tip-induced adsorbate interactions.

6.2.2 Crystal preparation - Type A defects

The TiO₂ crystals used in the presented studies were epipolished crystals from ESCETE and MTI. The crystals were prepared by multiple cleaning cycles consisting of sputtering (10 min 800 eV Ar⁺ ions) and annealing (800–1000 K, 0–15 min in 10⁻⁶ mbar O₂ followed by 10–15 min under UHV conditions). The annealing temperature was gradually increased for each crystal starting from approximately 800 K during the first cleaning cycles and ending somewhere in the range between 900 and 1000 K. The optimal annealing temperature depends crucially on the mounting position of the thermocouple, thus indicating that the measured temperature is not necessarily the same as the surface temperature during annealing. The annealing temperature was therefore fine-tuned individually for each crystal. In this way, large terraces of approximately 300 × 300 Å² were routinely formed with a typical density of Type A defects around 8–10%. The density

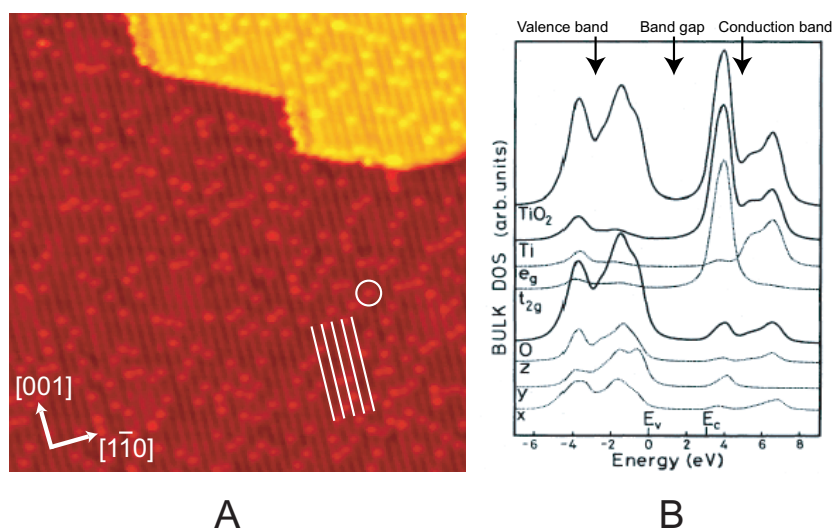


Figure 6.2: **A:** STM image ($300 \times 300 \text{ \AA}^2$) of the clean $\text{TiO}_2(110)$ surface. The bright rows are Ti atoms (indicated by white lines), and the protrusions between the rows (white circle) are Type A defects (see discussion in Section 6.2.2). **B:** Density of states (DOS) of bulk TiO_2 decomposed in Ti-derived states and O-derived states, respectively. It is clearly seen that Ti atoms contribute mostly to the conduction band and O atoms contribute mostly to the valence band states of TiO_2 . Reproduced from [193].

of Type B defects after such preparations is very low ($\leq 1\%$), and we have found no influence of these defects on the oxygen experiments presented in this thesis. The oxygen dosing during annealing gives rise to a small number of remnant oxygen molecules on the freshly prepared surface ($\leq 0.01 \text{ ML}$), but even if oxygen dosing is skipped, a minute amount of oxygen molecules is unavoidable on the surface.

As discussed above, there is by now general agreement in the literature that the Type A defects should be ascribed to bridging oxygen vacancies [167, 169], but recent studies have, however, indicated that water dosing may lead to hydroxyl species adsorbed at vacancy sites, which give rise to similar signatures in the STM images [179, 194]. The hydroxyl species can be distinguished from oxygen vacancies when comparing the height and the width of the protrusions in STM images [179].

Despite the general agreement that the Type A defects should be ascribed to vacancies, we find that inhomogeneities exist in the height distribution of the defects, even on freshly prepared hydroxyl-free surfaces. Such variations in height are particularly pronounced when the $\text{TiO}_2(110)$ surface is cooled to $\sim 100 \text{ K}$ immediately after crystal preparation. Fig. 6.3 shows a typical STM image of the surface where the crystal has been cooled to 100 K after a sputtering and annealing cycle. Even without thorough analysis, a range of different defects are readily observed. By measuring the height of these defects, a tri-modal distribution is found (also shown in Fig. 6.3), and it therefore

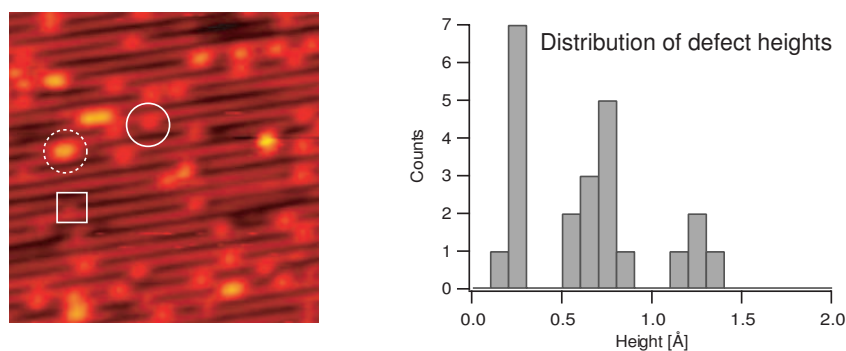


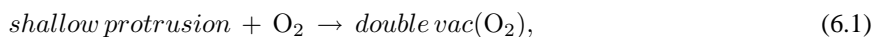
Figure 6.3: **Left:** Typical STM image ($108 \times 108 \text{ \AA}^2$) of $\text{TiO}_2(110)$ after sputtering and annealing. Three different “Type A” defects are marked; Circle: Bridging oxygen vacancy; Dashed circle: Double vacancy; Square: Shallow protrusion. **Right:** Histogram of defect heights compared to the average height of the Ti rows. The histogram reveals three distinct peaks: “Shallow protrusions” with a height of approximately $0.2\text{--}0.3 \text{ \AA}$, vacancies with a height of $0.6\text{--}0.8 \text{ \AA}$ and double vacancies with a height of $1.2\text{--}1.4 \text{ \AA}$. The assignment is described in the text.

seems necessary to include at least three different types of defects in the description of the freshly prepared surface at low temperatures. Ideally, we would like to perform experiments on a surface where oxygen vacancies are the only (or at least the predominant) defects, and fortunately we find that it is indeed possible to create such surfaces: When oxygen molecules are present on the surface, reactions occur that eventually transform all defects into vacancies, as we will see below. Even though the study of oxygen adsorption on $\text{TiO}_2(110)$ is not discussed in detail until Section 6.3, the interaction of oxygen with the three different types of defects will be discussed here, because our definition of a “clean” surface depends crucially on the ability of oxygen to create surfaces with pure vacancies only. For the purpose of the present section it thus suffices to know that upon oxygen dosing a diffusing adsorbate attributed to molecular oxygen is observed on the Ti rows [185].

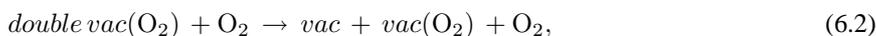
The interaction of oxygen with the defects of intermediate height (marked with a full circle in Fig. 6.3) has previously been studied in our group by Schaub *et al.*, who ascribed these defects to bridging oxygen vacancies [185]. By means of high-resolution STM movies, a peculiar diffusion mechanism of the vacancies was revealed, in which oxygen molecules were found to mediate the diffusion of the vacancies perpendicular to the bridging oxygen rows [185]. This diffusion mechanism is discussed in further detail in Section 6.3. In the present studies we adopt the interpretation by Schaub *et al.* concerning the nature of the defects of intermediate height, and we hence assign these defects to bridging oxygen vacancies. This assignment is justified by the oxygen reactions discussed in the rest of this chapter: We find that different reactions of oxygen adsorbates with the defects of intermediate height result in the removal and recreation of these defects. Such findings strongly suggest that the defects should be ascribed to oxy-

gen vacancies, and that the investigated reactions with oxygen adsorbates illustrate the ability of adsorbed oxygen to heal and recreate the oxygen vacancies. These experimental findings are the topic of Section 6.3.1. Furthermore, the defects ascribed to bridging oxygen vacancies have been found to facilitate water adsorption and subsequent dissociation to form hydroxyl species [179, 195], and these findings also significantly corroborate the chosen assignment. In the following, the nature of the low and high defects will be discussed.

Fig. 6.4 displays a series of STM images from an STM movie following the interaction of oxygen molecules with one of the “low” defects, which we will refer to as *shallow protrusions* (marked with a square in Fig. 6.3), and with one of the high defects (marked with a dashed circle in Fig. 6.3). When an oxygen molecule interacts with a shallow protrusion (Fig. 6.4A+B), one of the high defects is created and the oxygen molecule disappears (C). The high defect is stable until a second oxygen molecule encounters the defect (D). The interaction of this second oxygen molecule with the high defect leads to the formation of two defects of intermediate height (E+F), and after some time the first (disappeared) oxygen molecule reappears next to one of these two defects (G+H). A subsequent height analysis of the two resulting defects of intermediate height confirms that these are of the same type as the ones ascribed to bridging oxygen vacancies by Schaub *et al.*, and the high defects are accordingly ascribed to double vacancies, i.e. two neighboring bridging oxygen vacancies. The reaction from A to B in Fig. 6.4 can hence be written as:



where we have indicated that the disappeared oxygen molecule is adsorbed *in* the double vacancy since it reappears later on. The reaction from C to F can be written as:



where the *hidden* O₂ is now adsorbed in one of the vacancies; and finally the reaction from G to H can be written as:



The existence of double vacancies on the TiO₂(110) surface is rather unexpected; The repulsive interaction between vacancies has previously been shown to be fairly large, and double oxygen vacancies are therefore not believed to exist at thermodynamical equilibrium on the surface [191, 196, 197]. This finding is, however, in good agreement with our data: Following the evolution of the defect distribution over longer timescales, each double vacancy is indeed found to split up into two separate vacancies upon the encounter with an oxygen molecule, and after a large number of subsequent vacancy diffusion events, a distribution of the vacancy positions on the surface is revealed which clearly reflects the repulsive vacancy-vacancy interaction [196, 197].

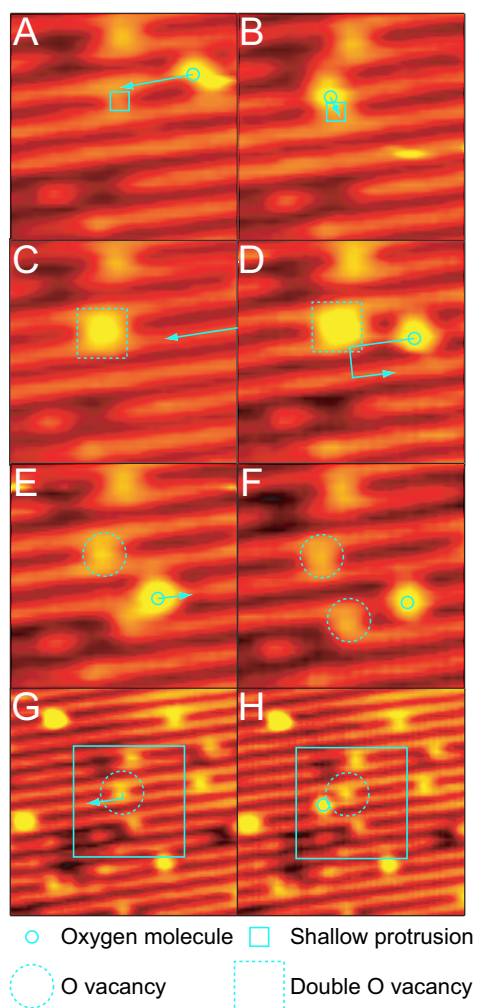


Figure 6.4: STM images from an STM movie showing the interaction of an oxygen molecule (small circle) with a shallow protrusion (small square) (A+B). A double vacancy is created (large dashed square) (C), and subsequent interaction with a second oxygen molecule splits the double vacancy into two vacancies (large dashed circles) (D-F). Later, the oxygen molecule used in the reaction from a shallow protrusion to a double vacancy reappears next to one of the vacancies (G+H).

The nature of the shallow protrusions has not been satisfactorily clarified yet, and at the time of writing this thesis, there is still uncertainty about their composition. The height difference between shallow protrusions and vacancies is $\sim 0.4\text{--}0.5$ Å, and the shallow protrusions can therefore clearly be distinguished from e.g. the hydroxyl species discussed in [179]. The height difference between hydroxyls and vacancies is only 0.1–0.2 Å and it is thus much harder to distinguish between hydroxyls and vacancies than to distinguish between shallow protrusions and vacancies.

Other adsorbates located in the oxygen vacancies may constitute the shallow protrusions. The rest gas in the UHV chamber consists mainly of H₂, CO and water, and these molecules (or combinations of these) are therefore the most likely candidates for adsorption during crystal preparation. A possible explanation of the observed reaction in Fig. 6.4 could e.g. be that the shallow protrusion consists of a CO molecule adsorbed in a bridging oxygen vacancy: When an oxygen molecule encounters the shallow protrusion, the CO molecule reacts with one of the neighboring bridging oxygen atoms and with the diffusing oxygen molecule. This could result in the formation of a CO₂ molecule that desorbs from the surface plus the formation of a double vacancy with an adsorbed oxygen molecule, i.e. $\text{vac}(\text{CO}) + \text{O}_2 \rightarrow \text{CO}_2(\text{g}) + \text{doublevac}(\text{O}_2)$. Even though such a reaction would explain the experimental findings, we have not been able to find any correlation between CO dosing (or dosing of other gasses) and the amount of shallow protrusions. Another possible explanation of the shallow protrusions could instead be related to subsurface defects or a combination of subsurface defects and bridging oxygen vacancies. Despite our efforts to unravel the intrinsic nature of the shallow protrusions, we must, however, conclude that this subject remains an open question.

The diversity of Type A defects revealed in the STM image above (Fig. 6.3) clearly serves as an example of the complexity even of the “clean” TiO₂(110) surface, and an indispensable prerequisite for performing adsorption studies is of course a reasonable and reproducible concept of cleanliness of the surface. Even though the nature of the shallow protrusions remains unclear, we fortunately find that if the surface is left at room temperature for approximately an hour after annealing, all shallow protrusions and double vacancies are transformed into regular vacancies, and no further development is seen with time. Even the small concentrations of oxygen molecules remnant from the oxygen dosing during annealing is sufficient to facilitate the interaction and transformation of the different species. If, however, the sample is cooled to, e.g., 100 K immediately after sample preparation, the mobility of the remnant oxygen molecules is frozen out before equilibration of the surface, and we find a trimodal distribution of the defects as depicted in Fig. 6.3.

In the studies presented in the following, a thorough analysis of the Type A defects has been performed before each oxygen dosing experiment. We have mainly focused on the interaction of oxygen with surfaces where the bridging oxygen vacancies are the predominant defect, but a few results are also presented of oxygen adsorption on surfaces with large densities of shallow protrusions. We find that the interaction of oxygen with TiO₂(110) is very different in the two cases, which emphasizes the need for atomic-scale information to reach unambiguous conclusions concerning gas adsorption on the TiO₂(110) surface.

When shallow protrusions are found on the surface after sputtering and annealing,

the surface has been left at room temperature to facilitate the reaction of oxygen species with the protrusions to form clean vacancies (Eq. 6.1-6.3). Following this recipe, clean surfaces with bridging oxygen vacancies being the predominant defect are routinely prepared.

6.3 Oxygen adsorption on TiO₂(110)

The adsorption and interaction of oxygen with the TiO₂(110) surface has proven to be a complex system. A number of recent studies by different groups using complementary techniques have provided evidence for a wealth of different oxygen-related species and processes occurring on the surface upon O₂ exposure [165, 169, 185, 198–203]. In earlier studies, oxygen adsorption was merely assumed to lead to the filling of surface oxygen vacancies on TiO₂(110) (see e.g. [181, 182]), but the more recent studies have revealed that the processes of oxygen adsorption and vacancy filling are far from understood.

The recent studies of oxygen adsorption on TiO₂(110) include experiments with electron energy loss spectroscopy (EELS) [165, 202], temperature-programmed desorption (TPD) [165, 201, 202], photo-desorption [198–200], and STM [169, 185]. The interaction of molecular oxygen with the bridging oxygen vacancies is known to play a key role in the adsorption process, and it has been found that oxygen adsorption on the stoichiometric surface (no vacancies) is inhibited above ~ 150 K [202]. At least five different adsorbed oxygen species have been reported: Three oxygen species have been identified through studies of the photo-reactivity and photo-desorption of adsorbed oxygen. Two of them, α_1 and α_2 , are formed by oxygen exposure at 100 K and are believed to reside in oxygen vacancies, and the third species, β , is formed by heating the sample after the low-temperature formation of α species [198–200];¹ A saturation coverage of three oxygen molecules per vacancy has been found upon low-temperature exposure, and tentatively two of the adsorbed species, α_1 and α_2 , have been assigned to adsorption *in* the vacancy or adjacent to the already oxygen-filled vacancy, respectively [202]. An oxygen TPD peak has been found centered at 410 K after low-temperature oxygen exposure (100 K) by Henderson and co-workers [202], but, on the other hand, no oxygen has been detected in TPD experiments by Yates and co-workers after similar preparations [199]. A conflict thus seems to exist in the literature as to whether the so-called β species desorb upon heating or not. The oxygen species adsorbed at low temperatures can furthermore be detected in EELS experiments, where a 2.8 eV loss peak is revealed. This peak has been assigned to a Ti-O₂⁻ loss feature [202]. Experiments with isotopically labelled oxygen molecules by Yates *et al.* and Henderson *et al.*, respectively, indicate that the oxygen molecules do not exchange oxygen atoms with the surface oxygen (so-called isotopical scrambling) [198, 202].

The fourth type of oxygen adsorbate reported in the literature was first evidenced through reactions of remnants of oxygen surviving annealing to temperatures above the TPD peak (410 K) [201]. The reacting oxygen species were found to shift the water desorption peak and isotopically scramble with adsorbed water, and tentatively these species were assigned to oxygen adatoms on the surface formed when oxygen molecules oxidize

¹The α, β -nomenclature has been adopted from Yates and co-workers [198–200].

the vacancies [165, 203]. A recent paper by Schaub *et al.*, however, questions the validity of this assignment [185]. In [185], molecular oxygen was shown to diffuse on the Ti rows and thereby mediate the diffusion of encountered oxygen vacancies perpendicular to the close-packed rows [185]. The vacancy diffusion mechanism was thoroughly investigated at low temperatures, where the movement of the oxygen molecules could be tracked in STM movies, and in this way a surprising model for the vacancy diffusion process was found: When an oxygen molecule meets a vacancy, a new meta-stable species is observed on the Ti-row, which is ascribed to atomic oxygen. The oxygen molecule thus dissociates, re-oxidizes the vacancy and leaves an oxygen ad-atom on the Ti-row. The oxygen ad-atom is, however, very reactive and immediately after its formation it recombines with a bridging oxygen atom from either side of the Ti-row. This process creates a new vacancy, either at the same position as the original vacancy or at an adjacent row of bridging oxygen atoms, and in this way the vacancy diffusion is facilitated perpendicular to the bridging oxygen rows. The adsorbed diffusion “mediator” is clearly associated with oxygen, because a correlation between oxygen exposure and the number of diffusion events is presented in [185]. Moreover, the adsorbate cannot be atomic oxygen; Schaub *et al.* performed dosing experiments with atomic oxygen, and observed a large increase both in the number of vacancies and in the number of “mediator” adsorbates. This observation shows that atomic oxygen combines with a bridging oxygen atom when it adsorbs on the surface, and the observed adsorbates must therefore be molecular oxygen. From the diffusion process of the vacancies it is clear that the oxygen molecules scramble with the substrate oxygen, and in the experimental data presented below we find that these diffusing oxygen molecules are the basic entity of mobile oxygen on the surface. Since these species interact with other species and perform scrambling with the surface, it is reasonable to associate these molecules with the reacting species studied by Henderson *et al.* in [165, 201, 203], and we will thus collectively refer to these species as γ species (continuing the Yates nomenclature).

Finally, Diebold and co-workers performed oxygen exposure at RT and observed a decrease in the number of Type A defects [169]. This was one of the main pillars in the identification of the Type A defect as an oxygen vacancy. Besides the decrease in the density of oxygen vacancies, a number of species, named “Type C defects”, appeared at the surface upon oxygen exposure. The Type C species are located on the Ti rows of the surface, and their density remains rather constant as a function of O₂ exposure.

Recent density functional theory calculations have confirmed the importance of oxygen vacancies for the adsorption of oxygen on TiO₂(110) : In [191] molecular oxygen was found not to bind on the stoichiometric surface. When vacancies are present, however, oxygen molecules may adsorb both *in* the vacancies and on the titanium rows. These findings are thus in good agreement both with the finding of vacancy-related adsorption by the Yates and Henderson groups and with the existence of oxygen adsorbates on the Ti rows as found by Schaub *et al.*

In the following we will present STM data investigating the different oxygen species found on TiO₂(110) upon oxygen exposure in the temperature range from 100 K to 300 K. By means of time-lapsed sequential STM imaging, we have acquired STM movies at varying temperatures to monitor the dynamics and appearance of the individual oxygen species, and we provide evidence for the existence of two “fundamental”

building blocks among a variety of adsorbate species observable with STM. These two species will be associated with the β and γ species discussed above. A number of other complexes are also seen on the surface, but by following the formation and subsequent disintegration of such species they can all be ascribed to complexes consisting of combinations of β and γ species. Scrutiny of the interaction between the oxygen complexes furthermore leads to the identification of complicated agglomerates of oxygen species, where fast-moving oxygen atoms apparently jump back and forth between the individual oxygen complexes at shorter timescales than the scanning speed of our STM. The interaction of oxygen with the TiO₂(110) surface revealed through the STM studies is thus much more complex than anticipated from the literature, but by scrutinizing the different reaction mechanisms between oxygen species and surface oxygen vacancies a consistent model is derived, which accounts for the observations previously reported in the literature. The model particularly addresses the issue of vacancy filling by the adsorption of oxygen molecules and, furthermore, it provides an explanation of the discrepancy between the TPD experiments from different groups.

The table below briefly summarizes the nomenclature of the oxygen-related species and thus serves as a quick reference guide for the reader during the rest of the chapter. A short description of our interpretation of each species based on the experiments presented below have also been added.

| | Description in literature: | Our interpretation (based on the studies below): |
|----------|--|--|
| α | Adsorption state at 100 K - transformed to β upon annealing [198–200] | Physisorbed oxygen molecule either in vacancy or at Ti-rows. Not observed in STM |
| β | Adsorption state found at higher T upon low T O ₂ exposure. Ascribed to vacancy adsorption [198–200, 202] | Adsorbate located on Ti-rows consisting of 3 oxygen atoms |
| γ | Adsorbate reacting and isotopically scrambling with other adsorbates and with the surface [165, 185, 201, 203] | Molecular oxygen adsorbed on the Ti-rows |
| C | Oxygen related species adsorbed on the Ti-rows observable at RT with STM [169] | Complexes of β and γ species |

6.3.1 Experimental results

To investigate the oxygen chemistry on $\text{TiO}_2(110)$ and to facilitate a comparison with the oxygen studies discussed above, we performed STM experiments where the surface was saturated with O_2 (5–50 L) at 100 K and subsequently annealed to successively higher temperatures. In this way the evolution of different oxygen species could be monitored. All STM images in these experiments were acquired at ~ 100 K to freeze out the diffusive motion and further evolution of oxygen species during observation. Furthermore, smaller oxygen exposures were performed in the temperature range from 100 K to 300 K to complement the low-temperature experiments. For these additional experiments, STM movies have been acquired at varying temperatures, whereby the dynamics of the different species could be tracked. The information gained from such movies has proven invaluable in the identification of the different species and in the unravelling of their inherent nature.

Low-temperature dosing and subsequent annealing

When the $\text{TiO}_2(110)$ surface with bridging oxygen vacancies² is saturated with oxygen (5–50 L) at low temperatures (~ 100 K), we find only small changes in the observed STM images compared to the images prior to dosing. The upper part of Fig. 6.5 shows examples of STM images before and after oxygen dosing together with the corresponding height distributions of Type A defects. A small number of shallow protrusions and double vacancies are revealed before dosing, but a clear predominance of vacancies is observed in the figure. A slight lowering of the vacancy height can be seen upon oxygen dosing in this particular case, but these changes fall within the uncertainty imposed by the rather broad height distribution of the vacancies. Returning to the STM image after oxygen dosing, we furthermore note that no (or very few) oxygen-derived protrusions are revealed on the Ti rows upon oxygen exposure.

These findings are in striking contrast to the experimental results obtained when shallow protrusions are present at the surface before oxygen dosing.³ The lower part of Fig. 6.5 shows examples of STM images and height distributions of the defects before and after oxygen exposure in the case where shallow protrusions are the predominant defects. In the figure the shallow protrusions are observed to disappear when oxygen is dosed, and new protrusions appear on the adjacent Ti rows. The characteristics of the oxygen-derived protrusions are discussed in the following section when the dynamics of oxygen species have been presented, and we merely note here that a proper characterization of the Type A defects before oxygen exposure is of crucial importance for the outcome of the experiments.

²See discussion in section 6.2.2.

³The shallow protrusions are discussed in Section 6.2.2.

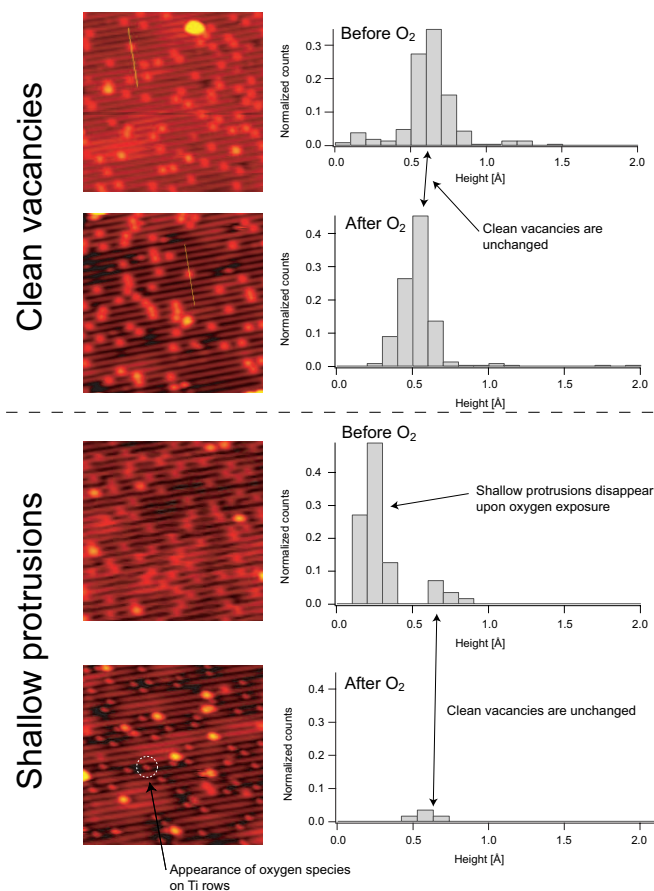


Figure 6.5: STM images ($150 \times 150 \text{ \AA}^2$) before and after O₂ dosing at $\sim 100 \text{ K}$ on a surface dominated by vacancies (top) and a surface with predominance of shallow protrusions (bottom), respectively. The right part of the figure shows the height distributions of Type A defects (vacancies and shallow protrusions) before and after oxygen dosing. We observe that oxygen exposure leads to only minute changes in the height of the vacancies, whereas the shallow protrusions disappear upon oxygen dosing. Very few oxygen species are observed on the Ti-rows if clean vacancies are predominant before dosing, but a large number of oxygen species are found upon oxygen dosing on a surface with shallow protrusions (one of these species is marked by a white dashed circle). These oxygen species are referred to as β' species in the following sections. Each height distribution has been normalized to the number of Type A defects prior to oxygen exposure.

Returning to the oxygen dosing on a surface with vacancies, it may seem puzzling at a first glance that no significant changes are found in the STM images after oxygen exposure. According to the results by Henderson *et al.*, up to three oxygen molecules should be adsorbed in the vicinity of each vacancy after such preparations (α species) [202]. By annealing the sample, however, different oxygen species do appear on the Ti rows, and this fact leads us to the conclusion that the oxygen molecules are indeed present on the surface after low temperature dosing even though they are not imaged by STM. A possible explanation of the apparent invisibility in STM images could be that the α species are weakly bound physisorbed species, which either diffuse too fast to be imaged by STM or are easily swept away by the tip. Some of the molecules may, however, also be located in the vacancies if an STM image of a “clean” vacancy and an image of a vacancy filled with an oxygen molecule are similar.

When the sample is annealed to successively higher temperatures after low-temperature dosing of oxygen, a number of different protrusions appear on the titanium rows. An overview of these oxygen-derived protrusions is shown in Fig. 6.6, where STM images and line scans of each type of species are provided. The naming of the oxygen species is based on the results from the rest of this section, where comparison is made to previous studies of O₂/TiO₂(110). The γ and β species shown in the top part of the figure are found to be the building blocks for all other species on the surface. Two types of β species are found, and these are accordingly named β and β' . All other species revealed with STM can be ascribed to combinations of γ and β species, and examples of such larger complexes are shown in the lower part of the figure. The unravelling of the nature of the larger complexes cannot be done solely based on “static” STM images as the ones presented in Fig. 6.6. From the line scans, we observe that for example the $\gamma\gamma$ and $\gamma\beta$ species are virtually indistinguishable in STM images. The identification and naming of the single species have therefore mainly been based on the different dynamics of each species, which have been investigated with STM movies. These results are discussed below.

The γ species are identical to the diffusing species discussed by Schaub *et al.* [185], and these oxygen adsorbates are thus ascribed to molecular oxygen, which among other things mediates the diffusion of vacancies [185]. As is evident from the chosen nomenclature, the β species observed with STM are associated with the β species discussed by Yates and co-workers [198–200]. This assignment is rationalized by measuring the density of the various oxygen adsorbate species as a function of the annealing temperature. The result of such experiments is depicted in Fig. 6.7. The top part of the figure shows the density of oxygen-related adsorbates after annealing to different temperatures from ~ 100 to 500 K. The density of bridging oxygen vacancies (red curve) is rather constant at low temperatures, but from ~ 250 –350 K it drops to zero, and no vacancies are found at higher temperatures.

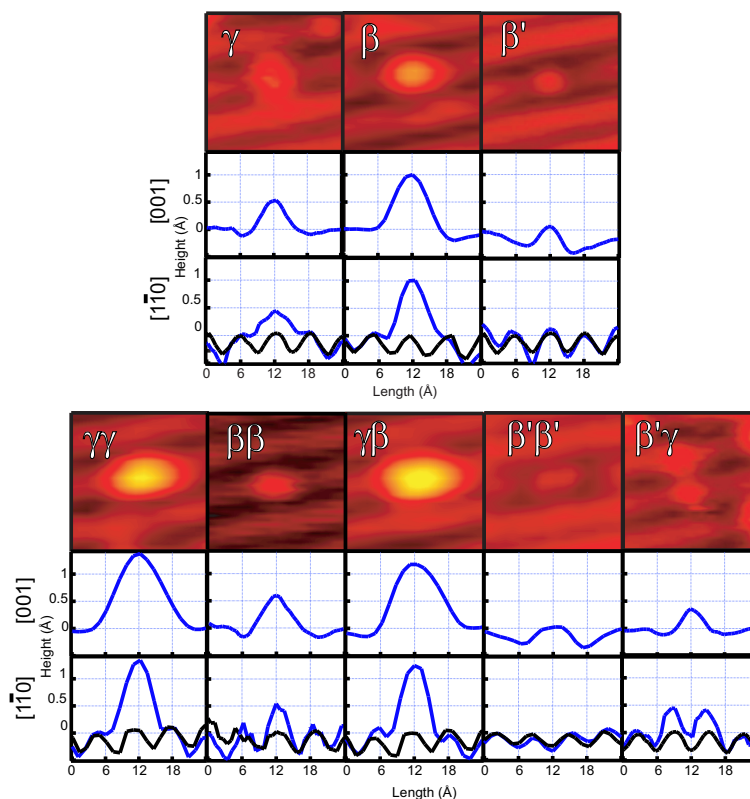


Figure 6.6: Close-up STM images ($23 \times 23 \text{ \AA}^2$) and line scans along, $[001]$, and perpendicular, $[\bar{1}\bar{1}0]$, to the Ti-rows of the oxygen-related adsorbate species found on the surface after oxygen exposure and subsequent annealing to higher temperature. The blue lines are line-scans of the oxygen species, and the black lines are line-scans across the (oxygen-free) Ti rows for comparison. The γ and β species (top part of figure) are found to be the main building blocks of the oxygen chemistry on the surface. The β species are found in two different configurations, β and β' . All other species (lower part of figure) can be assigned to combinations of γ and β species, which is reflected in the naming of each species. The assignment is based on STM movies, as discussed below. The γ and β species are located on-top of a titanium atom whereas the larger species are centered at bridge positions. The height of the species extracted from the images and the line scans can change by $\sim \pm 0.2 \text{ \AA}$ depending on the tip state.

The β -type adsorbate species (blue curve) are the most prominent features on the surface. A clear peak in the number of β species is found around 350 K, whereafter the density declines and no β species are found above 500 K. A number of the larger oxygen complexes are also found, but the density of these is rather low compared to the β density on the surface. Some of the larger complexes contain β species,⁴ and if these are added to the β curve we arrive at the dashed blue line in Fig. 6.7, which is an estimate of the total amount of β species on the surface. This curve exhibits a more broad maximum ranging from ~ 250 K to ~ 350 K.

The development of β species as seen with STM can be compared to the photo-desorption data published by Yates and co-workers [198–200]. The lower part of Fig. 6.7 reproduces the photo-desorption based data described in [198], and a correlation between the appearance and decay of the number of β species in photo-desorption experiments and the β protrusions observed in the STM experiments presented in this thesis is clearly observed. This is the main argument for adopting the β terminology from Yates and co-workers for the description of these protrusions.

The photo-desorption data show that a rather large amount of β species are found on the surface already at low temperatures after oxygen dosing. This finding is in contrast to the rather low density of β species as seen with STM. Returning, however, to the oxygen-derived species occurring at shallow protrusions (lower part of Fig. 6.5), we find that a large amount of β species can indeed be observed immediately after oxygen exposure if shallow protrusions are present on the surface. A possible interpretation of the large amount of β species observed in the photo-desorption data at low temperatures could therefore be that the Type A defects on the TiO₂(110) surface studied by Yates and co-workers were composed of a mixture of clean vacancies and shallow protrusions. As we will see in the discussion below (Section 6.3.2) this suggestion may also explain the discrepancy between O₂-TPD spectra from the Yates and Henderson groups, respectively.

Dynamics and transformation of oxygen species

As can be seen from Fig. 6.6 and 6.7, a large variety of oxygen-related species exist on the surface. By following the formation and interaction of the different species we have, however, been able to determine the oxygen content of each type of species, i.e. the number of oxygen atoms in the various protrusions. This is done through a careful tracking of the different species at the surface with STM movies, following the creation and healing of vacancies as well as the formation and breaking up of oxygen clusters. The chosen nomenclature for the species reflects the oxygen content in each protrusion, and e.g. β and β' are thus assigned to the same category, because the interactions with other species reveal that they contain the same number of oxygen atoms. At all temperatures both types of β species are immobile on the surface and are therefore easily distinguished from the other species. On the other hand, all larger complexes containing γ oxygen molecules diffuse along the [001] direction on the surface and are much harder to distinguish from each other, as seen in the STM images in Fig. 6.6.

⁴See Fig. 6.6.

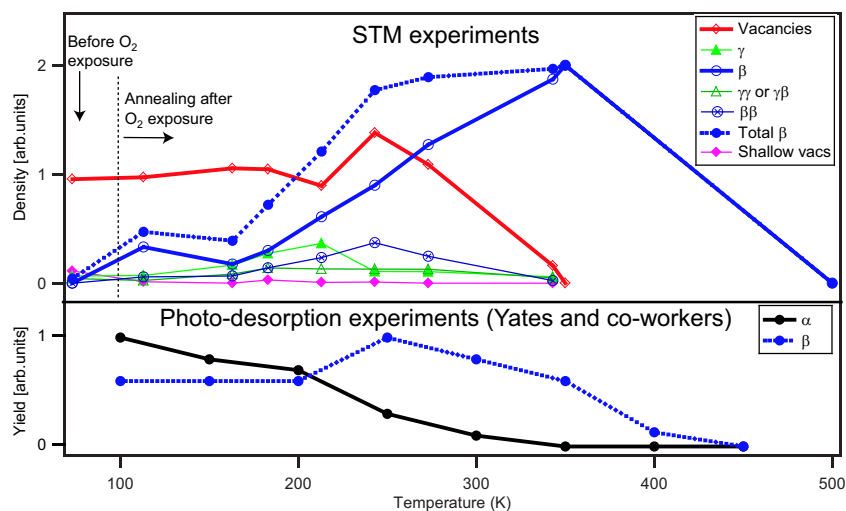


Figure 6.7: **Top:** Graphical illustration of the evolution of different oxygen species upon annealing to subsequently higher temperatures. The TiO₂(110) surface was saturated with oxygen at ~ 100 K which was also the scanning temperature between each annealing. The first data points (left) show the density of species prior to oxygen exposure. At low temperatures (≤ 200 K), the densities of γ , β and larger oxygen complexes are comparable, but at higher temperatures a clear predominance of β species is seen. These findings are compared to the development of α and β species observed with photo-desorption (**Bottom** graph). The presented photo-desorption data are reproduced from [198].

As discussed above, the γ species have been assigned to oxygen molecules by Schaub *et al.* based on a detailed analysis of the role of these molecules in the vacancy diffusion [185]. The nature of the β species, however, has only been indirectly assessed by measuring the desorption products with photo-desorption [198–200]. Molecular oxygen (O₂) was found to desorb from the surface in [198–200], but no information of the adsorbate configuration *on* the surface was revealed from these studies.

By examining the interaction of two γ species, we have been able to determine the oxygen content of the β species: Fig. 6.8 shows STM images from an STM movie following the evolution on the surface when two γ species diffuse and encounter each other (Fig. 6.8a). A larger protrusion is created, which we naturally refer to as $\gamma\gamma$, and as mentioned above, this entity also diffuses along the [001] direction like the single γ species. In some cases the $\gamma\gamma$ species undergoes reaction whereby a bridging oxygen vacancy is produced next to the oxygen complex (Fig. 6.8b). The produced oxygen complex must hence contain 5 oxygen atoms. Following the further development of the complex until it disintegrates, we find that the end result is a γ and a β species (Fig. 6.8c),

and the total reaction can thus be written as:



As indicated by the reversibility of the reaction, we have found similar examples of the reverse reaction where a γ and a β species meet and form a $\beta\gamma$ complex which diffuses until it finds a vacancy. The vacancy is re-oxidized, whereby a $\gamma\gamma$ species is created, and upon dissociation two γ species are finally formed. Such reactions strongly indicate that β species contain three oxygen atoms, as sketched in the ball models in Fig. 6.8. It is important to emphasize that all ball models of oxygen species presented in this chapter only represent the *number* of oxygen atoms that we associate with each oxygen group. They do not in any way suggest exact positions or configurations of the different oxygen atoms within the species. The only purpose of the ball models is thus to illustrate the concept of conservation of the number of oxygen atoms, which leads to the assignment of three oxygen atoms to the β species. The larger clusters, like $\gamma\gamma$ and $\gamma\beta$ in Fig. 6.8b, are generally impossible to distinguish in STM images (see line scans in Fig. 6.6), but by following the formation and disintegration of each larger protrusion we find that they can all be ascribed to different agglomerates of β and γ species like $\gamma\gamma$, $\gamma\beta$, $\beta\beta$, and even larger clusters like $\gamma\gamma\gamma$ and $\gamma\gamma\beta$.

Apart from the $\gamma\gamma$ reaction described above, exchange reactions between γ and β species are often observed on the surface,



where the “extra” oxygen atom on the β species is transferred to the γ species. Such reactions are even found to occur between β and γ species adsorbed on adjacent Ti rows separated by a row of bridging oxygen atoms, as illustrated in Fig. 6.9. When larger groups of oxygen complexes agglomerate, the probability for such exchange reactions increases, and we observe a situation where the different oxygen complexes continuously exchange oxygen atoms with each other, creating a destabilized entity which yields a flickering appearance in STM of the involved species.

The transition from α species to β , γ and larger complexes, which is depicted in Fig. 6.7 can also be scrutinized directly with STM movies at low and intermediate temperatures: When STM movies are acquired after oxygen exposures, the appearance of γ , $\gamma\gamma$, β +vacancy, and $\beta\beta$ can be observed at apparently arbitrary positions on the previously clean titanium rows. The position of appearance shows no correlation with the position of vacancies or other nearby adsorbates. On the other hand, we also observe the formation of β species directly adjacent to vacancies or shallow protrusions with concomitant re-oxidation (healing) of these defects. In the discussion of Fig. 6.6, it was mentioned that two different types of β species are found on the surface, β and β' . Especially at low-temperature exposures, the β' species are predominant and they are distinguished from other species both through their imaging characteristics in STM (see Fig. 6.6) and through their reaction with γ species: When a γ oxygen molecule encounters a β' species an immobile $\beta'\gamma$ -entity is created which can be stable for a long time at low temperatures. When the temperature is raised, the $\beta'\gamma$ complex, however,

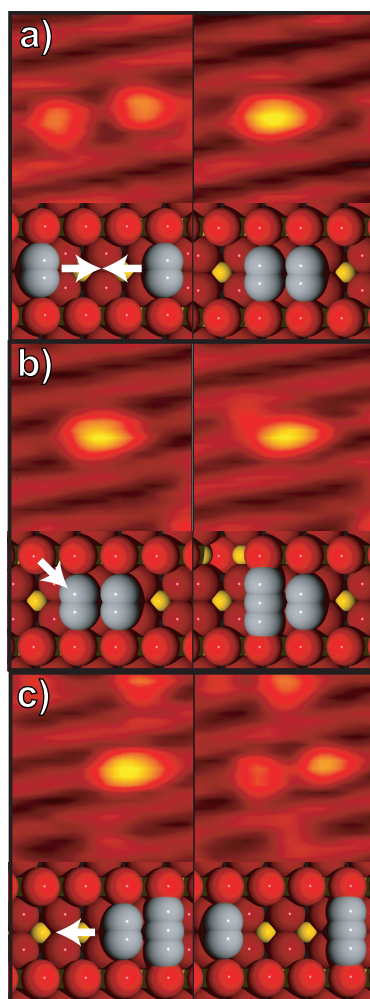


Figure 6.8: STM images ($30 \times 30 \text{ \AA}^2$, $T=225 \text{ K}$) from an STM movie following the interaction of oxygen molecules on the surface: Two diffusing γ species meet on the surface (a), to form a pair ($\gamma\gamma$) which is also mobile. The $\gamma\gamma$ pair can extract a vacancy from an oxygen row (b), thereby forming a mobile complex containing five oxygen atoms ($\gamma\beta$). This complex can, finally, split into two different species recognized as the mobile γ oxygen molecule and the immobile β species. From such events, we conclude that the β species contain 3 oxygen atoms. The ball models merely illustrate the number of oxygen atoms in each species and are not suggestions of the actual configuration of the oxygen atoms.

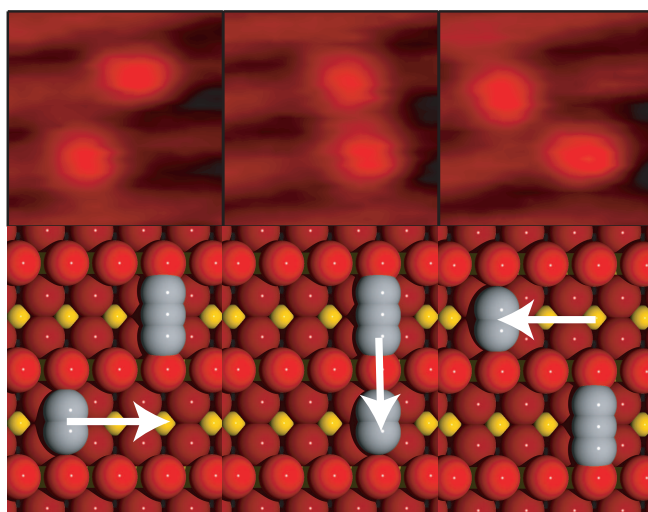
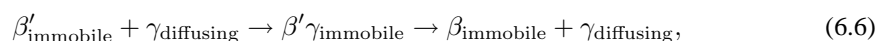


Figure 6.9: Exchange between a β and a γ (See Eq. 6.5). The mobile γ approaches the immobile β on an adjacent row. When the two species are adjacent an oxygen atom may be transferred $T=225\text{ K}$

disintegrates and a regular β species is formed together with the γ molecule. The low-temperature formation and subsequent disintegration of immobile $\beta'\gamma$ complexes can thus be written as,



which should be compared to the dissimilar “exchange” reaction of β and γ molecules (Eq. 6.5), where no stable and immobile intermediate entity is formed. An example of an immobile $\beta'\gamma$ complex is provided in Fig. 6.6. Eq. 6.6 shows that the oxygen content of β and β' is indeed the same, although they react differently with other adsorbate species. A more systematic investigation of the further differences and similarities between the two types of β species has, however, not been pursued.

6.3.2 Discussion

The experimental findings presented above show that the adsorption of oxygen on TiO₂(110) is highly complicated and that a huge number of different oxygen-derived adsorbate species exist on the surface and interact with each other. One of the main results from the presented STM experiments is thus that simple models of molecular oxygen adsorption in and around vacancies are much too simplistic to grasp the complex chemistry of oxygen adsorbates on TiO₂(110).

In the following section the general implications of the experimental findings presented above are discussed. First, the peculiar “invisibility” of the α species is considered together with the transition of these species to the observed β , γ and larger

oxygen complexes. Secondly, the healing of oxygen vacancies by oxygen exposure is discussed based on the observed reactions on the surface, and finally a brief paragraph addresses the discrepancies between TPD experiments from the Henderson and Yates groups [199, 202].

α and the transition to other species

From previous studies it is known that the saturation coverage of oxygen on TiO₂(110) corresponds to three oxygen molecules per oxygen vacancy [202]. This finding immediately leads to the conclusions that *no* oxygen molecules can adsorb on the stoichiometrical surface and that the oxygen vacancies must play a key role in the adsorption process. In [202] it was therefore (intuitively appealingly) concluded that three oxygen molecules adsorb *in* and *around* each vacancy at saturation coverage. The role of the oxygen vacancies presented in [202] is thus rather local: Saturation occurs when each vacancy is filled with the maximum number (three) of oxygen molecules. Looking at our STM data this interpretation, however, seems questionable. First of all, no changes of the imaging characteristics of the vacancies are found upon low-temperature oxygen dosing (Fig. 6.5), and secondly, a large variety of oxygen-related species appear at arbitrary positions on the titanium rows when the temperature is raised (Fig. 6.6 and 6.7). Comparing the two different approaches (STM presented here and TPD discussed in [202]), we are thus led to the conclusion that the saturation of oxygen adsorption and the correlation with the oxygen vacancy density must be caused by a more non-local interaction, where the oxygen molecules are not directly adsorbed in the vacancies: On semiconductor surfaces (like TiO₂(110)) as opposed to metal surfaces, only a certain amount of charge is available in the conduction band at low temperatures for the formation of chemisorption bonds. Upon adsorption, the oxygen molecules are negatively charged, and the conduction band is thus depleted in the vicinity of the surface. Such an effect is experimentally supported by the rather large band bending measured upon O₂ adsorption at RT [182]. At a certain oxygen coverage, the charge depletion will hinder further adsorption of oxygen, thereby leading to the saturation observed in [202]. We thus propose that the main effect of the surface vacancies for oxygen adsorption is the introduction of (surface) electronic states in the band gap giving rise to a certain amount of electrons in the TiO₂ conduction band. Our proposed interpretation explains the saturation of oxygen adsorption and the correlation of the oxygen saturation coverage with the vacancy density found by Henderson *et al.* at low temperature [202], and at the same time it is in agreement with the appearance of oxygen species on the Ti rows, as observed with STM in our studies.

Even if the main role of the oxygen vacancies concerning oxygen adsorption is to provide free charge to the formation of chemisorption bonds, it is likely that some of the oxygen molecules are indeed bound *in* the vacancies; Some of the oxygen species observed with STM always appear next to vacancies. This is for example the case for the β' species discussed above, which is found next to a vacancy which is re-oxidized upon the formation of β' . These findings suggest that one type of α species, e.g. α_1 , may be adsorbed *in* the vacancies whereas the other type, α_2 , is adsorbed in a weakly bound physisorbed state, which is not localized around the vacancies.

The idea of a more non-local role of the bridging oxygen vacancies is supported by recent DFT calculations by Rasmussen *et al.* [191]. These calculations show that the stoichiometric TiO₂(110) surface does not bind oxygen molecules, but as soon as vacancies are present at the surface, the molecules are found to bind both to the vacancies and to the Ti rows.

When studying the appearance of oxygen species on the surface in the context of a transition from physisorbed α species to chemisorbed β and γ complexes, all the observed oxygen species can be rationalized as a product of the interplay between a number of α species and the surface vacancies, as illustrated by the following reactions:

- Formation of γ at an arbitrary position on a titanium row corresponds to the transformation of one α_2 molecule into a γ species. Correspondingly γ appearing in the immediate vicinity of a vacancy might originate from an α_1 . (1 α molecule transformed).
- Formation of β +vacancy corresponds to the transformation of an α_2 followed by the immediate uptake of a surface bridging oxygen atom to create the β species. (1 α molecule transformed).
- Formation of $\gamma\gamma$ species at an arbitrary position corresponds to an encounter between two α_2 molecules and the subsequent transformation to chemisorbed $\gamma\gamma$. (2 α molecules transformed).
- Formation of β' and concurrent healing of a vacancy corresponds to the encounter of a single α_2 molecule with an α_1 molecule in a vacancy (1 atom fills the vacancy, the three others constitute the β' species). (2 α molecules transformed).
- Formation of $\beta\beta$ species corresponds to the encounter of three α_2 molecules. (3 α molecules transformed).

We thus find that all species appearing on the surface during or after oxygen exposure are consistent with a model where one or several physisorbed α species meet and transform into the β and γ complexes. Depending on the number of α molecules, different oxygen species will be formed on the surface as indicated above and illustrated in Fig. 6.10. The appearance of other oxygen complexes like $\beta\gamma$ or even larger clusters may be rationalized within the same model, but we have found no experimental evidence for the transition to such species directly from the physisorbed states. Apparently the $\beta\gamma$ species are only formed by reactions between γ and β molecules according to Eq. 6.4.

Healing of vacancies

The understanding of oxygen's ability to heal the bridging oxygen vacancies at the TiO₂(110) surface is important in a general description of the chemical properties of the material. It is known that quite high oxygen exposures (300 Langmuir) are needed to heal the surface oxygen vacancies at room temperature [169,182], while much smaller

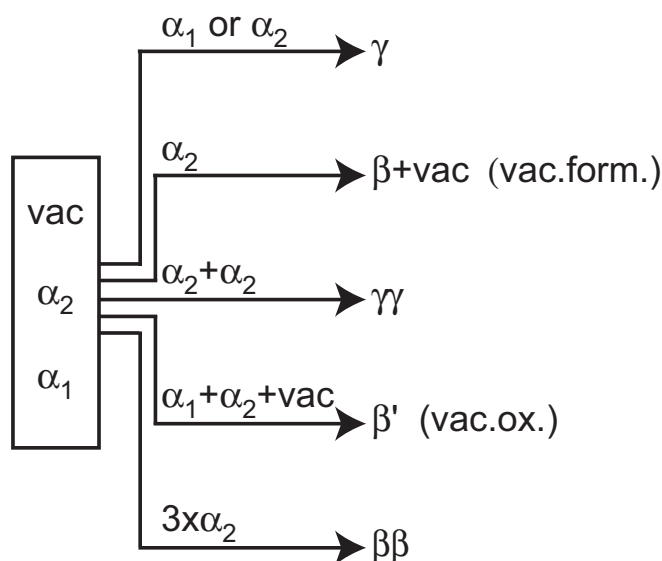


Figure 6.10: Illustration of the proposed adsorption pathways for the different observed oxygen species appearing on the surface after oxygen dosing.

doses are needed at 100 K for re-stoichiometrizing the surface in a subsequent annealing.⁵ Our STM experiments described in this chapter show that oxygen-induced vacancy healing is a complex process and that a simple picture with dissociatively filling of vacancies from single oxygen molecules is a much too simplistic model.

Of the oxygen adsorption routes and reactions presented above, only two will evidently lead to the healing of oxygen vacancies: When two α oxygen molecules meet at a vacancy and form a β' species (See Fig. 6.10), or when a $\beta\gamma$ complex encounters a vacancy and transforms into a $\gamma\gamma$ complex (Equation 6.4). Both of these processes are rather complex and involve a number of oxygen-related adsorbates. We propose that the ability of oxygen to heal surface vacancies at various temperatures should be described as a complex interplay between the various oxygen reactions on the surface, as discussed in this chapter. At varying temperatures both the rate and the equilibrium constant for the different reactions will change, and this will naturally affect the ability of oxygen to heal vacancies. At elevated temperatures the residence time in the physisorbed α state is likely to be much shorter than at low-temperature conditions, and the probability of α - α encounter is hence significantly diminished e.g. at room temperature. Looking at Fig. 6.10, we see that 2- α processes are indeed important in the route towards vacancy healing. At e.g. room temperature conditions, the production of β' species is likely to be low, and the healing of surface vacancies will therefore require larger oxygen ex-

⁵A few Langmuir is enough to saturate the surface with oxygen at 100 K [202], and a subsequent annealing to $T > 350$ K re-stoichiometrizes the surface, as seen in Fig. 6.7.

posures. It should, however, be emphasized that the discussion of room temperature results is an extrapolation of our results. We are not able to follow the fast diffusion of oxygen species at room temperature conditions, and the discussion of vacancy healing is therefore only based on low-temperature measurements. We find it likely that the oxygen-related protrusions observed by Diebold *et al.* at room temperature (Type C defects) are large β and γ -based oxygen clusters like the ones observed in our studies at low-temperature conditions, but such a hypothesis cannot, however, be proved without the ability to follow the diffusion, formation and disintegration of each single oxygen species on the surface at the relevant temperature.

TPD experiments and the nature of β species

The discrepancy between TPD experiments from the Yates and Henderson groups, respectively, may be explained by differences in the nature of the Type A defects on the crystals from the two groups. As discussed in Section 6.2.2, oxygen adsorption follows a different route when shallow protrusions are present at the surface compared to the adsorption process at a surface with bridging oxygen vacancies.

We have performed two different types of TPD experiments to investigate if the presence of the shallow protrusions influences the outcome of thermal desorption: In one experiment, a surface with a large amount of shallow protrusions (>70% of the Type A defects) was saturated with oxygen at 100 K, and in the other experiment, a surface with predominance of clean vacancies was prepared in the same way. In both cases, the surface was heated with a ramp of 2 K/s in front of the mass spectrometer. The two TPD spectra, which are presented in Fig. 6.11, clearly show a large difference: On the surface initially dominated by shallow protrusions, no TPD peak can be found, whereas the surface with initially clean vacancies exhibits a clear and well-defined TPD peak at 410 K, in agreement with the studies of Henderson and co-workers [202]. In Section 6.2.2 we showed that oxygen exposure at 100 K leads to an immediate formation of β' species at shallow protrusions, whereas annealing is needed for β species to be found on the surface if the Type A defects are dominated by vacancies (Fig. 6.3 and 6.7). In the experiments by Yates and coworkers, a relatively large amount of β species are found immediately after oxygen exposure at low-temperature conditions (see lower part of Fig. 6.7), and together with the TPD results from Fig. 6.11 we thus propose that the surface studied by Yates and co-workers may contain a large fraction of shallow protrusions.

We have not performed any spectroscopic measurements (e.g. XPS) to investigate if shallow protrusions would give rise to a different signature compared to oxygen vacancies. Such measurements would be highly interesting, because they could shed new light on the other O₂/TiO₂(110) studies existing in the literature. In the studies by Yates and co-workers, it seems, however, as if no characterization of the vacancies has been performed before the oxygen experiments [198–200], and it is therefore difficult to go into further detail about the composition of their surface.

It is impossible to follow the evolution of oxygen species with STM all the way up to the 410 K TPD peak, because the diffusion of γ species is too fast already at room temperature conditions, and a more complete explanation of the desorption process would

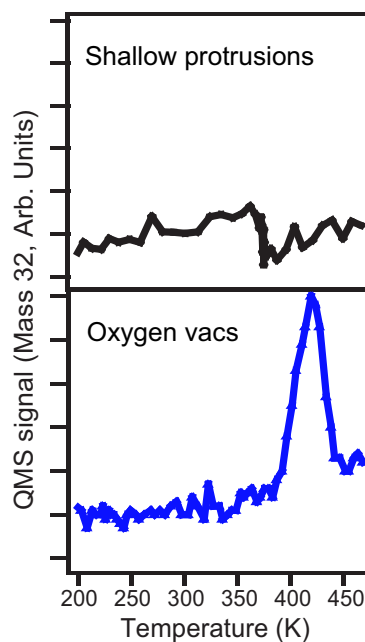


Figure 6.11: O₂-TPD spectra on two differently prepared TiO₂(110) surfaces. In one case a surface with a large fraction of shallow protrusion was investigated, and in the other case a surface with predominance of clean vacancies was investigated. The surface was saturated with oxygen at 100 K in both experiments and TPD was performed with a ramp of 2 K/s.

thus require other techniques. From the presented STM data it is, however, obvious that the desorption process must be a complicated interplay between the variety of different adsorbed oxygen species.

Neither Henderson nor Yates find evidence of isotopic scrambling with the surface oxygen in TPD and photo-desorption experiments, respectively [198–200, 202]. This finding may seem contradictory compared to our STM experiments, as we find a very vivid interaction between β , γ and the bridging oxygen on the surface. It should, however, be stressed that the *reactions* between adsorbate species discussed in this chapter have been studied at surfaces with oxygen coverages much lower than the saturation coverage. In the following section, we will see that charge transfer to the adsorbed oxygen species plays an essential role for the dynamical processes on the surface, and it is likely that the saturation of oxygen on the surface may block many of the reactions, thereby inhibiting the isotopic scrambling in the experiments performed by Yates and Henderson.

6.3.3 Summary

From the presented oxygen adsorption experiments at low and intermediate temperatures ($<RT$), we have found evidence of a range of different oxygen-related adsorbate species on the TiO₂(110) surface. Two main “building blocks”, the β and γ species, have been identified, and by scrutiny of the adsorbate dynamics and interactions we have found that all other adsorbate species may be ascribed to complexes containing combinations of the β and γ species. The γ species have previously been identified as molecular oxygen [185] and through the investigations of adsorbate interactions we find that β species contain three oxygen atoms. Further information about the nature of the β species cannot be extracted from STM studies: It may be speculated that ozone molecules are formed, but another possibility could simply be an oxygen molecule (O₂) located next to an oxygen adatom (O). Spectroscopic measurements are necessary to distinguish between such possibilities. In the literature, evidence is found for a third oxygen adsorbate species (α) formed upon oxygen exposure at low temperatures (~ 100 K). This type of adsorbate species is not revealed in STM images, and we propose that the α species are weakly bound, physisorbed molecules, which are not necessarily localized at the oxygen vacancies. The appearance of different oxygen species on the TiO₂(110) surface has been rationalized in a model, where the physisorbed α species are transformed to chemisorbed β and γ species together with larger (β,γ)-based clusters, and the ability of oxygen to heal the surface oxygen vacancies has been shown to be a complicated process which probably comprises an interplay between different types of reactions on the surface. Finally, we have provided an example of the importance of atomic-scale control of the composition of the surface when oxygen adsorption experiments are performed. With a combination of TPD and STM experiments, we have shown why apparently similar experiments may give rise to completely different results.

6.4 Diffusion of oxygen on TiO₂(110)

In Section 6.3.1 we saw that the oxygen chemistry on the TiO₂(110) surface is rather complex. Two basic constituents, the β and γ species, are the main building blocks, but at intermediate and high temperatures a large number of different reactions can occur leading to vacancy diffusion and the formation of other and more complex agglomerates. A cornerstone in the complex behavior of oxygen is the diffusion of the γ species and of the larger γ -containing clusters: All reactions presented in section 6.3.1 are based on diffusing γ species encountering other species, and the understanding of γ diffusion is therefore essential for any discussion of the oxygen chemistry on the TiO₂(110) surface. In the following, a thorough analysis of γ diffusion reveals that the diffusion process itself exhibits peculiar characteristics, which cannot be explained within standard theories of diffusion of adsorbates on surfaces. Before entering the analysis of the γ diffusion, a survey of the basic concepts of diffusion theory will be given. When such analysis is applied to our experimental data we are faced with a number of observations, which are best explained in terms of charge transfer processes between the TiO₂ conduction band and the adsorbed γ species. For this purpose a section has been devoted to the discussion of some basic semiconductor physics concepts that connect the TiO₂ defects to the

electron density in the conduction band. Through the use of such concepts, a model is derived which fits the observed data quite well, and the implication of the derived model is finally discussed in terms of general oxygen reactivity on the surface.

6.4.1 Diffusion analysis

Diffusion of adsorbed species often plays a crucial role in a large range of surface processes like chemical reactions and epitaxial film growth. In surface catalyzed reactions, adsorbed species generally diffuse to meet each other before a reaction occurs, and the importance of diffusion is even more pronounced when so-called spill-over effects between active metal particles and oxide supports participate in the reactions. In the case of Au nano-particles on TiO₂, it has for example been suggested that the oxide support serves as an oxygen supplier for the CO oxidation process whereas CO is adsorbed on the Au particles where the reaction between CO and O₂ occurs [204].

Studies of adsorbate diffusion on surfaces have been pursued by many groups over the years with a range of different techniques. The experimental techniques can roughly be divided into two groups [205]: In one group, the development of adsorbate concentration profiles is followed starting from a non-equilibrium distribution of the adsorbates. The initial concentration profile can for example be created by laser-induced desorption (see e.g. [206,207]), whereafter the migration of adsorbates to the empty area on the surface is examined. The main problem with such techniques, however, is their averaging character. The diffusion of each single adsorbate is not followed, and only the average density of adsorbates is measured over the surface. Different diffusion pathways and mechanisms on terraces, along steps or at other defect sites are therefore impossible to distinguish [205].

Another group of experimental approaches to surface diffusion comprises field ion microscopy (FIM) and STM studies of the diffusion of adsorbates. For these techniques the movement of each *single* adsorbate can be followed at the atomic scale, and the problems of distinguishing different diffusion paths are thus solved by restricting the observations to e.g. adsorbates diffusing on defect-free regions on flat terraces. The first experimental achievements along these lines were presented by Ehrlich in 1966, where FIM was used to study the diffusion of tungsten adatoms on a tungsten surface [208], and since then a large amount of FIM studies have been devoted to the atomic-scale study of the diffusion of metal adatoms on metal surfaces [209]. STM-based studies of adsorbate diffusion have also recently been pursued for a large number of systems (see e.g. [?, 210–222]), and as opposed to FIM the diffusion of non-metallic adsorbates can be investigated by STM. Diffusion data may be obtained from STM experiments by two different methods: First of all, time-resolved image acquisition in the form of STM movies can be used to acquire the position of the adsorbates at discrete time intervals, whereby a subsequent tracking analysis of each single adsorbate reveals the diffusive motion. Secondly, the motion of a single adsorbate may be followed by so-called *atom-tracking STM*, where the tip is *locked* to the position of a single adsorbate and follows the motion of the diffusing adsorbate by a dedicated lateral feedback loop (see e.g. [212, 216, 222]). The latter method have some advantages in that the time resolution may be improved dramatically compared to conventional STM movies; on the other hand,

problems concerning tip-adsorbate interactions may arise since the tip is restricted to a confined area close to the investigated adsorbate (see e.g. [222]). In the studies presented in this thesis, we have used conventional STM movies to track the diffusion of several oxygen molecules simultaneously.

Fig. 6.12 illustrates the basic concepts of surface diffusion. Adsorbates are located in energy minima on the surface, and potential energy barriers must be overcome to move from one adsorption site to another. The adsorbate state with the highest energy on the path between two neighboring energy minima is called the transition state (TS), and the energy barrier, E_d , is thus the difference between the transition state energy and the adsorption energy. Usually the energy required to overcome the diffusion barrier is gained from a coupling to the phonon bath of the crystal, whereby thermal energy is transferred to the adsorbate. If the thermal energy is much smaller than the diffusion barrier, $k_B T \ll E_d$, the particle spends most of its time in the ground state adsorption sites (GS), and all memory effects of hopping direction are thus lost between each jump. For such cases, the diffusion is well-described by a random walk process, which can be modelled mathematically by a Poisson process with a mean hopping rate, h [223, 224]. The probability that an adsorbate will perform N jumps during a certain time, t , is given by:

$$p(N) = \frac{(ht)^N e^{-ht}}{N!}, \quad (6.7)$$

and especially the probability of not jumping at all in a given time has the simple expression:

$$p(0) = e^{-ht} \quad (6.8)$$

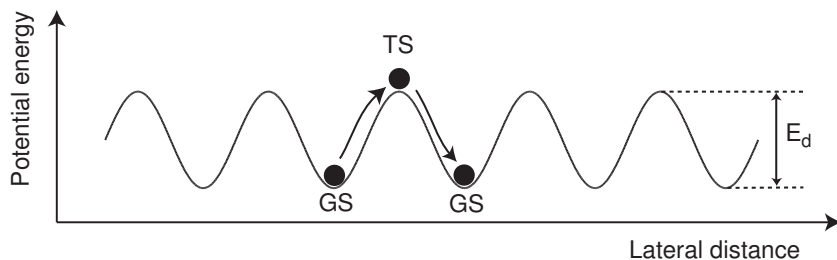


Figure 6.12: Illustration of the conceptual basis of diffusion analysis. Most of the time, the adsorbate is situated in one of the potential energy minima (or ground states, GS) on the surface, but from time to time it performs a “jump” to a neighboring energy minimum. The transition state (TS) is defined as the state with the highest energy on the path along the potential energy surface leading from one adsorption site to another.

The mean hopping rate, h , is closely related to the energy barriers and nature of the diffusion process, and, like other activated processes, it generally follows an Arrhenius equation (see Section 3.2):

$$h = h_0 e^{-E_a/k_B T}. \quad (6.9)$$

The energy barrier for a given diffusion process is thus readily extracted from the diffusion data if the mean hopping rate can be determined. Equation 6.8 suggests a simple way of evaluating h , but as illustrated in Fig. 6.13, STM does not necessarily capture all hopping events, and uncritical usage of Eq. 6.8 would thus lead to erroneous conclusions. STM is a discrete technique, which samples the position of adsorbates with time-lapsed STM images (indicated by the vertical arrows in Fig. 6.13), and the observation that an adsorbate is located at the same site in two consecutive images does not allow the conclusion that no jump has been performed between the two images. The statistical treatment of displacement distributions obtained by discrete sampling of adsorbate positions has been developed in detail by Ehrlich and co-workers [224, 225]. In general, diffusion with different jump lengths can be considered, i.e. diffusion where not only nearest-neighbor jumps contribute but also jumps of several lattice constants, so-called long jumps (see e.g. [210, 218, 225]). In this thesis, however, only single-jumps between nearest-neighbor sites will be discussed.

The lower part of Fig. 6.13 illustrates a displacement distribution that can be obtained from the STM data; P_x is the probability for an adsorbate to be displaced the distance x in the time t between two consecutive images. The displacement distribution can also be calculated analytically taking into account that many different diffusion paths may lead to the same “net displacement”, x . Following the analysis by Ehrlich [224], the displacement probability can thus be expressed as

$$P_x = \sum_{N=0}^{\infty} p_x(N) p(N), \quad (6.10)$$

where $p_x(N)$ is the probability of finding an adsorbate having a displacement x after a time interval t during which it has made N jumps, and $p(N)$ is accordingly the probability of performing the N jumps [224]. By letting the sum run from zero to infinity, any possible number of jumps giving rise to the displacement x are accounted for.

The probability $p_x(N)$ is given by the binomial expression

$$p_x(N) = \left(\frac{1}{2}\right)^N \frac{N!}{\left(\frac{N+x}{2}\right)! \left(\frac{N-x}{2}\right)!} \quad (6.11)$$

and the probability of performing N jumps is given by the Poisson distribution (Eq. 6.7). By inserting into equation 6.10 we get:

$$P_x = e^{-ht} \left(\frac{ht}{2}\right)^x \sum_{k=0}^{\infty} \frac{\left(\frac{ht}{2}\right)^{2k}}{(k+x)! k!} = e^{-ht} I_x(ht), \quad (6.12)$$

where the substitution $N = 2k + x$ has been used to simplify the expression. I_x is the modified Bessel function of the first kind of order x , and a closed analytical expression

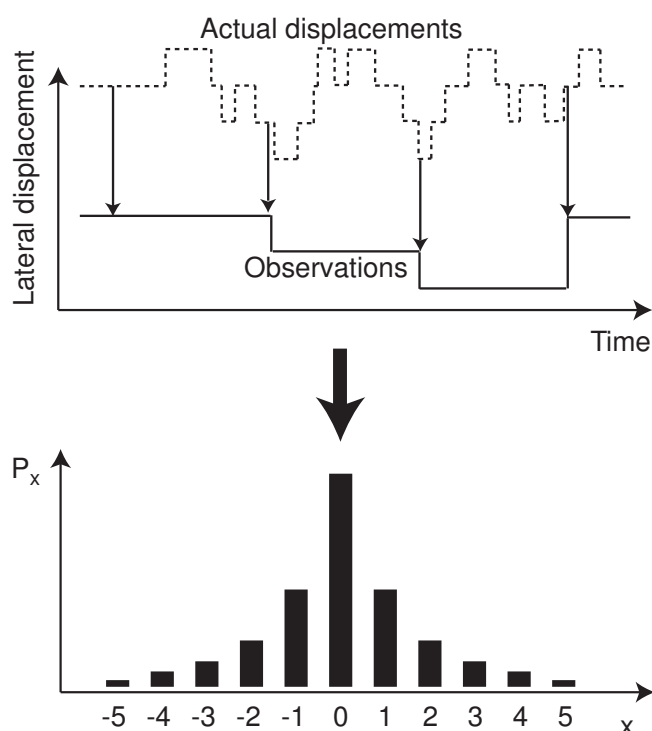


Figure 6.13: STM movies sample the adsorbate positions discretely as illustrated with the arrows. Some jumps may therefore not show up in the STM-based analysis. From the observed displacements (solid line) a displacement distribution can be obtained (lower part of figure), which depicts the probability for an adsorbate to diffuse the distance x (measured in units of lattice site jumps) between two consecutive images.

relating the displacement distribution, P_x , to the mean hopping rate, h , has thus been obtained.

From Eq. 6.12, the hopping rate can be obtained, and by performing experiments at different temperatures and making use of the Arrhenius equation (Eq. 6.9) the activation barrier, E_d , and pre-factor, h_0 , can be extracted. To perform a complete displacement distribution analysis, where P_x is extracted for all x is very cumbersome. It is, however, possible to choose a more facile route, where only the probability for “non-jumps” is analyzed (P_0). From Eq. 6.12, it is seen that such a single measurement is actually enough to extract the hopping rate:

$$P_0 = e^{-ht} I_0(ht) \quad (6.13)$$

A full displacement distribution analysis has been performed for a few of the data sets presented in this chapter to confirm that the hypothesis of only single jumps (no long

jumps) gives a good representation of the data. For most of the data, however, the more simple extraction of h in Eq. 6.13 has been used.

A theoretical foundation for the Arrhenius equation behavior of the hopping rate, Eq. 6.9, is provided by the so-called transition state theory [219,226]. Within this theory, the prefactor, h_0 , has been shown to depend on the partition function for the adsorbates in the ground state and transition state, respectively, and when entropy differences between the two states are neglected (as a first approximation), it amounts to $\sim 10^{12} \text{ s}^{-1}$ [219]. The prefactor, which is often called the *attempt frequency*, has been measured for a large number of diffusion processes with typical values from 10^{11} s^{-1} to 10^{13} s^{-1} , in good agreement with such simple estimates [219]. Significantly smaller values have been reported for some diffusion processes (See e.g. [227,228]), but these findings have, however, been questioned by subsequent reinterpretations [229,230].

6.4.2 Experimental results

In Section 6.3.1 we saw that the oxygen γ species diffuse on the surface, and in the following, an analysis of this diffusion will be presented based on the methods described above. The tracking of the single molecules has been performed with a semi-automatic routine, including a pattern recognition feature, whereby the pixel position of each molecule could be obtained. To obtain reliable information on the diffusion process each STM movie was drift compensated by tracking immobile features on the surface (e.g. impurity atoms or kink sites at step edges). The acquired pixel positions of the immobile features were subsequently subtracted from all other surface positions to obtain coordinates of the genuine diffusive motion of each adsorbate molecule. The diffusion of γ O₂ molecules is strictly one-dimensional along the [001] direction on the titanium rows. When the molecules encounter a surface oxygen vacancy they may, however, dissociate and flip the vacancy, and such events may eventually lead to an apparent diffusion of the γ species in the [1 $\bar{1}$ 0] direction [185]. The direct interaction with the vacancies and mediation of the vacancy diffusion is, however, excluded from the analysis, and only diffusion events in the [001] direction on the Ti rows are considered. Fig. 6.14 shows examples of STM images from a movie, where the diffusion of a γ oxygen molecule can be tracked (white circle). The density of oxygen species has been kept low in the diffusion experiments, and no effects from adsorption-induced band bending on the diffusion of the oxygen species has been observed.

Fig. 6.15 presents an example of a displacement distribution, which was obtained by tracking the γ species in an STM movie acquired at 222 K with a scanning speed of 2.78 seconds per image. The distribution has been fitted with Eq. 6.12 and a good agreement is seen to exist between the fit and the data, indicating that single jumps are the predominant hopping mechanism (see the discussion in Section 6.4.1). Within the uncertainty bars the distribution is symmetric, thus indicating that the interaction between the tip and the oxygen molecules is sufficiently weak that no preferential (tip-induced) hopping direction can be observed. Furthermore, we have investigated the oxygen diffusion at a range of different tunneling resistances,⁶ and we find no dependence of the hopping rate

⁶The tunneling resistance is defined as the ratio between the bias voltage and the tunnel current. The current has been varied in the range from 0.05 to 0.2 nA and the bias voltage was fixed at 1.25 V

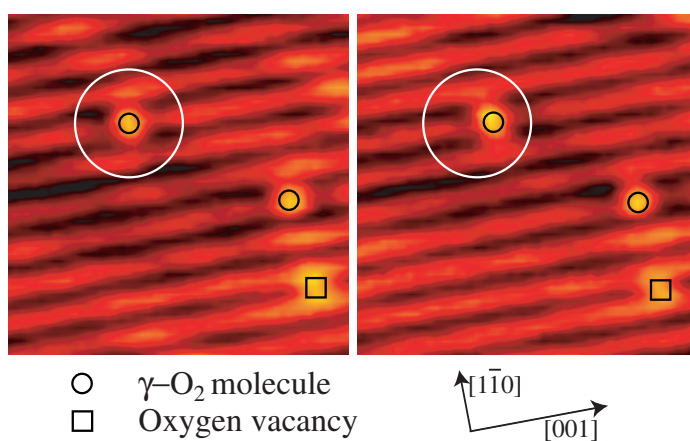


Figure 6.14: Two consecutive STM images ($65 \times 65 \text{ \AA}^2$) from an STM movie showing the diffusion of a γ oxygen molecule along the $[001]$ direction on the Ti row. $T=240 \text{ K}$.

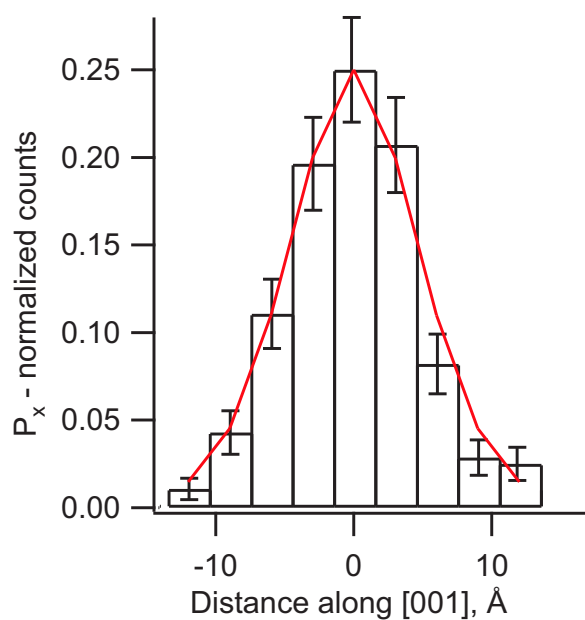


Figure 6.15: Displacement distribution obtained by tracking the γ molecules in an STM movie acquired at 222 K. The scanning speed in the movie was 2.78 s/frame and a total number of 280 diffusion events have been analyzed in the presented graph.

on the tunneling parameters within the investigated range. We therefore conclude that the observed diffusion is genuine for the molecules and is not influenced by the presence of the tip.

Analysis of STM movies acquired at different temperatures, T , leads to the data presented in the Arrhenius plot in Fig. 6.16, where the logarithm of the hopping rate is plotted versus $1/T$. All experimental data points follow a general linear trend in the graph, and from a fit to Eq. 6.9 an activation barrier of ~ 0.3 eV and a prefactor of $\sim 10^6$ s⁻¹ are extracted. The prefactor is very low compared to what is expected from standard phonon-activated diffusion theory (typically $h_0 \sim 10^{12}$ s⁻¹, as mentioned in Section 6.4.1), and furthermore, the statistical scatter of the measured γ -O₂ hopping rates is rather large, thus indicating that other sample characteristics might influence the O₂ dynamics.

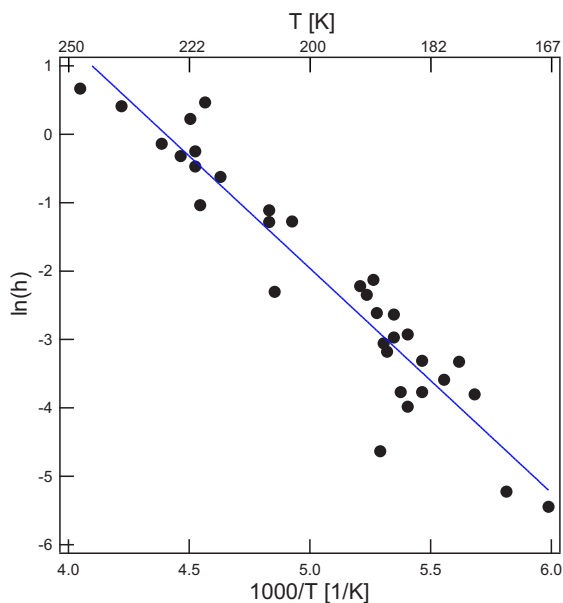


Figure 6.16: Arrhenius plot of the hopping rate for γ oxygen species on $\text{TiO}_2(110)$. A fit with the Arrhenius equation (blue line) yields an activation energy of ~ 0.3 eV and a prefactor of $\sim 10^{-6}$ s⁻¹.

By scrutinizing the data in Fig. 6.16 we find that the hopping rate depends on the concentration of surface oxygen vacancies: The more vacancies on the surface, the higher the hopping rate at a given temperature. We have analyzed the O₂ diffusion as a function of the distance from the diffusing γ molecules to nearby vacancies, but within the experimental uncertainty we find no evidence of any change in the hopping rate close to the vacancies as compared to the hopping rate at larger separations. The hopping rate is homogeneous on the surface, and the modifications induced by changing the vacancy

density are therefore concluded not to be a local effect (only affecting molecules in the vicinity of vacancies) but rather a general modification of the surface properties.

We note that this finding resembles the effect of vacancies on the oxygen *adsorption* at low temperature: In Section 6.3.1, we found that the role of oxygen vacancies on the adsorption of oxygen species is best described as a general modification of the surface properties, rather than a local model where the vacancies serve as (the only) adsorption sites for the adsorbates. As discussed in that context, the charging of oxygen molecules is probably highly important for the adsorption, since the low density of electrons in the conduction band of semiconductors, like TiO₂, is one of the properties that differentiates such materials from metals. The electron density in the conduction band of TiO₂ is governed by the chemical potential, which has an energy close to the midpoint between the vacancy donor states and the conduction band minimum.⁷ Returning to the Arrhenius plot in Fig. 6.16, we observe that the activation energy for oxygen hopping has a value (~ 0.3 eV) which is close to the energy difference between the chemical potential and the conduction band ($\sim 0.75/2$ eV $\simeq 0.38$ eV [167, 182, 184]), and this finding, together with the non-local effect of the vacancies and the peculiarly low prefactor, indicate that the investigated diffusion process may be strongly coupled to the electronic properties of the TiO₂ crystal instead of the ordinary coupling to the phonon-bath. To develop a simple model based on such ideas, the basic concepts of electronic properties of semiconductors will be briefly reviewed in the following section. An expression correlating the density of vacancies with the electron density in the conduction band is derived, and this expression is subsequently used for the modelling of our experimental data.

6.4.3 Electron densities in semiconductors

When discussing the electron density in solids, the chemical potential, μ , plays a crucial role through the Fermi-Dirac distribution. The density of electrons in the conduction band of TiO₂ is thus given by

$$n_c = \int_{\epsilon_c}^{\infty} d\epsilon g_c(\epsilon) f_{FD}(\epsilon) = \int_{\epsilon_c}^{\infty} d\epsilon g_c(\epsilon) \frac{1}{e^{(\epsilon-\mu)/k_B T} + 1} \quad (6.14)$$

where g_c is the density of states in the conduction band, ϵ_c is the conduction band minimum, f_{FD} is the Fermi-Dirac distribution and μ is the chemical potential [64]. At $T=0$ K the chemical potential in metals is identical to the Fermi energy, but for semiconductors the concept of a Fermi surface is ambiguous and therefore reference is usually only made to the chemical potential although the name Fermi level is also seen from time to time.

For semiconductors as TiO₂, a good approximation is the so-called non-degeneracy approximation: When the chemical potential is far away from the conduction band minimum compared to thermal energies (i.e. $k_B T \ll \epsilon_c - \mu$) the Fermi-Dirac distribution is well described by simple Maxwell-Boltzmann statistics in the conduction band,

$$\frac{1}{e^{(\epsilon-\mu)/k_B T} + 1} \approx e^{-(\epsilon-\mu)/k_B T}$$

⁷This fact is discussed in further detail in the following section.

and in this way Eq. 6.14 can be reduced to the much simpler form

$$n_c = N_c(T)e^{-(\epsilon_c - \mu)/k_B T} \quad (6.15)$$

where N_c is given by the integral

$$N_c(T) = \int_{\epsilon_c}^{\infty} d\epsilon g_c(\epsilon) e^{-(\epsilon - \epsilon_c)/k_B T} \quad (6.16)$$

Two issues are important to notice here:

- The “prefactor” N_c has a weak temperature dependence because μ is not part of the integral. In a simple estimate a $T^{3/2}$ dependence of the integral is a good approximation.
- Equation 6.15 has an exponential term where the difference in energy between the chemical potential and the conduction band minimum is the relevant energy term.

When no donor or acceptor states are present in the band gap or when the temperature is so high that all impurity states are fully ionized, the chemical potential will be pinned close to the center of the band gap (intrinsic semiconductor), and a simple expression for the conduction band electron density can thus be derived from Eq. 6.15. The introduction of (unionized) defect states, however, moves the position of the chemical potential and thus leads to huge changes in the electron density (extrinsic semiconductor). It is indeed such effects that make TiO₂ sufficiently conducting to render studies with STM and other electron based techniques possible.

The position of the chemical potential in the TiO₂ crystal upon the introduction of an impurity donor state is readily calculated by equating the conduction band electron density, n_c , to the number of electrons which are excited from the donor level:

$$n_c(\mu, T) = N_d - n_d(\mu, T). \quad (6.17)$$

N_d is the total density of donors and n_d is the electron density in donor levels, i.e. the density of unionized donors. Eq. 6.17 does not consider band-to-band electron excitations, which is a reasonable approximation for TiO₂ that exhibits a very large band gap (3.1 eV) compared to the impurity ionization energy (0.75 eV). Both n_c and n_d depend on the chemical potential, and Eq. 6.17 therefore determines the position of the chemical potential uniquely for a given donor concentration, N_d , and temperature, T . When inserting expressions for the donor electron density⁸ and the conduction band electron density (Eq. 6.15) we arrive at the following equation:

$$N_c e^{-\beta(\epsilon_c - \mu)} = N_d - \frac{N_d}{\frac{1}{2}e^{\beta(\epsilon_d - \mu)} + 1} = N_d \frac{\frac{1}{2}e^{\beta(\epsilon_d - \mu)}}{\frac{1}{2}e^{\beta(\epsilon_d - \mu)} + 1}, \quad (6.18)$$

⁸The electron density in the donor levels follows a slightly modified version of Fermi-Dirac statistics, because only singly occupied donor levels are considered [64]. Actually two electrons are bound to each vacancy, but the second ionization potential is significantly higher (see e.g. [231]) and is therefore unimportant for the present discussion.

where the substitution $\beta = 1/k_B T$ has been invoked to simplify the expression. By collecting similar terms containing powers of $e^{\beta\mu}$ a quadratic equation is revealed,

$$[2e^{-\beta\epsilon_c}](e^{\beta\mu})^2 + [e^{\beta(\epsilon_d - \epsilon_c)}]e^{\beta\mu} + [-\frac{N_d}{N_c}e^{\beta\epsilon_d}] = 0, \quad (6.19)$$

which can be solved to give:

$$e^{\beta\mu} = \frac{-e^{\beta(\epsilon_d - \epsilon_c)} + \sqrt{e^{2\beta(\epsilon_d - \epsilon_c)} + 8\frac{N_d}{N_c}e^{\beta(\epsilon_d - \epsilon_c)}}}{4e^{-\beta\epsilon_c}} \quad (6.20)$$

Equation 6.20 is in principle exact, when only one donor type is present and when excitations from the valence band can be neglected. The equation is easily solved but no further physical insight is gained. More interestingly, though, one could consider the so-called *freeze-out* limit where $(\epsilon_c - \epsilon_d) \gg k_B T$. This is relevant for the oxygen vacancies in TiO₂ in the entire temperature range of our studies.⁹ In the freeze-out limit, power terms of $e^{\beta(\epsilon_d - \epsilon_c)}$ can be neglected except for the lowest power term, whereby Eq. 6.20 can be reduced to

$$e^{\beta\mu} \approx \frac{\sqrt{8\frac{N_d}{N_c}e^{\beta(\epsilon_d - \epsilon_c)}}}{4e^{-\beta\epsilon_c}} = \sqrt{\frac{N_d}{2N_c}}e^{\beta(\epsilon_d + \frac{\epsilon_c - \epsilon_d}{2})}. \quad (6.21)$$

The determination of the chemical potential from Eq. 6.21 follows easily:

$$\mu = \frac{1}{\beta} \ln\left(\sqrt{\frac{N_d}{2N_c}}e^{\beta(\epsilon_d + \frac{\epsilon_c - \epsilon_d}{2})}\right) = \epsilon_d + \frac{\epsilon_c - \epsilon_d}{2} + \frac{1}{2}k_B T \ln\left(\frac{N_d}{2N_c}\right). \quad (6.22)$$

The first two terms in Eq. 6.22 pin the chemical potential in the middle between the donor levels and the conduction band minimum, and the last term describes deviations from this pinning. As is seen, the position of μ depends on the *density* of donors when the temperature is above 0 K. When the donor density increases, the chemical potential is shifted upwards, and when it decreases, a downward shift of μ is found. With the derived expression for the chemical potential it is straight forward to find n_c by using Eq. 6.15:

$$n_c = \sqrt{\frac{N_d N_c}{2}}e^{-\beta(\frac{\epsilon_c - \epsilon_d}{2})}, \quad (6.23)$$

and from this equation we observe that a higher donor concentration will result in a larger prefactor without changing the exponential term in the expression for the conduction band electron density. As long as the freeze-out limit approximation, invoked above, is a good approximation, the apparent activation energy in an Arrhenius plot of conduction band electron density versus $1/T$ will be half of the ionization energy of the donor levels. This finding is an important argument for the model described in the following section.

⁹All diffusion experiments were performed below RT, where the thermal energy, $k_B T$, is 25 meV. For comparison $(\epsilon_c - \epsilon_d) = 0.75$ eV.

6.4.4 Model of O₂ diffusion

Equation 6.23 shows that the conduction band electron density, n_c , has a qualitatively similar dependency on the donor density (surface oxygen vacancies) and on the temperature as the dependency found for the hopping rate, h , in the experimental data. Both the electron density and the hopping rate increase when the vacancy density is increased at a given temperature, and both quantities follow an Arrhenius behavior with an activation energy of approximately 0.3–0.4 eV. These findings may suggest that electron transfer from the conduction band to the γ oxygen molecules facilitates the diffusion and establishes the link between h and n_c . To test this idea, we have reanalyzed the data from the Arrhenius plot in Fig. 6.16 by grouping the measured hopping rates according to the density of surface oxygen vacancies in each experiment. The grouping is shown by different colors in Fig. 6.17A. As a simple approximation for testing the validity of an electron-transfer model for diffusion, we assume that the hopping rate is linearly dependent on the conduction band electron density, i.e.:

$$h = k \cdot n_c = k \sqrt{\frac{N_d N_c}{2}} e^{-\left(\frac{\epsilon_c - \epsilon_d}{2k_B T}\right)}. \quad (6.24)$$

A possible way to test the model is hence to assume that Eq. 6.24 gives a correct description of the experimental data, whereby the donor density, N_d , can be evaluated from the prefactors. The donor density extracted in this way may then subsequently be compared to the *actual* density of bridging oxygen vacancies measured by STM, whereby the validity of the model can be assessed.

In the data analysis shown in Fig. 6.17A, we have initially determined the average activation energy for the four groups of data points. A value of 0.34 ± 0.02 eV is found, which is in good agreement with the value suggested by Eq. 6.24, $(\epsilon_c - \epsilon_d)/2 \simeq 0.38$ eV. By fitting each data series with an Arrhenius equation where the activation energy is fixed to this average value (as suggested by Eq. 6.24),¹⁰ the prefactors are extracted as a function of vacancy density (the grouping of the data points). It is impossible in this simple model to obtain an absolute value for the donor density, N_d , since we have no way of evaluating, e.g., the cross section for electron transfer from the conduction band to the γ oxygen molecules. By squaring the prefactors, a quantity can, however, be derived which is proportional to the donor density. This gives us a relative measure of N_d , which is plotted versus the measured density of bridging oxygen vacancies in Fig. 6.17B. At high vacancy densities ($\geq 5\%$) a linear relation between the donor density, N_d , and the density of vacancies is found, which shows that the model gives a good description of these data: The electron density is determined by the number of bridging oxygen vacancies, and the hopping rate of the γ oxygen molecules is proportional to the electron density.

Deviations from linearity are found at low vacancy densities, which indicate that the simple model suggested here cannot account for all of the experimental data. It is, however, important to bear in mind that other defect states in the subsurface region may also

¹⁰The N_c term in Eq. 6.24 exhibits a weak temperature dependence according to Eq. 6.16. This has been included in the fitting.

influence the properties of the diffusion. When the density of (surface) oxygen vacancies is low, other defects may particularly govern the electronic properties in the surface region, and the deviations are therefore expectable. A more thorough explanation of the offset therefore calls upon computationally more advanced models and measurements of the subsurface properties with other techniques than STM. From the plot in Fig. 6.17, however, we conclude that our experimental data are in good agreement with a model where electron transfer from the conduction band to the γ oxygen molecules governs the diffusion. Furthermore, the bridging oxygen vacancies are found to dominate the electronic properties at the surface when the density of these is $\geq 5\%$.

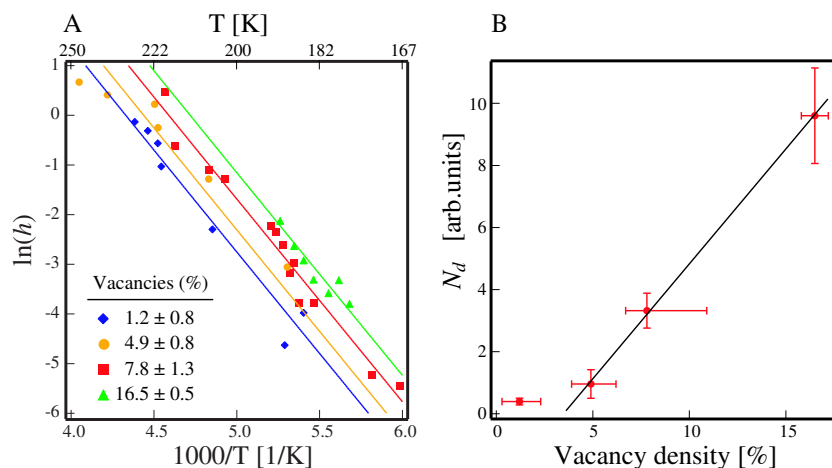


Figure 6.17: Diffusion data for O_2 molecules on the $\text{TiO}_2(110)$ surface as a function of vacancy density. (A) Hopping rate of the molecules as a function of temperature. The four lines are the fits according to Eq. 6.24 to the data originating from different oxygen vacancy concentrations assuming the same averaged activation energy of 0.34 eV. (B) The (relative) donor density, N_d , extracted from fits displayed in (A) plotted against the surface oxygen vacancy concentration found from STM images.

One may speculate about the actual effect of the electron transfer on the diffusion process of the adsorbed oxygen molecules. A possible explanation of the diffusion could be that the barrier for diffusion of oxygen molecules becomes significantly lower upon the transfer of an extra electron from the conduction band. The (charged) oxygen molecules would thus perform several jumps before the electron leaves the molecule again. The displacement distribution shown in Fig. 6.15, however, suggests that the diffusion process consists of single jumps to nearest-neighbor sites, and the idea of fast diffusing charged species is therefore somehow dubious.

We propose another model where the electron transfer results in a change in equilibrium position of the oxygen molecules whereby hopping is enabled: In Section 6.3.1 we found that γ species are adsorbed in on-top sites at the Ti rows (see Fig. 6.6). The

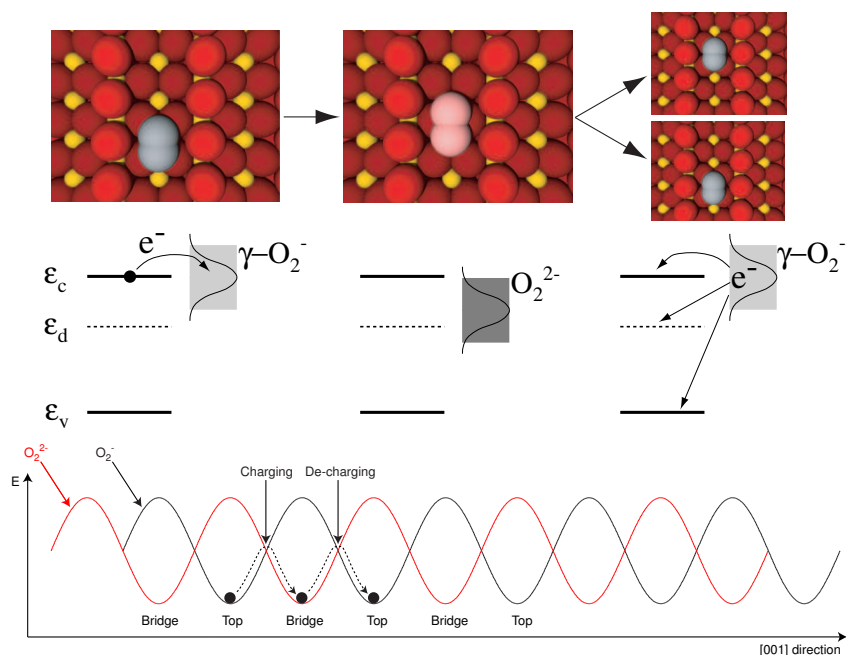


Figure 6.18: Ball model illustrating the presented diffusion model. Charging of the γ oxygen molecules leads to a shift in equilibrium position, and subsequent decharging results in a net motion of one (or zero) lattice constant. The γ molecules are described as single-charged molecules in the figure, and the electron transfer thus leads to a double-charged oxygen molecule. The lower part of the figure illustrates an energy diagram with two different potential energy curves along the [001] direction for single and double-charged oxygen, respectively.

adsorbed γ molecules are most probably charged to some degree, and for simplicity they can be thought of as O_2^- species. One could envision that resonance states in the γ species overlap with the conduction band, and that electron transfer results in the formation of meta-stable O_2^{2-} species (see Fig. 6.18). Such double-charged peroxide molecules feel a different potential energy surface, which might have the energy minima located e.g. at the bridge sites between two Ti atoms, as sketched in Fig. 6.18. The binding of the extra electron to the oxygen molecule gives rise to an electronic state somewhere in the band gap, and decharging probably occurs on a short timescale by electron transfer either back to the conduction band, to ionized vacancies, or by attracting holes from the valence band. Upon decharging, the oxygen molecule chooses between two neighboring on-top positions resulting in a total movement of either one or zero lattice constants from the original position along the [001] direction. The model is thus in good agreement with the finding that only single jumps participate in the diffusion (Fig. 6.15). We have never observed any meta-stable intermediates at bridge

positions during the diffusion of the γ species, but the process may be too fast to follow by STM. From the scanning speed of the STM we therefore estimate an upper time limit for the charging and discharging process of ~ 5 ms.

6.4.5 Diffusion of larger oxygen clusters

Not only the γ molecules are diffusing on the TiO₂(110) surface. The β , and $\beta\beta$ species are immobile, but all larger complexes containing one or more γ molecules are diffusing, and the hopping can be tracked in a similar way as for the γ species above. The statistics is, however, scarce; The larger clusters typically disintegrate after a few hopping events or react with each other and form new species. In a few cases, though, the diffusion of the larger species can be tracked, and these data have been plotted in an Arrhenius plot in Fig. 6.19 together with the γ diffusion data from Fig. 6.16.

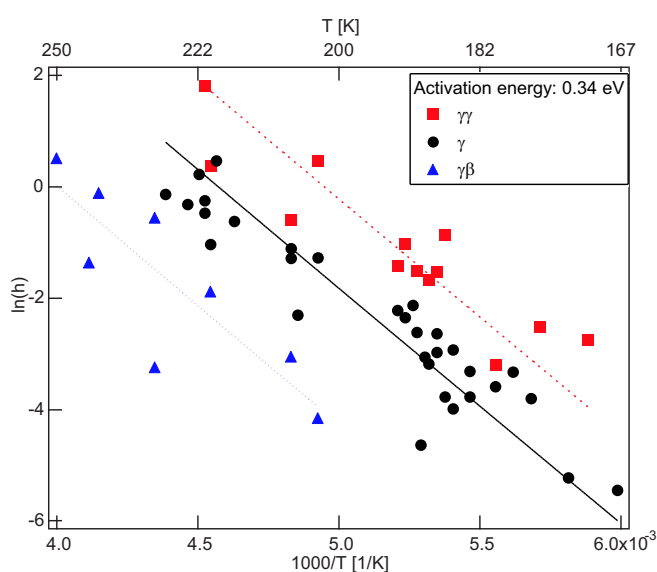


Figure 6.19: Diffusion data for the larger oxygen complexes, $\gamma\gamma$ and $\gamma\beta$, compared to the diffusion of the γ species. The 0.34 eV activation barrier extracted for γ diffusion is in good agreement with the diffusion of $\gamma\gamma$ and $\gamma\beta$ species. The prefactors are, however, different.

The Arrhenius plot indicates that the diffusion of the larger species follows similar trends as the γ diffusion discussed above. The amount of data is too small to perform a detailed analysis on the dependency of vacancy concentration, but we note that the extracted activation energy from the γ diffusion is in reasonable agreement with the experimental data for the larger complexes. The extracted data therefore interestingly suggest that the diffusion of larger clusters may also be governed by electron transfer from the conduction band to the adsorbates. In spite of the scattering due to variations

in the vacancy density it seems as if the prefactors for the diffusion of each type of adsorbate is different, thus indicating that the cross section for electron transfer depends on the type of adsorbate.

If we go a step further, we may also consider other oxygen reactions on the TiO₂(110) surface. In addition to diffusion, the reaction of $\gamma\gamma$ or $\gamma\beta$ species with the bridging oxygen vacancies is of great importance for the oxygen chemistry on the surface. The statistics of such reactions is too small to extract any rate information for an Arrhenius plot, but we note that the reactions are observable with STM over a large temperature interval similar to the range of temperatures where γ diffusion is observed. The fact that the same large temperature range constitutes the “active” range, both for diffusion of oxygen species and for reactions between the species, indicates that all oxygen-related processes on TiO₂(110) may be governed by electron transfer from the conduction band. If this is the case, large implications for the understanding of oxygen reactivity on the TiO₂(110) surface - or maybe even on oxide surfaces in general - may result from our experimental findings presented above. In the following section, such ideas and perspectives are considered as an outlook on the presented TiO₂ studies.

6.5 Outlook - modifying the reactivity

As discussed in the introduction to this chapter, oxygen chemistry on TiO₂ is relevant for a range of applications, especially within the field of oxidation catalysis. As for other catalysts, it is of course of general interest to gain insight into the elementary steps at the atomic-scale level, and in that respect the studies presented above strongly indicate that new and scientifically fascinating phenomena may govern the elementary steps of the oxygen chemistry on TiO₂(110). A major goal within surface science is to be able to use the acquired knowledge to design new and better catalysts which could eventually be used in industrial applications. In Chapter 5, we saw that catalyst modification could be achieved by the blocking of special active sites, whereby specific elementary steps could be selectively inhibited. The discussions in Chapter 3 described other suggestions for the design of new catalysts where the general idea was based on “*d*-band engineering”, i.e. modifications of the *d*-band position with respect to the Fermi level in order to change the bond strength between a given surface and the relevant adsorbates.

On the TiO₂(110) surface we have found that completely different electronic properties apparently control the reactivity of the surface: As opposed to metal surfaces, the availability of charge in the conduction band is a major issue on large-band-gap semiconductors, and the energy difference between the chemical potential and the conduction band minimum is therefore particularly important for the surface chemistry. When considering new ideas for modifying the reactivity of oxide surfaces, it may thus be feasible not only to think in terms of localized “active” sites, but also to consider ways of altering the position of the chemical potential at the surface. Much of the recent work on TiO₂(110) has focused on surface oxygen vacancies as being the active sites for a range of processes [160, 179], and the concept of active sites is without doubt also relevant on oxide surfaces. However, a new dimension may be added by considering general modifications of the surface electron density by means of “chemical potential engineer-

ing". In the semiconductor industry a range of technologies are available, enabling well-controlled doping of crystals with impurity atoms. In this way either n-type or p-type semiconductors are routinely created, and these materials are subsequently used in the transistors which constitutes the main building blocks in our computer-based information society. It would be highly interesting to use similar methods to dope TiO_2 crystals with impurity atoms, whereby the position of the chemical potential would be altered. The prospects are manifold: The reactivity may be strongly increased by dopants introducing donor levels close to the conduction band, and unreactive $\text{TiO}_2(110)$ surfaces may be formed by the introduction of acceptor levels which cancel the effect of the vacancies.

Concerning the role of TiO_2 as a support for Au nanoparticles in oxidation catalysts, the presented results will evidently have a high impact, both on the understanding of the role of the support and concerning new ideas for improving the catalysts. Recently, it was shown by Schubert *et al.* that reducible metal-oxide supports serve as an oxygen reservoir for the oxidation reactions on supported Au nanoparticles [204]. Our results indicate that the modifications of the chemical potential by the oxygen vacancies may play a key role in that respect by enabling both the adsorption (availability of charge for the creation of chemisorption bonds) and the subsequent diffusion of the oxygen species. Adsorption and migration of oxygen species are indeed important issues if the role as oxygen reservoir is to be improved for TiO_2 .

CHAPTER 7

Surface oxide formation on platinum

This last chapter describes preliminary results from a pilot study of high-coverage oxygen structures on platinum surfaces. Using scanning tunneling microscopy (STM) and temperature programmed desorption (TPD), we have investigated the behavior of the Pt(110) surface under strongly oxidizing conditions involving either high-pressure O₂ or atomic oxygen exposure. At low temperatures, only disordered structures are observed by STM, and from TPD studies these are associated with an unordered platinum oxide phase. When exposing the Pt(110) surface to oxygen at higher temperatures, however, ordered islands of a surface oxide are observed to coexist with a highly stable reconstructed (12 × 2)-O chemisorption structure. A comparison of the experimental findings to DFT calculations confirms the existence of a meta-stable surface oxide structure in good agreement with the STM images.

7.1 Motivation

The understanding of the formation of oxides on transition metal surfaces is of interest in many disciplines including surface coatings and heterogeneous catalysis. The growth of oxide phases is in general known as corrosion and is, in that respect, most often an unwanted process. Within catalysis, however, oxidation of metals may be of great importance for the reactivity, and a number of recent studies have therefore focused on the initial stages of oxide growth on single-crystal metal surfaces [37, 38, 232–244]. The role of metal oxidation in catalysis has especially been emphasized in recent studies of CO oxidation on ruthenium [37]. Under UHV conditions, ruthenium is a poor oxidation catalyst due to a strong chemisorption bond of oxygen to the surface, but at high oxygen pressures an oxide phase is formed, which is even better than Pt as a catalyst for CO oxidation [37]. The oxide is believed to participate in the oxidation of CO in a so-called Mars-van-Krevelen type oxidation/reduction cycle, where oxygen atoms from the oxide react with CO to form CO₂, and where the oxygen vacancies thus created are continuously replenished with oxygen from the gas phase. For many catalytic oxidation processes the binding energy of oxygen on the catalyst should be as low as possible, and the Mars-van-Krevelen mechanism may therefore open up new catalytic reaction routes in cases where the oxygen binding energy in the oxide phase is lower than in a chemisorbed phase on the metal surface.

Platinum is one of the technologically most important catalyst materials for oxidation processes [1], but the fundamental understanding of platinum-based oxidation catalysis is, however, still scarce, and one of the open questions is whether a surface oxide is formed on platinum surfaces during high-pressure reaction conditions, and whether such an oxide would enhance the catalytic activity similar to the effect found for ruthenium oxide [39]. The late transition metals are, in general, more resilient towards oxidation, and for e.g. silver, rhodium and palladium, thin surface oxides have primarily been found upon high-pressure oxygen exposure on single crystal surfaces [233, 234, 236, 239, 245] as opposed to the multilayer oxide growth found for the more reactive metals in the left part of the transition metal group. Two types of platinum oxides are known to exist, PtO and PtO₂, the latter in two different forms, α -PtO₂ and β -PtO₂ [246]. Nevertheless, the mere existence of (bulk) platinum oxides does not necessarily lead to the formation of similar structures on metallic platinum surfaces under oxidizing gas conditions. Kinetic restrictions may hinder the growth of oxides even if the bulk oxide phase is thermodynamically favorable [234].

In a recent study of CO oxidation on Pt(110) at high-pressure conditions, the evolution of surface structures was followed with STM while the gas composition was simultaneously monitored with a mass spectrometer [39, 247, 248]. A bistable behavior was revealed for the CO₂ production as a function of oxygen pressure, and the rate of CO₂ formation exhibited a discontinuous jump to a higher value when the pressure ratio between the two reactant gasses was increased above a certain threshold value. Such bistable behavior of the reactivity is well-known for CO oxidation on platinum surfaces both under UHV and at high-pressure conditions, and it has previously been rationalized in terms of a kinetic phase transition between the low reactivity on a mainly CO-covered surface at high CO partial pressures (CO poisoning) and the higher reactivity on a mainly

oxygen-covered surface [249]. The increased reactivity for CO oxidation observed by Hendriksen *et al.* [39] was, however, followed by an increase in surface roughness, and they therefore concluded that the higher reactivity was caused by the formation of a surface oxide layer, which subsequently participated in the CO oxidation reaction via the Mars-van-Krevelen mechanism. The continuous removal and replenishment of oxygen in the oxide phase was proposed to lead to the roughness observed in STM after running the reaction for an extended time at the high oxygen pressure conditions. Even though the unique combination of gas analysis and structural determinations presented in [39] provided new insight into the CO oxidation on Pt(110), the lack of atomic resolution of their STM inhibited any detailed investigation of the proposed reactive oxide phase.

In the studies presented in this chapter, we have used STM and TPD experiments to investigate the atomic-scale details of the oxidation of Pt(110). As we will see below, the formation of ordered surface oxide structures is only possible at temperatures above ~ 500 K. The temperature in our high-pressure cell is, however, limited to ~ 380 K, and most of the presented results have therefore been acquired by exposing the Pt(110) surface to atomic oxygen in the UHV chamber. In this way the surface temperature could be controlled (300–600 K) during oxygen exposure. The chemical potential of atomic oxygen is very high, and *effective* high pressures of oxygen could therefore be obtained at UHV compatible pressures.

7.2 Previous studies

When the Pt(110) surface with its characteristic missing-row reconstruction (see Fig. 4.1) is exposed to molecular oxygen at UHV conditions, a variety of complex adsorbate-induced structures are found. These structures have recently been investigated by TPD and LEED [250] and by STM experiments combined with DFT calculations [251, 252]. Oxygen adsorbs dissociatively on the Pt(110) surface at room temperature and the preferred binding site for the atomic oxygen adsorbates are found to be the fcc sites on the side of the protruding ridges [251]. At low oxygen coverage and room temperature conditions, the oxygen atoms diffuse fast on the surface and are not imaged by STM. At higher coverages, however, a stripe-like structure develops, which consists of apparently higher segments of the Pt ridges, as seen with STM, aligned along the [001] direction with a periodicity of 10–14 lattice constants along the $[1\bar{1}0]$ direction. The coverage of the stripe structure grows as a function of oxygen exposure, and saturates when the entire surface is covered by protruding stripes except for a few Pt atoms in-between the stripes [252]. The super-cell periodicity of the oxygen-induced stripes observed with STM is also confirmed by LEED studies [250]. By comparison to density functional calculations, it was concluded by Helveg *et al.* that the stripe structure consists of Pt-ridges with oxygen atoms adsorbed at *each* fcc site on both sides of the ridge, as illustrated in Fig. 7.1. The very high density of oxygen atoms, corresponding to a local density of 2 ML, is enabled by an outward relaxation of the Pt-atoms, whereby the binding energy of oxygen to the Pt atoms is increased.

Molecular beam experiments on Pt(110) by Walker *et al.* have revealed the existence of two TPD peaks, β_1 and β_2 , from dissociated oxygen, and a single TPD peak

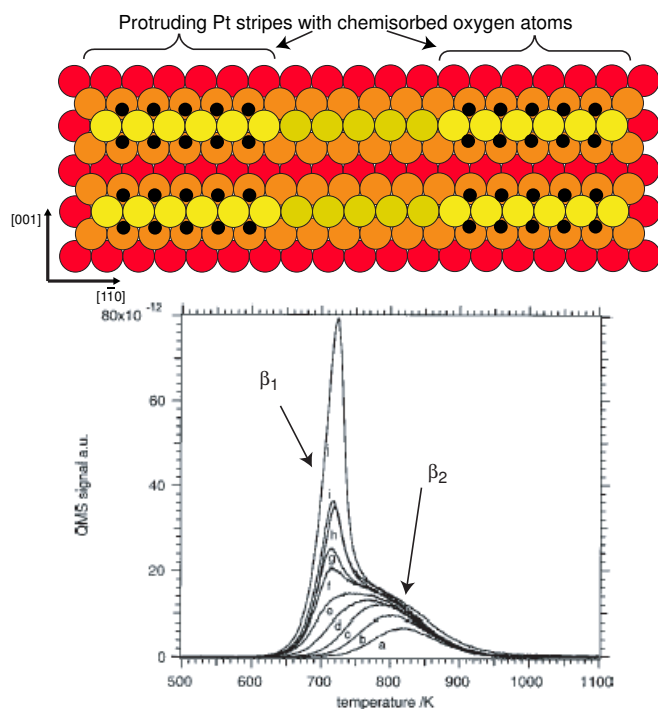


Figure 7.1: **Top:** Model of the chemisorption structure found by Helveg et al. after molecular oxygen dosing at low pressures [251, 252]. Oxygen atoms (dark filled circles) adsorb in the fcc sites below the Pt ridges, and a striped pattern is formed due to the outward relaxation of the Pt atoms. **Bottom:** $O_2/Pt(110)$ -TPD spectra reproduced from [250]. Two peaks are found from the associative desorption of oxygen, β_1 and β_2 . The β_1 peak is ascribed to desorption from the chemisorbed oxygen forming the striped structure depicted in the model above, and the β_2 peak is ascribed to oxygen adsorbed at defect sites, e.g. steps.

from molecularly adsorbed oxygen, α , at low temperatures [250]. At low oxygen coverages, only a single broad peak (β_2) is observed, which shifts to lower temperatures as the coverage is increased. At higher oxygen coverages, a sharper and apparently first order peak (β_1) appears at ~ 720 K. The two β peaks are shown in the reproduced TPD spectrum from [250] in Fig. 7.1. The amount of oxygen desorption in the β_2 peak depends on the preparation conditions of the crystal. By quench-cooling the crystal after annealing, a larger peak area can be obtained, and the β_2 peak has therefore been associated with oxygen adsorption at defects or steps on the surface [250]. The β_1 peak, on the other hand, is associated with oxygen desorption from the stripe structures.

The existence of oxygen phases on platinum surfaces with even higher coverages than the (local) 2 ML chemisorption phase have been studied either during the catalytic

CO oxidation, where workfunction changes indicate the existence of subsurface oxygen species (see e.g. [253, 254]), or by ozone exposure [255] or prolonged oxygen dosing [256], the two latter methods leading to additional low-temperature peaks in the O₂-TPD spectrum compared to the TPD spectrum depicted in Fig. 7.1. No detailed structural information has, however, been obtained from such studies.

7.3 High-coverage oxygen structures

In the following, we present STM and TPD results on the formation of high-coverage oxygen structures, and based on atomically resolved STM images, a structural model for a surface oxide is derived. High-pressure oxygen dosing was performed in the high-pressure cell at temperatures up to 110°C, and atomic oxygen exposure was done with the thermal cracker described in Chapter 2. All atomic oxygen experiments were performed with a cracking power of 56 W¹ and an oxygen pressure of $\sim 10^{-7}$ mbar. The cracking efficiency for O₂ was estimated to be approximately 50% by following the mass 32 signal (molecular oxygen) on the mass spectrometer before and after the onset of cracking. As a guide for the reader, the experimental findings have been summarized in the table on page 138.

When Pt(110) is exposed to either high pressures of O₂ (>1 mbar) or to atomic oxygen at low temperatures ($T < 500$ K), a disordered overlayer structure develops as observed with STM (see Fig. 7.2). At low oxygen exposures, the structure exhibits weak ordering along the [1 $\bar{1}$ 0] direction with the Pt(110)-(1 × 2) structure discernible underneath, but with increasing exposures all traces of the original surface structure are erased.

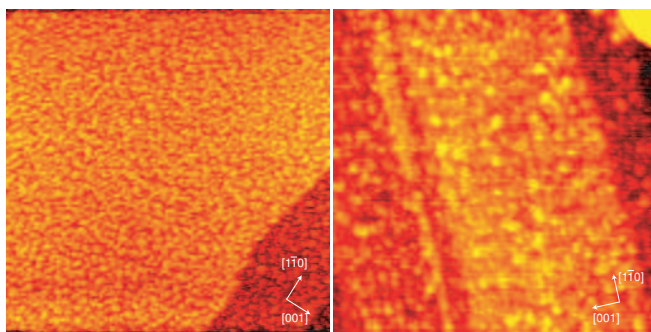


Figure 7.2: STM images showing the disordered structure which is evolving at low-temperature oxygen exposures. **Left:** High-pressure exposure, 1 mbar at 110°C for 10 minutes ($1000 \times 1000 \text{ \AA}^2$), **Right:** Atomic oxygen exposure, 5 min at RT ($500 \times 500 \text{ \AA}^2$).

¹2 kV bias voltage on the heating filaments and an electron emission current of 28 mA.

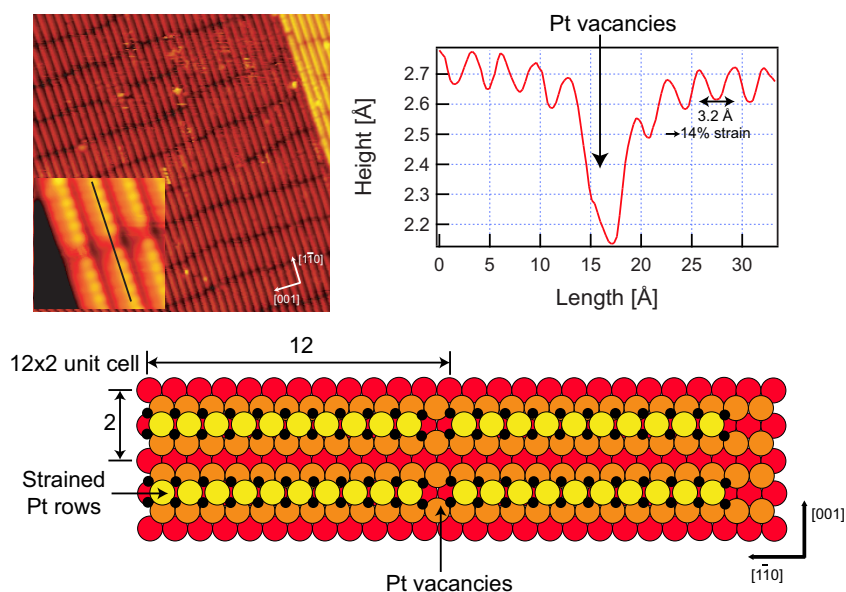


Figure 7.3: **Top:** STM image, ($300 \times 300 \text{ \AA}^2$) after atomic oxygen exposure at 600 K (60 minutes). Aligned stripes are clearly observed. Atomically resolved images (see inset, $35 \times 35 \text{ \AA}^2$ and line scan) show that the Pt atoms are strained $\sim 14\%$ along the $[\bar{1}\bar{1}0]$ direction. The holes between the stripes are accordingly assigned to Pt vacancies. **Bottom:** Schematic ball model of the strained Pt atoms enabled by the formation of Pt vacancies. The registry of the stripes with the underlying Pt crystal cannot be derived from STM images and is therefore only a tentative suggestion. It can, however, be argued that the central part of the stripes is likely to be in registry (fcc positions), as suggested in the ball model, and that close to the ends, the Pt atoms are out of registry.

New, ordered structures are, however, found on the surface after a brief annealing or when atomic oxygen exposure is performed at $T \geq 500 \text{ K}$. After atomic oxygen dosing at 600 K, the surface is completely covered by a superstructure consisting of stripes along the $[\bar{1}\bar{1}0]$ direction, which are aligned along the $[001]$ direction (see Fig. 7.3). The revealed structure resembles the oxygen-induced stripes described by Helveg *et al.* (see Fig. 7.1) [251, 252], and the observed stripes are therefore ascribed to a chemisorption phase of oxygen. STM images show that this chemisorption phase forms a (12×2) superstructure, in which each unit cell contains stripes of ~ 10 distinct protrusions, separated by $5 \pm 2 \text{ \AA}$ wide and $0.6 \pm 0.2 \text{ \AA}$ deep depressions.² Atomically resolved images reveal that the Pt atoms within the stripes are under a $\sim 14\%$ tensile strain in the $[\bar{1}\bar{1}0]$ direction compared to the nearest-neighbor distance on Pt(110). Furthermore, the depressions between the stripes are deeper and more narrow than those found in the chemisorption structures studied by Helveg *et al.*, where the Pt(110) surface remains intact and un-

²The (12×2) cell is an average unit cell. The periodicity varies between a (10×2) and a (13×2) structure.

strained [251,252,257], and it is therefore natural to assign the depressions to vacancies, where two Pt atoms have been pushed out between neighboring stripes. The remaining (strained) Pt atoms within the stripes are expected to allow for the adsorption of a total of ~ 22 oxygen atoms per stripe according to DFT calculations, as illustrated in the ball model in Fig. 7.3 [258]. We note that the surface appears slightly smoother with larger terraces after atomic oxygen exposure at 600 K compared to the clean Pt(110) surface, thus suggesting that the missing Pt atoms from the ridges (from the formation of vacancies) bind to the step edges. A very similar striped chemisorption structure has previously been observed on the Rh(110) surface after oxygen exposure [259].

When the surface is exposed to atomic oxygen at slightly lower temperatures (500 K), a mixture of structures is revealed, as seen in the STM image in Fig. 7.4. The (12×2) chemisorption structure with strained Pt atoms is still observed, but furthermore a number of small islands with a novel structure are clearly distinguished in the STM images. Stable STM imaging over these islands is only possible at a bias voltage of ≥ 1 V, which suggests that the electronic structure of the islands exhibits a band gap. We therefore assign these islands to patches of a surface oxide structure. High-resolution STM images of the islands reveal that they consist of stripes with protrusions exhibiting a $\sim 14\%$ tensile strain along the $[1\bar{1}0]$ direction similar to the stripes in the (12×2) chemisorption structure. The stripes of the novel island structures can be divided into two groups according to their $[001]$ spacing and their height:

1. The central part of the islands typically consists of stripes which are protruding $0.2\text{--}0.4$ Å compared to the surrounding chemisorption phase. These stripes are compressed $\sim 29\%$ along the $[001]$ direction compared to the Pt(110) missing-row distance (see zoom-in image and line scan in Fig. 7.4). This novel structure is ascribed to a surface oxide.
2. The other type of rows observed at the ends of the islands,³ on the other hand, are protruding ~ 1.4 Å, and the distance between the rows is ~ 7.9 Å. These rows are ascribed to second layer Pt atoms (a Pt step) with oxygen chemisorbed in the (12×2) structure, which is supported both by the height, the inter-row distance and the registry with the surrounding chemisorption structure (25% shift along the $[001]$ direction).

The surface oxide coverage is found to be $\sim 15\%$, which corresponds well to the amount of Pt removed from the lattice to form the underlying (12×2) structure (2 out of 12 Pt atoms are removed). This indicates that the surface oxide islands are formed by a rearrangement of Pt atoms ejected from the Pt ridges.⁴ In addition to the well-ordered areas exhibiting a mixture of the oxygen chemisorption phase and the surface oxide islands, a few disordered domains are also observed on the surface after atomic oxygen exposure at 500 K, a finding that is in good agreement with the TPD spectra presented below.

³Two in the left side of the presented island in Fig. 7.4 and one in the right side.

⁴The terrace sizes after atomic O exposure at 500 K are similar to the terrace sizes found on the clean Pt(110) surface thus indicating that the Pt atoms from the formation of vacancies do not diffuse to the step edges at this temperature.

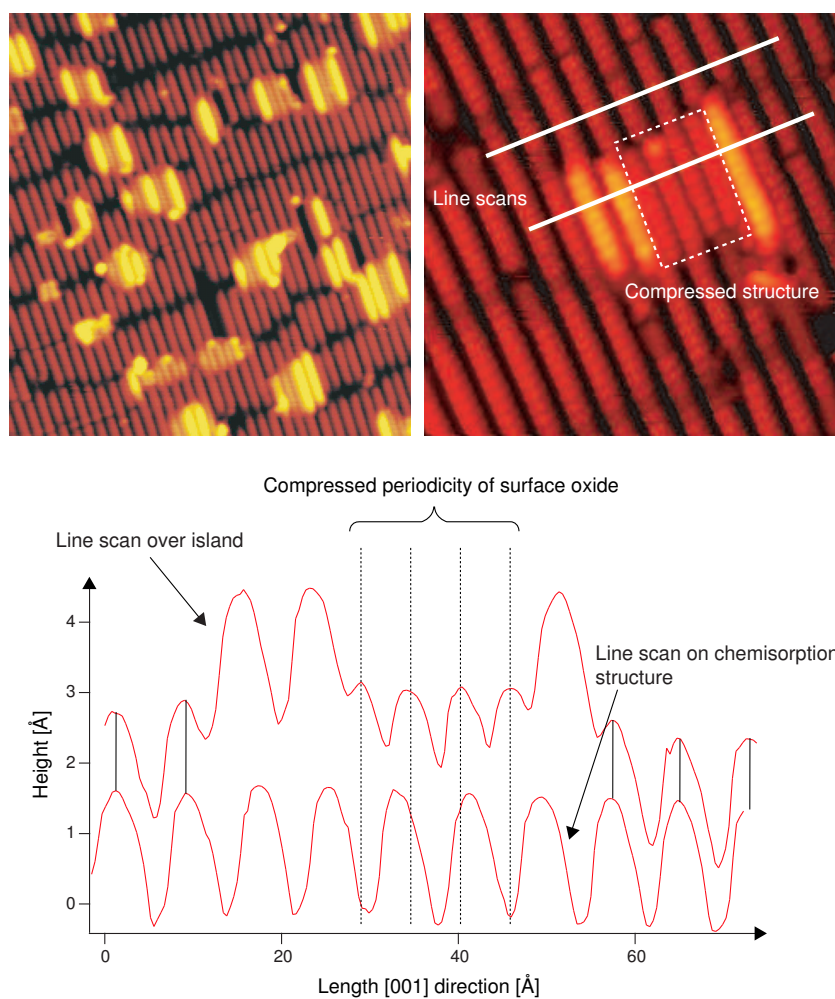


Figure 7.4: **Top:** STM images ($300 \times 300 \text{ \AA}^2$ and $100 \times 100 \text{ \AA}^2$) after atomic oxygen exposure at 500 K. The zoom-in (right) reveals a new and compressed structure of the clusters. **Bottom:** Comparison of a line scan over a cluster and a line scan on the stripe structure (chemisorption structure). The rows in the cluster are compressed $\sim 29\%$ along the [001] direction. Second layer rows are found at the end of the cluster, and the distance between these rows corresponds to the Pt(110) distance (i.e. uncompressed). It is thus likely that the highly protruding rows are simple second layer continuations of the chemisorbed structure at the end of the cluster.

Figure 7.5 displays a series of O₂-TPD spectra obtained after atomic oxygen exposure at different temperatures. The peak at 730 K with the high temperature shoulder at ~800 K corresponds to oxygen desorption from the (12×2) stripe structure and from defect sites, respectively, and these peaks are in perfect agreement with the studies by Walker *et al.* discussed above (β_1 and β_2). Such an assignment is proven by the TPD spectrum obtained after atomic oxygen deposition at 600 K (lower part of Fig. 7.5) where the β_1 and β_2 peaks are the only observable features in TPD (STM images only show the (12×2) structure after such preparations, see Fig. 7.3). This finding motivates us to use the β_1 peak for absolute coverage calibration. The total oxygen coverage associated with the β_1 peak is 1.83 ML (22 oxygen molecules per (12×2) unit cell, see ball model in Fig. 7.3).

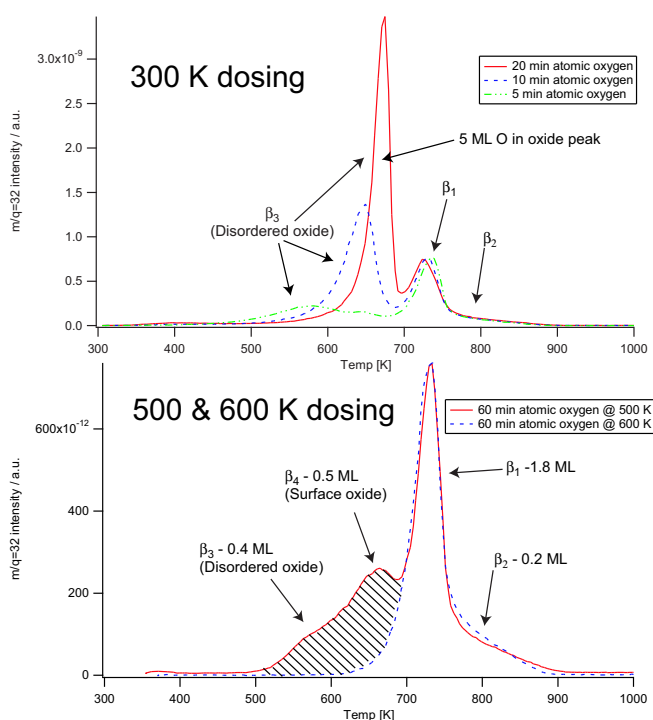


Figure 7.5: **Top:** O₂-TPD spectra after atomic oxygen dosing performed at room temperature for 5, 10 and 20 minutes, respectively. The β_1 and β_2 peaks from chemisorbed oxygen are recognized at high temperatures, and at lower temperatures a prominent oxide peak builds up from 580 K at low exposures to 670 K at higher exposures. **Bottom:** O₂-TPD spectra after atomic oxygen dosing performed at 500 K and 600 K, respectively. Only the β_1 and β_2 peaks are observed after 600 K exposure in agreement with the STM images. Upon 500 K exposure an additional peak is found at ~650 K, which is ascribed to the surface oxide islands observed with STM.

A prominent TPD peak, β_3 , is found at lower temperatures upon atomic oxygen exposures at room temperature (see the upper part of Fig. 7.5). The β_3 peak shifts from ~ 580 K at low exposures to 670 K upon increasing exposure, and at the highest oxygen exposures this peak is the main desorption peak observed in the TPD spectrum, containing an oxygen coverage corresponding to 5 ML.

When atomic oxygen exposure is performed at 500 K, another peak, β_4 , is revealed at 650 K (see lower part of Fig. 7.5). We ascribe this peak to the surface oxide structures observed with STM (Fig. 7.4) since these islands are formed at the same temperature (500 K). A substantially reduced β_3 peak is also observed as a low-temperature shoulder in the TPD spectrum after 500 K exposure, and the reminiscence of such a peak correlates well with the existence of a few disordered areas, as observed with STM. By using the island coverage of $\sim 15\%$ from the STM measurements, a local oxygen density of 3.3 ± 1.3 ML is extracted for the surface oxide islands.

| Preparation: | STM: | TPD: |
|--------------------------|--|--|
| Low-pres. O ₂ | O-induced stripes. Unstrained Pt atoms. Local 2 ML coverage. [251, 252, 257] | Two peak. β_1 (730 K) corresponds to local 2 ML structure and β_2 (~ 800 K) corresponds to defect adsorption. [250] |
| Atomic Oxygen 300 K | Disordered structures | Three peaks. β_1 and β_2 similar to above. β_3 shifts from 580 to 670 K. β_3 =disordered structures |
| Atomic Oxygen 500 K | (12 \times 2) chemisorption stripes with strained Pt atoms ($\sim 14\%$) coexisting with surface oxide islands | $\beta_1 + \beta_2$ observed (chemisorption structure). β_4 (650 K) corresponds to surface oxide island, coverage ~ 0.5 ML. Small reminiscence of β_3 . |
| Atomic Oxygen 600 K | (12 \times 2) chemisorption stripes with strained Pt atoms ($\sim 14\%$). No surface oxide islands | Only β_1 and β_2 observed. β_1 has been used for coverage calibration for the other data. |

7.4 Comparison to theoretical results

DFT calculations have been performed by Wei-Xue Li, Thorbjørn M. Pedersen and Bjørk Hammer to elucidate the origin of the structures found in our STM experiments (for details concerning the calculations, see [258]). Knowing from our STM images that the stripes in the surface oxide islands are compressed in the [001] directions, the structure and stability of a variety of platinum/oxygen stripe configurations with different

compression were investigated with DFT.

A very stable structure was found consisting of Pt-O rows, which are compressed by 25% along the [001] direction. The [001] strain for this structure is comparable to the 29% strain in the surface oxide islands as measured by STM, and the modelled structure is therefore in good agreement with the observed islands. The theoretically modelled structure is shown in Fig. 7.6 together with the line scan from the high-resolution STM image in Fig. 7.4. In the proposed model the highly protruding rows at the ends of the cluster are assigned to second layer Pt rows with chemisorbed oxygen,⁵ and the central part of the island is ascribed to a surface oxide. The oxygen content in the modelled structure corresponds to a coverage of 2.67 ML, which agrees well with the extracted coverage of 3.3 ± 1.3 ML from the β_4 peak in the TPD spectrum. The small discrepancy between the experimental 29% and the theoretical 25% compression is probably due to the neglect of the island character of the structure in the theoretical modelling.

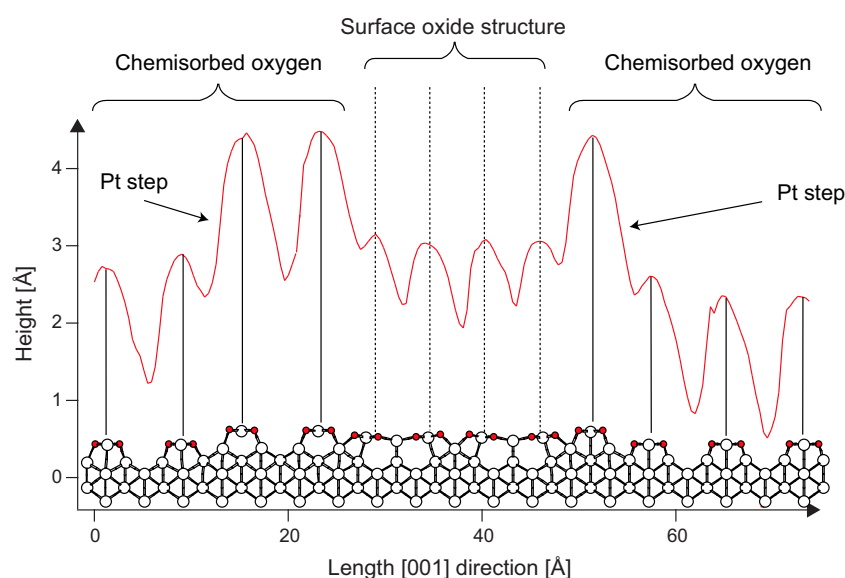


Figure 7.6: Comparison of the ball-and-stick model of the surface oxide islands suggested by DFT calculations and the line scan over one of the islands from the STM images. Good agreement between the protrusions is found. The central part of the island is ascribed to a surface oxide structure and the protruding rows at the edges are most probably second layer Pt rows, which stabilizes the structure.

⁵The (12×2) structure.

The DFT calculations have, furthermore, addressed the stability of such islands compared to the formation of bulk oxide structures or to the formation of the chemisorbed (12×2) structure. From the calculations it is concluded that the surface oxide structure shown in Fig. 7.6 is thermodynamically unstable at all temperatures and oxygen pressures compared to the (12×2) oxygen chemisorption structure or to the formation of bulk oxides. At oxygen-rich conditions and low temperatures, bulk oxides are thermodynamically favored according to the calculations, and when the temperature is increased the chemisorption structure becomes favorable. The surface oxide may, however, be stabilized by the presence of defects in the surrounding chemisorption structure, a fact which has not been considered in the theoretical modelling. An example of such defects is the second layer Pt atoms, which are formed at the ends of most of the observed surface oxide islands.

7.5 Conclusion and discussion

From TPD experiments, we have found evidence for the growth of multilayer oxide phases under oxygen-rich conditions at room temperature. The STM images of these structures, however, show no ordering, and annealing results in decomposition and formation of structures with lower oxygen coverages. At 600 K, a (12×2) oxygen chemisorption phase has been found, which resembles the structures described by Helveg *et al.* and Walker *et al.*, respectively. The characteristic stripe structure has a similar periodicity as the superstructures found upon molecular oxygen dosing at low-pressure conditions [251, 252], but Pt vacancies are formed between the stripes, thereby allowing for a relaxation of the Pt atoms along the $[1\bar{1}0]$ direction resulting in a $\sim 14\%$ tensile strain. Oxygen dosing at 500 K leads to the formation of a mixture of the chemisorption phase and small patches of a surface oxide, which consists of Pt-O rows compressed $\sim 29\%$ along the $[001]$ direction compared to the chemisorbed structure. The existence of surface oxide islands is found to be in good agreement with DFT, but the calculations, however, show that the chemisorption phase and bulk oxides are thermodynamically more stable than the surface oxide. The STM observations of these meta-stable islands are therefore probably due to kinetical limitations or stabilizing defects when the surface is prepared at 500 K.

The TPD experiments show that both the surface oxide islands and the disordered multilayer structures contains oxygen with a binding energy which is lower than the binding energy in the oxygen chemisorption phase, and it is therefore reasonable to believe that the reactivity of such oxide phases towards oxidation catalysis may be larger than the reactivity of the highly-stable chemisorbed phase of oxygen. The finding of additional low-temperature peaks (β_3 and β_4) is in good qualitative agreement with previous studies of high-coverage oxygen structures on platinum surfaces formed by ozone dosing [255] or prolonged exposure of molecular oxygen [256]. The meta-stable surface oxide decomposes between 500 and 600 K and it may therefore be of relevance in the description and understanding of catalytic processes on Pt(110) at lower temperatures. In [39] it was suggested that the rough structure found at high $O_2:CO$ pressure ratios was caused by a Mars-van-Krevelen type reaction of CO with a surface oxide, but our

measurements at room temperature, however, show that a rough, disordered structure may be formed by high pressures of oxygen alone, and we therefore find it questionable to use the roughness as an argument for such a reaction scheme.

The formation of ordered multilayer structures is a competition between kinetics, which limits the ordering at low temperatures, and thermodynamics, which renders low-coverage phases more stable when the temperature is raised. The transition temperature between the chemisorption structure and oxide formation depends on the oxygen pressure, and it would therefore be highly interesting to be able to scan in an oxygen atmosphere at e.g. 500 K. According to DFT calculations, bulk oxides of the α -PtO₂ and β -PtO₂ would form under such conditions, and the STM results presented here indicates that kinetical barriers may be overcome at such temperatures. During the UHV-based preparation with atomic oxygen at 500 K such multilayer structures, however, decompose and only the surface oxide islands and the chemisorption structure are revealed.

CHAPTER 8

Summary and Outlook

In this thesis, a number of experimental, STM-based studies have been presented, in which surface processes have been investigated as model systems with relevance for the fundamental understanding of catalytical processes. The topics discussed may be ascribed to two main categories, one of them being the investigation of the gaps between surface science studies and applied catalysis, and the other being the general concept of active sites controlling the dynamics and reactivity on surfaces. The studies of CO adsorption on platinum surfaces and on the AuNi surface alloy, and the studies of platinum oxide formation are all examples of investigations, in which the complexity of the model systems has been increased in order to bridge the gaps between surface science studies and applied catalysis. The reactivity studies of nickel step sites and the investigation of oxygen dynamics on the $\text{TiO}_2(110)$ surface, on the other hand, provide two very different examples of the influence of active sites on the chemical properties of surfaces. The main results from the different studies are briefly summarized in the following.

From the investigations of CO adsorption on two different platinum surfaces in Chapter 4, we found that the high-coverage adsorbate structures formed at high-pressure conditions (1 bar of CO) can also be formed under low-pressure and low-temperature conditions. No *fundamental* differences are thus observed concerning adsorbate structures at the two sides of the pressure gap. It must be noted, however, that different structures may indeed also be found at low-temperature conditions, and care must therefore be taken when a direct comparison between adsorption structures is performed. Especially, CO adsorption on the Pt(111) surface has previously been used as an example of the pressure gap between surface science based model systems under UHV conditions and surfaces at realistic pressure conditions [70, 72], and the results presented in this thesis are therefore important in a general discussion of pressure gap effects.

The concept of active sites for CO dissociation on a nickel surface was investigated in Chapter 5, and a number of routes were explored whereby the catalytic properties of nickel-based catalysts may be changed. We have shown that the step edges of the Ni(111) surface exhibit a much higher rate for CO dissociation than the terrace sites, and by adding small amounts of silver, gold or sulfur, all binding preferentially to the step sites, this dissociation channel is completely blocked. Gold and nickel form a surface alloy, and the CO binding energy on nickel atoms in such an alloy is diminished compared to the binding to pure nickel. Such modified nickel surfaces may be applicable e.g. as fuel cell anode catalysts, and the stability of the alloy was therefore investigated under high-pressure conditions. High pressures of CO were found to induce a phase separation of the alloy, and the details of the de-alloying process were investigated with time-resolved STM experiments.

Studies of the adsorption and diffusion of oxygen molecules on a titanium dioxide surface revealed a different effect of active sites compared to the studies at nickel surfaces. Surface oxygen vacancies are known to play a crucial role in the adsorption and reaction of molecules on the surface, and in general such vacancies have been considered as active sites in a similar way as e.g. the step edges on metal surfaces. In the STM studies presented in Chapter 6, however, we found that the role of the vacancies may be more profound than simply being a localized site for molecular adsorption and reaction. The vacancies control the position of the chemical potential in the band gap of the crystal, and this property is found to be of significant importance for the dynamics of adsorbed oxygen molecules.

The investigation of high-coverage oxygen phases on the Pt(110) surface presented in Chapter 7 provides an example of the complexity of surface structures which is found on metal surfaces under oxygen-rich conditions. Upon oxygen exposure at room temperature, only disordered structures evolve on the surface, but when oxygen dosing is performed at elevated temperatures, ordered islands of a surface oxide are observed to coexist with a highly stable chemisorption structure.

Outlook

The results presented in the thesis give rise to a number of ideas for future studies, some of which have already been initiated in the group at the time of writing.

The studies of platinum surfaces under high-pressure conditions are being further pursued, and new studies now focus on the effect of co-adsorption of CO and water under high-pressure conditions. In this way, the relevant conditions in e.g. PEM fuel cells are further approached. Another interesting continuation of the high-pressure studies may be to investigate the reaction between CO and oxygen on Pt surfaces, thereby combining the knowledge gained from Chapters 4 and 7.

The finding that the active sites for CO dissociation on nickel can be blocked in a controlled manner may be pursued for the dissociation of other adsorbate molecules, and a highly interesting perspective would be to consider the possibilities of designing selective catalysts, which e.g. enable the breaking of specific adsorbate bonds and preserve others. On-going experiments presently investigate the dissociation of ethylene on the nickel surface, and it has been found that this molecule decomposes both at the step

edges and on the nickel terraces (although with different rates). Such findings may provide promising new ideas for surface science based design of selective catalysts where C=O bonds are preserved whereas C=C bonds are broken.

Preliminary experiments, which suggest that carbonyl formation on the Au/Ni alloy may be inhibited by the presence of water, are promising for the possible use of such alloys as CO tolerant catalysts in aqueous environments (e.g. in PEM fuel cells). Future experiments may hence focus both on the stability of the alloy under high-pressure conditions and on other key issues like the ability to dissociate hydrogen.

The present stage of knowledge of the surface chemistry on titanium dioxide may serve as a suitable platform for further studies in at least three different directions: First of all, an obvious experiment along the lines of the thesis would be to bridge the pressure gap for oxygen adsorption on TiO₂(110) and to investigate the effect on the various adsorbate species and their interaction with bridging oxygen vacancies when the pressure is raised. Secondly, it would be very interesting to explore the reactivity of the oxygen adsorbate species, e.g. towards CO oxidation, and to investigate if charge transfer processes control adsorbate reactions in a similar way as for the investigated diffusion mechanism. Such studies may finally also be extended to investigations of the reactivity of Au clusters supported on TiO₂. The detailed knowledge of the oxygen chemistry would be an excellent starting point for a thorough investigation of spill-over effects between TiO₂ and the Au clusters, and fundamental insight into the nature of the peculiarly high reactivity of “nano-Au” on active supports may be gained from such investigations.

The importance of the chemical potential in the surface region may be investigated in a broader perspective: The possibility of designing tailor-made chemical reactivities of metal oxides by “chemical potential engineering” is a fascinating and appealing idea, which may be investigated by the introduction of dopants in the near-surface region of TiO₂(110). The generality of the ideas could furthermore be tested by similar studies on other reducible oxides, which may lead to the founding of new concepts and models for the description of the reactivity on metal oxides. In Chapter 3, the conceptually simple *d*-band model was discussed, in which the trends of adsorption energies and reactivities of transition metals find an intuitively simple explanation. The revealed correlation between the position of the chemical potential and the dynamics at the TiO₂(110) surface thus calls upon theoretical calculations, whereby similar conceptual models may possibly be established for transition metal oxide surfaces.

In the presented TiO₂(110) studies, the electrons were thermally excited to the conduction band from the donor levels in the band gap, but from photo-catalysis it is well-known that photons with the right energy may enable similar electron excitations. A fascinating future perspective would be to integrate a light source with the present STM setup, thereby enabling the exploration of photon-induced electron excitations and their effect on the surface chemistry. Such a setup, where the availability of electrons in the conduction band would be continuously adjustable, would allow for a range of extremely interesting experiments where the direct coupling between electrons and chemistry could be controlled and witnessed at the atomic scale.

One of the drawbacks with the use of STM in studies of model systems for catalysis is its lacking ability to investigate reaction products leaving the surface. In the progression towards atomic-scale understanding of surface chemistry at realistic conditions,

new and complementary experimental approaches are therefore needed [28, 39]. In the group, we are currently in the process of building-up a new small-volume, high-pressure reaction cell, which will be integrated with the existing HP-STM. The reaction cell will enable the detection of trace amounts of gasses, and both reactants and reaction products from catalytic processes occurring at the surface can thereby be monitored. The combination of such reactivity measurements with the atomic-scale structural information from the high-pressure STM constitutes a very strong experimental setup, where the atomic-scale details *and* the reactivity of new material phases, e.g. oxides, formed during reaction conditions can be studied.

Acknowledgments

The past four years as a PhD student in the CAMP group have been a pleasure, and I have had the opportunity to collaborate with a large number of highly competent and inspiring people on different projects. It is a great pleasure for me to thank all the people in the group who have supported and encouraged my work during the last years. Especially the initial build-up of the UHV chamber was a hard struggle, and the help and advice from many people during that period are greatly acknowledged.

The three group seniors, Erik Lægsgaard, Ivan Stensgaard, and Flemming Besenbacher are acknowledged for invaluable advice in the laboratory and in the discussions of projects, and for creating a stimulating environment with world-class scientific equipment. Especially Flemming is thanked for his constant interest and trust in my work and for his enthusiasm, drive and optimistic viewpoints, even in situations when everything seemed hopeless.

The people with whom I have collaborated directly in the laboratory and have had useful discussions of the different projects with are thanked for good collaborations and for contributing to the work presented in this thesis: Toshu An, Stig Helveg, Jakob Kibsgaard, Jan Knudsen, Sarah R. Longwitz, Jesper Matthiesen, Anders Rønnau, Renald Schaub, Joachim Schnadt, Krishna Swamy, Peter Thostrup, Ronnie T. Vang, Erik Wahlström and Lars Österlund. Furthermore, it has been a pleasure to interact and discuss with the theoreticians Wei-Xue Li, Maria D. Rasmussen, Thorbjørn M. Pedersen and Bjørk Hammer.

A number of people have made suggestions for improvements during the making of this thesis, and they are all acknowledged for their good and useful comments. Particularly, Renald Schaub, Ronnie T. Vang and Erik Wahlström are gratefully remembered for their very thorough readings of large parts of the thesis. Jeanette Dandanell is thanked for correcting linguistic errors and typos.

Anders Rønnau and Kristian Rechendorff receive a special thank for good friendship both at and outside the department. Their support has been invaluable during my time in the CAMP group. Finally, I am deeply indebted to my lovely wife Anne for her patience and support.

Ebbe Kruse Vestergaard

Bibliography

- [1] G. A. Somorjai, *Surface Chemistry and Catalysis* (Wiley, New York, 1994).
- [2] I. E. Maxwell, "Combinatorial chemistry: Connecting with catalysis", *Nature* **394**, 325 (1998).
- [3] S. M. Senkan, "High-throughput screening of solid-state catalyst libraries", *Nature* **394**, 350 (1998).
- [4] I. Langmuir, "The mechanism of the catalytic action of platinum in the reactions $2\text{CO} + \text{O}_2 = 2\text{CO}_2$ and $2\text{H}_2 + \text{O}_2 = 2\text{H}_2\text{O}$ ", *Trans. Farad. Soc.* **17**, 621 (1922).
- [5] G. Ertl, "Reactions at well-defined surfaces", *Surface Science* **299/300**, 742 (1994).
- [6] H. S. Taylor, "A Theory of the Catalytic Surface", *Proceedings of the Physical Society of London, Series A* **108**, 105 (1925).
- [7] F. Besenbacher, I. Chorkendorff, B. S. Clausen, B. Hammer, A. M. Molenbroek, J. K. Nørskov, and I. Stensgaard, "Design of a Surface Alloy Catalyst for Steam Reforming", *Science* **279**, 1913 (1998).
- [8] T. H. Rod and J. K. Nørskov, "The Surface Science of Enzymes", *Surface Science* **500**, 678 (2002).
- [9] "Press release from The White House:", <http://www.whitehouse.gov/news/releases/2003/01/20030130-20.html>, January 2003.
- [10] "Homepage of the consortium "Icelandic New Energy Ltd" :", <http://www.newenergy.is>.
- [11] A. Fujishima and K. Honda, "Electrochemical Photolysis of Water at a Semiconductor Electrode", *Nature* **238**, 37 (1972).
- [12] M. Grätzel, "Photoelectrochemical cells", *Nature* **414**, 338 (2001).
- [13] R. D. Cortright, R. R. Davda, and J. A. Dumesic, "Hydrogen from catalytic reforming of biomass-derived hydrocarbons in liquid water", *Nature* **418**, 964 (2002).
- [14] R. R. Davda and J. A. Dumesic, "Catalytic Reforming of Oxygenated Hydrocarbons for Hydrogen with Low Levels of Carbon Monoxide", *Angewandte Chemie - International Edition* (2003).
- [15] L. Carrette, K. A. Friedrich, and U. Stimming, "Fuel Cells: Principles, Types, Fuels, and Applications", *ChemPhysChem* **1**, 162 (2000).
- [16] B. C. H. Steele and A. Heinzl, "Materials for fuel-cell technologies", *Nature* **414**, 345 (2001).
- [17] E. Christoffersen, P. Liu, A. Ruban, H. L. Skriver, and J. K. Nørskov, "Anode Materials for Low-Temperature Fuel Cells: A Density Functional Theory Study", *Journal of Catalysis* **199**, 123 (2001).
- [18] M. Haruta, "Catalysis of Gold Nanoparticles Deposited on Metal Oxides", *CATTECH* **6**, 102 (2002).
- [19] H. F. Oetjen, V. M. Schmidt, U. Stimming, and F. Trila, "Performance Data of a Proton Exchange Membran Fuel Cell Using H_2/CO as Fuel Gas", *J. Electrochem. Soc.* **143**, 3838 (1996).
- [20] M. Bowker, *The Basis and Applications of Heterogeneous Catalysis* (Oxford University Press, Oxford, 1998).

- [21] C. J. H. Jacobsen, I. Schmidt, A. Boisen, and K. Johannsen, *Katalytisk kemi - et spørgsmål om miljø og ressourcer* (Holte Bogtrykkeri A/S, Lyngby, 2002).
- [22] G. Ertl and H.-J. Freund, "Catalysis and Surface Science", *Physics Today* **32** (1999).
- [23] D. W. Goodman, "Correlations between Surface Science Models and "Real-World" Catalysts", *Journal of Physical Chemistry* **100**, 13090 (1996).
- [24] D. W. Goodman, "Model catalysts: from imagining to imaging a working surface", *Journal of Catalysis* **216**, 213 (2003).
- [25] A. Zangwill, *Physics at surfaces* (Cambridge University Press, Cambridge, 1988).
- [26] P. Stoltze and J. K. Nørskov, "Bridging the "Pressure Gap" between Ultrahigh-Vacuum Surface Physics and High-Pressure Catalysis", *Physical Review Letters* **55**, 2502 (1985).
- [27] C. V. Ovesen, B. S. Clausen, B. S. Hammersh, G. Steffensen, T. Askgaard, I. Chorkendorff, J. K. Nørskov, P. B. Rasmussen, P. Stoltze, and P. Taylor, "A Microkinetic Analysis of the Water-Gas Shift Reaction under Industrial Conditions", *Journal of Catalysis* **158**, 170 (1996).
- [28] H.-J. Freund, H. Kuhlenbeck, J. Libuda, G. Rupprechter, M. Bäumer, and H. Hamann, "Bridging the pressure and materials gaps between catalysis and surface science: clean and modified oxide surfaces", *Topics in Catalysis* **15**, 201 (2001).
- [29] M. Valden, X. Lai, and D. W. Goodman, "Onset of Catalytic Activity of gold Clusters on Titania with the Appearance of Nonmetallic Properties", *Science* **281**, 1647 (1998).
- [30] C. R. Henry, "Surface studies of supported model catalysts", *Surface Science Reports* **31**, 235 (1998).
- [31] C. T. Campbell, "Ultrathin metal films and particles on oxide surfaces: Structural, electronic and chemisorptive properties", *Surface Science Reports* **27**, 3 (1997).
- [32] K. H. Hansen, T. Worren, S. Stempel, E. Lægsgaard, M. Bäumer, H.-J. Freund, F. Besenbacher, and I. Stensgaard, "Palladium Nanocrystals on Al₂O₃: Structure and Adhesion Energy", *Physical Review Letters* **83**, 4120 (1999).
- [33] M. Bäumer and H.-J. Freund, "Metal deposits on well-ordered oxide films", *Progress in Surface Science* **61**, 127 (1999).
- [34] M. Haruta, N. Yamada, T. Kobayashi, and S. Iijima, "Gold Catalysts Prepared by Coprecipitation for Low-Temperature Oxidation of Hydrogen and of Carbon Monoxide", *Journal of Catalysis* **115**, 301 (1989).
- [35] M. Haruta and M. Date, "Advances in the catalysis of Au nanoparticles", *Applied Catalysis A* **222**, 427 (2001).
- [36] B. Hammer and J. Nørskov, "Why gold is the noblest of all the metals", *Nature* **376**, 238 (1995).
- [37] H. Over, Y. D. Kim, A. P. Seitsonen, S. Wendt, E. Lundgren, M. Schmid, P. Varga, A. Morgante, and G. Ertl, "Atomic-Scale Structure and Catalytic Reactivity of the RuO₂(110) Surface", *Science* **287**, 1474 (2000).
- [38] C. Stampfl, M. V. Ganduglia-Pirovano, K. Reuter, and M. Scheffler, "Catalysis and corrosion: the theoretical surface-science context", *Surface Science* **500**, 368 (2002).
- [39] B. L. M. Hendriksen and J. W. M. Frenken, "CO Oxidation on Pt(110): Scanning Tunneling Microscopy Inside a High-Pressure Flow Reactor", *Physical Review Letters* **89**, 046101 (2002).
- [40] G. Rupprechter and H.-J. Freund, "Adsorbate-induced restructuring and pressure-dependent adsorption on metal nanoparticles studied by electron microscopy and sum frequency generation spectroscopy", *Topics in Catalysis* **14**, 3 (2001).
- [41] T. Dellwig, G. Rupprechter, H. Unterhalt, and H.-J. Freund, "Bridging the Pressure and Materials Gaps: High Pressure Sum Frequency Generation Study on Supported Pd Nanoparticles", *Physical Review Letters* **85**, 776 (2000).
- [42] A. Kolmakov and D. W. Goodman, "Imaging gold clusters on TiO₂(110) at elevated pressures and temperatures", *Catalysis Letters* **70**, 93 (2000).

- [43] A. Kolmakov and D. W. Goodman, "Scanning tunneling microscopy of gold clusters on TiO₂(110): CO oxidation at elevated pressures", *Surface Science* **490**, L597 (2001).
- [44] D. P. Woodruff and T. A. Delchar, *Modern Techniques of Surface Science, Cambridge Solid State Science Series*, 2nd ed. (Cambridge University Press, Cambridge, 1994).
- [45] E. Lægsgaard, L. Österlund, P. Thostrup, P. B. Rasmussen, I. Stensgaard, and F. Besenbacher, "A high-pressure scanning tunneling microscope", *Review of Scientific Instruments* **72**, 3537 (2001).
- [46] G. Binnig, H. Rohrer, C. Gerber, and E. Weibel, "Surface Studies by Scanning Tunneling Microscopy", *Physical Review Letters* **49**, 57 (1982).
- [47] R. Wiesendanger, *Scanning Probe Microscopy and Spectroscopy: Methods and Applications* (Cambridge University Press, Cambridge, 1994).
- [48] E. Lægsgaard, F. Besenbacher, K. Mortensen, and I. Stensgaard, "A fully automated, 'thimble-size' scanning tunnelling microscope", *Journal of Microscopy* **152**, 663 (1988).
- [49] F. Besenbacher, "Scanning tunnelling microscopy studies of metal surfaces", *Reports on Progress in Physics* **59**, 1737 (1996).
- [50] W. A. Hofer, A. J. Fisher, R. A. Wolkow, and P. Grütter, "Surface Relaxations, Current Enhancements, and Absolute Distances in High Resolution Scanning Tunneling Microscopy", *Physical Review Letters* **87**, 236104 (2001).
- [51] J. Tersoff and D. R. Hamann, "Theory and Application for the Scanning Tunneling Microscope", *Physical Review Letters* **50**, 1998 (1983).
- [52] J. Tersoff and D. R. Hamann, "Theory of the scanning tunneling microscope", *Physical Review B* **31**, 805 (1985).
- [53] J. Bardeen, "Tunneling from a Many-Particle Point of View", *Physical Review Letters* **6**, 57 (1961).
- [54] N. D. Lang, "Theory of Single-Atom Imaging in the Scanning Tunneling Microscope", *Physical Review Letters* **56**, 1164 (1986).
- [55] A. Davies, J. A. Stroscio, D. T. Pierce, and R. J. Celotta, "Atomic-Scale Observations of Alloying at the Cr-Fe(001) Interface", *Physical Review Letters* **76**, 4175 (1996).
- [56] N. Nilius, T. M. Wallis, and W. Ho, "Influence of a heterogeneous Al₂O₃ surface on the electronic properties of single Pd atoms", *Physical Review Letters* **90**, 046808 (2003).
- [57] J. W. Niemantsverdriet, *Spectroscopy in Catalysis* (Wiley-VCH, Weinheim, 2000).
- [58] B. Hammer, Y. Morikawa, and J. K. Nørskov, "CO Chemisorption at Metal Surfaces and Overlayers", *Physical Review Letters* **76**, 2141 (1996).
- [59] B. Hammer and J. K. Nørskov, in *Chemisorption and Reactivity on Supported Clusters and Thin Films*, Vol. 331 of *NATO ASI Series E*, edited by R. M. Lambert and G. Pacchioni (Kluwer Academic Publishers, Dordrecht, 1997), pp. 285–351.
- [60] B. Hammer and J. K. Nørskov, "Theoretical Surface Science and Catalysis—Calculation and Concepts", *Advances in Catalysis* **45**, 71 (2000).
- [61] J. K. Nørskov, T. Bligaard, A. Logadottir, S. Bahn, L. B. Hansen, M. Bollinger, H. Bengaard, B. Hammer, Z. Sljivancanin, M. Mavrikakis, Y. Xu, S. Dahl, and C. J. H. Jacobsen, "Universality in Heterogeneous Catalysis", *Journal of Catalysis* **209**, 275 (2002).
- [62] G. Blyholder, "Molecular Orbital View of Chemisorbed Carbon Monoxide", *Journal of Physical Chemistry* **68**, 2772 (1964).
- [63] A. Logadottir, T. Rod, J. Nørskov, B. Hammer, S. Dahl, and C. Jacobsen, "The Brønsted-Evans-Polanyi relation and the volcano plot for ammonia synthesis over transition metal catalysts", *Journal of Catalysis* **197**, 229 (2001).
- [64] N. W. Ashcroft and N. D. Mermin, *Solid State Physics* (Saunders College Publishing, New York, 1976).
- [65] M. Ø. Pedersen, S. Helveg, A. Ruban, E. Lægsgaard, J. K. Nørskov, and F. Besenbacher, "How a gold substrate can increase the reactivity of a Pt overlayer", *Surface Science* **426**, 395 (1999).

- [66] F. Buatier de Mongeot, M. Scherer, B. Gleich, E. Kopatzki, and R. J. Behm, "CO adsorption and oxidation on bimetallic Pt/Ru(0001) surfaces - a combined STM and TPD/TPR study", *Surface Science* **411**, 249 (1998).
- [67] A. V. Ruban, B. Hammer, P. Stoltze, H. L. Skriver, and J. K. Nørskov, "Surface electronic structure and reactivity of transition and noble metals", *Journal of Molecular Catalysis A: Chemical* **115**, 421 (1997).
- [68] R. J. Farrauto and R. M. Heck, "Catalytic converters: state of the art and perspectives", *Catalysis Today* **51**, 351 (1999).
- [69] L. Carrette, K. A. Friedrich, and U. Stimming, "Fuel Cells - Fundamentals and Applications", *Fuel Cells* **1**, 5 (2001).
- [70] J. A. Jensen, K. B. Rider, M. Salmeron, and G. A. Somorjai, "High Pressure Adsorbate Structures Studied by Scanning Tunneling Microscopy: CO on Pt(111) in Equilibrium with the Gas Phase", *Physical Review Letters* **80**, 1228 (1998).
- [71] B. J. McIntyre, M. Salmeron, and G. A. Somorjai, "In situ scanning tunneling microscopy study of platinum (110) in a reactor cell at high pressures and temperatures", *Journal of Vacuum Science and Technology A* **11**, 1964 (1993).
- [72] X. Su, P. S. Cremer, Y. R. Shen, and G. A. Somorjai, "Pressure Dependence (10^{-10} -700 Torr) of the Vibrational Spectra of Adsorbed CO on Pt(111) Studied by Sum Frequency Generation", *Physical Review Letters* **77**, 3858 (1996).
- [73] P. Thostrup, E. Christoffersen, H. T. Lorenzen, K. W. Jacobsen, F. Besenbacher, and J. K. Nørskov, "Adsorption-Induced Step Formation", *Physical Review Letters* **87**, 126102 (2001).
- [74] P. Liu and J. K. Nørskov, "Kinetics of the Anode Processes in PEM Fuel Cells - The Promoting Effect of Ru in PtRu Anodes", *Fuel Cells* **1**, 192 (2001).
- [75] A. V. Myshlyavtsev and V. P. Zhdanov, "Surface Reconstruction and Thermal Desorption: The Missing-Row Model for CO/Pt(110)", *Langmuir* **9**, 1290 (1993).
- [76] P. Hofmann, S. R. Bare, and D. R. King, "Surface phase transitions in CO chemisorption on Pt{110}", *Surface Science* **117**, 245 (1982).
- [77] S. R. Bare, P. Hofmann, and D. A. King, "Vibrational studies of the surface phases of CO on Pt{110} at 300 K", *Surface Science* **144**, 347 (1984).
- [78] T. Gritsch, D. Coulman, R. J. Behm, and G. Ertl, "Mechanism of the CO-induced $1 \times 2 \rightarrow 1 \times 1$ Structural Transformation of Pt(110)", *Physical Review Letters* **63**, 1086 (1989).
- [79] T. Gritsch, D. Coulman, R. J. Behm, and G. Ertl, "A Scanning Tunneling Microscopy Investigation of the $1 \times 2 \rightleftharpoons 1 \times 1$ Structural Transformation of the Pt(110) Surface", *Applied Physics A* **49**, 403 (1989).
- [80] R. K. Sharma, W. A. Brown, and D. A. King, "The adsorption of CO on Pt{110} over the temperature range from 90 to 300 K studied by RAIRS", *Surface Science* **414**, 68 (1998).
- [81] H. H. Rotermund, W. Engel, M. Kordesch, and G. Ertl, "Imaging of spatio-temporal pattern evolution during carbon monoxide oxidation on platinum", *Nature* **343**, 355 (1990).
- [82] H. H. Rotermund, "Imaging pattern formation in surface reactions from ultra-high vacuum up to atmospheric pressures", *Surface Science* **386**, 10 (1997).
- [83] M. Kim, M. Bertram, M. Pollmann, A. v. Oertzen, A. S. Mikhailov, H. H. Rotermund, and G. Ertl, "Controlling Chemical Turbulence by Global Delayed Feedback: Pattern Formation in Catalytic CO Oxidation on Pt(110)", *Science* **292**, 1357 (2001).
- [84] K.-D. Shiang and T. T. Tsong, "Energetics and atomic steps in the reconstruction of the Pt(110) surface", *Physical Review B* **51**, 5522 (1995).
- [85] P. Hanesch and E. Bertel, "Mesoscopic Self-Organisation Induced by Intrinsic Surface Stress on Pt(110)", *Physical Review Letters* **79**, 1523 (1997).
- [86] T. Gritsch, D. Coulman, R. J. Behm, and G. Ertl, "A scanning tunneling microscopy investigation of the structure of the Pt(110) and Au(110) surfaces", *Surface Science* **257**, 297 (1991).

- [87] J. Tersoff, "Surface stress and self-organization of steps", *Physical Review Letters* **80**, 2018 (1998).
- [88] I. K. Robinson, P. J. Eng, C. Romainczyk, and K. Kern, "Higher order reconstructions of Pt(110) induced by impurities", *Surface Science* **367**, 105 (1996).
- [89] P. Thostrup, Ph.D. thesis, University of Aarhus, 2002.
- [90] P. Sprunger, F. Besenbacher, and I. Stensgaard, "STM study of the Ni(110)-(2×1)-2CO system: Structure and bonding-site determination", *Surface Science* **324**, L321 (1995).
- [91] M. M. D. Ramos, A. M. Stoneham, A. P. Sutton, and J. B. Pethica, "Effects of the STM tip on atomic positions: an explanation for the non-observation of adsorbed molecules?", *Journal of Physics: Condensed Matter* **2**, 5913 (1990).
- [92] J. S. McEwen, S. H. Payne, H. J. Kreuzer, M. Kinne, R. Denecke, and H.-P. Steinrück, "Adsorption and desorption of CO on Pt(111): a comprehensive analysis", *Surface Science* **545**, 47 (2003).
- [93] G. Rupprechter, T. Dellwig, H. Unterhalt, and H.-J. Freund, "High-Pressure Carbon Monoxide Adsorption on Pt(111) Revisited: A Sum Frequency Generation Study", *Journal of Physical Chemistry B* **105**, 3797 (2001).
- [94] M. Ø. Pedersen, M.-L. Bocquet, P. Sautet, E. Lægsgaard, I. Stensgaard, and F. Besenbacher, "CO on Pt(111): binding site assignment from the interplay between measured and calculated STM images", *Chemical Physics Letters* **299**, 403 (1999).
- [95] B. E. Hayden and A. M. Bradshaw, "The adsorption of CO on Pt(111) studied by infrared reflection-absorption spectroscopy", *Surface Science* **125**, 787 (1983).
- [96] G. Ertl, M. Neumann, and K. M. Streit, "Chemisorption of CO on the Pt(111) surface", *Surface Science* **64**, 393 (1977).
- [97] B. N. J. Persson, M. Tüshaus, and A. M. Bradshaw, "On the nature of dense CO adlayers", *Journal of Chemical Physics* **92**, 5034 (1990).
- [98] K. Kobayashi, "Moiré pattern in scanning tunneling microscopy: Mechanism in observation of subsurface nanostructures", *Physical Review B* **53**, 11091 (1996).
- [99] E. K. Vestergaard, P. Thostrup, T. An, E. Lægsgaard, I. Stensgaard, B. Hammer, and F. Besenbacher, "Comment on "High Pressure Adsorbate Structures Studied by Scanning Tunneling Microscopy: CO on Pt(111) in Equilibrium with the Gas Phase"", *Physical Review Letters* **88**, 259601 (2002).
- [100] H. Steininger, S. Lehwald, and H. Ibach, "On the adsorption of CO on Pt(111)", *Surface Science* **123**, 264 (1982).
- [101] I. Villegas and M. J. Weaver, "Carbon monoxide adlayer structures on platinum (111) electrodes: A synergy between *in situ* scanning tunneling microscopy and infrared spectroscopy", *Journal of Chemical Physics* **101**, 1648 (1994).
- [102] P. Cernota, K. Rider, H. A. Yoon, M. Salmeron, and G. A. Somorjai, "Dense structures formed by CO on Rh(111) studied by scanning tunneling microscopy", *Surface Science* **445**, 249 (2000).
- [103] F. Grey and J. Bohr, in *Phase Transitions in Surface Films, NATO ASI Series*, edited by H. Taub (Plenum, New York, 1990).
- [104] F. Grey and J. Bohr, "A Symmetry Principle for Epitaxial Rotation", *Europhysics Letters* **18**, 717 (1992).
- [105] J. Bohr and F. Grey, "Epitaxial rotations and finite size effects", *Condensed Matter News* **1**, 12 (1992).
- [106] C. Quiros, O. Robach, H. Isern, P. Ordejon, and S. Ferrer, "Compressibility of CO adsorbed on Ni(111) from 10⁻⁶ mbar to 1.2 bar ambient CO pressures investigated with X-ray diffraction", *Surface Science* **522**, 161 (2003).
- [107] M. Watanabe and S. Motoo, "Electrocatalysis by ad-atoms part II. Enhancement of the oxidation of methanol on platinum by ruthenium ad-atoms", *Journal of Electroanalytical Chemistry* **60**, 267 (1975).
- [108] H. A. Gasteiger, N. M. Markovic, and P. M. Ross, "H₂ and CO Electrooxidation on Well-Characterized Pt, Ru, and Pt-Ru. 1. Rotating Disk Electrode Studies of the Pure Gases Including Temperature Effects", *Journal of Physical Chemistry B* **99**, 8290 (1995).

- [109] B. N. Grgur, N. M. Markovic, and P. M. Ross, "Electrooxidation of H₂, CO, and H₂/CO Mixtures on a Well-Characterized Pt₇₀Mo₃₀ Bulk Alloy Electrode", *Journal of Physical Chemistry B* **102**, 2494 (1998).
- [110] J. C. Davies, B. E. Hayden, and D. J. Pegg, "The modification of Pt(110) by ruthenium: CO adsorption and electro-oxidation", *Surface Science* **467**, 118 (2000).
- [111] J. C. Davies, R. M. Nielsen, L. B. Thomsen, I. Chorkendorff, A. Logadottir, Z. Lodziana, J. K. Nørskov, W. Li, B. Hammer, S. R. Longwitz, J. Schnadt, E. K. Vestergaard, R. T. Vang, and F. Besenbacher, "CO desorption rate dependence on CO partial pressure over platinum fuel cell catalysts", Submitted to Fuel Cells, 2003.
- [112] H. Nakano, J. Ogawa, and J. Nakamura, "Growth mode of carbide from C₂H₄ or CO on Ni(111)", *Surface Science* **514**, 256 (2002).
- [113] J. R. Rostrup-Nielsen, in *Catalytic Steam Reforming*, Vol. 5 of *Catalysis, Science and Technology*, edited by J. R. Anderson and M. Boudart (Springer-Verlag, Berlin, 1983).
- [114] J. R. Rostrup-Nielsen and T. Rostrup-Nielsen, "Large-scale hydrogen production", *CATTECH* **6**, 150 (2002).
- [115] J. R. Rostrup-Nielsen, "Sulfur-Passivated Nickel Catalysts for Carbon-Free Steam Reforming of Methane", *Journal of Catalysis* **85**, 31 (1984).
- [116] D. W. Goodman, "Chemisorption and Reactivity Studies of H₂ and CO on Sulfided Ni(100)", *Surface Science* **105**, L265 (1981).
- [117] W. Erley and H. Wagner, "Thermal decomposition of CO on a stepped Ni surface", *Surface Science* **74**, 333 (1978).
- [118] S. Dahl, A. Logadottir, R. C. Egeberg, J. H. Larsen, I. Chorkendorff, E. Törnquist, and J. K. Nørskov, "Role of Steps in N₂ Activation on Ru(0001)", *Physical Review Letters* **83**, 1814 (1999).
- [119] T. Zambelli, J. Wintterlin, J. Trost, and G. Ertl, "Identification of the "Active Sites" of a Surface-Catalyzed Reaction", *Science* **273**, 1688 (1996).
- [120] H. S. Bengaard, J. K. Nørskov, J. Sehested, B. Clausen, L. P. Nielsen, A. M. Molenbroek, and J. R. Rostrup-Nielsen, "Steam Reforming and Graphite Formation on Ni Catalysts", *Journal of Catalysis* **209**, 365 (2002).
- [121] H. Nakano, S. Kawakami, T. Fujitani, and J. Nakamura, "Carbon deposition by disproportionation of CO on a Ni(977) surface", *Surface Science* **454-456**, 295 (2000).
- [122] H. Nakano and J. Nakamura, "Carbide-induced reconstruction initiated at step edges on Ni(111)", *Surface Science* **482-485**, 341 (2001).
- [123] S. Helveg, C. López-Cartes, P. L. Sehested, J. Hansen, B. S. Clausen, J. R. Rostrup-Nielsen, F. Abild-Pedersen, and J. K. Nørskov, "Atomic-scale imaging of carbon nanofibre growth", *Nature* **427**, 426 (2004).
- [124] C. Klink, I. Stensgaard, F. Besenbacher, and E. Lægsgaard, "An STM study of carbon-induced structures on Ni(111): evidence for a carbidic-phase clock reconstruction", *Surface Science* **342**, 250 (1995).
- [125] J. J. McCarroll, T. Edmonds, and R. C. Pitkethly, "Interpretation of a Complex Low Energy Electron Diffraction Pattern: Carbonaceous and Sulphur-containing Structures on Ni(111)", *Nature* **223**, 1260 (1969).
- [126] R. T. Vang, K. Honkala, E. K. Vestergaard, J. Schnadt, J. K. Nørskov, and F. Besenbacher, "Ethylene Dissociation on Ni(111): Selective Blocking of Special Active Sites", To be published, 2004.
- [127] C. T. Campbell, Y.-K. Sun, and W. H. Weinberg, "Trends in preexponential factors and activation energies in dehydrogenation and dissociation of adsorbed species", *Chemical Physics Letters* **179**, 53 (1991).
- [128] R. T. Vang, E. K. Vestergaard, and F. Besenbacher, Unpublished data, 2003.
- [129] F. Abild-Pedersen and J. K. Nørskov, Work in progress, 2004.

- [130] F. Besenbacher, L. P. Nielsen, and P. T. Sprunger, in *The Chemical Physics of Solid Surfaces and Heterogeneous Catalysis*, edited by D. A. King and D. P. Woodruff (Elsevier Science Publishers, AD-DRESS, 1997).
- [131] J. Jacobsen, L. P. Nielsen, F. Besenbacher, I. Stensgaard, E. Lægsgaard, T. Rasmussen, K. W. Jacobsen, and J. K. Nørskov, "Atomic-Scale Determination of Misfit Dislocation Loops at Metal-Metal Interfaces", *Physical Review Letters* **75**, 489 (1995).
- [132] L. P. Nielsen, Ph.D. thesis, University of Aarhus, 1995.
- [133] D. P. Woodruff, "Adsorbate-induced reconstruction of surfaces: an atomistic alternative to microscopic faceting?", *Journal of Physics: Condensed Matter* **6**, 6067 (1994).
- [134] V. Maurice, N. Kitakatsu, M. Siegers, and P. Marcus, "Low-coverage sulfur induced reconstruction of Ni(111)", *Surface Science* **373**, 307 (1997).
- [135] L. Ruan, I. Stensgaard, F. Besenbacher, and E. Lægsgaard, "Observation of a Missing-Row Structure on an fcc (111) Surface: The $(5\sqrt{3}\times 2)S$ Phase on Ni(111) Studied by Scanning Tunneling Microscopy", *Physical Review Letters* **71**, 2963 (1993).
- [136] P. M. Holmblad, J. H. Larsen, and I. Chorkendorff, "Modification of Ni(111) reactivity toward CH_4 , CO and D_2 by two-dimensional alloying", *Journal of Chemical Physics* **104**, 7289 (1996).
- [137] P. M. Holmblad, J. H. Larsen, I. Chorkendorff, L. P. Nielsen, F. Besenbacher, I. Stensgaard, E. Lægsgaard, P. Kratzer, B. Hammer, and J. K. Nørskov, "Designing surface alloys with specific active sites", *Catalysis Letters* **40**, 131 (1996).
- [138] A. Eichler, "CO adsorption on Ni(111) – a density functional theory study", *Surface Science* **526**, 332 (2003).
- [139] L. D. Mapledoram, M. P. Bessent, A. Wander, and D. A. King, "An automated tensor LEED analysis of the Ni(111)-c(4×2)-2CO structure", *Chemical Physics Letters* **228**, 527 (1994).
- [140] P. T. Sprunger, F. Besenbacher, and I. Stensgaard, "STM investigation of the Ni(111)-c(4×2)-2CO structure", *Chemical Physics Letters* **243**, 439 (1995).
- [141] J. Nerlov, S. Sckerl, J. Wambach, and I. Chorkendorff, "Methanol synthesis from CO_2 , CO and H_2 over Cu(1 0 0) and Cu(1 0 0) modified by Ni and Co", *Applied Catalysis A* **191**, 97 (2000).
- [142] E. Christoffersen, P. Stoltze, and J. K. Nørskov, "Monte Carlo simulations of adsorption-induced segregation", *Surface Science* **505**, 200 (2002).
- [143] P. de Groot, M. Coulon, and K. Dransfeld, "Ni(CO)₄ formation on single Ni crystals: Reaction kinetics and observation of surface faceting induced by the reaction", *Surface Science* **94**, 204 (1980).
- [144] W. A. Schmidt, J. H. Block, and K. A. Becker, "The topography of nickel crystals during the reaction towards Ni(CO)₄; A field ion microscope study", *Surface Science* **122**, 409 (1982).
- [145] K. Lascelles and L. V. Renny, "The rate of formation of nickel carbonyl from carbon monoxide and nickel single crystals", *Surface Science* **125**, L67 (1983).
- [146] V. K. Medvedev, R. Börner, and N. Kruse, "Nickeltetracarbonyl formation on non-equilibrium Ni surfaces", *Surface Science* **401**, L371 (1998).
- [147] L. Mond, C. Langer, and F. Quincke, "Action of Carbon Monoxide on Nickel", *Journal of the Chemical Society* **57**, 749 (1890).
- [148] V. E. Henrich and P. A. Cox, *The surface science of metal oxides* (Cambridge University Press, Cambridge, 1996).
- [149] B. Kasemo and J. Gold, "Implant Surfaces and Interface Processes", *Advances in Dental Research* **13**, 8 (1999).
- [150] N. V. Skorodumova, S. I. Simak, B. I. Lundqvist, I. A. Abrikosov, and B. Johansson, "Quantum Origin of the Oxygen Storage Capability of Ceria", *Physical Review Letters* **89**, 166601 (2002).
- [151] U. Gesenhues and T. Rentschler, "Crystal growth and defect structure of Al^{3+} -doped rutile", *Journal of Solid State Chemistry* **143**, 210 (1999).

- [152] A. Fujishima, T. N. Rao, and A. Tryk, "Titanium dioxide photocatalysis", *Journal of Photochemistry and Photobiology C: Photochemistry Reviews* **1**, 1 (2000).
- [153] R. Wang, K. Hashimoto, A. Fujishima, M. Chikuni, E. Kojima, A. Kitamura, M. Shimohigoshi, and T. Watanabe, "Light-induced amphiphilic surfaces", *Nature* **388**, 431 (1997).
- [154] B. Kasemo, "Biological Surface Science", *Surface Science* **500**, 656 (2002).
- [155] M. Valden, S. Pak, X. Lai, and D. W. Goodman, "Structure sensitivity of CO oxidation over model Au/TiO₂ catalysts", *Journal of Catalysis* **56**, 7 (1998).
- [156] Z. Zhang and M. G. Lagally, "Atomistic Processes in the Early Stages of Thin-Film Growth", *Science* **276**, 377 (1997).
- [157] Z. Yang, R. Wu, and D. W. Goodman, "Structural and electronic properties of Au on TiO₂(110)", *Physical Review B* **61**, 14066 (2000).
- [158] F. Boccuzzi, A. Chiorino, and M. Manzoli, "Au/TiO₂ nanostructured catalyst: effects of gold particle sizes on CO oxidation at 90 K", *Materials Science and Engineering C* **15**, 215 (2001).
- [159] N. Lopez and J. Nørskov, "Theoretical study of the Au/TiO₂(110) interface", *Surface Science* **515**, 175 (2002).
- [160] E. Wahlström, N. Lopez, R. Schaub, P. Thostrup, A. Rønnau, C. Africh, E. Lægsgaard, J. K. Nørskov, and F. Besenbacher, "Bonding of Gold Nanoclusters to Oxygen Vacancies on Rutile TiO₂(110)", *Physical Review Letters* **90**, 026101 (2003).
- [161] M. Mavrikakis, P. Stoltze, and J. K. Nørskov, "Making gold less noble", *Catalysis Letters* **64**, 101 (2000).
- [162] C. Lemire, R. Meyer, S. Shaikhutdinov, and H.-J. Freund, "Do Quantum Size Effects Control CO Adsorption on Gold Nanoparticles?", *Angewandte Chemie, Int. Ed.* **43**, 118 (2004).
- [163] A. Linsebigler, G. Lu, and J. T. J. Yates, "Photocatalysis on TiO₂ Surfaces: Principles, Mechanisms, and Selected Results", *Chemical Reviews* **95**, 735 (1995).
- [164] D. F. Ollis, "Heterogeneous photocatalysis", *CATTECH* **2**, 149 (1998).
- [165] M. A. Henderson, W. S. Epling, C. H. F. Peden, and C. L. Perkins, "Insights into Photoexcited Electron Scavenging Processes on TiO₂ Obtained from Studies of the Reaction of O₂ with OH Groups Adsorbed at Electronic Defects on TiO₂(110)", *Journal of Physical Chemistry B* **107**, 534 (2003).
- [166] A. Yamakata, T. Ishibashi, and H. Onishi, "Water- and Oxygen-Induced Decay Kinetics of Photogenerated Electrons in TiO₂ and Pt/TiO₂: A Time-Resolved Infrared Absorption Study", *Journal of Physical Chemistry B* **105**, 7258 (2001).
- [167] U. Diebold, "The surface science of titanium dioxide", *Surface Science Reports* **48**, 53 (2003).
- [168] K. M. Glassford and J. R. Chelikowsky, "Structural and Electronic-Properties of Titanium-Dioxide", *Physical Review B* **46**, 1284 (1992).
- [169] U. Diebold, J. Lehman, T. Mahmoud, M. Kuhn, G. Leonardelli, W. Hebenstreit, M. Schmid, and P. Varga, "Intrinsic defects on a TiO₂(110)(1×1) surface and their reaction with oxygen: a scanning tunneling microscopy study", *Surface Science* **411**, 137 (1998).
- [170] D. C. Cronmeyer, "Electrical and Optical Properties of Rutile Single Crystals", *Physical Review* **87**, 876 (1952).
- [171] D. C. Cronmeyer, "Infrared Absorption of Reduced Rutile TiO₂ Single Crystals", *Physical Review* **113**, 1222 (1959).
- [172] R. Breckenridge and W. Hosler, "Electrical properties of titanium dioxide semiconductors", *Physical Review* **91**, 793 (1953).
- [173] E. Yagi, R. R. Hasiguti, and M. Aono, "Electronic conduction above 4 K of slightly reduced oxygen-deficient rutile TiO_{2-x}", *Physical Review B* **54**, 7945 (1996).
- [174] N. C. Yu and J. W. Halley, "Electronic-Structure of Point-Defects in Rutile TiO₂", *Physical Review B* **51**, 4768 (1995).

- [175] U. Diebold, M. Li, O. Dulub, E. L. D. Hebenstreit, and W. Hebenstreit, "The relationship between bulk and surface properties of rutile $\text{TiO}_2(110)$ ", *Surface Review and Letters* **7**, 613 (2000).
- [176] M. A. Henderson, "A surface perspective on self-diffusion in rutile TiO_2 ", *Surface Science* **419**, 174 (1999).
- [177] M. Li, W. Hebenstreit, L. Gross, U. Diebold, M. A. Henderson, D. R. Jennison, P. A. Schultz, and M. P. Sears, "Oxygen-induced restructuring of the $\text{TiO}_2(110)$ surface: a comprehensive study", *Surface Science* **437**, 173 (1999).
- [178] G. Charlton, P. B. Howes, C. L. Nicklin, P. Steadman, J. S. G. Taylor, C. A. Muryn, S. P. Harte, J. Mercer, R. McGrath, D. Norman, T. S. Turner, and G. Thornton, "Relaxation of $\text{TiO}_2(110)-(1 \times 1)$ Using Surface X-Ray Diffraction", *Physical Review Letters* **78**, 495 (1997).
- [179] R. Schaub, P. Thostrup, N. Lopez, E. Lægsgaard, I. Stensgaard, J. K. Nørskov, and F. Besenbacher, "Oxygen vacancies as active sites for water dissociation on rutile $\text{TiO}_2(110)$ ", *Physical Review Letters* **87**, 6104 (2001).
- [180] S. Suzuki, K. Fukui, H. Onishi, and Y. Iwasawa, "Hydrogen Adatoms on $\text{TiO}_2(110)-(1 \times 1)$ Characterized by Scanning Tunneling Microscopy and Electron Stimulated Desorption", *Physical Review Letters* **84**, 2156 (2000).
- [181] J.-M. Pan, B. L. Maschhoff, U. Diebold, and T. E. Madey, "Interaction of water, oxygen, and hydrogen with $\text{TiO}_2(110)$ surfaces having different defect densities", *Journal of Vacuum Science and Technology A* **10**, 2470 (1992).
- [182] R. L. Kurtz, R. Stockbauer, T. E. Madey, E. Román, and J. L. de Segovia, "Synchrotron radiation studies of H_2O adsorption on $\text{TiO}_2(110)$ ", *Surface Science* **218**, 178 (1989).
- [183] G. Rocker, J. A. Schaefer, and W. Göpel, "Localized and delocalized vibrations on $\text{TiO}_2(110)$ studied by high-resolution electron-energy-loss spectroscopy", *Physical Review B* **30**, 3704 (1984).
- [184] M. A. Henderson, "Evidence for bicarbonate formation on vacuum annealed $\text{TiO}_2(110)$ resulting from a precursor-mediated interaction between CO_2 and H_2O ", *Surface Science* **400**, 203 (1998).
- [185] R. Schaub, E. Wahlström, A. Rønnau, E. Lægsgaard, I. Stensgaard, and F. Besenbacher, "Oxygen-Mediated Diffusion of Oxygen Vacancies on the $\text{TiO}_2(110)$ Surface", *Science* **299**, 377 (2003).
- [186] M. Ramamoorthy, R. D. King-Smith, and D. Vanderbilt, "Defects on $\text{TiO}_2(110)$ surfaces", *Physical Review B* **49**, 7709 (1994).
- [187] D. Vogtenhuber, R. Podloucky, A. Neckel, S. G. Steinemann, and A. J. Freeman, "Electronic structure and relaxed geometry of the TiO_2 rutile (110) surface", *Physical Review B* **49**, 2099 (1994).
- [188] P. J. D. Lindan, N. M. Harrison, M. J. Gillan, and J. A. White, "First-principles spin-polarized calculations on the reduced and reconstructed $\text{TiO}_2(110)$ surface", *Physical Review B* **55**, 15919 (1997).
- [189] S. P. Bates, G. Kresse, and M. J. Gillan, "A systematic study of the surface energetics and structure of $\text{TiO}_2(110)$ by first-principles calculations", *Surface Science* **385**, 386 (1997).
- [190] A. T. Paxton and L. Thiên-Nga, "Electronic structure of reduced titanium dioxide", *Physical Review B* **57**, 1579 (1998).
- [191] M. D. Rasmussen, L. M. Molina, and B. Hammer, "Adsorption, diffusion, and dissociation of molecular oxygen at defected $\text{TiO}_2(110)$: A density functional theory study", *Journal of Chemical Physics* **120**, 988 (2004).
- [192] U. Diebold, J. Anderson, K.-O. Ng, and D. Vanderbilt, "Evidence for the Tunneling Site on Transition-Metal Oxides: $\text{TiO}_2(110)$ ", *Physical Review Letters* **77**, 1322 (1996).
- [193] S. Munnix and M. Schmeits, "Electronic structure of ideal $\text{TiO}_2(110)$, $\text{TiO}_2(001)$, and $\text{TiO}_2(100)$ surfaces", *Physical Review B* **30**, 2207 (1984).
- [194] I. M. Brookes, C. A. Muryn, and G. Thornton, "Imaging Water Dissociation on $\text{TiO}_2(110)$ ", *Physical Review Letters* **87**, 266103 (2001).
- [195] E. Wahlström, Ongoing studies, 2004.

- [196] A. Rønnau, R. Schaub, E. Wahlström, E. K. Vestergaard, E. Lægsgaard, I. Stensgaard, and F. Besenbacher, "Long-Range Repulsive Vacancy-Vacancy Interactions on Rutile TiO₂(110)", *In preparation* (2003).
- [197] A. Rønnau, Ph.D. thesis, University of Aarhus, 2003.
- [198] G. Q. Lu, A. Linsebigler, and J. T. Yates, "The Photochemical Identification of 2 Chemisorption States for Molecular-Oxygen on TiO₂(110)", *Journal of Chemical Physics* **102**, 3005 (1995).
- [199] G. Q. Lu, A. Linsebigler, and J. T. Yates, "The Adsorption and Photodesorption of Oxygen on the TiO₂(110) Surface", *Journal of Chemical Physics* **102**, 4657 (1995).
- [200] C. N. Rusu and J. T. J. Yates, "Defect Sites on TiO₂(110). Detection by O₂ Photodesorption", *Langmuir* **13**, 4311 (1997).
- [201] W. S. Epling, C. H. F. Peden, M. A. Henderson, and U. Diebold, "Evidence for oxygen adatoms on TiO₂(110) resulting from O₂ dissociation at vacancy sites", *Surface Science* **412-413**, 333 (1998).
- [202] M. A. Henderson, W. S. Epling, C. L. Perkins, and C. H. F. Peden, "Interaction of Molecular Oxygen with the Vacuum-Annealed TiO₂(110) Surface: Molecular and Dissociative Channels", *Journal of Physical Chemistry* **103**, 5328 (1999).
- [203] C. L. Perkins and M. A. Henderson, "Photodesorption and Trapping of Molecular Oxygen at the TiO₂(110)-Water Ice Interface", *Journal of Physical Chemistry B* **105**, 3856 (2001).
- [204] M. M. Schubert, S. Hackenberg, A. C. van Veen, M. Muhler, V. Plzak, and R. J. Behm, "CO Oxidation over Supported Gold Catalysts—"Inert" and "Active" Support Materials and Their Role for the Oxygen Supply during Reaction", *Journal of Catalysis* **197**, 113 (2001).
- [205] R. Gomer, "Diffusion of Adsorbates on Metal Surfaces", *Reports on Progress in Physics* **53**, 917 (1990).
- [206] C. H. Mak, J. L. Brand, A. A. Deckert, and S. M. George, "Surface diffusion of hydrogen on Ru(001) studied using laser-induced thermal desorption", *Journal of Chemical Physics* **85**, 1676 (1986).
- [207] J. L. Brand, M. V. Arena, A. A. Deckert, and S. M. George, "Surface diffusion of n-alkanes on Ru(0001)", *Journal of Chemical Physics* **92**, 5136 (1990).
- [208] G. Ehrlich and F. Hudda, "Atomic View of Surface Self-Diffusion: Tungsten on Tungsten", *Journal of Chemical Physics* **44**, 1036 (1966).
- [209] G. L. Kellogg, "Field ion microscope studies of single-atom surface diffusion and cluster nucleation on metal surfaces", *Surface Science Reports* **21**, 1 (1994).
- [210] T. R. Linderoth, S. Horch, E. Lægsgaard, I. Stensgaard, and F. Besenbacher, "Surface Diffusion of Pt on Pt(110): Arrhenius Behavior of Long Jumps", *Physical Review Letters* **78**, 4978 (1997).
- [211] S. Horch, H. T. Lorensen, S. Helveg, E. Lægsgaard, I. Stensgaard, K. W. Jacobsen, J. K. Nørskov, and F. Besenbacher, "Enhancement of surface self-diffusion of platinum atoms by adsorbed hydrogen", *Nature* **398**, 134 (1999).
- [212] B. S. Swartzentruber, "Direct Measurement of Surface Diffusion Using Atom-Tracking Scanning Tunneling Microscopy", *Physical Review Letters* **76**, 459 (1996).
- [213] T. R. Linderoth, S. Horch, L. Petersen, S. Helveg, E. Lægsgaard, I. Stensgaard, and F. Besenbacher, "Novel Mechanism for Diffusion of One-Dimensional Clusters: Pt/Pt(110)-(1×2)", *Physical Review Letters* **82**, 1494 (1999).
- [214] R. v. Gastel, E. Somfai, W. v. Saarloos, and J. W. M. Frenken, "A giant atomic slide-puzzle", *Nature* **408**, 665 (2000).
- [215] R. v. Gastel, E. Somfai, S. B. v. Albada, W. v. Saarloos, and J. W. M. Frenken, "Nothing Moves a Surface: Vacancy Mediated Surface Diffusion", *Physical Review Letters* **86**, 1562 (2001).
- [216] M. L. Grant, B. S. Swartzentruber, N. C. Bartelt, and J. B. Hannon, "Diffusion Kinetics in the Pd/Cu(001) Surface Alloy", *Physical Review Letters* **86**, 4588 (2001).
- [217] M. Ø. Pedersen, L. Österlund, J. J. Mortensen, M. Mavrikakis, L. B. Hansen, I. Stensgaard, E. Lægsgaard, J. K. Nørskov, and F. Besenbacher, "Diffusion of N Adatoms on the Fe(100) Surface", *Physical Review Letters* **84**, 4898 (2000).

- [218] M. Schunack, T. R. Linderoth, F. Rosei, E. Lægsgaard, I. Stensgaard, and F. Besenbacher, "Long Jumps in the Surface Diffusion of Large Molecules", *Physical Review Letters* **88**, 156102 (2002).
- [219] J. V. Barth, "Transport of adsorbates at metal surfaces: from thermal migration to hot precursors", *Surface Science Reports* **40**, 75 (2000).
- [220] S. Renisch, R. Schuster, J. Winterlin, and G. Ertl, "Dynamics of Adatom Motion under the Influence of Mutual Interactions: O/Ru(0001)", *Physical Review Letters* **82**, 3839 (1999).
- [221] J. C. Dunphy, P. Sautet, D. F. Ogletree, and M. B. Salmeron, "Application of Scanning-Tunneling-Microscopy to Study Adatom Diffusion and Lateral Interactions - Sulfur on Re(0001) at Low Coverages", *Journal of Vacuum Science and Technology A* **11**, 2145 (1993).
- [222] T. Mitsui, M. K. Rose, E. Fomin, D. F. Ogletree, and M. Salmeron, "Water Diffusion and Clustering on Pd(111)", *Science* **297**, 1850 (2002).
- [223] P. G. Hoel, S. C. Port, and C. J. Stone, *Introduction to Probability Theory* (Houghton Mifflin Company, Boston, 1971).
- [224] G. Ehrlich, "Atomic Displacements in One- and Two-Dimensional Diffusion", *Journal of Chemical Physics* **44**, 1050 (1966).
- [225] S. C. Wang, J. D. Wrigley, and G. Ehrlich, "Atomic jump lengths in surface diffusion: Re, Mo, Ir, and Rh on W(211)", *Journal of Chemical Physics* **91**, 5087 (1989).
- [226] G. Wahnström, in *Interaction of Atoms and Molecules with Solid Surfaces*, edited by V. Bortolani, N. H. March, and M. P. Tosi (Plenum Press, New York, 1990).
- [227] J. Winterlin, R. Schuster, and G. Ertl, "Existence of a "Hot" Atom Mechanism for the Dissociation of O₂ on Pt(111)", *Physical Review Letters* **77**, 123 (1996).
- [228] H. Brune, K. Bromann, H. Röder, K. Kern, J. Jacobsen, P. Stoltze, K. Jacobsen, and J. K. Nørskov, "Effect of strain on surface diffusion and nucleation", *Physical Review B* **52**, 14380 (1995).
- [229] A. Bogicevic, J. Strömquist, and B. I. Lundqvist, "First-principles diffusion-barrier calculation for atomic oxygen on Pt(111)", *Physical Review B* **57**, R4289 (1998).
- [230] A. Bogicevic, S. Ovesson, P. Hyldgaard, B. I. Lundqvist, H. Brune, and D. R. Jennison, "Nature, Strength, and Consequences of Indirect Adsorbate Interactions on Metals", *Physical Review Letters* **85**, 1910 (2000).
- [231] W. Göpel, G. Rucker, and R. Feierabend, "Intrinsic defects of TiO₂(110): Interaction with chemisorbed O₂, H₂, CO, and CO₂", *Physical Review B* **28**, 3427 (1983).
- [232] E. Lundgren, G. Kresse, C. Klein, M. Borg, J. N. Andersen, M. De Santis, Y. Gauthier, C. Konvicka, M. Schmid, and P. Varga, "Two-Dimensional Oxide on Pd(111)", *Physical Review Letters* **88**, 246103 (2002).
- [233] J. Gustafson, A. Mikkelsen, M. Borg, E. Lundgren, L. Köhler, G. Kresse, M. Schmid, P. Varga, J. Yuhara, X. Torrelles, C. Quirós, and J. N. Andersen, "Self-limited growth of a thin oxide layer on Rh(111)", Submitted, 2003.
- [234] E. Lundgren, J. Gustafson, A. Mikkelsen, J. N. Andersen, A. Stierle, H. Dosch, M. Todorova, J. Rogal, K. Reuter, and M. Scheffler, "Kinetic hindrance during the initial oxidation of Pd(100) at ambient pressures", *Physical Review Letters* **92**, 046101 (2004).
- [235] M. Todorova, E. Lundgren, V. Blum, A. Mikkelsen, S. Gray, J. Gustafson, M. Borg, J. Rogal, K. Reuter, J. N. Andersen, and M. Scheffler, "The Pd(100)-($\sqrt{5} \times \sqrt{5}$)R27°-O surface oxide revisited", *Surface Science* **541**, 101 (2003).
- [236] C. I. Carlisle, D. A. King, M.-L. Bocquet, J. Cerdá, and P. Sautet, "Imaging the Surface and the Interface Atoms of an Oxide Film on Ag(111) by Scanning Tunneling Microscopy: Experiment and Theory", *Physical Review Letters* **84**, 3899 (2000).
- [237] M. Todorova, W. X. Li, M. Ganduglia-Pirovano, C. Stampfl, K. Reuter, and M. Scheffler, "Role of Subsurface Oxygen in Oxide Formation at Transition Metal Surfaces", *Physical Review Letters* **89**, 096103 (2002).

- [238] C. I. Carlisle, T. Fujimoto, W. S. Sim, and D. A. King, "Atomic imaging of the transition between oxygen chemisorption and oxide film growth on Ag(111)", *Surface Science* **470**, 15 (2000).
- [239] W.-X. Li, C. Stampfl, and M. Scheffler, "Why is a Noble Metal Catalytically Active? The Role of the O-Ag Interaction in the Function of Silver as an Oxidation Catalyst", *Physical Review Letters* **90**, 256102 (2003).
- [240] K. Reuter, C. Stampfl, M. V. Ganduglia-Pirovano, and M. Scheffler, "Atomistic description of oxide formation on metal surfaces: the example of ruthenium", *Chemical Physics Letters* **352**, 311 (2002).
- [241] K. Reuter and M. Scheffler, "Composition, structure, and stability of RuO₂(110) as a function of oxygen pressure", *Physical Review B* **65**, 035406 (2002).
- [242] K. Reuter, M. V. Ganduglia-Pirovano, C. Stampfl, and M. Scheffler, "Metastable precursors during the oxidation of the Ru(0001) surface", *Physical Review B* **65**, 165403 (2002).
- [243] M. Kulawik, N. Nilius, H.-P. Rust, and H.-J. Freund, "Atomic Structure of Antiphase Domain Boundaries of a Thin Al₂O₃ Film on NiAl(110)", *Physical Review Letters* **91**, 256101 (2003).
- [244] R. M. Jaeger, H. Kuhlenbeck, H.-J. Freund, M. Wuttig, W. Hoffmann, R. Franchy, and H. Ibach, "Formation of a well-ordered aluminium oxide overlayer by oxidation of NiAl(110)", *Surface Science* **259**, 235 (1991).
- [245] E. Lundgren, J. Gustafson, A. Mikkelsen, J. N. Andersen, A. Stierle, H. Dosch, M. Todorova, J. Rogal, K. Reuter, and M. Scheffler, "Kinetic hindrance during the initial oxidation of Pd(100) at ambient pressures", *Phys. Rev. Lett.*, in press, 2003.
- [246] G. V. Samsonov, *The Oxide Handbook* (IFI/Plenum, New York, 1973).
- [247] B. Hendriksen, Ph.D. thesis, University of Leiden, 2003.
- [248] P. B. Rasmussen, B. L. M. Hendriksen, H. Zeijlemaker, H. G. Ficke, and J. W. M. Frenken, "The "Reactor-STM": a scanning tunneling microscope for investigation of catalytic surfaces at semi-industrial reaction conditions", *Review of Scientific Instruments* **69**, 3879 (1998).
- [249] V. P. Zhdanov and B. Kasemo, "Kinetic phase transitions in simple reactions on solid surfaces", *Surface Science Reports* **20**, 113 (1994).
- [250] A. V. Walker, B. Klötzer, and D. A. King, "Dynamics and kinetics of oxygen dissociative adsorption on Pt{110}(1×2)", *Journal of Chemical Physics* **109**, 6879 (1998).
- [251] S. Helveg, H. T. Lorensen, S. Horch, E. Lægsgaard, I. Stensgaard, K. W. Jacobsen, J. K. Nørskov, and F. Besenbacher, "Oxygen adsorption on Pt(110)-(1×2): new high-coverage structures", *Surface Science* **430**, L533 (1999).
- [252] S. Helveg, Ph.D. thesis, University of Aarhus, 2000.
- [253] A. v. Oertzen, A. Mikhailov, H.-H. Rotermund, and G. Ertl, "Subsurface oxygen formation on the Pt(110) surface: experiment and mathematical modeling", *Surface Science* **350**, 259 (1996).
- [254] A. v. Oertzen, A. S. Mikhailov, H. H. Rotermund, and G. Ertl, "Subsurface Oxygen in the CO Oxidation Reaction on Pt(110): Experiments and Modeling of Pattern Formation", *Journal of Physical Chemistry B* **102**, 4966 (1998).
- [255] N. Saliba, Y.-L. Tsai, C. Panja, and B. Koel, "Oxidation of Pt(111) by ozone (O₃) under UHV conditions", *Surface Science* **419**, 79 (1999).
- [256] M. Berdau, S. Moldenhauer, A. Hammoudeh, J. H. Block, and K. Christmann, "Interaction of oxygen with Pt(210): formation of new oxygen states at higher exposures", *Surface Science* **446**, 323 (2000).
- [257] S. Helveg and E. K. Vestergaard, Unpublished, 2003.
- [258] L. Österlund, W.-X. Li, E. K. Vestergaard, T. M. Pedersen, J. Matthiesen, R. T. Vang, B. Hammer, and F. Besenbacher, "Oxidation of Pt(110)", In preparation, 2004.
- [259] E. Vesselli, C. Africh, A. Baraldi, G. Comelli, F. Esch, and R. Rosei, "(10×2) strained reconstruction induced by oxygen adsorption on the Rh(110) surface", *Journal of Chemical Physics* **114**, 4221 (2001).